The role of the M4 α-helix in lipid sensing by a pentameric ligand-gated ion channel

Camille Hénault

Thesis submitted to the University of Ottawa
in partial fulfilment of the requirements for the
Doctorate in Philosophy degree in Biochemistry

Department of Biochemistry, Microbiology and Immunology
Faculty of Medicine
University of Ottawa

Abstract

Pentameric ligand-gated ion channels (pLGICs) are membrane-embedded receptors found extensively in pre- and post-synaptic membranes throughout the nervous system where they play an important role in neurotransmission. The function of the prototypic pLGIC, the nicotinic acetylcholine receptor (nAChR) is highly sensitive to changes in its lipid environment, while other pLGICs display varying lipid sensitivities. This thesis presents a multidisciplinary investigation into the features of the transmembrane domain (TMD) that determine the unique functional and physical traits of different pLGICs. Using two prokaryotic homologues of the nAChR, ELIC and GLIC, as models, I focus on the outermost, lipid-exposed α-helix, M4, which, despite being distant from the primary allosteric pathway coupling agonist binding to channel gating, exercises significant control over channel function. Here, I present evidence that M4 acts as a lipid sensor, detecting changes in the surrounding lipids and transmitting these changes to the channel pore via contacts with the adjacent TMD α-helices, M1 and M3, and/or with structures in the extracellular domain. Using ELIC and GLIC chimeras, I first show that the TMD is the main driver of pLGIC thermal stability. I then demonstrate that the M4 α-helices in each channel play different roles in channel maturation and function, which suggests a divergent evolutionary path. Following this, I show that the M4 C-terminus is essential to both maturation and function in GLIC, while in ELIC its role is less defined, again showcasing possible evolutionary differences. Building on these findings, I examined the role of aromatic residues at the M4 – M1/M3 interface, and found that they predictably determine the interactions between M4 and M1/M3. Notably, the addition of aromatic residues to enhance M4-M1/M3 interactions in ELIC promotes channel function, while the elimination of aromatic residues at the M4-M1/M3 interface in GLIC is detrimental to channel function. Furthermore, I show that these same aromatics alter the strength of pLGIC lipid sensing and the sensitivity to certain disease-causing mutations, both indicating that aromatic residues are key players in channel function, stability and modulation. Finally, I and my collaborators identified and characterized a novel desensitization-linked lipid binding site in ELIC. Extensive mutagenesis studies coupled with biophysical measurements allowed us to develop a model describing how lipid binding influences the rates of ELIC desensitization to shape the agonist-induced response.

Acknowledgments

I first wish to thank my supervisor, Dr. John Baenziger. From the first undergrad Proteins lecture you gave, (you'll be horrified to learn that you told us to ignore how Fourier transform equations work and just trust the output), I felt like you were someone who appreciated the bigger picture without getting bogged down in useless details, and I wanted to work in your lab. Your light-handed mentorship was refreshing and welcome – you encouraged me to follow the paths I chose, and that freedom helped me achieve some of the work of which I'm most proud. You gave me confidence in my own abilities, in large part because I had confidence in yours. I'd often slump into your office with my data, hopelessly believing I was stuck, only to have you pointing out that the detail I'd missed wasn't a wall, it was a breakthrough! It wasn't just the research either. From lab camping trips to cross-country ski picnics, summer cottage trips, to drinks at the pub, it was a sincere pleasure to be a part of your research team, and I thank you for it all.

I also want to acknowledge my very first lab mentors, Casey and Peter. Peter, you showed such patience and willingness to teach me the basics when I was new and feeling utterly lost. All the good habits I learned about keeping lab records, I learned from you. Your reference letters helped me win my first scholarships, and I'm so grateful for all your help. Casey, you (mostly) patiently showed me the ropes even though you were trying hard to wrap up your own PhD and really didn't need a naïve undergrad underfoot. You also gave me one of the best pieces of advice about research that I've ever received: "If there's an experiment you think is worth running, write down what you want to do, why, the materials you'd need, and bring it to Dr. B. If he says no … do it anyway" That advice has served me well over the years. (Sorry Dr. B. – But I never went overboard, I swear!)

Jiayin, Jaimee and Dan, you guys were the best lab-mates and friends that I could have wished for, and I'm so happy for (and irrationally proud of) all your successes since you each moved on from the lab. You guys were a huge reason that I looked forward to coming in every day. Thanks for always being there to bounce ideas off, help troubleshoot experiments, to just chat with in the office or cook s'mores with over a campfire.

Diego, without your support and gentle pushing I don't think I would have been able to finish this. Finally, thank you to my parents. I love you both so much.

Preface

This thesis is a collection of 4 manuscripts, with data presented as follows:

Chapter 3: Hénault, C.M., and Baenziger, J.E. (2017). Functional characterization of two prokaryotic pentameric ligand-gated ion channel chimeras – role of the GLIC transmembrane domain in proton sensing. Biochim. Biophys. Acta - Biomembr. *1859*, 218–227. http://dx.doi.org/10.1016/j.bbamem.2016.11.006

Chapter 4: Hénault, C.M., Juranka, P.F., and Baenziger, J.E. (2015b). The M4 transmembrane α-helix contributes differently to both the maturation and function of two prokaryotic pentameric ligand-gated ion channels. J. Biol. Chem. *290*, 25118–25128. https://doi.org/10.1074/jbc.M115.676833

Chapter 5: Carswell, C.L., **Hénault, C.M*.,** Murlidaran, S., Therien, J.P.D., Juranka, P.F., Surujballi, J.A., Brannigan, G., and Baenziger, J.E. (2015b). Role of the Fourth Transmembrane α Helix in the Allosteric Modulation of Pentameric Ligand-Gated Ion Channels. Structure *23*, 1655–1664. http://dx.doi.org/10.1016/j.str.2015.06.020

***co-first author**

Chapter 6: Hénault, C.M., Govaerts, C., Spurny, R., Brams, M., Estrada-Mondragon, A., Lynch, J., Bertrand, D., Pardon, E., Evans, G.L., Woods, K., et al. (2019). A lipid site shapes the agonist response of a pentameric ligand-gated ion channel. Nat. Chem. Biol. *15*, 1156–1164. https://doi.org/10.1038/s41589-019-0369-4

There are additionally two review articles, included in the **Appendix**:

Hénault, C.M., Sun, J., Therien, J.P.D., DaCosta, C.J.B., Carswell, C.L., Labriola, J.M., Juranka, P.F., and Baenziger, J.E. (2015). The role of the M4 lipid-sensor in the folding, trafficking, and allosteric modulation of nicotinic acetylcholine receptors. Neuropharmacology *96*, 157–168. http://dx.doi.org/10.1016/j.neuropharm.2014.11.011

Baenziger, J.E., **Hénault, C.M**., Therien, J.P.D., and Sun, J. (2015). Nicotinic acetylcholine receptor-lipid interactions: Mechanistic insight and biological function. Biochim. Biophys. Acta - Biomembr. *1848*, 1806–1817. http://dx.doi.org/10.1016/j.bbamem.2015.03.010

Table of Contents

Abbreviations

^{1}H	Hydrogen
^{125}I-TID	3-trifluoromethyl-3-(m-[^{125}I]-iodophenyl)diazirine
^{2}H	Deuterium
$^{2}H_2O$	Deuterium oxide
5-HT_3R	Serotonin receptor
α-BTX	α-bungarotoxin
ACh	Acetylcholine
AChBP	acetylcholine-binding protein
AMPA	α-amino-3-hydroxy-5-methyl-4-isoxazolepropionic acid
ANAP	3-(6-acetylnaphthalen-2-ylamino)-2-aminopropanoic acid
ANOVA	Analysis of variance
ATP	Adenosine triphosphate
Aso-ELIC	ELIC reconstituted into asolectin lipids
Aso-EG	EG reconstituted into asolectin lipids
Aso-GE	GE reconstituted into asolectin lipids
Aso-GLIC	reconstituted into asolectin lipids
cAMP	Cyclic adenosine monophosphate
Ca^{2+}	Calcium ion
CNS	Central nervous system
DTT	Dithiothreitol
DDM	N-dodecyl-β-D-maltoside
DLPE	1,2-dilauroyl-sn-glycero-3-phosphoethanolamine
K^{+}	Potassium ion
GPCR	G-protein coupled receptor
IC_{50}	Concentration at half-maximal inhibition
ICD	Intracellular domain
IPTG	Isopropyl β-d-thiogalactopyranoside
E. coli	*Escherichia coli*
EC_{50}	Half maximal effective concentration
ECD	Extracellular domain
EG	ELIC-GLIC chimera
GDP	Guanosine diphosphate
ELIC	*Erwinia* ligand-gated ion channel
GE	GLIC-ELIC chimera
GTP	Guanosine triphosphate
GLIC	*Gloeobacter* ligand-gated ion channel
GlyR	Glycine receptor
LB	Luria bertani
MES	2-(N-morpholino)ethanesulfonic acid

MTSR	methanethiosulfonate-rhodamine
Na^+	Sodium ion
nAChR	Nicotinic acetylcholine receptor
NMDA	N-methyl-D-aspartate
OD_{600}	Optical density (600nm)
PA	Phosphatidic acid
PI	Phosphatidylinositol
PS	Phosphatidylserine
pLGIC	Pentameric ligand-gated ion channel
PNS	Peripheral nervous system
POPC	1-palmitoyl-2-oleoyl-sn-glycero-3-phosphocholine
POPE	1-palmitoyl-2-oleoyl-sn-glycero-3-phosphoethanolamine
TEVC	Two-electrode voltage clamp
Td	Thermal denaturation temperature
TMD	Transmembrane domain
UDM	n-undecyl-β-D-maltoside

List of Tables

List of Figures

Chapter 1. Introduction

The human brain is the control center for essential processes including thought, emotion, decision-making, memory, and learning. It also drives how we perceive and interact with the world around us. Yet the brain is just one part of the nervous system, which is an intricate biological network formed from interconnected nerve cells, called neurons, that function to send signals and feedback to and from different areas of the body. The nervous system can be divided into two main parts: the central and the peripheral nervous systems. The brain and spinal cord form the central nervous system (CNS), which receives and processes information, and then sends feedback to the rest of the body. The peripheral nervous system (PNS) acts as an extension of the CNS, connecting it to the different body parts. Together, the two nervous systems form a complex interrelated network, where innumerable components work in a delicate balance to allow our bodies to function.

Although a high level of complexity is required for the CNS and PNS to carry out their functions, this complexity comes with increased risk of disruptions, with minor, molecular scale misfires over time leading to cascading failure resulting in organismal disease, dysfunction or even death. In order to fully understand and ultimately treat, neurological disease, it is necessary to go beyond the organismal level and to examine physiological processes on a cellular and molecular level. Although the latter has allowed us to progressively gain insight into global biological functions, with the medical field making constant steady advances in the treatment of myriad diseases, in many cases the underlying molecular mechanisms remain a mystery.

The work presented in this thesis focuses on one set of actors implicated in neurological signaling and thus both neurological function and disease: the superfamily of pentameric ligand-gated ion channels (pLGICs). Ultimately, the goal of my research was to gain a greater understanding of the most abundant pLGIC, the nicotinic acetylcholine receptor (nAChR). nAChRs are ligand-gated ion channels that are found throughout the central and peripheral nervous systems where they play important roles in the chemical signaling between cells. I am interested in the mechanisms by which nAChR activity is modulated during both normal and abnormal brain function. In particular, the activity of the

prototypic nAChR, the muscle-type nAChR from *Torpedo*, is highly dependent on its lipid environment. The goal of my research was to explore how differences in the transmembrane domain (TMD) structures of pLGICs influence lipid-protein and protein-protein interactions. To accomplish these goals, I used two prokaryotic pLGICs as models to discern basic physical rules governing the function of the more complex eukaryotic pLGICs. To put my research into perspective, I will first review neuronal signal transduction, before delving into pLGIC structure and function.

1.1 The Nervous System

The CNS plays the role of a two-way central computer, receiving, processing and integrating external signals and simultaneously sending out information and instructions to the body via the PNS, effectively its extension throughout the body. Communication between distant sites is made possible by the specialized cells of which the nervous system is comprised: primarily glial and neuronal cells. Glial cells surround neurons, forming a matrix which supports, insulates and provides nutrients to neurons, facilitating neurotransmission. The neurons themselves permit the transmission of chemical and electrical signals throughout the body. Signal transduction is the process by which an external stimulus (mechanical, chemical etc.) is converted into physiological information and then transmitted, via neuronal pathways to the brain, or by which signals from the brain are conveyed to peripheral systems.

As a result of the sensitivity, complexity and modulability of the nervous system, organismal function can be significantly impacted by seemingly minor disturbances to normal neuronal activity, either indirectly through the effects of exogenous and endogenous compounds, or directly through genetic mutations. Even subtle changes within the CNS/PNS can have profound effects on human biology, however, consequently, many neuronal structures and components are excellent therapeutic targets for the treatment of neuronal disease and dysfunction. A deeper understanding of these components is essential to understanding both neuromuscular function and the human brain, and to the development of pharmaceuticals for the treatment of neurological or neuromuscular disorders.

1.1.1 Neuronal Structure and Neurotransmission

Many different types of neuron exist, even within the nervous system of a single species. Afferent sensory neurons conduct impulses from outer receptors for integration within the CNS and efferent motor neurons send impulses from the CNS to downstream effectors, such as glands and muscles, for both voluntary and involuntary physiological responses. Despite some variability in the structure of different types of neurons, as a general rule, neurotransmission occurs via the same basic process. An incoming inhibitory or excitatory signal is first detected by highly branching dendrites, which transmit that information to the cell body, also called the soma (Figure 1.1A). The signal is then sent via the axon hillock, as an electrical impulse, called an action potential, along the axon to the axon terminus. The axon itself is a thin, projected fiber, varying in length but potentially reaching up to 1.5M in length in adults. Many nerve cell axons are discontinuously coated in a lipid-rich substance called a myelin sheath, which serves to both insulate the fibers and to increase the rate at which action potentials move along the axon. Unmyelinated sections of the nerve, called nodes of Ranvier, are found at intervals along the axon, and these allow the more rapid transmission of action potentials via saltatory conduction, to "jump" each myelinated internode, moving directly to the next node of Ranvier, ultimately reaching the axon terminus more rapidly than by the steady wavelike action potentials seen in unmyelinated fibers.

The conduction of electrical signals within the nerve is based on the controlled diffusion of ions down their electrochemical gradients into the cell. Most cells in the body are electrically polarized, existing in a dynamic steady state, balanced by this ion flux. The difference in the interior and exterior cell membrane electric potential is called the membrane potential. At rest, the membrane potential of a cell remains constant, typically -70 mV. An action potential occurs when the membrane potential of an excitable cell such as the cell body, soma or axon hillock rapidly spikes upwards, then rapidly falls. This occurs when Na^+ channels open in the membrane in response to various stimuli, causing a rapid influx of Na^+ ions along their concentration gradient and thereby creating a locally positive environment within the cell, known as depolarization. As the depolarization reaches +30 mV, the positive environment activates voltage-gated potassium channels, which allow K^+ ions to exit the cell, again along an electrochemical gradient, thereby restoring, or repolarizing the membrane

Figure 1.1 Structure of a Neuron

A) Schematic representation of a neuron showing structural elements. A chemical signal is detected by the dendrites, converted into an electical signal, and transmitted via the soma to the axon hillock. From there the signal travels along the axon, jumping rapidly between myelinated segments by saltatory conduction. Upon arrival at the axon terminus, it is converted back into a chemical signal. **B)** The shape of an action potential, which occurs within the neuronal membranes. A stimulus perturbs the resting state, causing rapid depolarization of the membrane to +30mv, followed by a depolarization below resting potential, and a refractory period that maintains directional flow of the electrical impulse along the axon.

A

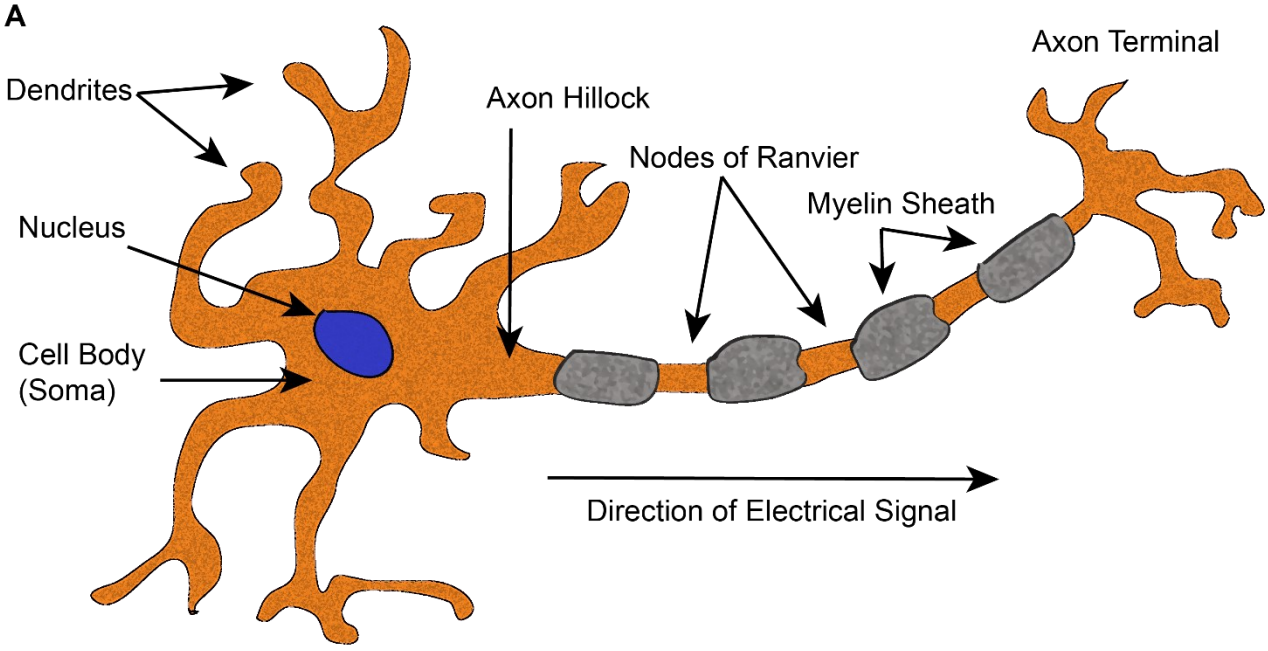
Dendrites
Axon Hillock
Axon Terminal
Nodes of Ranvier
Myelin Sheath
Nucleus
Cell Body
(Soma)
Direction of Electrical Signal

B

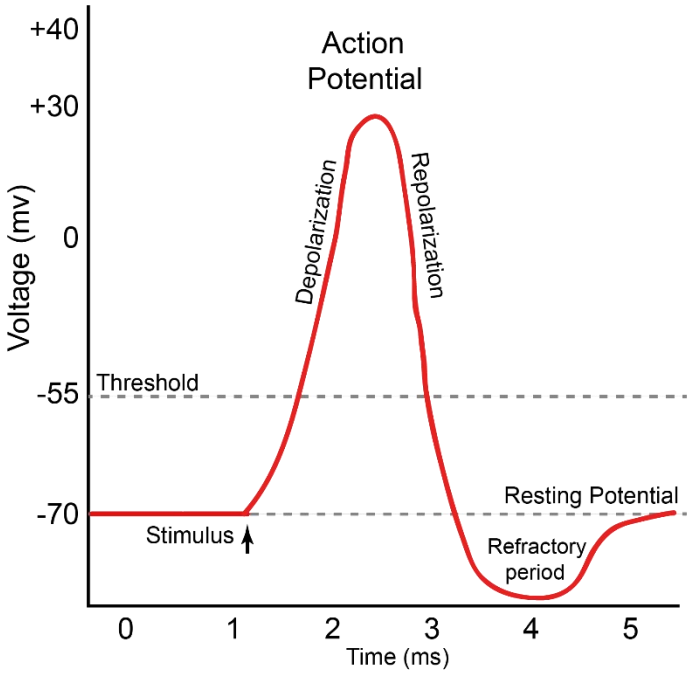
+40
+30
0
-55
-70
Voltage (mv)
Action
Potential
Depolarization
Repolarization
Threshold
Resting Potential
Stimulus
Refractory
period
0
1
2
3
4
5
Time (ms)

potential (Figure 1.1B), and even going beyond the standard resting potential to briefly hyperpolarize below normal membrane potential.

For an action potential to occur, a threshold membrane potential of -55 mV must be reached, triggering the opening of voltage-gated sodium channels. A stronger stimulus detected by the neuron increases the probability that an action potential will occur, though it does not affect its strength – an action potential is an all-or-none process. The electrical signal of the action potential is propagated along the length of the neuron as more voltage-gated Na^+ channels open in response to the increasingly positive cell environment, and depolarization spreads uni-directionally from node to node down the neuron as a result of the refractory period that occurs following repolarization. At the axon terminal, the electrical impulse is converted back to a chemical signal. Neurotransmitters are stored in synaptic vesicles at the axon terminal; these are released as the incoming action potential activates voltage-sensitive calcium (Ca^{2+}) channels which trigger the fusion of neurotransmitter-laden vesicles with the plasma membrane, releasing neurotransmitter (Figure 1.2). The neurotransmitter molecules diffuse into the microscopic extracellular space between neurons or between neurons and muscle, called the synaptic cleft, and then interact with the postsynaptic receptors found in neurons or muscle fibers, propagating the signal throughout the body.

Figure 1.2 Diagram of a Chemical Synapse

1) As the electrical impulse arrives at the axon terminus of the presynaptic neuron, it triggers the opening of voltage-gated calcium channels and an influx of Ca^{2+} ions. **2**) The increased calcium levels promote neurotransmitter-laden vesicles merging with the presynaptic membrane, releasing their contents into the extracellular space. **3**) Neurotransmitter molecules diffuse across the synaptic cleft, binding to receptors on the postsynaptic neuron, opening ion channels and propagating the signal. **4**) The unbound neurotransmitter molecules diffuse out of the cleft for either degradation or recycling by the presynaptic cell. Figure modified from the MSc thesis of JP Daniel Therien.

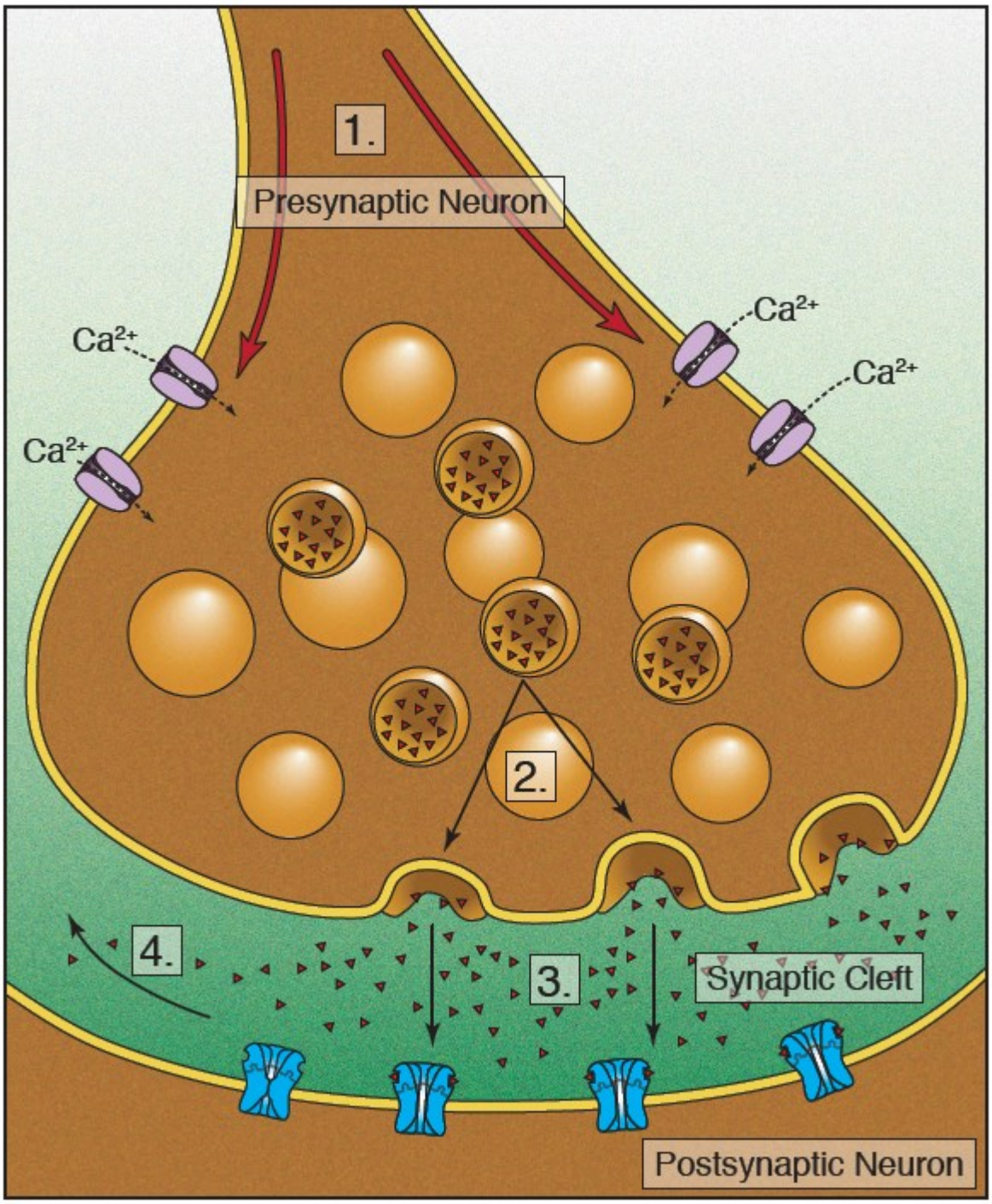
1.
Presynaptic Neuron
Ca2+
Ca2+
Ca2+
Ca2+
2.
3.
4.
Synaptic Cleft
Postsynaptic Neuron

Ion channels are major actors in the detection and propagation of these chemical signals. As described above, voltage-gated Na^+, K^+ and Ca^{2+} channels control ion balance across the cell membrane. Following *and* preceding an action potential, a variety of proteins, called receptors, embedded in the post-synaptic membrane bind the different neurotransmitter molecules that are released from the axon terminus to diffuse through the synaptic cleft. At the post-synaptic membrane, the diverse interactions of multiple families of transmembrane receptors permits both indirect and direct interpretation and propagation of the chemical signal detected. Indirect, or metabotropic, signaling is observed with certain protein family receptors, such as G-protein-coupled receptors (GPCRs). When a GPCR's agonist binds, conformational changes in the protein's 7 transmembrane segments activate a downstream signaling process, often involving GTP/GDP and ATP/cAMP messengers, which indirectly modulates a separate ion channel, rather than directly gating it. Conversely, in the case of direct modulation which occurs with ionotropic receptors, agonist binding rapidly causes these receptors to undergo a conformational change, resulting in the transient opening of a transmembrane channel. Both of these activation types alter the ionic balance of the postsynaptic cell, differing primarily in the speed at which activation occurs, with metabotropic receptors being considered "slow", on the seconds to minutes time scale, while ionotropic receptors are "fast" – activating in a fraction of a second. Certain neurotransmitter molecules can even interact with different types of receptors simultaneously to provoke opposing inhibitory or excitatory responses, and this, combined with the fact that most ion channels are ion-selective, limiting them to the transport of a single ion type, or charged state, generates the complex interplay of fast and slow activation and repression we observe during neuronal regulation.

Within the ionotropic receptor superfamily there are further structural divisions to be made: trimeric receptors such as ATP-gated P2X ion channels, tetrameric glutamate-activated receptors such as the well-known AMPA (α-amino-3-hydroxy-5-methyl-4-isoxazolepropionic acid), NMDA (N-methyl-D-aspartate) and Kainate receptors, and pentameric ligand-gated ion channels (pLGICs), which comprise a further superfamily of neurotransmitter-binding ion channels in multicellular organisms. The latter family includes the nicotinic acetylcholine (nAChR), serotonin ($5\text{-}HT_3$), Glycine (GlyR) and gamma-

aminobutyric acid ($GABA_A$) receptors, which, by convention fall into a group called the Cys-loop receptors, named for a distinct loop near the agonist-binding site that is closed by a conserved disulfide bond.

Together in the post-synaptic membrane, and indeed throughout the entire nervous system, these many different receptor protein families form the signaling bridge between neurons, allowing ions to continue to flow along their electrochemical gradient, producing an excitatory or inhibitory response in the cell and changing the probability that an action potential will occur, restarting the signaling process. Importantly, many of these receptors have been demonstrated to have either direct or indirect roles in both neurological and neuromuscular disease. In some cases, as part of normal function, they perform overlapping, complementary, opposing or even redundant roles, however each one is essential to organismal health, and all work in concert to maintain neuronal communication.

1.2 Pentameric ligand-gated ion channels

1.2.1 The Pentameric Ligand-gated Ion Channel superfamily

pLGICs are found throughout the CNS and PNS, are critical to information processing and are central to higher brain functions. pLGICs are also implicated in numerous neurological disorders, including Alzheimer's and Parkinson's diseases, schizophrenia, epilepsy and more. The superfamily is divided into four families of pLGICs, with each family responding to a different neurotransmitter: glycine, GABA, serotonin, or acetylcholine (ACh). The binding of GABA or glycine to their pLGICs leads to the flux of anions across the membrane and thus an inhibitory response, while the binding of serotonin or ACh leads to the flux of cations across the membrane and thus an excitatory response.

As discussed in detail below, all pLGICs exhibit a conserved architecture, with the five subunits arranged symmetrically (homopentamers) or pseudo-symmetrically (heteropentamers) around a central ion channel pore. Within each pLGIC family, however, varying subunit combinations confer on each pLGIC unique functional and pharmacological traits (Kozuska and Paulsen, 2012). These functional traits, along with distinct patterns of expression in the brain, lead to unique roles for each pLGIC type in neurological or

neuromuscular function. They also render each type of pLGIC a target for pharmaceutical treatment of specific neurological or neuromuscular disorders.

1.2.2 The nAChR

The most studied member of the pLGIC family is the nAChR. From comparatively naive studies, as early as the 19th century, of the Amazonian neurotoxin *curare*, nAChR research has progressed exceedingly far. One significant advance in our ability to study the receptor directly came from the discovery that the electric organ of the *Torpedo* ray is an abundant source of the fetal muscle-type nAChR ($\alpha_2\beta\gamma\delta$) (Changeux et al., 1970). In the living *Torpedo* organism, the nAChR-rich electroplaque organ generates an electric field which plays roles in navigation, mate selection, self-defense, and in sensing and stunning prey. nAChRs expressed in these organs share significant sequence and structural similarity with the human muscle type nAChR (Hille, 2001) and can be purified in much larger quantities than were, and are still, obtainable from any other natural sources (Eldefrawi et al., 1972). The *Torpedo* nAChR was the first neurotransmitter receptor to be isolated (Karlsson et al., 1972; Miledi et al., 1971; Olsen et al., 1972), the first to be imaged, the first to have its subunit N terminal amino acids sequenced and the first to have its entire nucleotide coding regions defined.

The ACh receptor family is further broken down into neuronal and neuromuscular receptor forms, based on their subunit composition. The different nAChR subunit types were originally classified in the muscle-type *Torpedo* nAChR based on SDS-PAGE gel migration as α, β, γ and δ in order of size. Since the first isolation of the muscle-type nAChR, a total of sixteen genes that code for sixteen homologous nAChR subunits have been identified in mammals, and the subunit classification similarly has been expanded to encompass α1-α7, α9-α10, β1-β4, γ, ε, and δ. Muscle-type nAChRs are composed of four distinct subunits in an $(\alpha1)_2\beta1\delta\gamma$ (fetal) or $(\alpha1)_2\beta1\delta\varepsilon$ (adult) hetero-pentamer, while neuronal nAChRs are homo- or heteropentamers, combining α (α2-α7, α9-α10) and non-α (β2-β4) subunits, with the homomeric α7 and heteromeric α4β2 nAChRs being particularly prevalent in the CNS.

1.2.3 pLGIC Structure and Function

In the early 2000s, a crystal structure of the water-soluble acetylcholine binding protein (AChBP), a homo-pentamer that shares significant sequence and structural homology with the nAChR extracellular domain, led to the first "high resolution" structural insight into the mechanisms of agonist binding. In 2005, electron microscopic images of crystalline tubes formed from native *Torpedo* membranes were interpreted, along with the high resolution AChBP crystal structure and the vast body of biophysical work compiled for the nAChR, to build and then refine a 4Å resolution a structure of the *Torpedo* nAChR (Unwin, 2005). For the greater part of a decade this structure served as the sole available model of a vertebrate pLGIC, and it has remained the only *Torpedo* structure available until the recent publication of 2.7Å Cryo-EM structure (Rahman et al., 2020). Although the *Torpedo* nAChR isolate remains relevant to current functional and structural research, advances in the techniques used to study pLGICs have allowed us to both view membrane proteins at a higher resolution, and to study functional channels in a more native-like environment.

The next major step in the elucidation of pLGIC structures came from the discovery of prokaryotic pLGICs, which are homologues of the nAChR. Not only was the simple existence of such proteins a surprise, as they were previously thought to be exclusively expressed in eukaryotes, but the prokaryotic homologues were subsequently shown to be amenable to crystallographic studies. The first prokaryotic pLGIC structure of the *Erwinia chrysanthemi* receptor (ELIC) in a presumed closed conformation was solved in 2008 (Hilf and Dutzler, 2008). This was followed by structures of apparently open conformations of the *Gloeobacter violaceus* receptor (GLIC) in 2009 (Hilf and Dutzler, 2009). Since then, numerous structures of ELIC and GLIC in various conformations and with different bound ligands have been solved, with expression and crystallographic techniques evolving in tandem as protocols became more refined, giving greater and greater structural resolution, and thus greater understanding and insight into pLGICs in general. Among these structures there were putative open, closed and desensitized states viewable for the first time, providing the first insight into the conformational changes that occur following ligand binding. In 2011, the first crystal structure of a eukaryotic pLGIC, the glutamate-gated chloride channel from *Caenorhabditis elegans* (Hibbs and Gouaux, 2011), was published, followed in 2014 by the

first vertebrate receptor structures: mouse 5-HT_{3A} (Hassaine et al., 2014) and human $GABA_A\beta3$ (Miller and Aricescu, 2014). In more recent years, the first neuronal nAChR structure was solved (Morales-Perez et al., 2016). Since then, technical advancements in single particle cryo-electron microscopy have led to an explosion of new structures for all members of the pLGIC super-family, including the above-noted α-bungarotoxin-bound structure of the *Torpedo* nAChR (Rahman et al., 2020).

Figure 1.3 Structure of the *Torpedo nAChR*

A) A side view of the nAChR is shown on the left, with the extracellular domain (ECD) in red, the transmembrane domain (TMD) in blue, and the intracellular domain (ICD) in green. Residues within the agonist binding site (αTrp149) and the channel gate (Leu 9' and Val 13') are shown as yellow spheres. Top-down views of the ECD and TMD are shown on the right, with agonist binding site and channel gate highlighted. **B)** A side view of a single α-subunit at the interface between the ECD and TMD, highlighting the loops that mediate communication between the two domains.

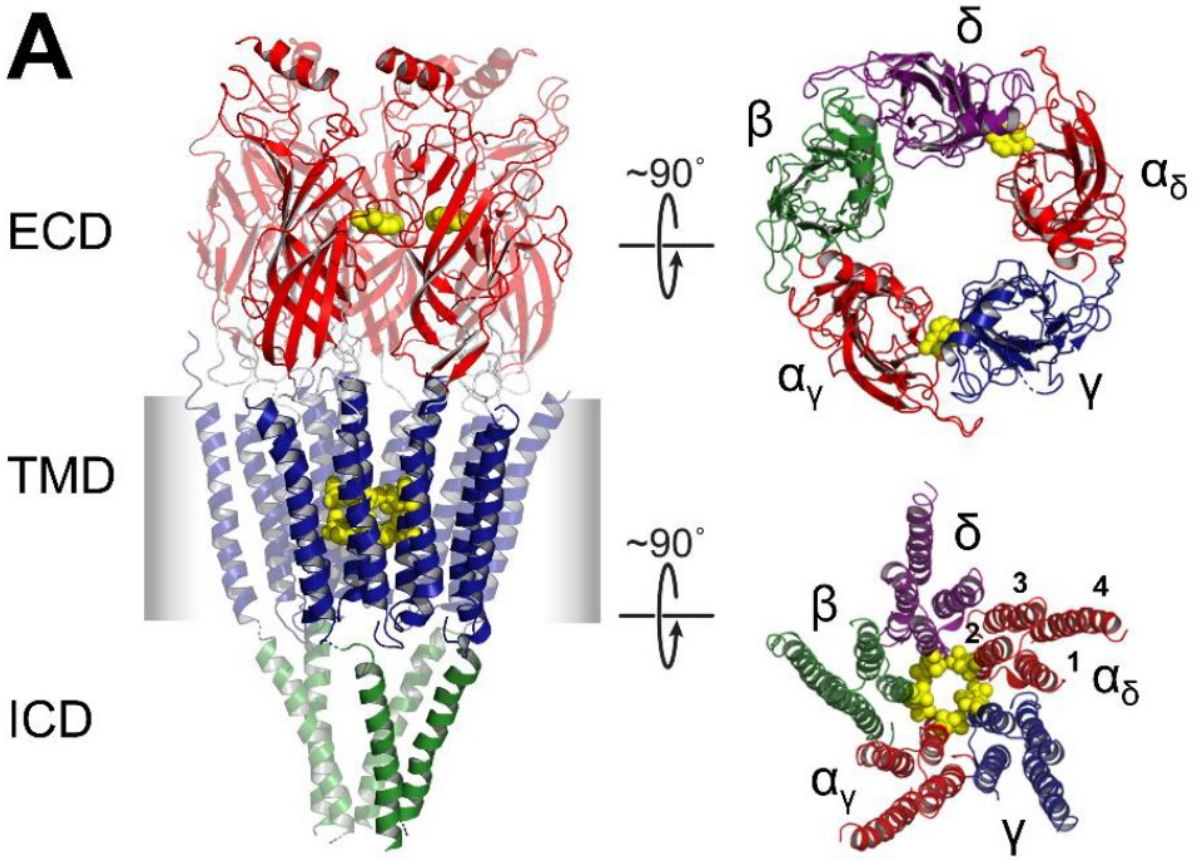
A
ECD
TMD
ICD
~90°
~90°
δ
β
α_δ
α_γ
γ
δ
β
3
4
2
1
α_δ
α_γ
γ

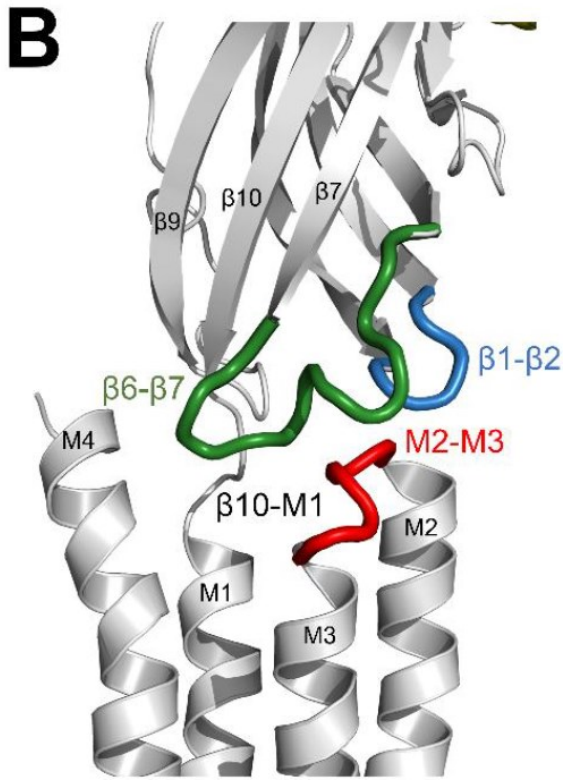
B
β9
β10
β7
β1-β2
β6-β7
M4
M2-M3
β10-M1
M2
M1
M3

Structurally, each pLGIC subunit is divided into three distinct domains: an extracellular, agonist-binding domain (ECD), a transmembrane ion-conducting domain (TMD), and an intracellular vestibule domain, for which complete structural information is not yet available. (Figure 1.3) Each of the N-terminal ECD segments is approximately 200 residues long, formed mainly by 10 β-strands, numbered β1- β10, and organized in a classic β-sandwich. The β-sandwich structures of each subunit interact with those of two adjacent subunits to ultimately form the pentamer, with between two and five neurotransmitter binding sites located at the interfaces between the subunits. In the muscle nAChR, the principal face of each agonist site is located on an α-subunit near the two vicinal cross-linked cysteine residues that define α versus non-α subunits (Kao and Karlin, 1986). Four aromatic residues (in *Torpedo*, Tyr93, Trp149, Tyr190, and Tyr198) from three separate loops (loops A, B, and C) play a key role in agonist binding (Dennis et al., 1988; Galzi et al., 1990; Middleton and Cohen, 1991). In muscle-type nAChRs, the complementary face of the binding site is formed from three loops (D, E, and F) located on the adjacent γ/ε- and δ-subunits (Corringer et al., 1995; Czajkowski et al., 1993) (Figure 1.3A). The agonist binding sites in heteromeric nAChRs are often distinct, each having a unique pharmacological profile. The ECD meets the TMD at an interface near the extracellular lipid bilayer surface and interacts with the TMD via "interlocking" loops found on both domains.

The ECD is separated from the adjacent ~150-residue long C-terminal TMD by a short linker (β10-M1) and is distinguished by an abrupt change in secondary structure. The transmembrane domain forms a single ion conducting pore along the pseudo-symmetry axis of the protein (Corringer et al., 2000; Miyazawa et al., 2003; Unwin, 2005), and each subunit contributes four α-helices, M1-M4, organized in a classic four-helix bundle, with the M2 helix from each subunit creating the channel pore, M1 and M3 forming a ring of α-helices that shield M2 from the membrane. The M4 α-helices are located on the periphery of each subunit and are highly exposed to the lipid bilayer. The ECD and TMD meet at an interface defined by the covalent link between β10 and M1, and by non-covalent interactions between the β1-β2/β6-β7 (called the Cys-loop in eukaryotic pLGICs) loops and the M2-M3 linker. Although the detailed structural changes that occur when agonist binding couples to channel gating remain to be defined, it is thought that concerted movements of the two β-sheets in the ECD lead to changes in structure of both the β1-β2 and β6-β7 loops, which then translate into

movement of the pore-lining M2 α-helices via direct interactions with the M2-M3 linker (Bocquet et al., 2009; Hibbs and Gouaux, 2011; Hilf and Dutzler, 2009; Lee and Sine, 2005; Lummis et al., 2005; Mitra et al., 2004; Sauguet et al., 2014; Unwin and Fujiyoshi, 2012). In the closed, or resting state, the ion pore is occluded by hydrophobic residues that form a barrier to the flow of a solvated ion (Beckstein and Sansom, 2006). Upon gating, a twisting and tilting of the pore-lining M2 α-helices lead to a widening of the channel pore by ~3 Å, allowing the flow of solvated ions down their electrochemical gradient into (Na^+ and Ca^{2+}) or out of (K^+) the cell. Prolonged exposure to agonist also leads to the formation of one or more poorly defined desensitized conformations, which are characterized by both a relatively high affinity for acetylcholine and channel inactivity (Changeux and Edelstein, 2005).

The intracellular domain, found only in eukaryotic pLGICs, is located between M3 and M4, and is characterized by a disordered region typically followed by a long amphipathic α-helix, termed the MA α-helix. In some pLGICs, a short α-helix, referred to as the MX α-helix, is also located just after M3 where it is oriented parallel to the bilayer surface. While the ECD and TMD show high sequence homology between different receptors, the ICD is highly divergent in both length and sequence across receptors. As well, it is not essential for function in all cases (Jansen et al., 2008) and indeed is absent in prokaryotic pLGICs. The role of the ICD is incompletely understood; however, it has been demonstrated that it plays a role in channel conductance (daCosta and Sine, 2013) and thus may serve as a tuning mechanism for receptor function or potency, among other roles.

1.2.3.1. The function of the *Torpedo* nAChR is sensitive to lipids

Because pLGICs are membrane-embedded proteins, it is reasonable to expect that they exhibit a structural, and thus functional, sensitivity to their surrounding lipid environment. Indeed, early attempts to isolate and reconstitute neurotransmitter-induced channel gating in model membranes quickly confirmed that the activity of the *Torpedo* nAChR is exquisitely sensitive to lipids (Criado et al., 1982; Epstein and Racker, 1978; Fong and McNamee, 1986; Heidmann et al., 1980; McNamee and Fong, 1988). In order to retain agonist-induced cation flux, the receptor had to be solubilized and purified in the presence of lipid, and then placed in a membrane with an appropriate “activating” lipid composition. In the early and mid-1980s, ion flux studies suggested that when the *Torpedo* nAChR is

reconstituted into vesicles composed of phosphatidylcholine (PC), anionic lipids and cholesterol at a molar ratio of 3:1:1, it displays robust agonist-induced response, while the *Torpedo* nAChR reconstituted into vesicles lacking either cholesterol, anionic lipids, or *both* does not. It was originally proposed that both cholesterol and phosphatidic acid (PA) or other anionic lipids bound at specific sites on the receptor and thereby each modified and/or stabilized the nAChR structure in complementary ways, with the binding of *both* being essential to receptor function, a view which is still commonly held by some, though there is increasing evidence for both non-specific lipid binding sites, and of modulation by bulk lipid physical properties (Baenziger et al., 2017; Thompson and Baenziger, 2020).

The early ion flux assays, however, suffered from the fact that the size of the reconstituted vesicles varied tremendously along with lipid composition, with vesicle size directly affecting the magnitude of the detected ion flux response. Although attempts were made to normalize for variations in vesicle size, the authors ultimately chose an arbitrary value of threshold flux response, with those vesicles producing a response below this threshold being deemed non-functional, and those above it considered to be supporting functional nAChRs. As these relatively crude assays were improved upon over time, it became evident that the impact of lipids on function was far more complex than initially suggested. It was later shown that increasing levels of *either* anionic lipids or cholesterol in a PC membrane led to an increasing proportion of agonist-responsive *Torpedo* nAChRs (Baenziger et al., 2000; Hamouda et al., 2006a). Likewise, cholesterol analogs and other neutral lipids were found to be capable of substituting for cholesterol in supporting *Torpedo* nAChR function, (Addona et al., 2003; Labriola et al., 2010; Sunshine and McNamee, 1992). Additionally, when the stabilizing properties of other anionic lipids were tested in the presence of cholesterol, PA was found to stabilize the largest population of activatable receptors, while other anionic lipids, such as phosphatidylserine (PS) and phosphatidylinositol (PI) produced only 50-60% of activatable, resting state receptors compared to PA. Notably, when levels of PA and cholesterol were varied, the stabilizing effect of cholesterol was found to saturate at 35mol %, which corresponds to the molar % of cholesterol found in native *Torpedo* membranes. PA, however, is found in relatively low molar ratios in native *Torpedo* membranes (<1%) but the stabilizing effect was found to

saturate at 12 mol %, suggesting that despite PA's greater stabilizing ability relative to other lipids, these others likely substitute for PA in native membranes (Hamouda et al., 2006a). Although these lipid and lipid analog studies confirmed that membranes composed of PC, PA and cholesterol are optimal for supporting nAChR function, they suggested that while allosteric binding sites for either lipid may exist, the lipid specificities of these sites is low and their occupancies are not absolutely required for channel function.

Beyond lipid binding sites, the nAChR can also be influenced by the physical properties of the surrounding lipid bilayer. Further studies have expanded our understanding of the receptor's lipid requirements, demonstrating that bulk membrane properties, in addition to putative specific lipid binding sites, likely play a role in stabilizing channel function. In PC membranes lacking cholesterol, only PA, added in sufficient quantities, can stabilize a large proportion of functional receptors (daCosta et al., 2002, 2004, 2009). This stabilizing effect, seen only from PA, is proposed to be a result of its unique physical characteristics. The PA molecule has a small phosphate headgroup, which gives the full lipid a tapered or "conical" shape, compared to other phospholipids with larger headgroups. Upon incorporation into PC membranes, PA may be able to "wedge" in and induce an ordering of the surrounding lipids, an effect that could mimic some of the effects observed upon cholesterol incorporation into membranes (daCosta et al., 2002). This stabilizing effect is not seen in PC/PS-incorporated membranes lacking cholesterol (PS, though also a net-negative lipid, has a large headgroup and thus a cylindrical, rather than tapered shape), suggesting that the ability of PC/PA membranes to stabilize a large proportion of agonist-activatable nAChRs is not solely a result of PA's anionic charge, but rather that PA may have the dual effect of creating a bilayer with both the anionic charge and the bulk membrane physical properties required for optimal *Torpedo* nAChR function. This understanding of the magnitude of modulation by lipids is further supported by the observation that membrane hydrophobic thickness influences *Torpedo* nAChR conformational transitions (daCosta et al., 2013) (See below).

It is now thought that lipid composition influences nAChR function by a conformational selection mechanism, whereby lipids modulate the equilibria between activatable and non-activatable states. Although this conformational selection mechanism

was originally interpreted in terms of the canonical resting (activatable) and desensitized (non-activatable) conformations (Baenziger et al., 2000; Hamouda et al., 2006a; McCarthy and Moore, 1992), the nAChR in reconstituted PC membranes lacking cholesterol and

Figure 1.4 nAChR conformational states

In the absence of agonist, the receptor primarily adopts a resting conformation (R). Agonist binding induces a transition to the open state (O) which allows ions to flow through the receptor. Prolonged exposure to agonist results in a non-functional desensitized (D) state which binds agonist with high affinity but no longer permits ion flux. The uncoupled conformation (U) is a lipid-dependent conformation which binds agonist with resting state-like affinity but does not undergo channel gating. Figure adapted from DaCosta and Baenziger, 2009.

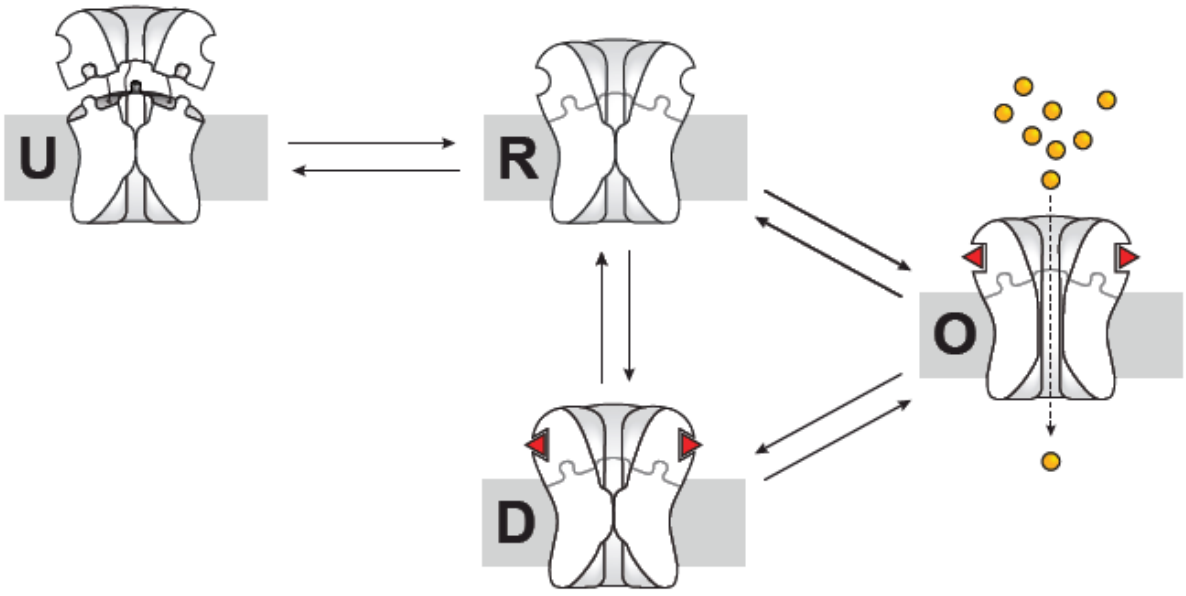
U
R
O
D

anionic lipids adopts an additional "uncoupled" conformation that exhibits resting state-like agonist binding, but does not undergo agonist-induced conformational transitions (daCosta and Baenziger, 2009). The proposed conformational selection mechanism is thus now interpreted in terms of resting, desensitized and uncoupled nAChRs. (Figure 1.4)

As mentioned above, membrane thickness has also been shown to affect the transitions between nAChR conformational states. When the nAChR is reconstituted in di-18:1-PC bilayers (18 carbon acyl chains) lacking activating lipids (Cholesterol/PA) it is locked in the uncoupled state that does not undergo agonist-induced conformational transitions under the time scales of most biochemical assays (seconds to minutes). However, when reconstituted into the thicker di22:1-PC (22 carbon acyl chain) membranes, the nAChR slowly transitions from uncoupled to coupled conformations on the minutes to hours timescale (daCosta et al., 2013). This observation suggests that membranes/lipids interact with the transition states that occur between conformations to influence the rates of conformational transitions (i.e., via a "kinetic" mechanism). Lipids and bulk membrane physical properties can thus influence function by both conformational selection and kinetic mechanisms.

1.2.3.2. Sites of lipid action

Attempts have been made to determine the various sites of lipid action in the nAChR. These putative sites of action include annular sites, at the periphery of the TMD, and non-annular sites, inside the TMD and thus shielded from the lipid environment. Notably, the M4 transmembrane α-helix in each subunit has the most extensive bridging contact with the TMD and the surrounding lipids, and thus represents a main site for annular lipid binding. This led to the suggestion that M4 plays a central role in lipid-sensing. Indeed, annular lipid binding sites have been detected in several pLGIC structures at the interfaces between M4 and the two adjacent TMD α-helices, M1 and M3. Also of significance, electrophysiology studies suggest that M4 moves during channel gating (see below), which would thus provide the opportunity for lipids to interact differently with one conformation versus another to impact on channel function (Mitra et al., 2004). In this context, the entire lipid-exposed

surface of the nAChR may serve as an annular “allosteric site” that is sensitive to both bound annular lipids and bulk membrane physical properties.

Chemical labeling studies in the early 1990's with the hydrophobic photo-reactive probe, [^{125}I]-TID (3-(trifluoromethyl)-3-(m-iodophenyl) diazirine), showed that the M4 transmembrane α-helix forms the predominant interface between the TMD and the lipid environment (Blanton and Cohen, 1992, 1994), a finding that has been confirmed in all pLGIC structures. Despite being peripheral to the structures that link the agonist site to the channel gate, M4, makes extensive contact with the lipid bilayer and is thus ideally situated to sense changes in the lipid environment. It has been suggested that M4 is thus an intrinsic “allosteric regulator” of pLGIC activity, and likely serves as a lipid sensor, transmitting information inward to the TMD core. (Antollini et al., 2005; Xu et al., 2005). To test this hypothesis, numerous mutations of lipid-facing residues on both *Torpedo* and muscle-type nAChRs have been constructed, and many were found to alter channel function (Blanton and Cohen, 1992; Bouzat et al., 1998; Lasalde et al., 1996; Lee et al., 1994; Li et al., 1992; Shen et al., 2006; Tamamizu et al., 2000). These studies confirmed that even though M4 is distant from both the agonist site and channel gate, its structure influences gating. The amino acid changes studied to date have typically altered channel opening and closing rates. Interestingly, homologous mutations on different subunits often have opposing effects on channel gating, with some mutations leading to gain, and others to loss of function phenotypes (Bouzat et al., 1998, 2000, 2002).

When shifting between resting and open conformational states, M4 is by no means a static structural element. In fact, the different motions of the M4 α-helices in the different subunits upon gating may account for the divergent functional effects observed with homologous lipid-facing M4 mutations on different subunits. When gating, the two αM4 α-helices in the $(\alpha 1)_2\beta 1\varepsilon\delta$ pentamer move synchronously, each moving as a unit roughly halfway along the reaction coordinate between agonist binding and the open transition state (Mitra et al., 2004). The motions of the εM4 and βM4 follow that of αM4, while δM4 has no apparent motion during gating. The temporal differences in various M4 positions can conceivably permit the pentamer to present a unique binding surface to the lipid bilayer in each distinct conformation and/or while transitioning between them. Such structural changes

in M4 could then expose or mask lipid binding sites, allowing for stronger or weaker interactions with the lipid bilayer that preferentially stabilize different conformations or promote/inhibit transitions between these states. In addition, biophysical measurements and molecular dynamics simulations suggest that the orientation of M4 relative to the membrane normal depends on the presence of cholesterol and bilayer thickness (Antollini et al., 2005; Xu et al., 2005). Lipids may preferentially stabilize different orientations of M4 relative to the remainder of the TMD, altering gating kinetics as M4 moves along the reaction coordinate leading from agonist binding to the open state. It has been suggested that it is in this manner, through lipid binding sites as well as bulk membrane properties, that a large proportion of information regarding the lipid environment is transmitted into functional activity of the nAChR protein.

Further implicating M4 and the TMD in lipid sensing and function, structural data has confirmed the presence of lipid binding sites at the interface between M4 and adjacent helices, as well as in other locations. The first x-ray crystal structure to show bound lipids was that of GLIC, a prokaryotic homologue of the nAChR (Bocquet et al., 2009). This apparently open-conformation structure of detergent-solubilized GLIC showed three densities attributed to indeterminate lipid molecules, bound to each subunit. The molecules were modeled as PC, and found bound in two sites (corresponding to the extracellular and cytoplasmic leaflets) at the M4/M1 interface, and to a third site (extracellular leaflet) at the M4/M3 interface. It is worth noting that GLIC was solubilized and crystallized in the absence of added lipids, so the lipids bound to the TMD were retained from the endogenous *E. coli* membranes in which GLIC was expressed. In addition, both cholesterol and neurosteroid photoaffinity probes label residues that broadly overlap with all the observed lipid binding sites on GLIC (Budelier et al., 2019; Cheng et al., 2018). These binding sites are notable as they were later discovered to overlap with both PC binding sites from the α1β3γ2 $GABA_AR$ and with a putative site of neurosteroid potentiation found in both the $GABA_AR$ and the α4β2 nAChR (Chiara et al., 2013; Forman and Miller, 2016; Forman et al., 2015). Likewise, lipids have recently been shown to bind at equivalent sites at the M1/M4 and M3/M4 interfaces in various nAChRs. Although bound lipids were not shown in the moderate resolution (4Å) 2005 Cryo-EM structure of the *Torpedo* nAChR, low-density

patches of lipid, attributed to cholesterol, were observed both in inter- and intra-helical spaces of the TMD (Unwin, 2005). More recently, multiple structures of various human nAChR constructs (α3β4, $(\alpha4)_2(\beta2)_3$ and $(\alpha4)_3(\beta2)_2$) (Gharpure et al., 2019; Morales-Perez et al., 2016; Rahman et al., 2020; Walsh et al., 2018) have been solved by Cryo-EM and crystallographic techniques, at up to 2.7Å resolution, and show regions of electron density corresponding to cholesterol in the cytoplasmic leaflet on the outer edge of the TMD, on each side of M4, the M1/M4 and M3/M4 interfaces. The two cytoplasmic leaflet-bound lipids bracket the C-terminal segment of M4 on either side, with the M4/M1 bound lipid extending to contact the M3 α-helix from the adjacent principal subunit. These sites correspond to positions that are labelled by a photoactivatable cholesterol probe in the *Torpedo* nAChR (Hamouda et al., 2006a), and also overlap with the binding of phospholipids to the $5HT_{3A}R$, α1β3γ2 $GABA_AR$, and ELIC, and to sterol/neurosteroid binding to the α4β2/α3β4 nAChRs and the α1/α5 $GABA_AR$. indicating a likely conserved cholesterol binding site across multiple nAChR and pLGIC subtypes, and again suggesting a significant role for M4 in modulating channel function via interactions with both bound and membrane-associated lipids.

The lipids binding to the M4/M1/M3 interfaces in the extracellular leaflet (described above) are particularly intriguing as this site is located near structures at the ECD/TMD interface that play an important role in channel gating. In GLIC structures showing the open conformation, the bound PC bridges interactions between aromatic residues on M4 and the extracellular β6-β7 loop (the Cys-loop in eukaryotic pLGICs) while the choline head group projects toward the pre-M1 loop. However, electron densities for this lipid, and for the arginine side chains seen in the open state, are not observed in structures of GLIC solved in resting or locally closed conformations (Prevost et al., 2012; Sauguet et al., 2014). One possible interpretation of these observations is that the lipid helps stabilize the open conformation by enhancing interactions between the β6-β7 loop and the M2-M3 linker.

Variable binding of the extracellular leaflet lipid is also observed in the presence of allosteric modulators. The binding of the inhibitory drugs, propofol and desflurane, both overlap with the lipid binding site, with propofol binding eliminating lipid binding and desflurane binding substantially altering the lipid binding pose so that the PC headgroup

angles towards the β6-β7 loop. In contrast, the fatty acid, docosahexaenoic acid (DHA), which enhances GLIC desensitization, binds to a site adjacent to the bound PC. DHA forms a salt bridge with Arg118 of the β6-β7 loop, with a consequent movement of Arg118 likely facilitating a subtle repositioning of both the PC headgroup and its fatty acyl chains (Basak et al., 2017). Significantly, mutating Arg118 to Ala reduces the effects of DHA on GLIC desensitization. In addition, electron paramagnetic resonance shows that the O_2 accessibility of residues in the lipid binding pocket is enhanced when GLIC transitions from the resting to desensitized states, suggesting a concomitant movement of the bound lipid (Basak et al., 2016; Velisetty et al., 2014). While further experiments are still required to establish a causative link between lipid binding and GLIC function, the altered lipid binding poses in different functional states implies a modulatory role.

Finally, the prokaryotic homologues GLIC and ELIC each display different lipid requirements and sensitivities. Since their discovery in the mid-2000s, GLIC and ELIC have increasingly been used as models for probing fundamental mechanisms underlying pLGIC-lipid interactions. Although the effects of lipids on GLIC and ELIC function in membranes of defined lipid composition have not yet been characterized, GLIC reconstituted in minimal PC membranes retains the ability to undergo agonist-induced cation flux while ELIC (as with the *Torpedo* nAChR) does not (Carswell et al., 2015a; Labriola et al., 2013). In addition to effects on channel gating, the rate of desensitization of GLIC is sensitive to membrane lipids, as increasing levels of cholesterol in soybean asolectin membranes leads to increasing rates of GLIC desensitization (Velisetty and Chakrapani, 2012).

1.2.3.3. pLGIC uncoupling

The M4 lipid-sensor model is clearly speculative, and many facets of this model require rigorous testing using structural, functional, and biophysical approaches. The importance of the model is that it provided a starting point for understanding the molecular mechanisms that underlie lipid-sensing. It should be noted, however, that the model is supported by considerable data. A central feature is the postulate that the ECD adopts an independent structure that can at least partially dissociate from the TMD to form what is known as the uncoupled conformation.

In addition to the canonical resting, open and desensitized conformations, membrane-reconstituted *Torpedo* nAChR adopts a lipid-dependent "uncoupled" conformation that exhibits resting state-like agonist binding, but does not undergo agonist-induced conformational transitions. With publication of the nAChR structure (Unwin, 2005), existing functional and biophysical data on lipid-nAChR interactions were consolidated into a structural model of uncoupling, wherein the ECD "uncouples" from the TMD, no longer forming the necessary contacts by which agonist binding is translated into channel gating. The feasibility of this conformation is supported by the structural independence of the ECD, demonstrated by the existence of stable pentameric water-soluble AChBPs, which are homologous to the ECD of the nicotinic ACh receptor (Brejc et al., 2001). Folded, stable, water soluble ECDs of both the nicotinic ACh receptor a-subunit and GLIC can also be expressed independently of their respective TMDs (Dellisanti et al., 2007; Nury et al., 2010a). Both pentameric and hexameric structures of the GLIC ECD have been solved by X-ray crystallography.

As noted above, considerable evidence had implicated the transmembrane α-helix, M4, in lipid-sensing. The atomic model and subsequent mutagenesis studies further highlighted the importance of noncovalent interactions between loops at the ECD/TMD interface in coupling agonist binding to channel gating (Jha et al., 2007; Lee et al., 2009). It was known that although the quaternary/secondary structures and thermal denaturation temperature of the uncoupled nAChR are both similar to that of resting and desensitized nAChRs (Bhushan and McNamee, 1990; daCosta et al., 2005; Methot et al., 1995), the uncoupled nAChR undergoes more rapid peptide N-^{1}H/N-^{2}H exchange. Significantly, the changes in peptide hydrogen exchange kinetics suggest that uncoupling is accompanied by the solvent exposure of previously buried peptide hydrogens (Baenziger and Methot, 1995; daCosta and Baenziger, 2009; Methot et al., 1995). Although the regions of the nAChR that become solvent-exposed were not defined in this experiment, the critical importance of the ECD/TMD interface in channel function led to the hypothesis that uncoupling results from structural changes at the ECD/TMD interface. Weakened interactions leading to an increased physical separation between the ECD and TMD could account for the loss of gating function,

retained agonist binding, and the increased solvent accessibility observed in the uncoupled state.

It was also evident from the 2005 nAChR structure that the C-terminus of M4 (post-M4, specifically Gln435) extends beyond the lipid bilayer to interact with a conserved residue (Phe137) in the Cys-loop. Given that the Cys-loop plays a central role at the interface between the ECD and TMD, it was postulated that interactions between post-M4 and the Cys-loop are important for coupling agonist-binding to channel gating, and that lipids influence nAChR function by modulating post-M4 interactions with the Cys-loop. Ineffective post-M4/Cys-loop interactions could lead to partial dissociation of the ECD from the TMD to form the uncoupled state, thus accounting for the increased solvent exposure of the peptide backbone (daCosta and Baenziger, 2009).

The assertion that direct interactions between post-M4 and the Cys-loop are important for nAChR activity was also supported by functional studies. Shortening M4 in the *Torpedo* nAChR alters both channel function and trafficking to the cell surface (Tobimatsu et al., 1987). M4 C-terminal deletions have deleterious effects on an α7-5HT_{3A} chimera, leading to the suggestion that interactions between the penultimate tyrosine in M4 and the Cys-loop lock the chimera in a mature agonist binding conformation that traffics to the cell surface (Pons et al., 2004). The C-terminus of M4 is also essential for neurosteroid-induced potentiation of α4β2 nAChRs, indicating a further role in channel modulation and function.

Finally, crystal structures of the prokaryotic pLGIC, ELIC, provide direct structural evidence for the proposed model of uncoupling. As discussed below, the ELIC structure exhibits many of the proposed features of the uncoupled state. Furthermore, crystallized ELIC adopts a conformation that does not gate open in response to agonist binding. The identification of homopentameric prokaryotic pLGICs, GLIC and ELIC, that are homologous to the nAChR represented a major advance in the structural characterization of pLGICs (Bocquet et al., 2007; Tasneem et al., 2005). Both GLIC and ELIC have been expressed in *Escherichia coli* at levels sufficient for both biochemical and structural studies, and each has yielded numerous high resolution crystal structures (Bocquet et al., 2009; Hilf and Dutzler,

2008; Sauguet et al., 2013; Zimmermann and Dutzler, 2011). These structures reveal two key features that impact on our understanding of lipid-nAChR interactions.

First, as discussed above, crystal structures of GLIC exhibit electron density located at the periphery of the TMD, corresponding to binding sites of partially ordered lipid molecules (Bocquet et al., 2009), with two of the three lipid binding sites on each subunit being found at the interfaces between M4 and the adjacent TMD a-helices M1 and M3. The finding that lipids bind to the interface between M4 and, M1 and M3 supports the hypothesis that lipids influence M4-M1/M3 interactions. Second, the crystal structures of ELIC (Gonzalez-Gutierrez et al., 2012; Zimmermann and Dutzler, 2011) provide insight into the lipid-dependent uncoupled conformation. Structures solved in the presence of agonist exhibit electron density in the agonist site likely corresponding to bound agonist, but show no structural rearrangements in the TMD pore relative to crystal structures solved in the absence of agonist. In fact, no movement of the pore-lining M2 α-helices was detected with mutants that prolong channel opening and exhibit no propensity to desensitize. The lack of change in the structure of the pore-lining α-helices in apo and holo forms of both desensitizing wild type and non-desensitizing mutant ELIC structures, as well as other functional data, were interpreted to suggest that the structures reflect a non-desensitized conformation that is refractory to agonist-induced conformational transitions (Gonzalez-Gutierrez and Grosman, 2010) - i.e. a conformation that is functionally equivalent to the lipid-dependent uncoupled state (daCosta et al., 2013; Gonzalez-Gutierrez et al., 2012).

Significantly, the ELIC structures exhibit many of the proposed structural features of the uncoupled nAChR. The M4 α-helix in this potentially uncoupled structure is partially unwound and tilted away from the remaining TMD, with several C-terminal M4 residues not observed. In contrast to the nAChR structure, the ELIC structure shows no direct contact between post-M4 and the β6-β7 loop. The tilting of M4 away from the remainder of the TMD is also accompanied by reduced contact between both the β1-β2 and β6-β7 loops of the ECD and the M2-M3 linker of the TMD. In the nAChR structure, the extended side chains of the β1-β2 and β6-β7 loops engage the M2-M3 linker in a fashion reminiscent of vice grips attached to a metal pipe (Figure 1.3B). In ELIC, the β1-β2 and β6-β7 loops no longer surround the M2-M3 linker, which itself tilts towards the membrane surface so that it

approaches the β8-β9 loop on the complementary face of the adjacent subunit. In effect, reduced interactions between M4 and M1/M3 are accompanied by weakened interactions between the ECD and TMD - as predicted by the M4 lipid-sensor model which proposes that effective M4 binding to the adjacent transmembrane α-helices, M1 and M3, is essential in coupling the ECD and TMD, and in the absence of effective M4-M1/M3 interactions, the nAChR adopts an uncoupled state.

Note also that the tilted orientation of the M4 α-helix away from the main body of the TMD in crystal structures of ELIC contrasts the conformation of the M4 α-helix in the GLIC structures, where M4 binds tightly to the adjacent TMD α-helices, M1 and M3 (daCosta and Baenziger, 2013). These structural differences between ELIC and GLIC are intriguing given the important role of aromatic residues in the binding of M4 to M1/M3 during folding of the homologous glycine receptor (Haeger et al., 2010). GLIC has nine aromatic residues at the interfaces between M1, M3, and M4 that are involved in extensive π-π interactions. Four of these are conserved in ELIC, with the remaining five aromatics replaced in ELIC by aliphatic residues (See figures 4.2, and 5.1B). In particular, ELIC lacks a cluster of three aromatic residues located near post-M4 that may be essential for effective binding of post-M4 to the remainder of the TMD and/or the β6-β7 loop. The lower number of aromatic interactions at the M4-M1/M3 interface may render M4 binding to M1/M3 weaker in ELIC and thus make ELIC more susceptible to the perturbing effects of detergent solubilization during crystallization than GLIC (daCosta and Baenziger, 2013).

The ability of GLIC, discussed above, to couple agonist binding to channel gating in minimal PC bilayers has been proposed to be a result of the complex network of aromatic residues that exist at the M4 - M1/M3 interface. These residues likely strengthen M4 – M1/M3 interactions making the TMD less malleable and thus less sensitive to surrounding lipids. In contrast, ELIC exhibits only a few aromatic residues at this interface, with these bulky single residues likely preventing close M4 associations with M1/M3, thus creating a more malleable M4 – M1/M3 interface that renders ELIC more sensitive to its surrounding membrane environment, and it is this hypothesis, as well as the role of M4 in lipid sensing, that the majority of the work presented here sought to test.

1.3 Summary and Thesis Objectives

The overall goal of my thesis was to explore the role of M4 and M4 – M1/M3 interactions in pLGIC function, and to look for elements therein which affect lipid sensing and lipid-dependent modulation of pLGICs. Given the different conformations and compositions of M4, and the different levels of aromatic residues in ELIC and GLIC, these two model systems provided a unique opportunity to probe the role of M4 in pLGIC function, channel modulation and uncoupling.

In Chapter 2, I describe the common materials and methods that I used while performing the experiments presented here, to avoid repetition, as the majority of the work has an electrophysiological component and uses the same techniques. Unique methods specific to a single paper are emphasized within that chapter.

Chapter 3 describes how I generated two pLGIC chimeras of GLIC and ELIC, by cross-combining the extracellular and transmembrane domains of each to create ELIC-GLIC (EG) and GLIC-ELIC (GE), in order to investigate how these distinctly different TMDs alter channel function.

In Chapter 4, I present a comparison between ELIC and GLIC M4 helices by alanine scanning mutagenesis, demonstrating the significant differences in the roles each M4 α-helix plays in its respective parent protein. I also look at the effects of M4 C-terminal deletions on both channel function, and surface expression of ELIC and GLIC.

Chapter 5 builds on the previous chapters where I show that ELIC and GLIC M4 helices perform different roles in each protein. In the work presented here, I attempt to make ELIC more GLIC-like, and GLIC more ELIC-like, through the insertion and deletion, respectively, of a feature I suspected played a role in the unique M4 helix roles and properties: aromatic residues. I also examine the effect of a gain of function mutation found in human nAChR. This mutation, which causes congenital myasthenic syndrome in humans, serves as a probe in this work, and is inserted into GLIC and ELIC, to measure changes in M4/M1/M3 interactions in various mutants, to investigate channel stability.

The work presented in Chapter 6 was initiated from an observation I made during the alanine scan, presented in chapter 4. Though I first thought that the ELIC P305A mutant was non-functional, when I attempted to confirm that, I discovered that it not only retained function, but that its activity was significantly altered. Chapter 6 looks at the role of this highly conserved proline residue found in the M4 of pLGICs, and suggests a role for it in forming a lipid binding pocket that affects channel desensitization.

Chapter 7 concludes the main body of the thesis by summarizing thesis highlights and briefly delving into ELIC's value as a pLGIC model.

Chapter 8 comprises the appendix, which contains two additional publications that I authored during my studies, both review articles, and references can be found in Chapter 9.

Chapter 2. Materials and Methods

Due to the overall consistency in nature of the methods between the papers presented in this thesis, this chapter consolidates the methods I used to perform the experiments, to avoid repetition. In cases where I collaborated with other researchers, an additional methods section is included in the chapter itself to present their methods.

2.1 Bacterial strains and plasmid generation

E. coli Dh5α or XL1-Blue/Gold strains were used for DNA amplification, RNA templates and cloning purposes. For the purposes of protein expression, the *E. coli* BL21(DE3) strain was used for ELIC/EG and C43 for GLIC/GE.

2.1.1 cRNA Constructs for Oocyte Expression

GLIC-pMT3 was kindly provided by Dr. Pierre-Jean Corringer (Bocquet et al., 2009). The GLIC coding sequence was transferred to pSP64 without the C-terminal hemagglutinin tag. ELIC-pTLN was kindly provided by Dr. Raimund Dutzler (Zimmermann et al., 2012). A C-terminal Ala, a cloning artifact not present in the GenBank sequence (GenBank: POC7B7), was removed. Both the GLIC and ELIC plasmids have the a7 nAChR signal sequence followed by the GLIC or ELIC coding sequence. ELIC-pTLN and GLIC-pSP64 were linearized by MluI and EcoRI, respectively, and used to produce capped cRNA by *in vitro* transcription using the mMESSAGE mMACHINE SP6 kit (Ambion). All mutants were created using QuikChange site-directed mutagenesis kits (Agilent) and verified by Sanger sequencing (uLaval).

2.1.2 Construction of plasmids for protein expression

A pET-26b expression vector containing the pelB signal sequence followed by a (His) 10-Tag and then the maltose binding protein fused to the N-terminus of ELIC was kindly provided by Dr. Raimund Dutzler. The GE and EG chimeras were transferred into pET20b and pET26b vectors, each containing the DNA sequence for the maltose binding protein (MBP) fused to the N-terminal of the GLIC or ELIC coding sequences via a thrombin-sensitive or HRV-3C protease-sensitive peptide linker, respectively.

2.1.3 GLIC/ELIC Chimera generation

Starting with the GLIC-pMT3 and ELIC-pTLN plasmids, two regions corresponding to the ECD and TMD of each gene were separately amplified using one normal and one overlapping chimeric primer to produce complementary "short" PCR products corresponding to the ECD and TMD of ELIC and GLIC. These products were then fused via a second PCR reaction to generate the pLGIC chimeras. The resulting full-length sequence-verified chimeric gene products GLIC-ELIC (GE) and ELIC-GLIC (EG) were inserted into the pSP64 oocyte expression vector. EG-pSP64 and GE-pSP64 were linearized by MluI and EcoRI, respectively and used to produce capped cRNA by in vitro transcription using the mMESSAGE mMACHINE® SP6 kit (Ambion). Further mutations, such as loop substitutions were generated using the QuikChange Lightning Mutagenesis kit (Agilent).

2.2 Electrophysiology

Stage V–VI oocytes from *X. laevis* were isolated as previously described (Laitko et al., 2006). Defolliculated oocytes were injected with the indicated amount of mRNA and allowed to incubate for 1 to 4 days at 16°C in ND96 + buffer (5 mM HEPES, 96 mM NaCl, 2 mM KCl, 1 mM $MgCl_2$, 1 mM $CaCl_2$, 2 mM pyruvate). Injected oocytes were placed in a RC-1Z oocyte chamber (Harvard Apparatus) containing the appropriate buffer (see below). Whole-cell currents were recorded using a two-electrode voltage-clamp apparatus (OC-725C oocyte clamp; Harvard Apparatus). The whole-cell currents were recorded while the appropriate buffer flowed through the oocyte chamber at a rate of 5–10 ml/min.

For GLIC, whole-cell currents were recorded from injected oocytes (3–13 ng cRNA) immersed in MES (2-(N-morpholino)ethanesulfonic acid) buffer (140 mM NaCl, 2.8 mM KCl, 2 mM $MgCl_2$, and 10 mM MES). Currents through the plasma membrane in response to pH jumps (pH 7.3 down to the indicated pH values) were measured with the transmembrane voltage clamped at voltages between -10 and -60 mV depending on the level of expression of each mutant GLIC. In most cases, the holding potential was -20 mV.

For ELIC, whole-cell currents were recorded from injected oocytes (0.2–10 ng cRNA) immersed in HEPES buffer (150 mM NaCl, 0.5 mM $BaCl_2$ 10 mM HEPES, pH 7.0,

1mM DTT). In most cases, currents through the plasma membrane in response to cysteamine concentration jumps (from 0 mM up to the indicated values) were measured with the transmembrane voltage clamped at -40 mV.

Dose responses for each mutant were acquired from at least two different batches of oocytes. Each individual dose-response experiment was fit with a variable slope sigmoidal dose response, and the individual EC_{50} and Hill coefficients from each experiment averaged to give the values ± SD. For the presented dose-response curves, the individual dose responses for each experiment were normalized and each data point averaged. Curve fits of the averaged data are presented, with the error bars referring to the SE.

2.2.1 Radioligand binding

To detect surface expression of GLIC mutants and of the GE chimera, the loop C sequence KPANFALEDRLESK (GLIC extracellular domain) was replaced by the sequence SERFYECCKEPYPD from the α7 AChR, as originally described (Wang et al., 2012), using the Quikchange lightning mutagenesis kit (Agilent). The expression of GE in the oocyte membrane was assayed by measuring the binding of ^{125}I-labelled α-Bungarotoxin (^{125}I-BTX; PerkinElmer Life Sciences (Boston,MA)) to intact oocytes. Oocytes were injected with cRNA (0.1–26 ng) encoding the BTX-tagged constructs. Following expression for 1–4 days, the oocytes were tested via two-electrode voltage clamp (TEVC) to determine activity levels, then incubated with occasional shaking, for 2 h at room temperature in 1×MOR2 buffer (82 mM NaCl, 2.5 mM KCl, 1mMNa_2HPO_4, 5 mM $MgCl_2$, 0.2 mM $CaCl_2$ and 5 mM HEPES, pH 7.4) with 2.5 nM ^{125}I-α-Bungarotoxin (α-BTX) (143.8 Ci/mmol; PerkinElmer Life Sciences) and 1mg/ml BSA. After incubation, the oocytes were washed 5×with 2ml ofMOR2. ^{125}I-BTX binding was quantified by γ-counting. Nonspecific binding was determined by the amount of toxin bound to mock-injected oocytes under the same conditions.

2.2.2 Inhibition assays

Propofol (2,6 diisopropylphenol) was obtained from Aldrich (D126608). A stock solution was made by diluting liquid propofol to 1 M in DMSO. This solution was stored in

glass in the dark and diluted in MES or HEPES buffer immediately before use. Each oocyte was exposed to at most two different propofol concentrations. To avoid cumulative inhibitory effects, GLIC and ELIC IC_{50} values were obtained through repeated measurement of relative inhibition caused by one concentration of propofol on a single oocyte, multiple times. The average inhibitory values at each concentration were used in calculation of the IC_{50} using Prism's log (inhibitor) versus response (three-parameter) analysis.

Cadmium inhibition was measured using variable concentrations of $CdSO_4$ (Sigma) and $CdCl_2$ (Fisher) at pH 5.0 (GLIC) or 0.7 mM cysteamine (ELIC), with buffer composition as above, although dithiothreitol (DTT) was not included in the cadmium IC_{50} measurements of ELIC to avoid the formation of a precipitate.

Amantadine inhibition was measured using variable concentrations of amantadine hydrochloride (Sigma) dissolved in the appropriate running buffer (see above) prior to pH adjustments.

2.2.3 Desensitization rates analysis

ELIC and nAChR traces that displayed increased desensitization rates were further analyzed to obtain agonist-dependent desensitization rates. Experimental data were fit with an exponential curve to obtain the time constant (τ) for the rate of decay of the whole cell agonist-induced response over multiple agonist concentrations. The reciprocal of the decay ($1/\tau$) was plotted as a log function of agonist concentration, with slope values reported for each mutant.

2.3 Protein expression and purification

Soybean asolectin (L-α-phosphatidylcholine, type II-S) was from Sigma (St. Louis, MO). Dodecylmaltoside (DDM) was from Affymetrix (Santa Clara, CA). ELIC was expressed, purified, and reconstituted into proteoliposomes as described previously for GLIC (Labriola et al., 2013), and ELIC (Carswell et al., 2015a).

ELIC, GE and EG were expressed in the BL21(DE3) strain of *E. coli*. Two litre cultures of transformed BL21 cells were grown in Terrific Broth containing 50 µg/mL kanamycin at 37°C to an OD600 of ~1.2 a.u, and the cultures induced overnight at 26°C with 200µM IPTG. Cells were harvested, resuspended in ELIC Buffer A (150 mM NaCl, 50 mM NaH_2PO_4, pH 8.0) in the presence of Roche Complete™ antiprotease tablets (Branford, CT). GLIC and GE were expressed in the C43 strain of *E. coli* transformed with a pET-20b(+) vector containing the DNA sequence for the maltose-binding protein fused to the N terminus of GLIC/GE through a thrombin-sensitive peptide linker (Bocquet et al., 2007). 2-liter cultures of the transformed C43 cells were grown in 2YT medium containing 50 µg/ml ampicillin at 37 °C to an A_{600} of ~1.2, and the cultures were induced overnight at 30 °C with 200µm IPTG. The cells were harvested, resuspended in GLIC Buffer A (250 mm NaCl, 25 mm Tris, pH 7.2) with antiprotease tablets (Roche).

Membrane fractions were lysed with an Avestin Emulsiflex-C3 homogenizer (Ottawa, Canada), then were solubilised in 1 % DDM in the appropriate Buffer A, and the fusion protein bound to an amylose affinity resin. After treatment with HRV 3C protease (Calbiochem; Gibbstown, NJ), ELIC/EG was eluted in 0.02% DDM and further purified in Buffer B (150 mM NaCl, 10 mM NaH2PO4, pH 8.0) on a Superose 6 10/300 gel-filtration column (GE Healthcare). Likewise, after treatment with plasminogen-free thrombin Calbiochem (Gibbstown, NJ), GLIC/GE was eluted in 0.02% DDM and further purified on a Superpose 6 10/300 gel filtration column (GE Healthcare).

2.3.1 Lipid reconstitution

The purified ELIC/GLIC/GE/EG in 0.02% DDM in the appropriate buffer was slowly diluted at least 1:4 with lipids solubilized in 0.625% cholate in buffer to give the desired final lipid to protein ratio, in this case 1:4 (vol:vol) (Carswell et al., 2008; Sayeed and Baenziger, 2009). After gently mixing for ~30 min, the protein/detergent/lipid mixture was dialyzed five times at 4 °C against 2 liters of detergent-free buffer, leading to a turbid solution of proteoliposomes, which were harvested by ultracentrifugation at 100,000 × *g* for 2 h. Samples were assayed for both protein (BCA™ assay from Thermo-Pierce) and lipid

(phospholipid C/choline assay from Wako Chemicals (Richmond, VA)), with values confirmed by NanoDrop (Thermo Fisher).

2.3.2 FTIR Thermal stability assays

Infrared spectra were recorded on either a Digilab FTS7000 spectrometer (Agilent). Membrane reconstituted samples were exchanged into $_2H_2O$ Buffer B for 24 h at 4 °C, and then stored at a temperature of −80 °C. Approximately 200μg of WT ELIC, WT GLIC, EG or GE was deposited on a CaF_2 window under a gentle stream of N_2 gas, and then rehydrated with 8μL of $_2H_2O$. 4000-scan spectra were recorded at 2 cm^{-1} resolution and then processed with GRAMS/AI software (Thermo Scientific) (daCosta and Baenziger, 2009). Resolution enhancement was performed between 1900 cm^{-1} and 1300 cm^{-1} using a $\gamma = 7$ and a Bessel smoothing function set to 70%. Intensity changes in the amide I band at either 1680 or 1620 cm^{-1} were plotted as a function of temperature to monitor the thermal denaturation (Td).

The Td was calculated by fitting the data (GraphPad Prism) with a Boltzmann sigmoidal, where the fraction denatured $F_d = y_{initial}+[(y_{final}-y_{initial}) / (1+\exp((Td-x) /m_b))$.

2.4 ELIC Homology Model

The homology model of ELIC was constructed using Swiss-Model (Schwede et al., 2003), with GLIC (pdb code 3EHZ) as a template. The majority (95%) of the φ and ψ angles of the model (the entire ELIC structure) are found in allowable regions of the Ramachandran plot (Lovell et al., 2003).

Chapter 3. Manuscript 1:

Hénault, C.M., and Baenziger, J.E. (2017). Functional characterization of two prokaryotic pentameric ligand-gated ion channel chimeras – role of the GLIC transmembrane domain in proton sensing. Biochim. Biophys. Acta - Biomembr. *1859*, 218–227.

Adapted as a post-print from Biochim. Biophys. Acta – Biomembr,
http://dx.doi.org/10.1016/j.bbamem.2016.11.006

3.1 Preface

This manuscript is the first of four first-author publications presented in this thesis. This paper was published in Biochimica et Biophysica Acta (BBA) – Biomembranes in 2017 and encompasses some of my earliest work. The goal of this research was to investigate the roles in lipid-sensing, agonist response and thermal stability played by the individual domains (ECD/TMD) of two prokaryotic pLGICs. My hypothesis was that the two TMDs would have highly different characteristics, due to the great chemical variability between the TMDs of the two proteins. As a secondary goal, the purpose of this work was to assess the ability of the two prokaryotic pLGICs to serve as models of the more complex vertebrate receptors.

I initiated and performed all the experiments presented in this manuscript. I wrote the manuscript in collaboration with my supervisor.

Note that due to a missing N-terminal residue, the numbering of the ELIC sequence deposited in the protein data bank with the original ELIC structure was off by one. We used the protein data bank numbering to define residues in manuscripts 1 to 3, but corrected the numbering in manuscript 4. For example, P305 (manuscript 4) is defined as P304 in manuscripts 2 and 3.

3.2 Abstract

With the long-term goal of using a chimeric approach to dissect the distinct lipid sensitivities and thermal stabilities of the pentameric ligand-gated ion channels (pLGIC), GLIC and ELIC, we constructed chimeras by cross-combining their extracellular (ECD) and transmembrane (TMD) domains. As expected, the chimera formed between GLIC-ECD and ELIC-TMD (GE) responded to protons, the agonist for GLIC, but not cysteamine, the agonist for ELIC, although GE exhibited a 25-fold decrease in proton-sensitivity relative to wild type. The chimera formed between ELIC-ECD and the GLIC-TMD (EG) was usually toxic, unless it contained a pore-lining Ile9′Ala gain-of-function mutation. No significant improvements in expression/toxicity were observed with extensive loop substitutions at the ECD/TMD interface. Surprisingly, oocytes expressing EG-I9′A responded to both the ELIC agonist, cysteamine and the GLIC agonist, protons – the latter at pH values ≤4.0. The cysteamine- and proton-induced currents in EG-I9′A were inhibited by the GLIC TMD pore blocker, amantadine. The cysteamine-induced response of EG-I9′A was also inhibited by protons at pH values down to 4.5, but potentiated at lower pH values. Proton-induced gating at low pH was not abolished by mutation of an intramembrane histidine residue previously implicated in GLIC TMD function. We show that the TMD plays a major role governing the thermal stability of a pLGIC, and identify three distinct mechanisms by which agonists and protons influence the gating of the EG chimera. A structural basis for the impaired function of GE is suggested.

3.3 Introduction

The prototypic member of the pentameric ligand-gated ion channel (pLGIC) family, the nicotinic acetylcholine receptor (nAChR) possesses a well-documented sensitivity to lipids. The driver of this lipid sensitivity resides within the transmembrane domain (TMD) (Baenziger et al., 2015; Barrantes, 2015), with the outermost M4 transmembrane α-helix of each subunit likely central to lipid sensing (Hénault et al., 2015a). A key feature of lipid sensing is the ability of the nAChR to adopt an uncoupled conformation that binds agonist, but does not undergo agonist-induced conformational transitions (Baenziger et al., 2008; daCosta and Baenziger, 2009; daCosta et al., 2009, 2013). One model proposes that uncoupling results from altered M4 "binding" to the adjacent TMD α-helices, M1/M3, with ineffective binding ultimately modifying interactions between the extracellular agonist-binding domain (ECD) and TMD to impair coupling between the agonist site and channel gate (daCosta and Baenziger, 2009; daCosta et al., 2013).

Due to their relative simplicity and ease of expression in bacterial systems, the prokaryotic homologs, GLIC and ELIC, are attractive targets for mechanistic studies. GLIC and ELIC have provided insight into the mechanism of channel gating (Bocquet et al., 2009; Chakrapani, 2015; Hilf and Dutzler, 2008, 2009; Kinde et al., 2015; Prevost et al., 2012; Sauguet et al., 2014; Velisetty et al., 2012, 2014), as well as the mechanisms by which allosteric modulators (Chen et al., 2010a; Ghosh et al., 2013; Nury et al., 2011b, 2011a; Willenbring et al., 2011), including lipids (Carswell et al., 2015a; Labriola et al., 2013), influence channel function. In the same minimal membranes that stabilize the uncoupled nAChR, GLIC retains the ability to undergo channel gating, while ELIC does not (Carswell et al., 2015a; Labriola et al., 2013). Differing levels of aromatic interactions at the M4–M1/M3 interface leading to different intrinsic strengths of M4 "binding" likely contribute to the distinct lipid sensitivities. Specifically, the abundance of aromatic residues at this interface in GLIC leads to intrinsically stronger interactions, a less malleable TMD, and thus a reduced sensitivity to its surrounding membrane environment (daCosta and Baenziger, 2013). Abundant intramembrane aromatic interactions may also contribute to the enhanced thermal stability of GLIC versus ELIC (~70 °C and ~62 °C, respectively (Carswell et al., 2015a; Labriola et al., 2013)).

With the long-term goal of dissecting the chemical features governing the different lipid sensitivities and thermal stabilities of GLIC and ELIC, we generated two chimeras formed by cross-combining the ECDs and TMDs of these two prokaryotic pLGICs (Figure 3.1). Here, we characterize both chimeras in terms of their function and thermal stability, with a particular focus on the role of the TMD of GLIC in proton sensing. We show that the chimera formed between the GLIC ECD and ELIC TMD (GE) has substantially weaker proton sensitivity compared to GLIC, suggesting relatively poor complementarity between the ECD and TMD. Building on previously published data (Schmandt et al., 2015), we surprisingly show that oocytes expressing the chimera formed between the ELIC ECD and GLIC TMD (EG) respond not only to the ELIC agonist, cysteamine, but also to the GLIC agonist, protons, with both responses inhibited by the GLIC TMD pore blocker, amantadine. In addition, the cysteamine-induced response of EG was inhibited by protons at pH values down to 4.5, but potentiated at the lower pH values where protons elicit channel gating. We identify three distinct mechanisms by which agonists and protons influence the gating of the EG chimera and show that the TMD plays a substantial role governing the overall thermal stability of both pLGICs.

Figure 3.1 Design of original and modified ELIC-GLIC chimeras

A) Extracellular and transmembrane domains from GLIC (left) and ELIC (right) were swapped and fused to create two chimeric proteins, GE and EG, shown as single subunits (structures generated in PyMol from GLIC (3EHZ) and ELIC (2VL0). Ile-9′ on M2, and extracellular loops at the interface of the two domains are indicated. Aromatic residues proposed to be involved in TMD stability are shown as yellow sticks. B) Linear representation of the chimeras, showing the extracellular loop sequences which were swapped to increase ECD-TMD complementarity. C) Schematic of the GE chimera, showing the sites of loop substitutions.

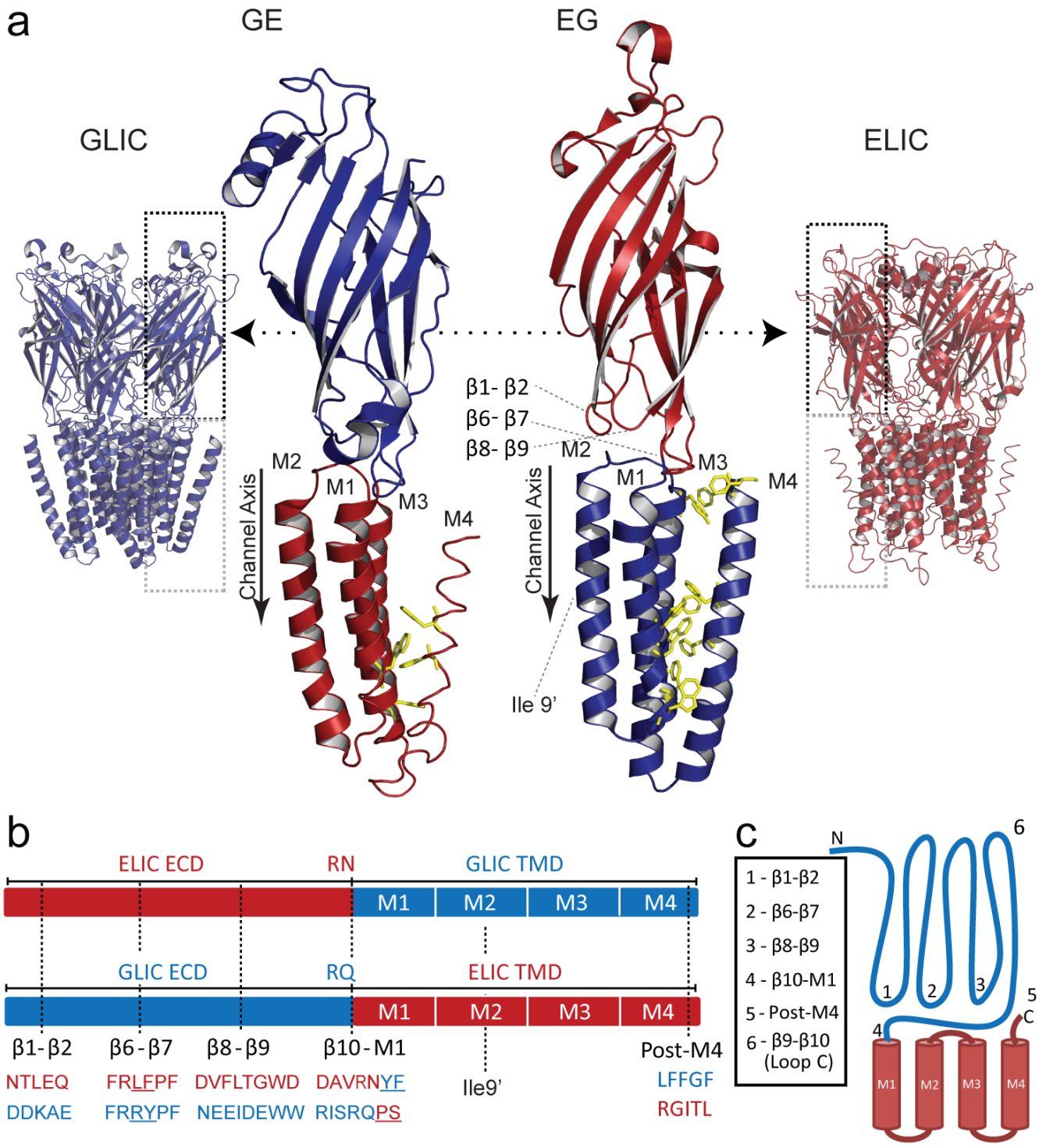
a
GE
EG
GLIC
ELIC
β1- β2
β6- β7
β8- β9
M2
M1
M3
M4
Channel Axis
Ile 9'
b
ELIC ECD
RN
GLIC TMD
M1
M2
M3
M4
GLIC ECD
RQ
ELIC TMD
β1-β2
β6-β7
β8-β9
β10-M1
Post-M4
NTLEQ
FRLFPF
DVFLTGWD
DAVRNYF
LFFGF
Ile9'
DDKAE
FRRYPF
NEEIDEWW
RISRQPS
RGITL
c
N
C
1 - β1-β2
2 - β6-β7
3 - β8-β9
4 - β10-M1
5 - Post-M4
6 - β9-β10 (Loop C)

3.4 Results

3.4.1 Chimera generation and expression

We chose a fusion site to join the ECD of ELIC with the TMD of GLIC, and vice versa, based on a previously designed GLIC-GlyR chimera (Duret et al., 2011). In the GLIC-GlyR chimera, the fusion point occurs right after a conserved "RQ" motif in the β10-M1 linker. An alignment between ELIC and GLIC shows a comparable "RN" residue pair at the corresponding site in ELIC (Figure 3.1). We generated chimeras GE (GLIC ECD linked to the ELIC TMD) and EG (ELIC ECD linked to the GLICTMD) by fusing the appropriate ECD to the appropriate TMD right after this RQ/RN sequence.

cRNAs for both the EG or GE chimeras were injected into *Xenopus* oocytes, and in both cases the appearance of proton- (GLIC) and cysteamine- (ELIC) activated currents across the oocyte plasma membrane were monitored using the two-electrode voltage clamp apparatus. To our surprise, both expressed chimeras have altered phenotypes relative to the wild type (WT) proteins (Figure 3.2). With WT-GLIC or WT ELIC, injection of appropriate amounts of cRNA leads to the appearance of robust agonist-induced currents in the 1–5μA range in close to 100% of the injected oocytes. In contrast, injection of EG cRNA resulted in the overnight death of ~60% of oocytes ($n > 175$). Of the surviving EG-injected oocytes, no currents above endogenous levels ($I_{max} \geq 0.5\mu A$) were observed in response to either cysteamine or protons. Although no toxicity was observed upon injection of GE cRNA, the expression of functional chimeras on the oocyte surface was unpredictable. Proton-activated currents above the background noise level were only detected in roughly 10% of GE-injected oocytes, with whole cell current levels typically ranging from 0.6–1.5μA, with no such anomalous currents detected in uninjected control oocytes ($n > 100$).

The toxicity of the EG chimera was explored further by varying the amounts of injected cRNA (0.05 ng–10 ng), the incubation times and the incubation buffer composition, but none of these variations reduced toxicity to a level where robust cysteamine-activated currents could be detected. We incubated EG cRNA-injected oocytes with the GLIC/ELIC inhibitors cadmium and amantadine at concentrations both above and below the IC_{50} of each

inhibitor, with no improvement in oocyte death rates. The latter suggests that chimera toxicity is not due to the expression of constitutively open channels on the oocyte surface.

We also explored further the unpredictable expression of GE using a GE chimera with a high-affinity α-bungarotoxin (α-BTX) binding site inserted into the GE ECD (Hénault et al., 2015b; Wang et al., 2012). ^{125}I-BTX binding suggests that the levels of surface-expressed GE were above background, but were ~15–20-fold lower than wild type α-BTX-GLIC (Figure 3.6). In addition, while the majority of oocytes expressing GE gave similar and consistent low levels of α-BTX binding, a small proportion of oocytes displayed slightly higher expression levels from which it was possible to perform a more detailed functional analysis.

Figure 3.2 Functional characterization of the chimeras

A) Whole cell TEVC traces recorded from oocytes expressing WT GLIC and ELIC, chimeras EG and GE, and mock-injected controls. Currents were detected for GE in response to protons, but not cysteamine (Cys). No significant response was observed in surviving EG-injected oocytes. Note that a test pulse at pH 3.0 was initially recorded (not shown) to screen for GE expressers. B) Left, dose response curves for GLIC (pH_{50} = 5.03 ± 0.08) and GE (pH_{50} = 3.63 ± 0.34). Right, cadmium inhibition of ELIC (IC50 = 0.12 ± 0.05 mM), GLIC (IC_{50}= 7.4 ± 2.0 mM) and GE (IC_{50} = 39.8 ± 7.3 mM). Error bars represent SE. C) Prolonged exposure of GE to low pH ranges does not cause the rapid desensitization seen in GLIC at the same pH.

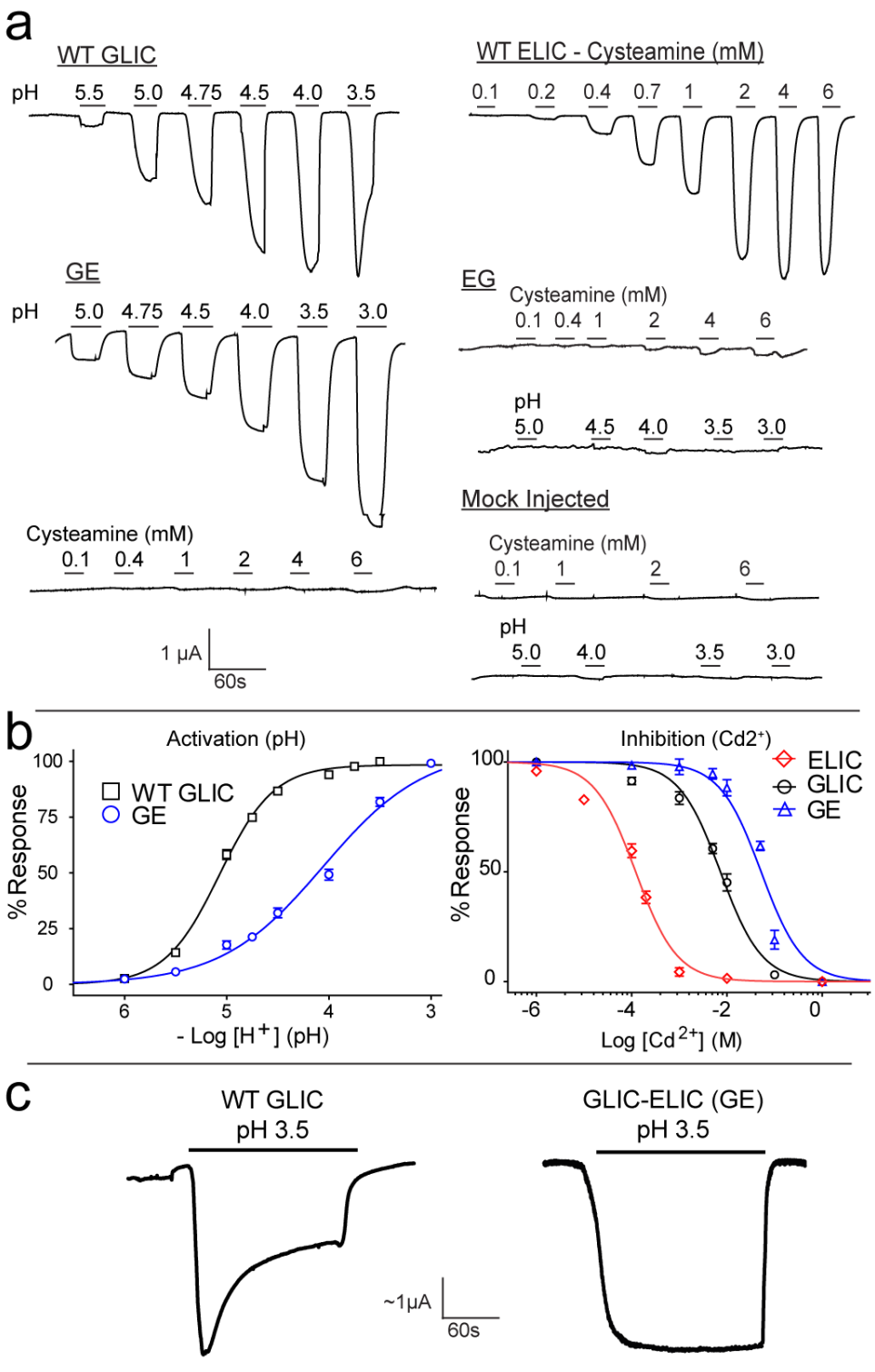
a
WT GLIC
pH 5.5 5.0 4.75 4.5 4.0 3.5
GE
pH 5.0 4.75 4.5 4.0 3.5 3.0
Cysteamine (mM)
0.1 0.4 1 2 4 6
1 µA
60s
WT ELIC - Cysteamine (mM)
0.1 0.2 0.4 0.7 1 2 4 6
EG
Cysteamine (mM)
0.1 0.4 1 2 4 6
pH
5.0 4.5 4.0 3.5 3.0
Mock Injected
Cysteamine (mM)
0.1 1 2 6
pH
5.0 4.0 3.5 3.0
b
Activation (pH)
WT GLIC
GE
% Response
- Log [H+] (pH)
Inhibition (Cd2+)
ELIC
GLIC
GE
% Response
Log [Cd2+] (M)
c
WT GLIC
pH 3.5
GLIC-ELIC (GE)
pH 3.5
~1µA
60s

3.4.2 Improving complementarity at the ECD-TMD interface

The inability to abundantly express functional GE and EG chimeras is surprising given that several chimeras formed by joining the ECD of one pLGIC to the TMD of another exhibit agonist-induced current with little or no modifications at the ECD-TMD interface (Duret et al., 2011; Eisele et al., 1993; Grutter et al., 2005). On the other hand, chimeras formed between the acetylcholine binding protein (AChBP) and the TMD of the serotonin receptor ($5HT_3R$), and between the ELIC ECD and the α7nAChR TMD require sequence modifications of loops at the ECD-TMD interface to improve inter-domain complementarity in order to generate functional channels (Bouzat et al., 2004; Tillman et al., 2014). Improved complementarity also enhanced channel folding and thus cell surface expression.

To test whether improved chemical complementarity at the ECD/TMD would improve expression of GE or reduce the toxicity of EG, we individually changed the β1–β2, β6–β7 and β8–β9 loops, and the β10-M1 linker in the ECD of each chimera to complement the TMD (Figure 3.1, Table 3.1). As the M4 α-helix of the TMD in wild type GLIC interacts with the β6–β7 loop of the ECD, we also changed the final 5 residues of the TMD to be complementary to the β6–β7 loop of the ECD. In the case of the GE chimera, the individual loop substitutions did not improve the erratic expression sufficiently to permit the characterization of EC_{50} values. In the case of EG, the loop substitutions had no effect on toxicity of the chimera, and again, no cysteamine- or proton-dependent currents were observed from the surviving oocytes.

Various combinations of the above loop substitutions were next introduced into both chimeras, including changing the sequences of all three loops (β1–β2, β6–β7 and β8–β9 loop) and the β10-M1 linker of the ECD to be complementary to the sequence of the transmembrane domain (Table 3.1). These mutations were performed either with or without changes to the sequence of the M4 C-terminus. As with the individual loop substitutions, there were no substantive improvements in either chimera expression levels (GE) or chimera toxicity (EG). The inability of these loop substitutions to improve expression is striking given that a similar approach leads to functional AChBP-$5HT_3R$ and ELIC-α7 nAChR chimeras.

Figure 3.3 Characterization of the EG-I9′A and ELIC-L9′A mutants

A) Whole cell TEVC traces showing the proton- or cysteamine-dependent (Cys) response, with amantadine inhibition of EGI9′A, ELIC-L9′A, and of an uninjected oocyte. B) Inhibition of the cysteamine response of EG-I9′A by amantadine (Amant.) (IC_{50} = 4.1 ± 3.3 μM) C) Cysteamine-dependent dose-response curves for EG-I9′A (EC_{50} = 0.55 ± 0.06 mM), ELIC-L9′A (EC_{50} = 0.18 ± 0.03 mM) and WT-ELIC (EC_{50} = 0.93 ± 0.13 mM) (top), and pH-dependent dose-response curves for EG-I9′A, EGI9′A+H242F, and mock-injected oocytes (bottom). D) Current amplitudes of EG-I9′A (1 or 2-day expression) and EG-I9′A+H242F when exposed to increasing pH, as measured by TEVC. Dose response errors (b, c) represent SE, bar graph errors (d) show the SD. Where noted $p < 0.05$ (*) or $p < 0.01$ (**), current amplitudes were statistically significant compared to control oocytes at the same pH as determined by Student's *t*-test.

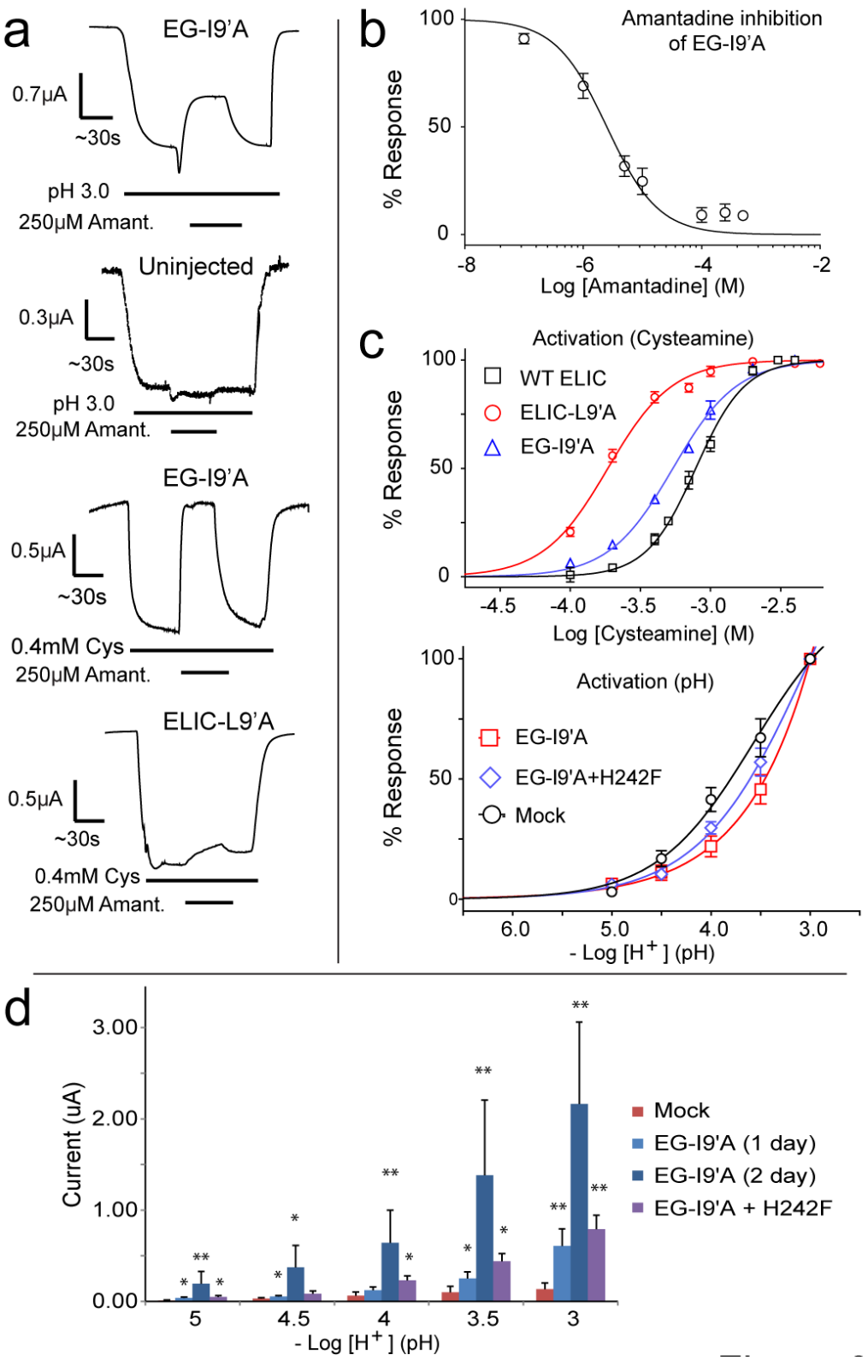
a
EG-I9'A
0.7μA
~30s
pH 3.0
250μM Amant.
Uninjected
0.3μA
~30s
pH 3.0
250μM Amant.
EG-I9'A
0.5μA
~30s
0.4mM Cys
250μM Amant.
ELIC-L9'A
0.5μA
~30s
0.4mM Cys
250μM Amant.
b
Amantadine inhibition of EG-I9'A
% Response
Log [Amantadine] (M)
c
Activation (Cysteamine)
WT ELIC
ELIC-L9'A
EG-I9'A
% Response
Log [Cysteamine] (M)
Activation (pH)
EG-I9'A
EG-I9'A+H242F
Mock
% Response
- Log [H+] (pH)
d
Current (uA)
Mock
EG-I9'A (1 day)
EG-I9'A (2 day)
EG-I9'A + H242F
- Log [H+] (pH)

Despite the fact that functional chimeras can be formed between the functional domains of prokaryotic and eukaryotic pLGICs (i.e., pLGICs separated by billions of years of evolution), a similar approach to creating chimeras between two "closely related" prokaryotic pLGICs leads to poor folding and thus trafficking to the cell surface, and/or poor function when expressed in oocytes (see Discussion).

3.4.3 Functional characterization of the GE chimera

Although the expression of GE in oocytes was sporadic, sufficient RNA injections were performed (~150 oocytes) to characterize its activity. As expected, the chimera responded to protons, the agonist for GLIC, but not cysteamine, the agonist for ELIC. The response of the chimera to protons, however, exhibited several unique features relative to that of WT GLIC.

First the measured pH_{50} (3.63 ± 0.34, n = 16) was right-shifted by more than a full pH unit relative to that of WT GLIC (5.03 ± 0.08, n = 38), and had a reduced Hill coefficient (n_H = 0.67 ± 0.07, n = 16 for GE; n_H = 1.42 ± 0.49, n = 38 for WT GLIC) (Figure 3.2). The change in pH_{50} corresponds to a ~25-fold reduction in proton sensitivity. Although some of these effects could reflect the absence of a protonatable His residue in the TMD (Rienzo et al., 2014; Schmandt et al., 2015; Wang et al., 2012), both the right-shifted EC_{50} and the reduced Hill coefficient suggest an impaired ability to couple proton binding into channel gating. In addition, the GLIC-Glycine receptor chimera, which also lacks the intramembrane proton binding site, exhibits a pH_{50} of 6.5 corresponding to a gain-of-function (Duret et al., 2011), as opposed to the loss-of-function observed here.

Second, the GE chimera did not exhibit the typical desensitization kinetics observed in most pLGICs, including WT GLIC and ELIC. At proton concentrations above the EC_{50} (i.e., pH values lower than the pH_{50}) WT GLIC desensitizes, as is seen in whole cell current traces recorded over prolonged exposure times at pH= 3.5 (Figure 3.2). At equivalent proton concentrations, no desensitization-associated changes in current were seen with GE – i.e., traces remained at I_{max} throughout the time of exposure to protons (Figure 3.2c). Although it was difficult to record high quality data at pH values below pH 3.5 due to the baseline variations that occur with prolonged oocyte exposure to low pH, desensitization was absent

in the traces that were obtained at pH 3.0 and 2.75 (the latter not shown). Further studies are required to assess whether GE desensitization kinetics are still slow at even lower pH.

Finally, the GE chimera was inhibited by the cation, cadmium, in a manner distinct from that of both GLIC and ELIC. Cadmium inhibits GLIC and ELIC with IC_{50} values of 7.4 ± 2.0 mM (n = 8) and 0.12 ± 0.05mM (n=15), respectively (Figure 3.2b) (Hilf et al., 2010). Note that in GLIC, cadmium binds to the TMD within, or just outside of the intracellular end of the channel pore (Hilf et al., 2010). In ELIC, the precise location of cadmium binding is uncertain. Multiple divalent cation binding sites have been identified in the extracellular domain (Zimmermann et al., 2012). Although the sample size of our study was limited due to the inconsistent nature of GE expression, we measured an IC_{50} of 39.8 ± 7.3mM (n=3) for GE. GE appears to be less sensitive to cadmium inhibition than either ELIC or GLIC, suggesting a distinct inhibition mechanism and/or that the GE TMD adopts a slightly different conformation than the same TMD in GLIC. The latter could contribute to the relatively poor complementarity discussed above between the ECD and TMD in the GE chimera.

3.4.4 Functional characterization of the EG-I9′A chimera

Although we could not record reliable currents from EG cRNA injected oocytes to characterize the functional properties of the EG chimera, a recent study demonstrated that incorporating a gain-of-function Ala mutation at position 9′ on the channel pore-facing surface of the EG M2 α-helix (I233A in the GLIC sequence) leads to enhanced expression (Schmandt et al., 2015).We generated both the ELIC-L9'A (L239A) mutant and the EG-I9′A chimera. As expected, the introduction of the L9'Amutation into WT ELIC leads to a left-shift in the dose response to cysteamine yielding an EC_{50} value of 0.18 ± 0.03 mM, which represents a 5-fold gain-of-function relative to WT ELIC (EC_{50} = 0.93 ± 0.13 mM) (Figure 3.3).We were able to record relatively strong dose-dependent currents with the EG-I9′A chimera in response to cysteamine, yielding an EC_{50} value of 0.55 ± 0.06 mM, which is in between the EC_{50} values obtained for ELIC-L9′A and WT ELIC. If we assume that the I9'A mutation in the EG chimera also leads to a five-fold gain-of-function, then we would predict

Figure 3.4 Acid inhibition of ELIC-L9′A and EG-I9′A

A) Whole cell TEVC trace and averaged dose response plot (n=5), showing the dose-dependent reduction in the response of ELIC-L9'A to cysteamine (Cys) with decreasing pH, followed by a repeat of the initial pulse. B) Whole cell TEVC trace and averaged dose response plot (n=3), normalized to Imax (pH 3.5), showing the initial reduction in cysteamine response with decreasing pH, followed by an increase in response at pH values of 4 and below. Error bars represent the standard error for each pH tested.

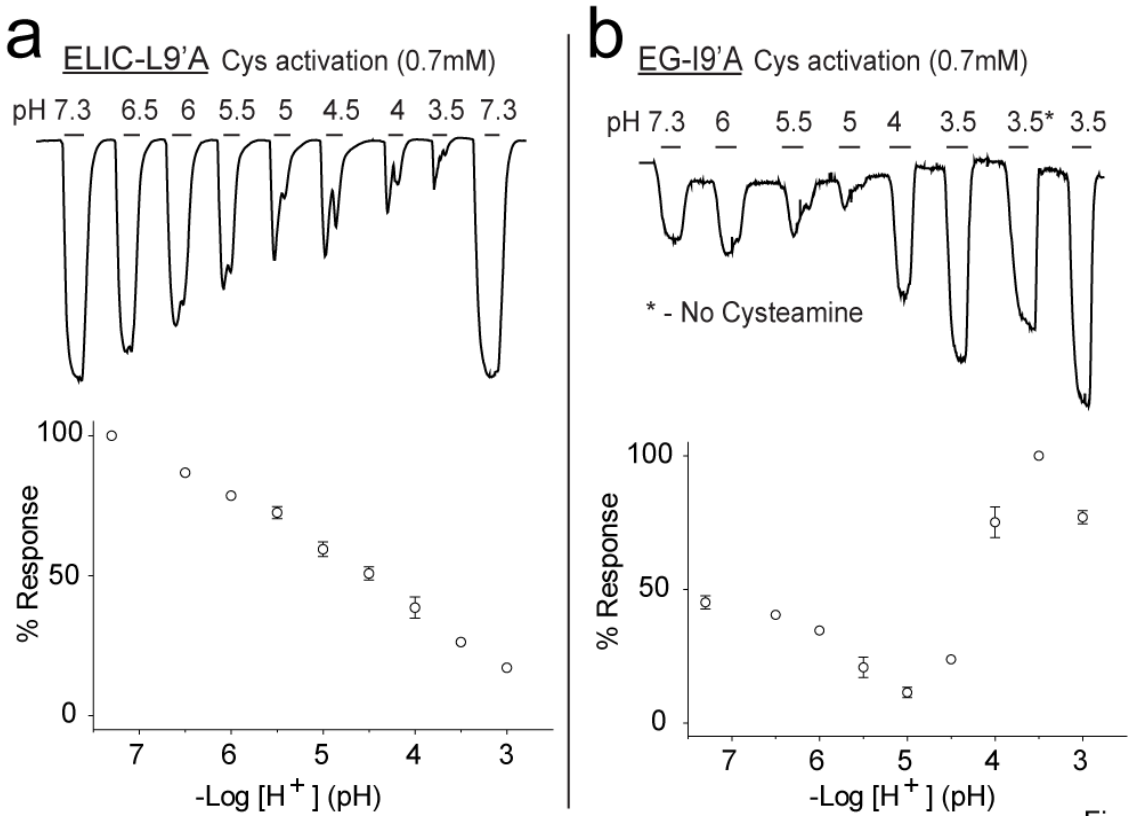
a
ELIC-L9'A Cys activation (0.7mM)
pH 7.3 6.5 6 5.5 5 4.5 4 3.5 7.3
100
50
0
% Response
7 6 5 4 3
-Log [H+] (pH)
b
EG-I9'A Cys activation (0.7mM)
pH 7.3 6 5.5 5 4 3.5 3.5* 3.5
* - No Cysteamine
100
50
0
% Response
7 6 5 4 3
-Log [H+] (pH)

that the EC_{50} value for the EG chimera without the I9′A mutation would be ≥ 2.8mM. This prediction suggests that the chimera has a slightly lower agonist sensitivity than WT ELIC (EC_{50} = 0.93 mM).

3.4.5 Proton-sensitivity of ELIC and the EG-I9′A chimera

As noted, GLIC gates open in response to protons, as does a chimera formed between the GLIC ECD and the GlyR TMD. The latter suggests that the proton-binding sites responsible for channel gating are located in the ECD. An intramembrane His residue (His235 in GLIC numbering) located on the distal side of the pore-lining M2 α-helix, however, has also been implicated in proton-induced gating. Schmandt et al. reported that the EG-I9′A mutant is responsive to protons, with relatively robust currents detected at pH 5.0, suggesting that the intramembrane His residue alone might gate open the chimera (Schmandt et al., 2015). Their analysis, however, did not demonstrate that the observed proton-gating of EG is distinct from that of acid-sensing channels that are endogenously expressed in frog oocytes (Labriola et al., 2013). To better understand the role of this His235 in proton-gating of GLIC, we further characterized the proton-sensing capacity of both ELIC and EG.

As shown above in Figure 3.2, ELIC does not respond to protons by gating open its channel. In contrast, EG-I9′A does gate open in response to increasing proton concentrations (Figure 3.3c). The magnitudes of the proton-gated currents are significantly higher than those observed in uninjected or mock-injected oocytes (Figure 3.3d). The proton-induced response increases with increasing time of EG 9′ expression, whereas that of endogenous channels does not. Significantly, the proton-induced response is sensitive to the GLIC pore-specific channel blocker, amantadine (IC_{50} = 4.1 ± 3.3 μM), while amantadine does not inhibit endogenous proton-sensitive channels (Figure 3.3a). The specificity of the amantadine-block to the GLIC TMD is further supported by the observation that amantadine fully blocks the cysteamine-induced response of EG-I9′A, but has no effect on the cysteamine-induced response of WT-ELIC (Figure 3.3). These findings demonstrate conclusively that EG gates open in response to proton binding. Note, however, that substantial acid-induced currents are only detected at pH values ≤4.0, and do not saturate at pH values as low as 3.0 (Figure 3.3c), suggesting a much weaker “agonist” sensitivity than reported previously. Due to instabilities

in the trace baselines at low pH, we could not explore the proton-induced response further to establish an accurate pH_{50} value.

One possible interpretation is that protonation of the intramembrane His 242 in the EG-I9′A chimera (His235 in GLIC) is responsible for channel gating. To test this possibility, we characterized the pH sensitivity of the His242Phe EG-I9′A mutant (Figure 3.3d). Perhaps not surprisingly given the weak pH response (i.e. the pH response is well below the pKa of His), His242Phe EG-I9′A still exhibited proton-induced channel currents above those of the endogenous acid-sensing channels, with the proton-sensitivity again too weak to characterize an accurate EC_{50}/pH_{50} value. These results show that other protonatable residues in the TMD are responsible for proton-induced gating of the EG chimera.

3.4.6 Sensitivity of the cysteamine-induced response in ELIC/EG to protons

The proton-induced gating of both GLIC and EG-I9′A is intriguing given that agonist-activation of eukaryotic pLGICs is inhibited by protons (Chen et al., 2004; Huang and Dillon, 1999; Li and McNamee, 1992). We explored the effects of protons on cysteamine-induced gating in both ELIC-L9'A and the EG-I9′A chimera. Although it was difficult to obtain whole cell traces with stable baselines when exposing oocytes to cysteamine at low pH, it is clear that the cysteamine-induced response of ELIC-L9′A is inhibited by protons. Inhibition occurs in a "linear" manner from which it is not possible to measure an IC_{50} value, suggesting complex mechanisms underlying channel inactivation that involve the protonation of numerous side chains, etc. (Figure 3.4). Interestingly, the cysteamine-induced response of EG-I9′A is also inhibited by protons over the pH range of 7 down to 4.5, but potentiated by protons below pH 4.5 (Figure 3.4b). The potentiation of the cysteamine-induced response at low pH values correlates with proton-induced gating of EGI9′A, suggesting that agonist- and proton-induced gating are independent and additive.

Figure 3.5 Secondary structure of membrane-reconstituted ELIC, GLIC, GE and EG

A) infrared spectra of aso-EG (left) and aso-GE (right) after gentle drying from $^{1}H_2O$ buffer (black) and immediately after the addition of $^{2}H_2O$ (gray). Note the immediate shift in the amide I band, and the decrease in amide II band intensity, resulting from the rapid peptide N-^{1}H/N-^{2}H exchange of solvent-exposed peptide hydrogens. **B**) amide I (left) and amide II (right) bands in IR spectra recorded after 24-hour exchange in $^{2}H_2O$ at 4°C for asolectin-reconstituted EG, GE, ELIC and GLIC. The amide I bands are shown before (gray) and after deconvolution (black). Spectra are the averages of at least three spectra recorded from two different purifications/reconstitutions. The relative intensity of the amide II vibration compared to the adjacent broad peak between 1560 and 1600 cm^{-1} shows the amount of $^{2}H_2O$ exchange. **C**) Secondary structure of aso-GE and aso-EG derived from spectral curve fitting. **D**) IR-derived thermal denaturation curves showing the similarity in Td between GE/ELIC (57 and 59 °C) and EG/GLIC (74 and 69 °C).

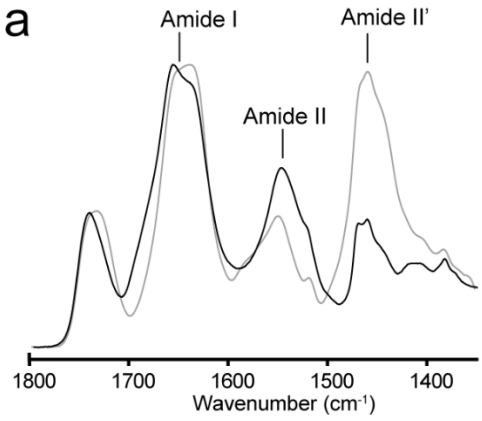

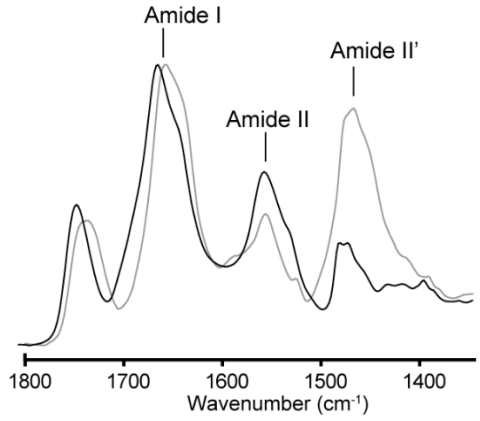

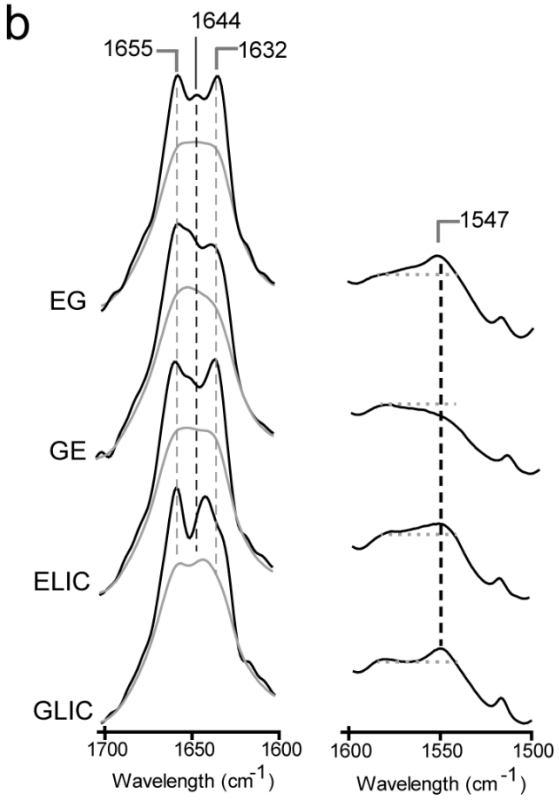

c

Band frequency	Band assignment	EG	GE
1692	T	2	2
1681	T	3	3
1673	T + β	9	9
1655	α	46	44
1643	Loop/random	2	7
1633	β	28	26
1624	β	10	9

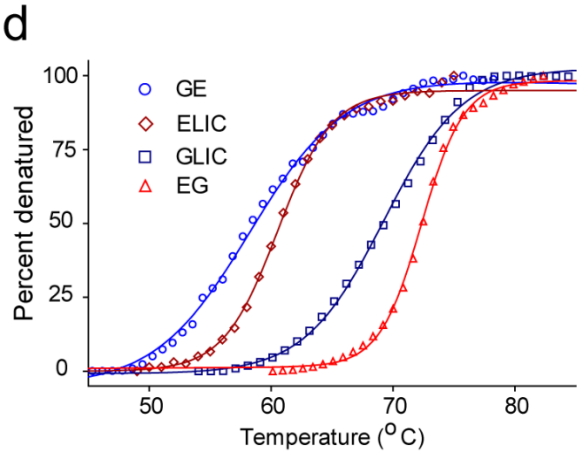

3.4.7 Structure and thermal stability of GE and EG

We expressed both the GE and EG chimeras in *E. coli*, and then reconstituted the affinity-purified pLGICs into soybean asolectin membranes (referred to as aso-GE and aso-EG, respectively). Both aso-GE and aso-EG exhibited the secondary structure and spectral features expected for a folded, membrane-incorporated pLGIC (Figure 3.5). Specifically, both aso-EG and aso-GE gave infrared spectra with relatively narrow and symmetric amide I bands (primarily C=O stretch) and underlying amide I component bands indicative of the expected mixed α-helix/β-sheet secondary structure. A substantial proportion of the backbone hydrogens exchange rapidly upon exposure to $^{2}H_2O$, while another population is resistant to peptide N-$_1$H/N-$_2$H exchange even after prolonged exposure to $^{2}H_2O$ (24 h) reflecting the existence of an exchange-resistant core, as observed in other pLGICs (daCosta and Baenziger, 2009; daCosta et al., 2011). The proportion of exchange-resistant peptide hydrogens is slightly higher in EG versus GE, as is the case in WT GLIC versus WT ELIC. The presence of intramembrane aromatic and other interactions in the TMD of GLIC may reduce thermal fluctuations leading to reduced peptide hydrogen exchange in both WT GLIC and the EG chimera.

The thermal denaturations of both aso-EG and aso-GE were examined by monitoring the changes in amide I band shape as a function of temperature. Aso-EG exhibits a clear, cooperative unfolding in response to temperature, giving a Td of 73.8 ± 2.8 °C (n = 7). Aso-GE exhibits a cooperative denaturation superimposed on a linear background, as observed in WT-ELIC. Subtraction of the linear component of the denaturation gave a Td of 57.1 ± 1 °C (n = 6) (Figure 3.5). Notably, the Td of EG, which contains the TMD of GLIC, is similar to that of WT aso-GLIC (68.8 ± 1.5 °C), while the Td of GE, which contains the TMD of ELIC, is similar to that of WT aso-ELIC (59.7 ± 3.5 °C) (Carswell et al., 2015b; Labriola et al., 2013). The data suggest that the TMD plays a major role dictating the thermal stability of a pLGIC, as has been suggested elsewhere (Moraga-Cid et al., 2015; Tol et al., 2013).

3.5 Discussion

The key findings of this study pertain to the generation of functional chimeras between the ECDs and TMDs of these two prokaryotic pLGICs and their proton sensing capabilities. Functional chimeras have successfully been formed between the ECDs and TMDs of several pLGICs, including the α7nAChR ECD fused to the TMD of either the $5HT_3R$ (Eisele et al., 1993) or the GlyR (Grutter et al., 2005), and the GLIC ECD fused to the GlyR TMD (Duret et al., 2011). In these three chimeras, minimal or no additional amino acid substitutions in the loops at the ECD-TMD interface were required to facilitate channel gating, although such substitutions did influence gating kinetics. The striking observation that the ECD of a prokaryotic pLGIC (GLIC) gates open the TMD of a eukaryotic pLGIC (GlyR) suggests that the motifs required for pLGIC conformational change have been conserved over billions of years of evolution (Duret et al., 2011).

In contrast to the α7nAChR-$5HT_3R$, α7nAChR-GlyR and GLIC-GlyR chimeras, chimeras formed between the AChBP and the $5HT_3R$ (Bouzat et al., 2004), and between ELIC and the α7nAChR (Tillman et al., 2014) require modification of the loops at the ECD-TMD interface to improve inter-domain complementarity and thus generate functional channels. The need to improve the inter-domain complementarity in the latter two cases, however, is not surprising. AChBP is not normally linked to, and thus has not evolved to interact with a TMD. In the case of the ELIC-α7nAChR chimera, there are substantial differences between the two parent pLGICs in terms of the lengths and chemistry of the ECD-TMD loops. The ability to obtain functional AChBP-$5HT_3R$ and ELIC-α7nAChR chimeras, once inter-domain sequence complementarity is established, further supports the evolutionary conservation of key functional motifs in both the ECDs and TMDs of pLGICs.

In this context, the difficulties associated with generating properly folded and functional chimeras between the ECDs and TMDs of GLIC and ELIC is striking, particularly given that extensive loop swapping was carried out at the ECD-TMD interface to improve inter-domain sequence complementarity with no apparent effect (Figure 3.1 and Table 3.1). In terms of expression in oocytes, GE expression was typically 15–20-fold lower than WT-GLIC, while EG expression was usually toxic. Note that the toxicity of EG is not likely due

to the expression of constitutively open channels, as incubation of oocytes with GLIC/ELIC inhibitors had no effect. In addition, previous studies with gain of function mutants of GLIC and the GLIC-GlyR chimera, which are constitutively active at physiological pH, are not toxic to oocytes (Duret et al., 2011). Note also that a comprehensive study was recently published describing the activation pathway in ELIC, with part of the study focusing on a chimera identical to the EG chimera studied here (Schmandt et al., 2015). Although the toxicity of the EG chimera in oocytes was not discussed, only weak (~0.02μA) agonist-induced currents were observed. In our hands, surviving EG-injected oocytes usually gave unstable baselines from which it was very difficult to record accurate cysteamine-induced currents. In the exceptional cases where stable baselines were obtained (see Figure 3.2), small cysteamine-induced currents could be observed. Without greater reproducibility, we considered a detailed characterization of such small currents to be unreliable.

When functional chimeras could be detected with GE, the GE chimera exhibited impaired channel function, as illustrated by both a 25-fold drop in proton sensitivity and a reduced Hill coefficient. The reduced agonist sensitivity of GE relative to WT-GLIC is in contrast to the agonist sensitivities of other ECD/TMD chimeras, where similar agonist sensitivities are typically observed between chimeras and the parent WT pLGIC from which the ECD was derived. The latter suggest conservation of both agonist affinity and the efficiency of coupling agonist binding to channel gating in the pLGIC chimeras. The impaired activity of GE suggests that the structural complementarity between the agonist binding and channel-gating motifs in the chimera is relatively poor.

One possible explanation for the reduced agonist-sensitivity of GE stems from the importance of a cluster of interacting aromatic residues in WT GLIC involving the N-terminus of M3, the C-terminus of M4 and the β6-β7 loop (Figure 3.7). In WT GLIC, mutation of any one of these interacting residues leads to a reduction in function ($\downarrow pH_{50}$), whereas simultaneous mutation of any two of the interacting aromatic residues leads to a complete loss of expression and/or function (Hénault et al., 2015b). ELIC lacks analogous aromatic residues on M3 and M4. In fact, the final five residues in M4 are not resolved in ELIC crystal structures, suggesting weak, if any interactions between the M4 C-terminus and

either M3 or the β6–β7 loop (daCosta and Baenziger, 2013; Hilf and Dutzler, 2008). Optimal proton-induced gating may not be possible in the GE chimera because the proton-induced gating via the GLIC ECD requires effective aromatic interactions between M4, M3, and the β6–β7 loop, which in the GE chimera are absent. Note that the GLIC ECD/GlyR TMD chimera is functional and exhibits enhanced proton sensitivity relative to WT GLIC (Duret et al., 2011). The GlyR TMD exhibits an abundance of aromatic residues at the M4–M1/M3 interface, as well as positively charged arginine/lysine residues on both the β6–β7 loop and M3. These residues may all contribute to form effective M4, M3, and β6–β7 loop interactions that promote channel function (Du et al., 2015; Duret et al., 2011). Unfortunately, the resolution in this area of the crystal structure of the GLIC-GlyR chimera does not allow the position of interacting side chains in this region to be assigned (Moraga-Cid et al., 2015).

Although we could not characterize the activity of EG, we estimate from the EG-I9′A chimera that its agonist sensitivity is impaired only about three-fold relative to wild type ELIC. This observation suggests that there is more effective coupling between the ECD and TMD in the EG chimera than in the GE chimera. The lack of substantially impaired function in the EG chimera may result because the ELIC ECD does not require extensive interactions between M4, M3 and the β6–β7 loop for channel function.

Our functional characterization of the GE and EG-I9′A chimeras supports the idea that pLGICs exhibit autonomous ECDs and TMDs with conserved conformational transitions elicited in the ECD upon agonist binding that couple with the TMD to elicit gating. As with the other pLGIC chimeras discussed above, the GE chimera is gated by protons, the agonist for GLIC, but not by the agonist for ELIC. Similarly, EG-I9′A is gated by cysteamine, the agonist for ELIC. A striking finding of this and another study (Schmandt et al., 2015), however, is that EG-I9′A also exhibits an acid-induced response. Here, we show that the acid-induced response of oocytes expressing EG-I9′A is significantly higher than the acid-induced response due to endogenous acid-sensing channels. In addition, the acid-induced response of EG-I9′A is inhibited by the GLIC channel blocker amantadine (as is cysteamine-induced gating of EG-I9′A) while the acid-induced response of endogenous

channels is not sensitive to amantadine. Proton binding to the TMD of GLIC thus appears to induce channel gating.

A TMD His residue (His235) in GLIC has been implicated in channel function (Rienzo et al., 2014; Wang et al., 2012), raising the possibility that the protonation of this His residue in EG-I9′A gates open the channel. The pH response of EG-I9′A, however, suggests a pH_{50} value lower than pH 3.0, which is several orders of magnitude below the typical pKa of His. In addition, proton-induced currents in EG-I9′A were still observed when the intramembrane His was mutated to Phe, suggesting that the protonation of other residues in the TMD is responsible for the acid-induced gating of EG-I9′A (see also (Schmandt et al., 2015)). Note that the substantially different pH_{50} values for WT GLIC (5.03 ± 0.08 ($n = 38$)) and EG-I9′A (≤ 3.0) confirm that the protonation of distinct residues in the ECD and TMD lead to channel gating. Clearly, proton-induced gating via the ECD and TMD of GLIC occurs through distinct mechanisms.

In a broader context, proton-induced gating of GLIC and both the GE and EG-I9′A chimeras is surprising given that agonist-induced gating in most pLGICs, including the muscle-type nAChR and both the GlyR and GABA receptors, is inhibited by protons (Chen et al., 2004; Huang and Dillon, 1999; Li and McNamee, 1992). We find that cysteamine-induced gating of ELIC-L9'A is inhibited by protons, suggesting that proton inhibition of agonist-induced channel function may be a characteristic of all pLGICs – except GLIC. In fact, cysteamine-induced gating of the EG-I9′A chimera is actually inhibited by protons at pH values down to a pH of roughly 4.5, although below pH 4.5 the acid-induced inhibition is reversed, and the cysteamine-induced response potentiated by protons. Notably, the potentiation of the cysteamine-induced response in EG-I9′A occurs over roughly the same pH range as proton-induced gating.

Our results thus suggest three distinct mechanisms by which ligands allosterically influence in EG channel function: 1) EG responds to agonist binding, in this case cysteamine, by undergoing channel gating, likely in a manner consistent with the mechanisms of agonist-induced gating in other pLGICs, 2) the agonist-induced response is inhibited by protons, likely in a manner that is analogous to proton-induced inhibition of

other pLGICs, and 3) high proton concentrations (pH ≤ 4.5) lead to channel gating via protonation of TMD residues, and thus by a mechanism distinct from that of agonist induced gating. Proton-induced gating of the GLIC TMD occurs through an unknown non-canonical mechanism.

Finally, we observe with *E. coli*-expressed GE and EG that the TMD plays a key role in determining thermal stability. The thermal denaturation temperature of aso-GE (57.1 ± 1°C) is similar to that of aso-ELIC (59.7 ± 3.5 °C), while that of aso-EG (73.8 ±2.8 °C) is similar to that of aso-GLIC (68.8±1.5 °C). This finding is consistent with the observation that the thermal stability of a GLIC-GlyR chimera also matches more closely that of the GlyR (Moraga-Cid et al., 2015). Previous studies have also suggested that the TMD of the $5HT_3R$ is to a large extent governed by the TMD (Tol et al., 2013). Aromatic interactions within the TMD contribute to overall pLGIC thermal stability (Carswell et al., 2015a).

3.6 Conclusions

Our data suggest that there is less structural complementarity between the ECD of GLIC and the TMD of ELIC, than between the same domains of other pLGICs. One possible rationale for our findings is that ELIC and GLIC form distinct branches of the pLGIC super-family. This hypothesis was recently suggested based on the atypical gating and cation-conduction properties of ELIC (Gonzalez-Gutierrez and Grosman, 2015), and is supported by the observation that the outermost TMD α-helix has dramatically different roles in the folding and function of GLIC versus ELIC (Hénault et al., 2015b).

While several chimeras between the ECD of one pLGIC and the TMD of another pLGIC have been generated, this is the first report where two chimeras were formed by cross-combining the ECDs and TMDs of the same two pLGICs. One chimera expressed poorly in oocytes, while the other was normally toxic. Both chimeras have impaired channel function with reduced agonist sensitivity, something not typically observed with chimeras formed between other prokaryotic and eukaryotic functional domains (Duret et al., 2011; Tillman et al., 2014). Further studies are required to fully understand all the structural features at the ECD/TMD interface that are required for both proper folding of a pLGIC and the efficient coupling of between agonist binding and channel gating.

Finally, we show that although the protonation of side chains in ELIC leads to inactivation of the agonist-induced response of both ELIC and the EG I9′A chimera, higher proton concentrations (< pH 4.5) both activate and potentiate the agonist-induced response of the EG I9′A chimera. The GLIC TMD thus has an intrinsic capacity to gate open its ion channel in the presence of protons, although this occurs via a noncanonical gating mechanism.

3.7 Supplementary Information

Table 3.1 - EG and GE Chimeras

Sequences for each modified ECD-TMD interface loop and the effects on EC_{50} (cysteamine) and pH_{50} values. GLIC sequences are shown in bold. ELIC sequences are italicized and underlined. A dash indicates no current detected above background (<0.5 μA, n≥8).

Construct	β1-β2 A	β6-β7 B	β8-β9 C	β10-M1 D	Post-M4 E	Cysteamine EC_{50}	pH_{50}
GLIC	**DDKAE**	**FRRYPF**	**NEEIDEWW**	**RISRQYF**	**LFFGF**	-	5.05
ELIC	*NTLEQ*	*FRLFPF*	*DVFLTHWD*	*DAVRNPS*	*RGITL*	0.94	
GE	**DDKAE**	**FRRYPF**	**NEEIDEWW**	**RISRQ***PS*	*RGITL*	-	3.63
EG	*NTLEQ*	*FRLFPF*	*DVFLTGWD*	*DAVRN***YF**	**LFFGF**	-	-
EG^{A}	**DDKAE**	*FRLFPF*	*DVFLTGWD*	*DAVRN***YF**	**LFFGF**	-	-
EG^{B}	*NTLEQ*	**FRRYPF**	*DVFLTGWD*	*DAVRN***YF**	**LFFGF**	-	-
EG^{C}	*NTLEQ*	*FRLFPF*	**NEEIDEWW**	DAVRN**YF**	**LFFGF**	-	-
EG^{D}	*NTLEQ*	*FRLFPF*	*DVFLTGWD*	**RISRQYF**	**LFFGF**	-	-
EG^{E}	*NTLEQ*	*FRLFPF*	*DVFLTGWD*	*DAVRN***YF**	RGITL	-	-
EG^{AB}	**DDKAE**	**FRRYPF**	*DVFLTGWD*	*DAVRN***YF**	**LFFGF**	-	-
EG^{AE}	**DDKAE**	*FRLFPF*	*DVFLTGWD*	*DAVRN***YF**	RGITL	-	-
EG^{ABC}	**DDKAE**	**FRRYPF**	**NEEIDEWW**	*DAVRN***YF**	**LFFGF**	-	-
EG^{ABD}	**DDKAE**	**FRRYPF**	*DVFLTGWD*	*DAVRNPS*	**LFFGF**	-	-
EG^{ABCD}	**DDKAE**	**FRRYPF**	**NEEIDEWW**	*DAVRNPS*	**LFFGF**	-	-
EG^{ACDE}	**DDKAE**	*FRLFPF*	**NEEIDEWW**	*DAVRNPS*	*RGITL*	-	-
EG^{ABCDE}	**DDKAE**	**FRRYPF**	**NEEIDEWW**	*DAVRNPS*	*RGITL*	-	-
GE^{A}	*NTLEQ*	**FRRYPF**	**NEEIDEWW**	**RISRQ***PS*	*RGITL*	-	-
GE^{B}	**DDKAE**	*FRLFPF*	**NEEIDEWW**	**RISRQ***PS*	*RGITL*	-	-
GE^{C}	**DDKAE**	**FRRYPF**	*DVFLTGWD*	**RISRQ**PS	*RGITL*	-	-
GE^{D}	**DDKAE**	**FRRYPF**	**NEEIDEWW**	**RISRQYF**	*RGITL*	-	-
GE^{E}	**DDKAE**	**FRRYPF**	**NEEIDEWW**	**RISRQ**PS	**LFFGF**	-	-
GE^{AB}	*NTLEQ*	*FRLFPF*	**NEEIDEWW**	**RISRQ**PS	*RGITL*	-	-
GE^{AE}	*NTLEQ*	**FRRYPF**	**NEEIDEWW**	**RISRQ**PS	**LFFGF**	-	-
GE^{ABC}	*NTLEQ*	*FRLFPF*	*DVFLTGWD*	**RISRQ**PS	*RGITL*	-	-
GE^{ABD}	*NTLEQ*	*FRLFPF*	**NEEIDEWW**	**RISRQYF**	*RGITL*	-	-
GE^{ABCD}	*NTLEQ*	*FRLFPF*	*DVFLTGWD*	**RISRQYF**	*RGITL*	-	-
GE^{ACDE}	*NTLEQ*	**FRRYPF**	*DVFLTGWD*	**RISRQYF**	**LFFGF**	-	-
GE^{ABCDE}	*NTLEQ*	*FRLFPF*	*DVFLTGWD*	**RISRQYF**	**LFFGF**	-	-

Figure 3.6 Surface Expression of GLIC and the GE chimera

αBTX-GLIC and αBTX-GE surface expression in oocytes over time, measured via binding of ^{125}I-labelled α-BTX binding assays. Error bars represent standard deviation. Inset: 8-fold magnification of GE expression, highlighting the above-background levels of GE expression.

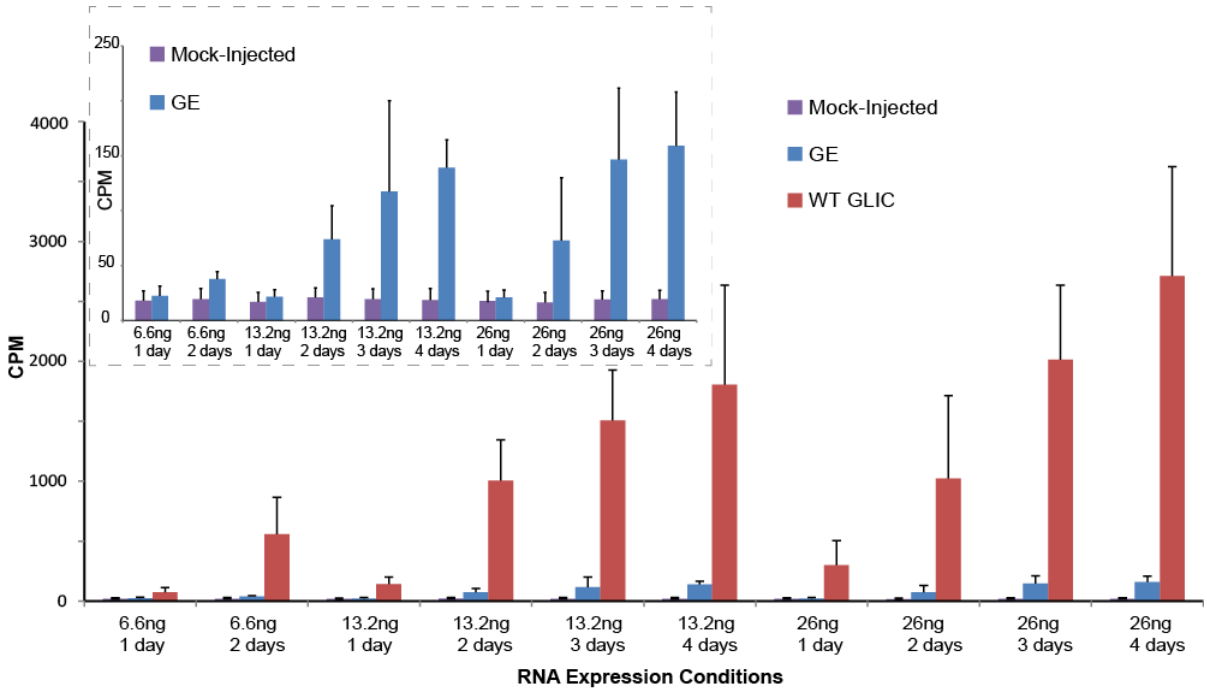
Mock-Injected
GE
WT GLIC
CPM
RNA Expression Conditions
6.6ng 1 day
6.6ng 2 days
13.2ng 1 day
13.2ng 2 days
13.2ng 3 days
13.2ng 4 days
26ng 1 day
26ng 2 days
26ng 3 days
26ng 4 days

Figure 3.7 Interactions at the ECD/TMD interface of GLIC and ELIC involving M4

The structure of GLIC, with a single subunit shown in a blue schematic representation is shown on the left, with the dashed box highlighting the approximate area zoomed in on the right. The top right panel shows interactions between M4 and the ECD/TMD interface in GLIC (Protein Data Bank code 4HFI). The bottom right shows interactions between M4 and the ECD/TMD interface in a homology model of ELIC (based on the GLIC structure). Interacting residues are colored according to their physicochemical properties, with aliphatic residues in tan, aromatic residues in yellow, charged residues (Arg-118) in blue, and polar residues (Asn-307) in green. A water molecule is shown as a cyan sphere. For visibility, the glycine residues are depicted *as* transparent spheres, and the β6-β7 loop is highlighted in green. (Figure from Henault et al 2015 – Chapter 4)

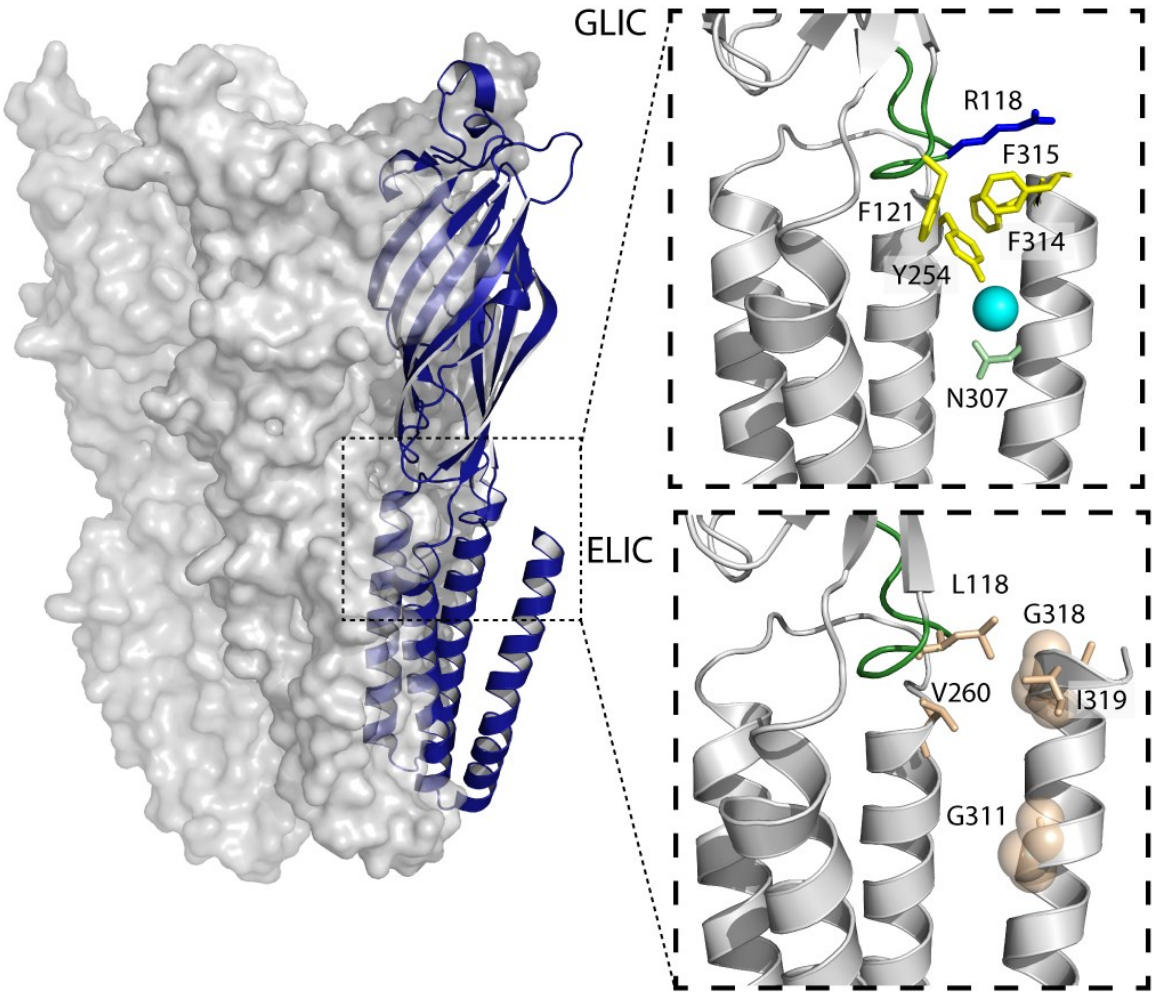
GLIC
R118
F315
F121
F314
Y254
N307
ELIC
L118
G318
V260
I319
G311

Chapter 4. Manuscript 2:

Hénault, C.M., Juranka, P.F., and Baenziger, J.E. (2015b). The M4 transmembrane α-helix contributes differently to both the maturation and function of two prokaryotic pentameric ligand-gated ion channels. J. Biol. Chem. *290*, 25118–25128.

Adapted as a post-print from J Biol.Chem, https://doi.org/10.1074/jbc.M115.676833

4.1 Preface

This manuscript is the second of four first-author publications presented in this thesis. This paper was published in the Journal of Biological Chemistry in 2015. This work was designed to probe the effect of changing the interactions between the M4 and M1/M3 helices, as well as the lipid membrane, through Ala-scanning mutagenesis, deletions and expression studies. This work builds on prior observations that the ELIC and GLIC M4 helices differ greatly in M4-M1/M3 interactions and stability.

The experiments performed were planned and determined by me, Peter Juranka and Dr Baenziger. Peter Juranka and Daniel Therien performed the GLIC M4 Ala-scan, and M4 deletions, and we worked together to generate the BTX-tagged mutants. I prepared all the figures, and I wrote the manuscript in collaboration with my supervisor.

Note that due to a missing N-terminal residue, the numbering of the ELIC sequence deposited in the protein data bank with the original ELIC structure was off by one. We used the protein data bank numbering to define residues in manuscripts 1 to 3, but corrected the numbering in manuscript 4. For example, P305 (manuscript 4) is defined as P304 in manuscripts 2 and 3.

4.2 Abstract

The role of the outermost transmembrane α-helix in both the maturation and function of the prokaryotic pentameric ligand-gated ion channels, GLIC and ELIC, was examined by Ala-scanning mutagenesis, deletion mutations, and mutant cycle analyses. Ala mutations at the M4-M1/M3 interface lead to loss-of-function phenotypes in GLIC, with the largest negative effects occurring near the M4 C terminus. In particular, two aromatic residues at the M4 C-terminus form a network of π-π and/or cation-π interactions with residues on M3 and the β6-β7 loop that is essential for both maturation and function. M4-M1/M3 interactions appear to be optimized in GLIC with even subtle structural changes at this interface leading to detrimental effects. In contrast, mutations along the M4-M1/M3 interface of ELIC typically lead to gain-of-function phenotypes, suggesting that these interactions in ELIC are not optimized for channel function. In addition, no cluster of interacting residues involving the M4 C terminus, M3, and the β6-β7 loop was found, suggesting that the M4 C terminus plays little role in ELIC maturation or function. This study shows that M4 makes distinct contributions to the maturation and gating of these two closely related homologs, suggesting that GLIC and ELIC exhibit divergent features of channel function.

4.3 Introduction

Pentameric ligand-gated ion channels (pLGICs) are the sites of action for a variety of both endogenous and exogenous compounds that alter synaptic communication by either potentiating or inhibiting channel function. Increasing interest has focused on allosteric modulators that interact with the transmembrane domain (TMD) (Baenziger and Corringer, 2011; Forman et al., 2015; Nury et al., 2011b, 2011a). The TMD of the prototypic pLGIC, the muscle-type nicotinic acetylcholine receptor (nAChR), is sensitive to a variety of compounds, including lipids (Baenziger et al., 2015; Barrantes, 2015). Both cholesterol and anionic lipids are important for nAChR function (Baenziger et al., 2000; Criado et al., 1982, 1984; daCosta et al., 2002, 2009; Fong and McNamee, 1986; Hamouda et al., 2006b). In the absence of these activating lipids, the nAChR adopts an uncoupled conformation that binds agonist, but in most membranes does not undergo agonist-induced conformational transitions (Baenziger et al., 2008; daCosta and Baenziger, 2009; daCosta et al., 2013).

The outermost lipid-exposed transmembrane α-helix, M4 (one in each nAChR subunit), is likely a site for lipid sensing (Antollini et al., 2005; Hénault et al., 2015a; Williamson et al., 2005; Xu et al., 2005). Mutations along the lipid-facing surface of M4 alter channel gating, suggesting that altered M4-lipid interactions influence coupling between the agonist site and channel gate (Bouzat et al., 1998, 2000; Lasalde et al., 1996; Lee et al., 1994; Li et al., 1990). One model proposes that lipids potentiate gating by enhancing M4 interactions with the adjacent α-helices, M1 and M3, to promote effective interactions between the M4 C terminus and the Cys-loop (daCosta and Baenziger, 2009), a structure at the interface between the extracellular domain (ECD) and TMD that plays a key role in coupling agonist binding to channel gating (Grutter et al., 2005; Jha et al., 2007; Lee and Sine, 2005; Lummis et al., 2005). Interactions between the M4 C terminus and Cys-loop may be essential for the Cys-loop to adopt a conformation that promotes channel function (daCosta and Baenziger, 2009; Pons et al., 2004). In the absence of effective M4-M1/M3 interactions, the M4 lipid-sensor model proposes that the Cys-loop adopts a non-functional conformation leading to the uncoupled state (daCosta and Baenziger, 2009).

As the prokaryotic pLGICs, GLIC and ELIC, are expressed in sufficient quantities for biophysical and crystallographic studies, both are excellent models for studying the mechanisms underlying pLGIC lipid sensing. Furthermore, the M4 α-helix in crystal structures of GLIC interacts extensively with M1/M3, with lipids bound at both the M4-M1 and M4-M3 interfaces (Bocquet et al., 2009; Hilf and Dutzler, 2009; Sauguet et al., 2013). In the ELIC crystal structure, the C-terminal 5 residues of M4 are not resolved, possibly due to differential crystal packing, the absence of bound lipids, and/or detergent perturbation of weaker M4 C-terminal interactions with M1/M3 (daCosta and Baenziger, 2013; Hilf and Dutzler, 2008; Pan et al., 2012; Zimmermann and Dutzler, 2011). Interestingly, differences in pore diameter are observed when GLIC is crystallized in the presence *versus* absence of agonist (Sauguet et al., 2014). A locally closed pore was also detected with several disulfide cross-linked GLIC mutants (Prevost et al., 2012). These results suggest that crystalline GLIC with tight M4-M1/M3 interactions undergoes agonist-induced conformational transitions. In contrast, ELIC has not yet been crystallized in open and closed structures, even though structures of ELIC have been solved in the presence and absence of bound agonist (Gonzalez-Gutierrez et al., 2012; Zimmermann and Dutzler, 2011). This raises the possibility that crystallized ELIC, with weakened or no interactions between the M4 C terminus and adjacent structures at the ECD/TMD interface, adopts a conformation that does not undergo agonist-induced conformational transitions (daCosta and Baenziger, 2013). Single amino acid substitutions engineered to weaken M4-M1/M3 interactions in GLIC reduce, whereas substitutions engineered to enhance M4-M1/M3 interactions in ELIC promote channel function (Carswell et al., 2015b). The intrinsic strengths of M4-M1/M3 interactions also influence the functional sensitivities of GLIC and ELIC to lipids (Carswell et al., 2015a; Labriola et al., 2013). Modulatable M4-M1/M3 interactions may play a role in lipid sensing.

Here, we examine the role of M4 in the maturation and gating of GLIC and ELIC. Through Ala scanning mutagenesis, M4 deletion mutations, and mutant cycle analyses, we show that the M4-M1/M3 interactions are optimized in GLIC for channel function, whereas in ELIC they are not. We identify a cluster of interacting residues on the M4 C terminus, M3, and the β6-β7 loop that is essential for GLIC maturation and function, with no analogous cluster located in ELIC. Our study shows that M4 contributes differently to the maturation

and gating of these two closely related homologs, and suggests that GLIC and ELIC exhibit divergent features of channel function/modulation.

4.4 Results

4.4.1 GLIC M4 Ala-scan

To probe the functional role of M4 in GLIC, we first performed an Ala scan of the entire α-helix, with the effects of each Ala mutation on channel function assessed using the two-electrode voltage clamp apparatus. The injection of wild type GLIC cRNA into *Xenopus* oocytes led to the expression of proton-activated channels on the oocyte surface that responded to protons in a dose-dependent manner (Figure 4.1), with a pH_{50} value of 5.03 ± 0.08 (n = 38), consistent with published data (Bocquet et al., 2007). Twenty-five of the 26 M4 Ala-mutants gave robust proton-activated currents, with the mutations displaying either no ($\Delta pH_{50} \leq 0.09$ for 8/26 mutants) or statistically significant changes in pH_{50} ($0.09 < \Delta pH_{50} \leq 0.6$ for 17/26 mutants, $p < 0.05$) relative to wild type. Five mutations led to shifts in pH_{50} >0.5 pH units, which correspond to a 5-fold increase in the concentration of protons required to elicit half-maximal gating. The lack of dramatic effects on pH_{50} is not surprising given that the introduced changes in side chain chemistry are predominantly modest and that they occur at positions peripheral to the primary structures implicated in coupling the agonist site to the channel gate (Grutter et al., 2005; Jha et al., 2007; Lee and Sine, 2005; Lummis et al., 2005). The magnitudes of the individual changes in pH_{50} for each Ala mutation are heat-mapped onto the GLIC M4 α-helix in Figure 4.2 (see also Table 4.1). Note that the proton binding sites for GLIC activation are located primarily in the ECD (Duret et al., 2011), although an intramembranous His residue on M2 is essential (Rienzo et al., 2014; Wang et al., 2012). Given the long distance between the sites of mutation and the agonist (proton) binding sites, the shifts in ligand sensitivity likely reflect changes in the ability to couple agonist binding to channel gating. This assertion is consistent with the previous observations that mutations in M4 of the muscle-type nAChR have no effect on agonist affinity (Bouzat et al., 2000; Mitra et al., 2004; Shen et al., 2006).

Figure 4.1 Functional characterization of GLIC and ELIC mutants

Whole cell electrophysiological traces recorded using the two-electrode voltage clamp apparatus. Currents were recorded from *Xenopus* oocytes expressing either GLIC (A) or ELIC (B) in response to either protons or cysteamine, respectively. The lower panel presents dose response curves (normalized current (I/I_{max}) versus ligand concentration) for select Ala mutants, with *n* = number of averaged traces. Error bars represent S.E.

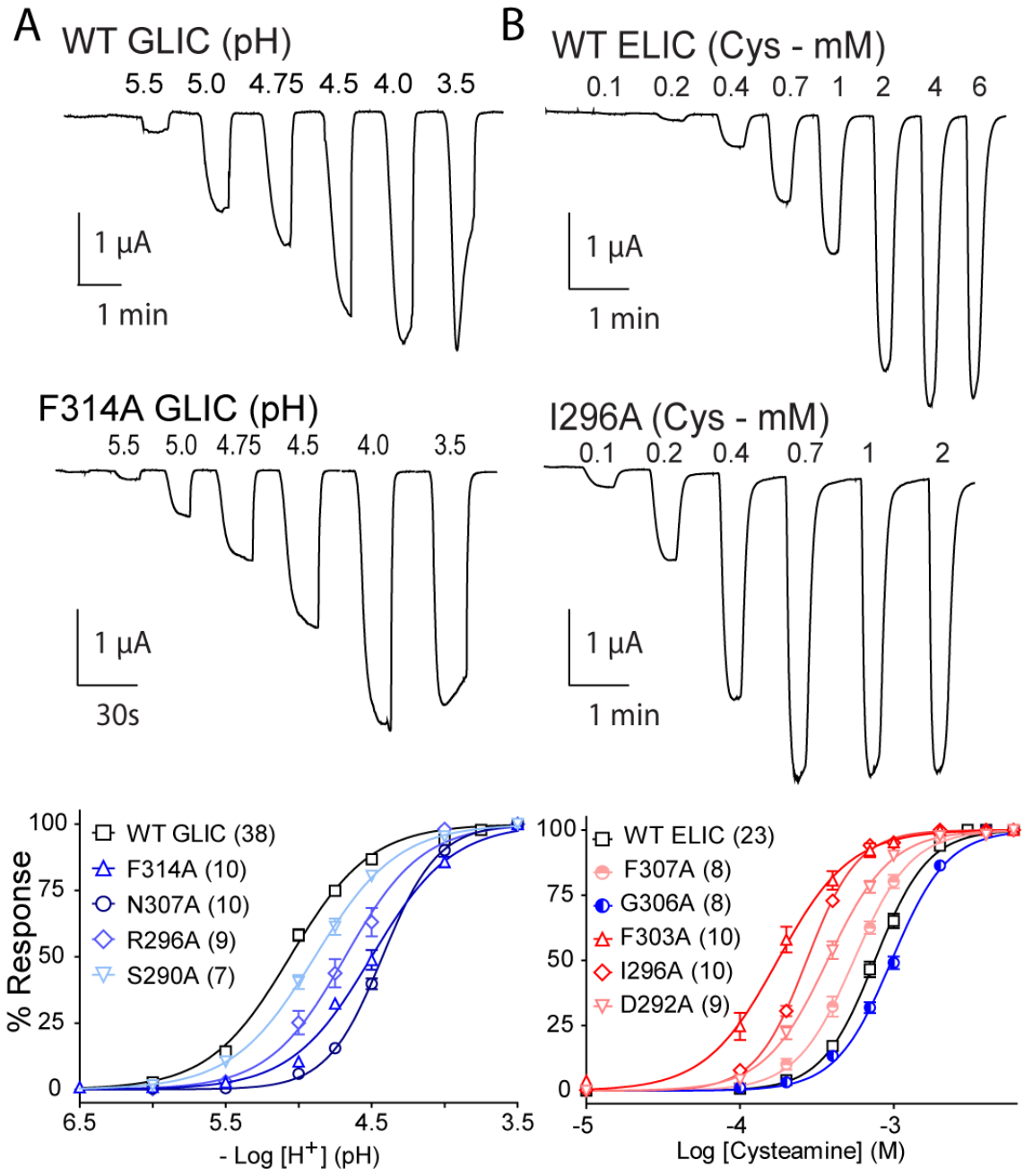
A
WT GLIC (pH)
5.5 5.0 4.75 4.5 4.0 3.5
1 µA
1 min
B
WT ELIC (Cys - mM)
0.1 0.2 0.4 0.7 1 2 4 6
1 µA
1 min
F314A GLIC (pH)
5.5 5.0 4.75 4.5 4.0 3.5
1 µA
30s
I296A (Cys - mM)
0.1 0.2 0.4 0.7 1 2
1 µA
1 min
% Response
100
75
50
25
0
WT GLIC (38)
F314A (10)
N307A (10)
R296A (9)
S290A (7)
6.5 5.5 4.5 3.5
- Log [H+] (pH)
WT ELIC (23)
F307A (8)
G306A (8)
F303A (10)
I296A (10)
D292A (9)
-5 -4 -3
Log [Cysteamine] (M)

Table 4.1 - The effects of M4 Ala mutations on the function of GLIC and ELIC

Dose Response[a]							
GLIC				ELIC			
Mutant	pH_{50}	Hill Slope	n	Mutant	EC_{50} (mM)	Hill slope	n
WT	5.03 ± 0.08	1.42 ± 0.49	38	WT	0.93 ± 0.13	2.13 ± 0.36	23
F317A	5.41 ± 0.08 [d]	1.31 ± 0.30	8	L321A	0.58 ± 0.08 [d]	2.99 ± 0.31	10
G316A	5.01 ± 0.08	1.74 ± 0.48	8	T320A	0.59 ± 0.06 [d]	2.53 ± 0.73	8
F315A	4.69 ± 0.01 [d]	1.71 ± 0.07	8	I319A	0.86 ± 0.16	2.20 ± 0.38	11
F314A	4.48 ± 0.02 [d]	1.61 ± 0.11	10	G318A	0.76 ± 0.13 [d]	2.13 ± 0.16	10
L313A	4.78 ± 0.05 [d]	1.14 ± 0.13	6	R317A	0.55 ± 0.11 [d]	2.41 ± 0.32	10
F312A	4.50 ± 0.01 [d]	1.84 ± 0.04	6	I316A	0.63 ± 0.10 [d]	2.52 ± 0.27	10
A311	-	-	-	V315A	0.60 ± 0.08 [d]	2.54 ± 0.14	9
L310A	4.47 ± 0.02 [d]	1.57 ± 0.11	6	L314A	0.42 ± 0.05 [d]	2.60 ± 0.36	8
I309A	5.05 ± 0.05	1.59 ± 0.24	7	V313A	0.95 ± 0.12	2.58 ± 0.41	10
I308A	5.08 ± 0.02	1.55 ± 0.09	6	C312A	0.55 ± 0.08 [d]	2.11 ± 0.26	10
N307A	4.42 ± 0.01 [d]	2.43 ± 0.13	10	G311A	0.51 ± 0.10 [d]	2.02 ± 0.20	11
A306	-	-	-	I310A	0.88 ± 0.09	1.99 ± 0.11	10
L305A	5.11 ± 0.09 [f]	1.53 ± 0.41	9	A309	-	-	-
L304A	5.08 ± 0.13	1.57 ± 0.74	7	L308A	0.52 ± 0.08 [d]	2.76 ± 0.53	8
F303A	4.48 ± 0.09 [d]	1.85 ± 0.65	8	F307A	0.57 ± 0.09 [d]	2.48 ± 0.24	8
V302A	4.81 ± 0.04 [d]	1.64 ± 0.27	7	G306A	0.97 ± 0.10	2.23 ± 0.23	8
V301A	4.92 ± 0.06 [e]	1.51 ± 0.35	8	L305A	0.57 ± 0.04 [d]	2.36 ± 0.40	8
P300A	NC[b]	NC[b]	8	P304A	*[c]	*[c]	10
F299A	5.04 ± 0.09	1.44 ± 0.38	6	F303A	0.19 ± 0.07 [d]	2.03 ± 0.40	10
A298	-	-	-	A302	-	-	-
I297A	4.99 ± 0.08	1.20 ± 0.26	6	L301A	0.40 ± 0.07 [d]	2.03 ± 0.34	9
R296A	4.65 ± 0.03 [d]	1.61 ± 0.13	9	R300A	0.40 ± 0.05 [d]	2.54 ± 0.37	11
S295A	5.12 ± 0.1	1.36 ± 0.39	6	C299A	0.56 ± 0.09 [d]	2.50 ± 0.18	9
A294	-	-	-	R298A	0.58 ± 0.21 [d]	2.09 ± 0.22	8
R293A	4.90 ± 0.12 [d]	1.32 ± 0.49	8	Q297A	0.56 ± 0.09 [d]	2.90 ± 0.43	7
T292A	4.86 ± 0.05 [d]	1.69 ± 0.32	6	I296A	0.27 ± 0.03 [d]	2.80 ± 0.45	10
I291A	4.78 ± 0.05 [d]	1.15 ± 0.15	7	L295A	0.50 ± 0.11 [d]	2.26 ± 0.28	8
S290A	4.89 ± 0.06 [d]	1.53 ± 0.30	7	L294A	0.69 ± 0.17 [d]	2.20 ± 0.13	8
A289	-	-	-	D293A	0.46 ± 0.21 [d]	2.13 ± 0.30	8
A288	-	-	-	D292A	0.38 ± 0.07 [d]	2.18 ± 0.20	9
R287A	4.93 ± 0.03 [f]	1.50 ± 0.14	6	E291A	0.41 ± 0.06 [d]	2.66 ± 0.48	11
A286	-	-	-	V290A	0.53 ± 0.10 [d]	2.00 ± 0.13	6
P285A	4.96 ± 0.07	1.47 ± 0.31	6	G289A	0.57 ± 0.03 [d]	2.15 ± 0.11	6

[a] Measurements performed 1–4 days after cRNA injection (V_{hold} ranging from −10 to −60 mV). Error values represent standard deviation.
[b] $p < 0.001$ relative to WT ELIC/GLIC via one-way ANOVA followed by Dunnet's post hoc test.
[c] Data from (Prevost et al., 2012)
[d] $p < 0.05$ relative to WT GLIC via one-way ANOVA followed by Dunnet's post hoc test.
[e] $p < 0.01$ relative to WT GLIC via one-way ANOVA followed by Dunnet's post hoc test.
[f] No significant current observed up to 4 days after cRNA injection.
[g] Functionally distinct, traditional EC_{50} values were not obtained.

Figure 4.2 GLIC and ELIC M4 Ala scan heat map

The changes in the EC_{50} values resulting from the mutation of each M4 residue to Ala are heat-mapped onto M4 for both (A) GLIC (Protein Data Bank code 4HFI) and (B) homology model of ELIC (based on the GLIC structure). The magnitude of the shift in EC_{50} (log scale) is depicted via color intensity, with no change in EC_{50} in white, gain-of-function in red, and loss-of-function in blue. A non-functional mutation, GLIC P300A (NC), is shown in black. The EC_{50} of the corresponding P304A mutant (colored gray) in ELIC is not presented, due to altered desensitization kinetics. C, graphical representation of EC_{50} changes (log scale, $\Delta EC_{50} = EC_{50}Mut - EC_{50}WT$), colored as gain/loss-of-function. Residues are grouped by helical turn (gray boxes), and vertically aligned with their position on the adjacent M4 structure. Wild type Ala residues are shown in gray. Changes in pH_{50}/EC_{50} were statistically significant by one-way ANOVA followed by Dunnett's post hoc test for all Ala mutants in GLIC, except for G316A, I309A, I308A, L304A, F299A, I297A, S295A and P285A, and for all Ala mutants in ELIC, except I319A, V313A, I310A, and G306A (see Table 4.1 for complete list of data). Error bars represent S.D. (GLIC) and log S.D. (ELIC).

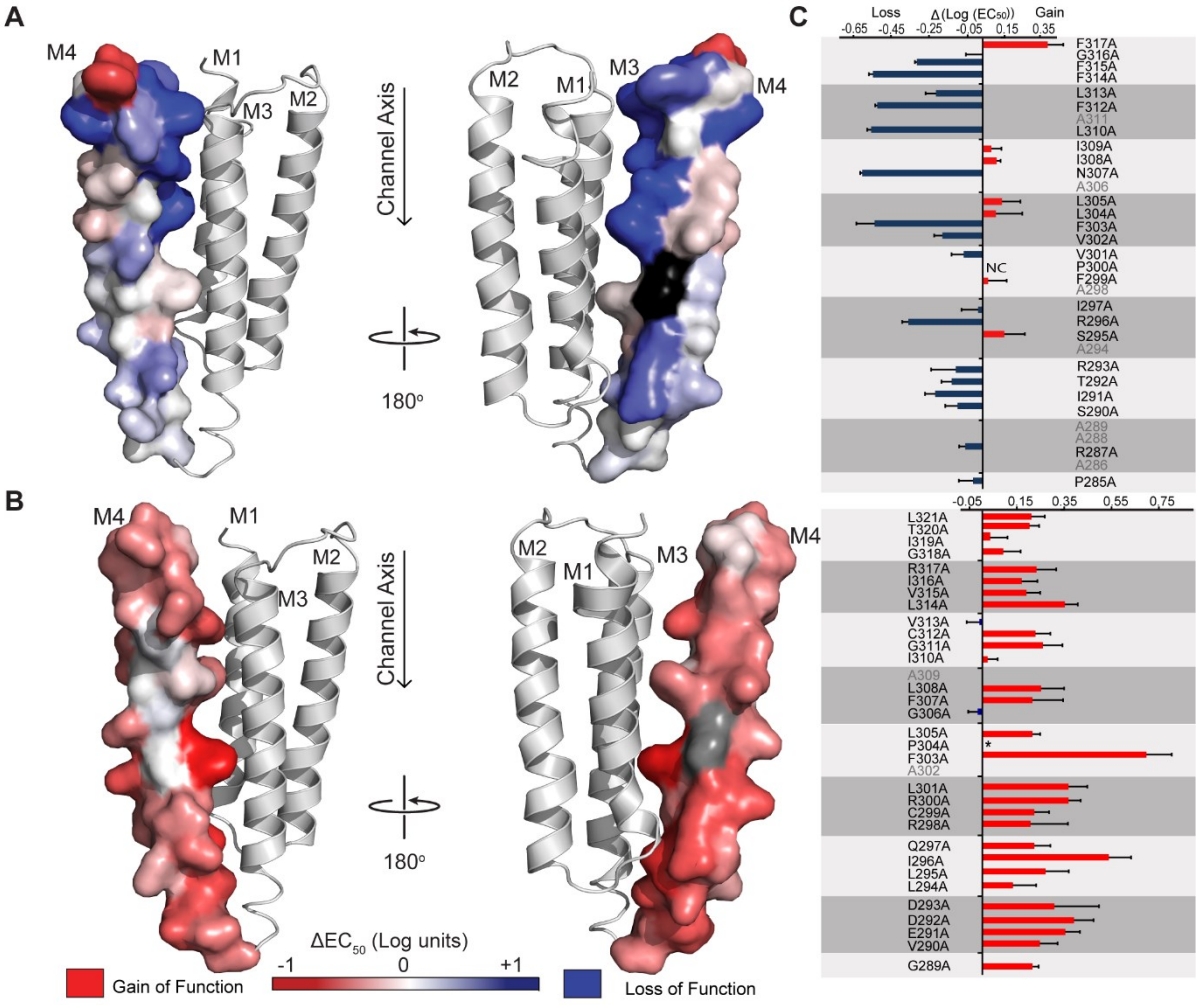
A
M4
M1
M2
M3
Channel Axis
180°
M2
M1
M3
M4
B
M4
M1
M2
M3
Channel Axis
180°
M2
M1
M3
M4
ΔEC50 (Log units)
-1
0
+1
Gain of Function
Loss of Function
C
Loss
Δ(Log (EC50))
Gain
-0.65 -0.45 -0.25 -0.05 0.15 0.35
F317A
G316A
F315A
F314A
L313A
F312A
A311
L310A
I309A
I308A
N307A
A306
L305A
L304A
F303A
V302A
V301A
P300A
F299A
A298
I297A
R296A
S295A
A294
R293A
T292A
I291A
S290A
A289
A288
R287A
A286
P285A
NC
-0.05 0.15 0.35 0.55 0.75
L321A
T320A
I319A
G318A
R317A
I316A
V315A
L314A
V313A
C312A
G311A
I310A
A309
L308A
F307A
G306A
L305A
P304A
F303A
A302
L301A
R300A
C299A
R298A
Q297A
I296A
L295A
L294A
D293A
D292A
E291A
V290A
G289A
*

Several important trends are observed in the GLIC Ala scan data set. First, 15 of the 17 function-altering mutations (ΔpH_{50} >0.09) led to an *increase* in the concentration of protons required to elicit channel gating and thus a decrease in channel function. The only mutation that led to a gain-of-function, F317A, is located at the C terminus of M4, where it projects away from the core of the protein to interact with adjacent phospholipids. Second, the deleterious effects of the Ala mutations are greater near the C terminus of M4, proximal to structures at the interface between the ECD and TMD (the β1-β2 and β6-β67 loops of the ECD and the M2-M3 linker of the TMD) that play a role coupling agonist binding to channel gating (Figure 4.3). Third, the deleterious effects are greater for residues located on the inner face of M4, oriented toward M1/M3, suggesting that interactions between the M4 C terminus and either the adjacent transmembrane α-helices or the loops at the ECD/TMD interface are important for function. Finally, the largest negative effects on channel function came from Ala substitution of aromatic residues on the M1/M3-facing surface of M4, consistent with the demonstrated essential role of aromatic interactions driving M4 binding to M1/M3 during folding (Haeger et al., 2010). Two or more simultaneous aromatic to Ala substitutions at the M4-M1/M3 interface in GLIC lead to a complete loss of folding and/or function (Carswell et al., 2015b).

Note that the mutation of a polar residue, N307A, led to a relatively large drop in the pH_{50} (~0.6 pH units). Asn-307 is located in the C-terminal half of M4 where it forms a hydrogen bond via a bridging water molecule with Tyr-254 on M3 (see Figure 4.3) (Sauguet et al., 2013). Finally, no pH-activated currents were observed with the P300A mutant, suggesting that this mutation abrogates channel function and/or the folding, oligomerization, and thus trafficking of the mutant to the cell surface. P300 is located near the middle of M4, where it kinks the α-helix such that the M4 C terminus interacts directly with both the N terminus of M3 and the β6-β7 loop (Figure 4.3). This kink may be important for positioning the M4 C terminus for effective interactions with M3 and the β6-β7 loop (see below), and might also position the C terminus of M4 so that it helps mask a pre-M1 sequence, which in muscle-type nAChRs acts as an ER-retention signal (see “Discussion”) (Wang et al., 2002).

Figure 4.3 Interactions at the ECD/TMD interface of GLIC and ELIC involving M4

The structure of GLIC, with a single subunit shown in a blue schematic representation is shown on the left, with the dashed box highlighting the approximate area zoomed in on the right. The top right panel shows interactions between M4 and the ECD/TMD interface in GLIC (Protein Data Bank code 4HFI). The bottom right shows interactions between M4 and the ECD/TMD interface in a homology model of ELIC (based on the GLIC structure). Interacting residues are colored according to their physicochemical properties, with aliphatic residues in tan, aromatic residues in yellow, charged residues (Arg-118) in blue, and polar residues (Asn-307) in green. A water molecule is shown as a cyan sphere. For visibility, the glycine residues are depicted *as* transparent spheres, and the β6-β7 loop is highlighted in green.

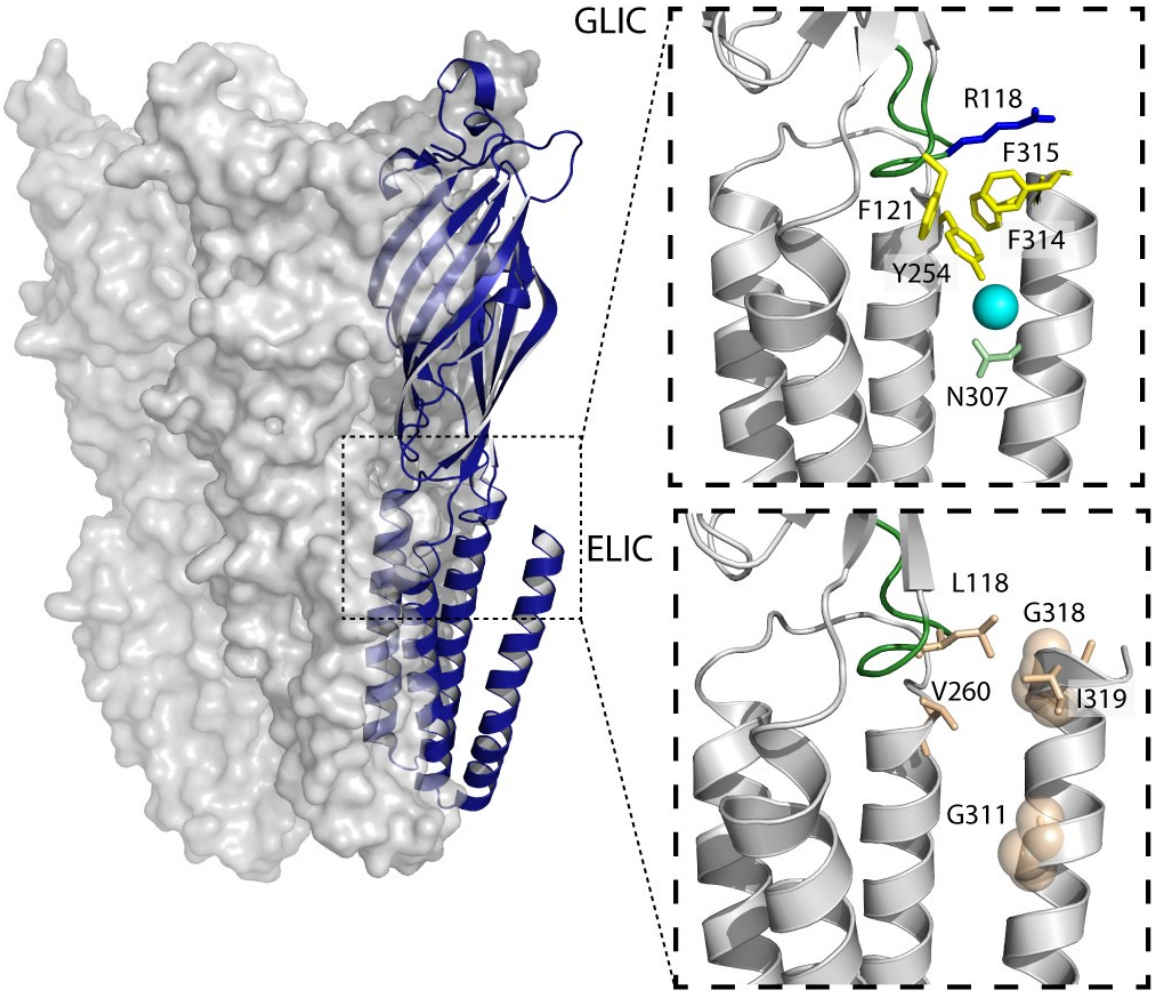
GLIC
R118
F315
F121
F314
Y254
N307
ELIC
L118
G318
V260
I319
G311

4.4.2 GLIC M4 C-terminal Deletions

We further explored the role of M4 in channel function by sequentially deleting residues located at the M4 C terminus (Figure 4.4; Table 4.2). Eliminating the terminal one (Phe-317; dF) or two (Gly-316 and Phe-317; dGF) residues, which project away from the remainder of the TMD into the lipid bilayer, had little effect on channel function, consistent with the minimal effects of the Ala mutations at these two sites. In contrast, the additional deletion of Phe-315 (dFGF) led to a relatively large drop in ligand sensitivity ($\Delta pH_{50} = 0.7$). Phe-315 projects toward the TMD, forming π-π and/or cation-π interactions with Tyr-254 on M3 and Phe-121 and Arg-118 on the β6-β7 loop (Figure 4.3). Further deletion of Phe-314 (dFFGF) and then Leu-313 (dLFFGF) led to a loss of detectible proton-activated current, suggesting a loss of function and/or impaired folding/trafficking of the mutants to the cell surface.

To test whether the loss of proton-activated current reflected reduced coupling of binding to gating or reduced expression on the oocyte surface, we engineered an α-BTX binding site into the wild type GLIC background (referred to as α-BTX-WT), as well as into each of the 5 C-terminal M4 deletion mutants (See (Wang et al., 2012)). We expressed each α-BTX deletion mutant in oocytes, characterizing each pH_{50} value. We also correlated the maximal current elicited by each mutant at pH 4.0 with the level of surface expression, as measured by radiolabeled α-BTX binding to that same oocyte (Figure 4.5). No α-BTX binding was observed with the α-BTX-dFFGF and α-BTX-dLFFGF mutants, suggesting that the lack of activity is due to a loss of surface expression. Interestingly, the α-BTX-dFGF mutant expressed on the cell surface, but the maximal response normalized to the level of expression is greatly reduced relative to the α-BTX-WT, α-BTX-dF, and α-BTX-dGF mutants. This result confirms that Phe-315 plays a key role in the coupling of proton binding to channel gating

Table 4.2 - The effects of M4 C-terminal deletions on the function of GLIC and ELIC

Dose Response							
GLIC				ELIC			
Mutant	pH_{50}	Hill Slope	n	Mutant	EC_{50} (mM)	Hill slope	n
WT	5.03 ± 0.08	1.42 ± 0.49	38	WT	0.93 ± 0.13	2.13 ± 0.36	23
1 - dF	5.15 ± 0.13 [b]	1.65 ± 0.26	9	1 - dL	0.62 ± 0.04 [a]	2.30 ± 0.26	5
2 - dGF	5.03 ± 0.20	1.42 ± 0.20	8	2 - dTL	0.56 ± 0.05 [a]	2.67 ± 0.42	11
3 - dFGF	4.42 ± 0.18 [a]	1.64 ± 0.46	10	3 - dITL	0.81 ± 0.08 [b]	2.62 ± 0.36	8
4 - dFFGF	NC	NC	8	4 - dGITL	0.68 ± 0.07 [a]	2.66 ± 0.43	9
5 - dLFFGF	NC	NC	8	5 - dRGITL	0.68 ± 0.09 [a]	2.63 ± 0.55	9
-	-	-	-	6 - dIRGITL	0.54 ± 0.08 [a]	2.40 ± 0.55	10
-	-	-	-	7 - dVIRGITL	0.50 ± 0.06 [a]	2.45 ± 0.28	12

[a] $p < 0.001$ relative to WT ELIC/GLIC via one-way ANOVA followed by Dunnet's post hoc test.
[b] $p < 0.05$ relative to WT ELIC/GLIC via one-way ANOVA followed by Dunnet's post hoc test.
NC signifies that no current was detected from that mutant.

4.4.3 Interactions between the C-terminus of M4 and M3 and the β6-β7 loop

Residues at the C terminus of M4 in GLIC interact with residues on both the adjacent transmembrane α-helix, M3, and the β6-β7 loop (Figure 4.3). As noted, Phe-315 is within roughly 4 Å of three residues, Tyr-254 on M3 and both Phe-121 and Arg-118 on the β6-β7 loop, thus potentially forming a network of both π-π and cation-π interactions that serve to enhance channel function. Phe-314 is relatively close to both Tyr-254 on M3 and Met-252 on the M2-M3 linker. Each of the noted aromatic and charged residues was mutated to Ala, and each led to a loss-of-function (Table 4.3). Double Ala mutations of potentially interacting pairs of residues were also generated, but in all but one case these double mutants did not lead to functional channels on the oocyte surface, suggesting that these interactions are essential for folding/trafficking and/or function. Only the R118A/F315A double mutant gave proton-activated currents. The pH_{50} of the R118A/F315A double mutant is essentially identical to that of each single mutation (R118A and F315A) suggesting that the two residues are energetically coupled, and that this coupling plays a role in channel function. Taken together, the data show that interactions between the M4 C terminus and both M3 and the β6-β7 loop are essential for folding and/or channel function, as previously suggested for the *Torpedo* nAChR (daCosta and Baenziger, 2009).

4.4.4 ELIC M4 Ala-scan

An equivalent M4 Ala scan was performed to explore the role of the M4 α-helix in ELIC function. Wild type ELIC cRNA injected into oocytes led to robust cysteamine-activated currents on the oocyte surface (Figure 4.1), with EC_{50} values of 0.94 ± 0.16 mm consistent with published data (Zimmermann and Dutzler, 2011; Zimmermann et al., 2012). Similar to the Ala mutations in GLIC, Ala mutations of M4 residues in ELIC led to relatively small changes in function (<10-fold), but the results were strikingly different from a qualitative perspective. Whereas M4 Ala mutations in GLIC typically had detrimental effects on channel function, the majority of the M4 Ala mutations in ELIC led to modest but statistically significant ($p < 0.001$) gain-of-function phenotypes ($\Delta EC_{50} \geq 0.09$ log units) (27/31 mutants), with no significant loss-of-function mutations observed (Figure 4.3 and

Table 4.1). In addition, the Ala mutations eliciting the greatest change in EC_{50} were located in the N-terminal half, as opposed to the C-terminal half of M4. Consistent with the Ala scan of GLIC, the strongest effects were again observed with the mutation of residues lining the inner face of M4 that orients toward M1/M3. Thus, in both pLGICs, interactions at the M4-M1/M3 interface most strongly influence channel function.

The Ala scan also revealed several unexpected effects. Contrasting the results obtained from GLIC, mutation of either of the two M1/M3-facing aromatic residues in the cytoplasmic half of M4 led to a gain, rather than a loss-of-function, with F303A leading to the largest observed increase in ligand sensitivity (~0.7 log units). As neither of these M4 aromatic residues (Phe-307 or Phe-303) is within range of an aromatic binding partner on M1/M3, their uncompensated-for bulk may impede, rather than enhance, the interaction of M4 with M1/M3. Second, the Ala-substitution of an inward-facing Ile (I296A) in the N-terminal half of M4 led to the second highest gain-of-function. It is possible that, as with aromatics, the mutation to a less bulky hydrophobic residue leads to more effective van der Waals contact with the adjacent Leu-278 and Ala-282 located on M3. Finally, a substantial effect was observed with the Ala substitution of a proline residue, which is conserved in the M4 of many pLGICs. Unlike the analogous P300A mutation in GLIC, P304A in ELIC remained functional, but exhibited more rapid desensitization kinetics. The effects of the P304A mutation on ELIC desensitization are explored in more detail elsewhere.

Figure 4.4 Effects of M4 C-terminal deletions on the function of GLIC and ELIC

A) whole cell electrophysiological traces recorded from oocytes expressing the key C-terminal deletion mutants in GLIC and ELIC (log scale, $\Delta EC_{50} = EC_{50}Mut - EC_{50}WT$). dn corresponds to the number (n) of C-terminal residues removed. **B)** effects of the C-terminal deletions on pH_{50}/EC_{50}. Error bars represent S.D. (GLIC) and log S.D. (ELIC). NC, no current. EC_{50} changes in all ELIC mutants and GLIC d1 and d3 were statistically significant as determined by one-way ANOVA followed by Dunnett's post hoc test. See Table 4.2 for EC_{50} values.

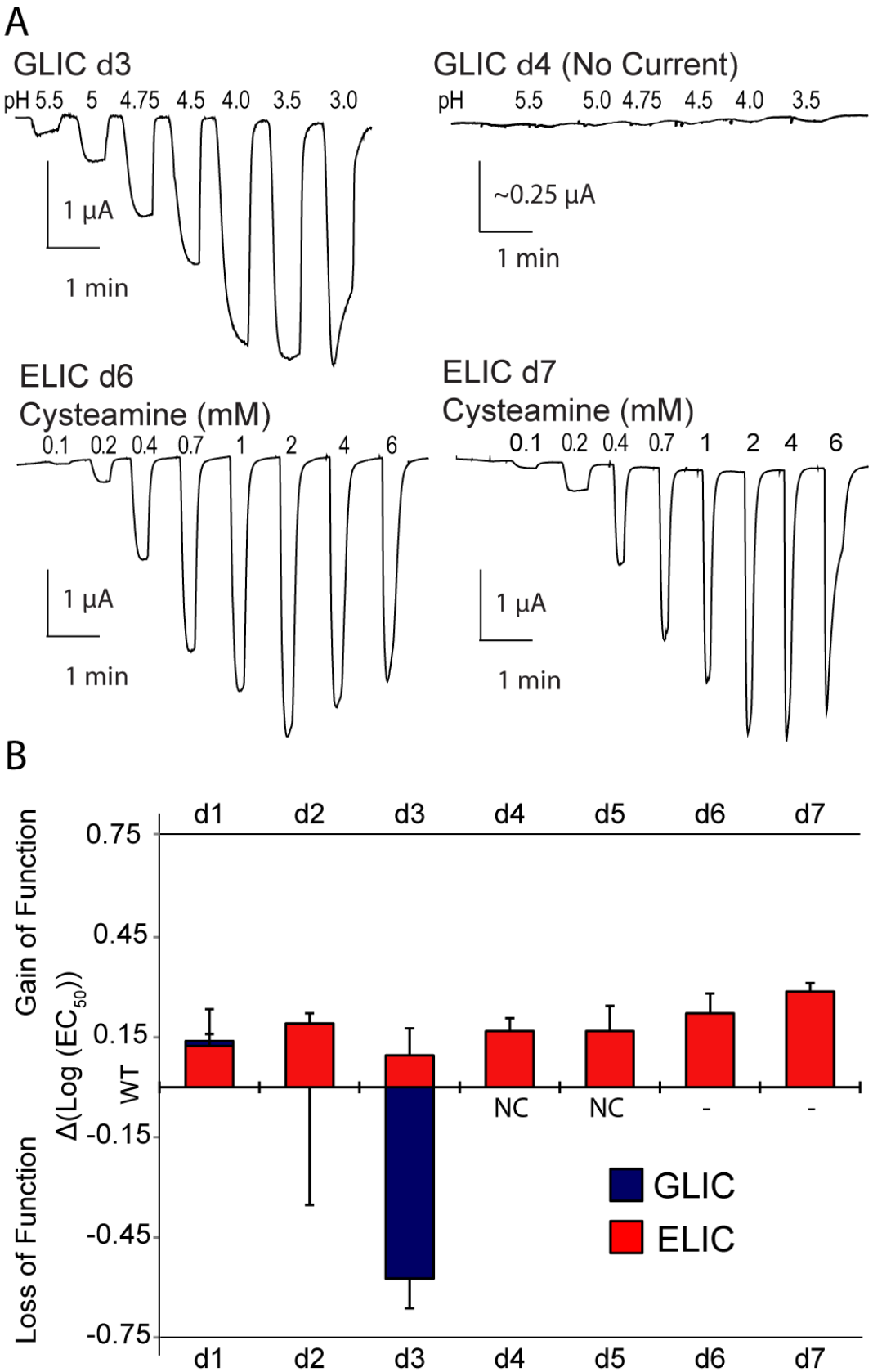
A
GLIC d3
pH 5.5 5 4.75 4.5 4.0 3.5 3.0
1 µA
1 min
GLIC d4 (No Current)
pH 5.5 5.0 4.75 4.5 4.0 3.5
~0.25 µA
1 min
ELIC d6
Cysteamine (mM)
0.1 0.2 0.4 0.7 1 2 4 6
1 µA
1 min
ELIC d7
Cysteamine (mM)
0.1 0.2 0.4 0.7 1 2 4 6
1 µA
1 min
B
Gain of Function
Loss of Function
Δ(Log (EC50))
WT
0.75
0.45
0.15
-0.15
-0.45
-0.75
d1 d2 d3 d4 d5 d6 d7
NC NC - -
GLIC
ELIC

4.4.5 ELIC M4 C-terminal deletions

The consistent gain-of-function phenotypes observed with the Ala mutations suggest that unlike GLIC, M4-M1/M3 interactions in ELIC are not optimized for effective channel function. We next explored the functional role of the M4 C terminus by performing C-terminal deletions. In stark contrast to the C-terminal deletions in GLIC, deletions of up to 7 residues (dL → dVIRGITL), *i.e.* two full turns at the C terminus of M4, led to no change, or even modest gain-of-function phenotypes (Figure 4.4 and Table 4.2). Thus, interactions between residues located at the M4 C terminus and residues on either M3 or the β6-β7 loop in ELIC are not essential, or even important, for channel function. Although this is perhaps not surprising given that the M4 C terminus in ELIC has primarily aliphatic residues, with Gly and Ile facing the M1/M3 interface, even deletion of the charged Arg-317 had no detrimental effect. As noted, the final 5 residues in the C-terminal half of M4 α-helix are not resolved in the ELIC crystal structure (Hilf and Dutzler, 2008; Pan et al., 2012). The crystal structure suggests weak interactions between the M4 C terminus and either M1/M3 or the β6-β7 loop. One explanation of our data is that removal of the loosely bound and thus likely dynamic M4 C terminus allows the remainder of M4 to interact more effectively with M1/M3 to promote channel function.

4.4.6 ELIC C-terminal M4 interactions with M3 and the β6-β7 loop

As we had previously observed that enhancing M4-M3 interactions via aliphatic-to-aromatic substitutions had a positive effect on ELIC channel function (Carswell et al., 2015b), we next tested whether introducing additional M4-M3 interactions would further improve the coupling of binding to gating. In GLIC, M4 Asn-307 (M4) is linked to Tyr-254 (M3) via a bridging water molecule (Figure 4.3). We inserted these residues at corresponding positions in ELIC, giving the mutant G311N/V260Y. Although individually each mutation induced a mild gain-of-function (EC_{50} = 0.32 ± 0.07 and 0.47 ± 0.21 mm, respectively) relative to the WT EC_{50} (0.94 ± 0.16 mm), no further enhancement was observed with the G311N/V260Y double mutant (EC_{50} = 0.41 ± 0.1 mm). The G311N mutation was also superimposed onto an ELIC mutant containing the equivalent C-terminal aromatic cluster to that found in GLIC (I319F/G318F/V260Y), but in this case the G311N mutation actually

reduced channel function relative to the mutant containing only the aromatic cluster (EC_{50} = 0.64 ± 0.15 for G311N/I319F/G318F/V260Y *versus* EC_{50} = 0.18 ± 0.02 for I319F/G318F/V260Y).

We also tested whether enhanced interactions between M4 and the β6-β7 loop could improve coupling between the agonist site and channel gate. In GLIC, an interaction between Phe-315 on M4 and Arg-118 in the β6-β7 loop promotes channel function. Although the corresponding individual mutations I319F (EC_{50} = 0.62 ± 0.18 mm) and L118R (EC_{50} = 0.35 ± 0.11 mm) in ELIC led to functional gains, the double L118R/I319F mutant gave no further enhancement (EC_{50} = 0.56 ± 0.18 mm). A double L118R/I319D mutant was also generated to replace the engineered cation-π interaction with an engineered salt bridge, but although I319D gave a WT-like EC_{50} value (0.89 ± 0.12), the double mutant had little additional effect (EC_{50} = 0.51 ± 0.19 mm). It may be, however, that these residues are too distant/improperly oriented in the actual protein to promote M4-β6-β7 interactions. With that in mind, we superimposed the β6-β7 loop L118R mutation onto a "M4-M1/M3 stabilized" ELIC mutant, which possesses the full C-terminal M4 aromatic cluster that is found in GLIC (Bouzat et al., 1994). Introduction of the L118R mutation into M4-M1/M3-stabilized ELIC did lead to a slight enhancement (EC_{50} goes from 0.18 ± 0.02 with the aromatic cluster (V260Y/G318F/I319F) to 0.08 ± 0.03 with both the aromatic cluster and the L118R mutation). Thus, it appears that in WT ELIC, there are no interactions between the C terminus of M4 and β6-β7 loop that impact on channel function. With the addition of aromatics to stabilize C-terminal M4-M3 interactions, however, enhanced M4 interactions with the β6-β7 loop slightly improve gating. In other words, as ELIC becomes more like GLIC in terms of its M4-M1/M3 interactions, its function becomes more easily modulated through mutation of M4 and/or the β6-β7 loop.

4.5 Discussion

This work sheds light on the mechanism(s) by which the outermost transmembrane M4 α-helix influences pLGIC function, and suggests further that M4 makes distinct contributions to the maturation and function of the two closely related prokaryotic pLGICs, GLIC and ELIC. The latter conclusion was unexpected, but is based on several observations.

Figure 4.5 Surface expression of GLIC and ELIC C-terminal deletions

WT and deletion mutant αBTX-GLIC surface expression in oocytes over time, measured via binding of ^{125}I-labeled α-BTX binding assays. Error bars represent S.D. Inset graph*:* maximum current in each oocyte at pH 4.0 plotted *versus* the level of surface expression in the same oocyte.

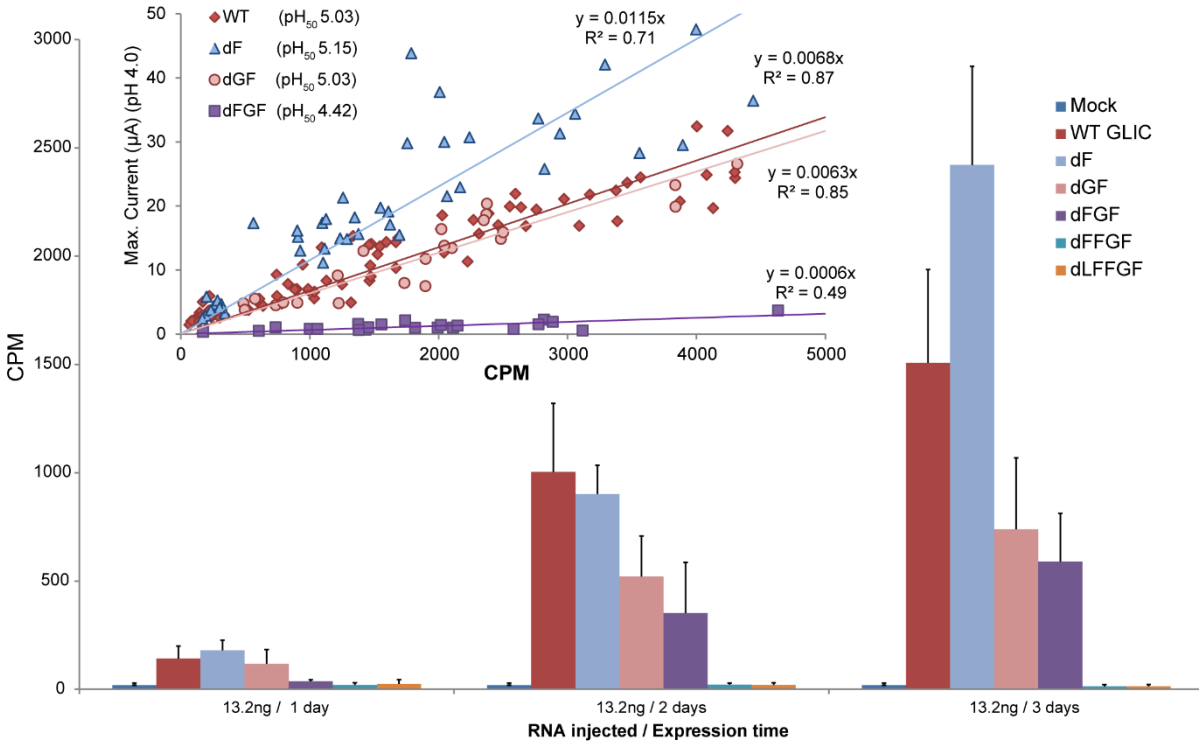
WT (pH50 5.03)
dF (pH50 5.15)
dGF (pH50 5.03)
dFGF (pH50 4.42)
y = 0.0115x
R² = 0.71
y = 0.0068x
R² = 0.87
y = 0.0063x
R² = 0.85
y = 0.0006x
R² = 0.49
Max. Current (µA) (pH 4.0)
CPM
Mock
WT GLIC
dF
dGF
dFGF
dFFGF
dLFFGF
13.2ng / 1 day
13.2ng / 2 days
13.2ng / 3 days
RNA injected / Expression time

First, an Ala scan of GLIC M4 shows that almost any disruption of the M4-M1/M3 interface has a detrimental effect on function, suggesting that M4-M1/M3 interactions are optimized in GLIC. In contrast, Ala mutations of residues at the M4-M1/M3 interface in ELIC typically lead to gain-of-function phenotypes, suggesting that M4-M1/M3 interactions are less than optimal. In fact, the replacement of large bulky hydrophobic side chains at the M4-M1/M3 interface in ELIC with a smaller methyl group of alanine seemingly leads to more effective M4-M1/M3 interactions that promote channel function. Even greater improvements in ELIC function are observed with the introduction of interacting aromatic residues at the M4-M1/M3 interface (Bouzat et al., 1994).

Second, a cluster of interacting residues on M3, M4, and the β6-β7 loop (*i.e.* at the ECD/TMD interface) in GLIC is essential to the maturation and function of GLIC, whereas no such counterpart is found in ELIC. Specifically, the aromatic residues, Phe-314 and Phe-315, on the M4 C terminus in GLIC form π-π and/or cation-π interactions with Tyr-254 on M3 and both Phe-121 and Arg-118 on the β6-β7 loop. Ala mutations of any of these interacting residues leads to a loss-of-function, whereas double Ala mutations of every interacting pair, except Phe-315 and Arg-118, completely eliminates folding and/or function (see also (Bouzat et al., 1994)). Furthermore, deletion of the final three M4 residues to eliminate Phe-315 (*i.e.* deletion of Phe-317, Gly-316, and Phe-315) leads to a substantial loss of both folding/cell surface expression and function, with the additional deletion of Phe-314 completely abrogating cell surface expression of GLIC. In contrast, Ala mutations of either of the residues in ELIC that are analogous to the residues Phe-314 and Phe-315 in GLIC (*i.e.,* ELIC Gly-317 and Ile-318) actually leads to a slight potentiation of channel function. In addition, deletion of two full turns at the M4 C terminus (7 residues) has no noticeable effect on expression and leads to a left shift in EC_{50} corresponding to a slight gain-of-function. We also engineered the interactions involving the M4 C terminus and residues on both M3 and the β6-β7 loop that are found in GLIC into ELIC, with limited benefits to channel function. It appears that ELIC has evolved to fold, traffic to the cell surface, and function in the absence of effective interactions between the M4 C terminus and residues at the ECD/TMD coupling interface.

Table 4.3 - Effects of mutations at the ECD/TMD interface on the function of GLIC and ELIC

GLIC Mutant	pH 50	n
R118A/F315A	4.54 ± 0.31 [a]	8
R118A	4.41± 0.22 [a]	7
F121A	4.66 ± 0.20 [a]	8
F121A/F315A	NC	
R118A/F121A	NC	
R118A/F121A/F315A	NC	
Y254A	4.58 ± 0.03 [a]	8
N307A/Y254A	4.39 ± 0.10[a]	9
ELIC Mutant	**EC_{50} (mM)**	**n**
L118R	0.35 ± 0.11 [a]	8
I319D	0.89 ± 0.13	8
I319F	0.62 ± 0.18 [a]	6
I319F/L118R	0.56 ± 0.18 [a]	9
L118R/I319D	0.51 ± 0.19 [a]	6
G311N	0.32 ± 0.07 [a]	9
V260Y	0.47 ± 0.21 [a]	4
G311//V260Y	0.41 ± 0.10 [a]	7
E3: V260Y/G318F/I319F	0.18 ± 0.02 [a]	9
E3 + G311N	0.64 ± 0.15 [a]	8
E3 + L118R	0.08 ± 0.03 [a]	6

[a] $p < 0.001$ relative to WT ELIC/GLIC via one-way ANOVA followed by Dunnet's post hoc test.

Finally, the contrasting contributions of the M4 C terminus to the maturation and function of GLIC and ELIC were highlighted by the Ala mutation of a lipid-facing Pro residue located midway along M4 in both prokaryotic pLGICs. In the GLIC structure, this proline (Pro-300) leads to a kink in M4 that positions the M4 C terminus so that it forms the above noted π-π and cation-π interactions with other residues at the ECD/TMD coupling interface. The P300A mutation should remove this kink and thus straighten the M4 α-helix, leading to the elimination or weakening of these essential interactions between the M4 C terminus and both M3 and the β6-β7 loop. Consistent with this hypothesis, the P300A mutation completely eliminates GLIC folding/trafficking and/or function. Intriguingly, the analogous Pro residue in ELIC (Pro-304) also leads to a kink in M4, which should position the M4 C terminus to interact with M3 and possibly the β6-β7 loop, yet the P304A mutant of ELIC still forms functional channels that traffic to the oocyte surface. The ability of P304A to gate open is consistent with our contention that interactions between the M4 C terminus and other residues at the ECD/TMD coupling interface are not essential for folding/trafficking or function. The observation that the P304A mutation leads to rapid desensitization kinetics, however, demonstrates that the C-terminal half of M4 still interacts with the adjacent M1 and M3 α-helices to shape the agonist-induced response. This finding is consistent with a recent study, which detected movement of M4 upon desensitization of GLIC ((Velisetty et al., 2014), and see also (Kinde et al., 2015; Tillman et al., 2014; Velisetty et al., 2012, 2014)).

The distinct contributions of M4 to the folding and function of GLIC and ELIC mirrors the distinct conformations of M4 observed in the GLIC and ELIC crystal structures. GLIC has an abundance of aromatic, polar, and charged residues that contribute to tight M4-M1/M3 interactions along the entire length of M4. Although many interactions are likely important facilitators of M4-M1/M3 interactions, aromatic interactions play a dominant role in M4 binding to M1/M3 during pLGIC folding (Haeger et al., 2010). The abundant aromatic interactions at the M4-M1/M3 interface in GLIC are sufficiently strong to maintain tight M4 “binding” to M1/M3, even in the detergent-solubilized state. This tight binding may facilitate channel function, as GLIC crystallized in the presence and absence of agonist exhibits differences in pore diameter that likely reflect channel gating (Bocquet et al., 2009; Hilf and

Dutzler, 2009; Prevost et al., 2012; Sauguet et al., 2014). In ELIC, however, the M4-M1/M3 interface is richer in aliphatic residues, and there are fewer aromatic, polar, and charged residues, particularly involving the M4 C terminus. Significantly, the five C-terminal M4 residues in the ELIC crystal structure are unresolved. Furthermore, although ELIC has been crystallized in both the presence and absence of bound agonist, no changes in pore diameter were observed (Gonzalez-Gutierrez et al., 2012; Zimmermann and Dutzler, 2011). Although further studies may yet lead to the crystallization of both open and closed ELIC conformations, one possible interpretation of the crystal structures is that the absence of effective interactions between the M4 C terminus and other residues at the ECD/TMD interface leads to an ELIC conformation that does not undergo conformational transitions (daCosta and Baenziger, 2013). Although the latter result appears to conflict with our M4 deletions mutations, which suggest that the M4 C terminus has no role in channel function, detergent solubilization followed by crystallization may lead to a more detrimental conformational perturbation than that observed with the M4 C-terminal deletion mutants of ELIC expressed in oocyte membranes.

The distinct contributions of M4 to the folding and function of GLIC and ELIC may also reflect different pathways for agonist-induced channel gating. GLIC is proton activated. A GLIC chimera formed between the GLIC ECD and the glycine receptor TMD is responsive to protons, showing that ECD protonation sites act to gate open the channel (Duret et al., 2011). An intramembrane proton binding site (His) also plays an important role in activation (Rienzo et al., 2014; Wang et al., 2012). Conversely, ELIC is activated by primary amines, which bind to the canonical agonist binding site found at the interface between subunits in the ECDs of eukaryotic pLGICs. One possible interpretation is that distinct roles for M4 in gating arise due to distinct mechanisms of activation, with GLIC activation intimately associated with protonation of the TMD His residue, whereas ELIC activation occurs through an allosteric pathway similar to that of eukaryotic pLGICs. This interpretation, however, is paradoxical with the observation that GLIC requires extensive interactions between the M4 C terminus and residues at the ECD/TMD interface for folding and function, whereas ELIC does not. Regardless, the data suggest that there may be distinct features in the mechanisms of activation in GLIC and ELIC, a finding supported by the

observation that ELIC exhibits atypical gating and cation-conduction properties relative to other pLGICs (Gonzalez-Gutierrez and Grosman, 2015). Double electron-electron resonance experiments also suggest that the x-ray structures of ELIC are not appropriate models for the resting state (Dellisanti et al., 2013). Taken together, these findings caution against the utility of comparing different conformations of GLIC and ELIC to probe the mechanisms underlying agonist-induced gating.

The effects of M4 C-terminal deletions on the folding and cell surface expression of GLIC are intriguing given that a mutation leading to truncation at a Cys residue located distal to the M4 α-helix in the muscle-type ϵ-subunit alters nAChR trafficking to the cell surface leading to one form of congenital myasthenic syndrome (Ealing et al., 2002). The M4 C terminus also plays an essential role in the maturation and function of the *Torpedo* nAChR, an α7–$5HT_{3A}$ chimeric homopentamer, and the full-length $5HT_{3A}$ homopentamer (Butler et al., 2009; Pons et al., 2004; Tobimatsu et al., 1987). One possibility is that the truncation mutations influence the masking of an endoplasmic retention signal located at the N terminus of the M1 (pre-M1) transmembrane α-helix (Wang et al., 2002). In the muscle-type nAChR, this sequence (PL(F/Y)(F/Y)*XX*N) is masked through both inter-subunit and M4-M1/M3 interactions. Although the corresponding pre-M1 sequence in GLIC (RQYFSYI) differs from that of the nAChR consensus, it may be sufficient to influence the trafficking of GLIC in oocytes. Specifically, an unmasking of this sequence by M4 C-terminal deletions could lead to a loss of cell surface expression. Interestingly, the same M4 deletions in ELIC have no effect on folding/trafficking. The analogous pre-M1 sequence in ELIC (RNPSYYL), however, exhibits greater variability relative to the muscle-type nAChR pre-M1 sequence, thus perhaps allowing ELIC to traffic in the absence of the M4 C terminus.

Previous studies addressing the role of M4 in pLGIC function have tended to focus on lipid-facing mutations in the muscle-type nAChR, including detailed kinetic analyses of a lipid facing αC418W mutation that leads to one form of congenital myasthenic syndrome (Lee et al., 1994; Ortiz-Miranda et al., 1997; Shen et al., 2006; Tamamizu et al., 1999). M4 Trp-scanning mutations have also been performed on the M4 α-helix of the α, β, γ, and δ subunits of the nAChR, with some mutations leading to loss-, and others to gain-of-function phenotypes (Caballero-Rivera et al., 2012; Diaz-De Leon et al., 2008; Ortiz-Acevedo et al.,

2004; Tamamizu et al., 2000). In fact, identical mutations of analogous M4 residues in different subunits can have opposite effects on channel function (Bouzat et al., 1998, 2000, 2002). The two αM4 α-helices both move as a single unit roughly halfway along the reaction coordinate leading from the resting to the channel open state, with the movements of both βM4 and ϵM4 following that of αM4 (Mitra et al., 2004). These along with our study highlight the importance of M4 in pLGIC function.

4.6 Conclusion

Our data show that M4 contributes differently to the maturation and function of the two closely related prokaryotic homologs, GLIC and ELIC. Specifically, the M4 C-terminus plays an essential role in GLIC, whereas the role of the M4 C-terminus in ELIC is less defined. An important extension of this work will be to assess how variable M4 sequences in different pLGICs influence both their response to agonist and their lipid sensitivities. This work builds on a previous study, which showed that sequence variations in M4 contribute to the functional differences between fetal and adult forms of the muscle-type nAChR (Bouzat et al., 1994). Sequence variations in the M4 transmembrane α-helices of different nAChR subunits may contribute to distinct subtype-specific channel properties and thus organismal health.

Chapter 5. Manuscript 3

Carswell, C.L., Hénault, C.M., Murlidaran, S., Therien, J.P.D., Juranka, P.F., Surujballi, J.A., Brannigan, G., and Baenziger, J.E. (2015b). Role of the Fourth Transmembrane α-Helix in the Allosteric Modulation of Pentameric Ligand-Gated Ion Channels. Structure *23*, 1655–1664.

Adapted as a post-print from Structure, http://dx.doi.org/10.1016/j.str.2015.06.020

5.1 Preface

This manuscript is the third of four first-author publications presented in this thesis. All authors contributed to the design of the research. Casey Carswell and I worked together on the majority of the electrophysiology (mutant creation and data collection) in this paper and are co-first authors. Daniel Therien, Peter Juranka and Julian Surujballi created and characterized the GLIC aromatic deletion mutants. Casey and I characterized the ELIC aromatic insertions. I characterized the nAChR C→W mutation, and equivalent mutants in GLIC and ELIC. I performed the propofol inhibition experiments. Molecular dynamics simulations were performed by Sruthi Murlidaran and Grace Brannigan (Rutgers University, New Jersey). Casey and I wrote the paper in collaboration with Dr Baenziger and Dr Brannigan. I created Figures 5.3 and 5.4, with contributions to 5.1 and 5.2 along with my co-authors.

This work builds on my previous observations from manuscripts 1 and 2, which suggested that the M4-M1/M3 interactions in GLIC and ELIC are highly different from each other, with ELIC exhibiting weaker "binding" and GLIC stronger.

Note that due to a missing N-terminal residue, the numbering of the ELIC sequence deposited in the protein data bank with the original ELIC structure was off by one. We used the protein data bank numbering to define residues in manuscripts 1 to 3, but corrected the numbering in manuscript 4. For example, P305 (manuscript 4) is defined as P304 in manuscripts 2 and 3.

5.2 Abstract

The gating of pentameric ligand-gated ion channels is sensitive to a variety of allosteric modulators that act on structures peripheral to those involved in the allosteric pathway leading from the agonist site to the channel gate. One such structure, the lipid-exposed transmembrane α-helix, M4, is the target of lipids, neurosteroids, and disease-causing mutations. Here we show that M4 interactions with the adjacent transmembrane α helices, M1 and M3, modulate pLGIC function. Enhanced M4 interactions promote channel function while ineffective interactions reduce channel function. The interface chemistry governs the intrinsic strength of M4-M1/M3 inter-helical interactions, both influencing channel gating and imparting distinct susceptibilities to the potentiating effects of a lipid-facing M4 congenital myasthenic syndrome mutation. Through aromatic substitutions, functional studies, and molecular dynamics simulations, we elucidate a mechanism by which M4 modulates channel function.

5.3 Introduction

Pentameric ligand-gated ion channels (pLGICs), such as the nicotinic acetylcholine receptor (nAChR), respond to neurotransmitter binding by transiently opening either cation- or anion-selective channels across the post-synaptic membrane. The sites for agonist binding are located at the interfaces between subunits in the extracellular domain (ECD), which extends away from the membrane surface into the synaptic cleft (Figure 5.1) (Unwin, 2005). Agonist binding induces rigid body motions, which are translated into transient movements of the pore lining M2 α-helices of the transmembrane domain (TMD) by a series of loops at the ECD/TMD interface (Althoff et al., 2014; Sauguet et al., 2014; Unwin and Fujiyoshi, 2012). Considerable attention has focused on elucidating the gating movements of these interfacial loops, which form the primary allosteric path leading from the agonist site to the channel gate (Grutter et al., 2005; Jha et al., 2007; Lee and Sine, 2005; Lummis et al., 2005). In contrast, structures not directly involved in the primary allosteric path have received less attention, even though a number of allosteric modulators influence gating via these auxiliary sites (Figure 5.1A).

The fourth transmembrane α-helix, M4, is located on the periphery of the TMD and is the target of both lipids and neurosteroids (Baenziger et al., 2015; Barrantes, 2003, 2015; Hénault et al., 2015a; Hosie et al., 2006; Paradiso et al., 2001). Lipid-facing mutations in M4 of the muscle-type nAChR influence channel gating, with at least one leading to a congenital myasthenic syndrome (CMS) (Bouzat et al., 1998; Lasalde et al., 1996; Lee et al., 1994; Li et al., 1992; Shen et al., 2006; Tamamizu et al., 2000). M4 extends beyond the bilayer to interact directly with the β6-β7 loop (often referred to as the Cys-loop), a key structure at the ECD/TMD interface that participates in channel gating. One model proposes that interactions between M4 and the adjacent α-helices, M1 and M3, are dynamic, in that effective M4-M1/M3 interactions lead to M4/Cys-loop contacts that promote channel function, while ineffective M4-M1/M3 interactions abolish M4/Cys-loop connections to reduce channel function (daCosta and Baenziger, 2009, 2013). In this context, it is intriguing to note that of the four transmembrane α-helices, M1–M4, M4 exhibits the greatest sequence variability among the various *Torpedo* and human nAChR subunits. This variability should lead to subunit-specific interactions at the interface between M4 and M1/M3, resulting in variable

Figure 5.1 Structures of pLGICs with Bound Modulators

A) Structures of the nAChR (PDB: 2BG9), GluCl (PDB: 3RIF), and GLIC (PDB: 3P50). In each case, a single subunit is shown as a dark-blue cartoon with the M4 α helix highlighted in red. In the nAChR (left), residues in the agonist site are highlighted as red spheres, while those forming the transmembrane gate are highlighted as yellow spheres. In GluCl (center), the agonist glutamine, the positive modulator ivermectin, the open channel blocker picrotoxin (aligned using 3RI5), and a bound detergent molecule are highlighted as red, orange, yellow, and marine spheres, respectively. In GLIC (right), the inhibitor propofol and bound lipids (aligned from 3EAM) are shown as yellow and marine spheres, respectively. **B)** A single TMD subunit of ELIC (left, 2VL0) and GLIC (right, PDB: 4HFI) with residues at the M4-M1/M3 interface shown as spheres. Aromatic, polar hydrogen bonding, positive, and aliphatic residues are highlighted in yellow, green, blue, and tan, respectively. The marine sphere corresponds to a water molecule.

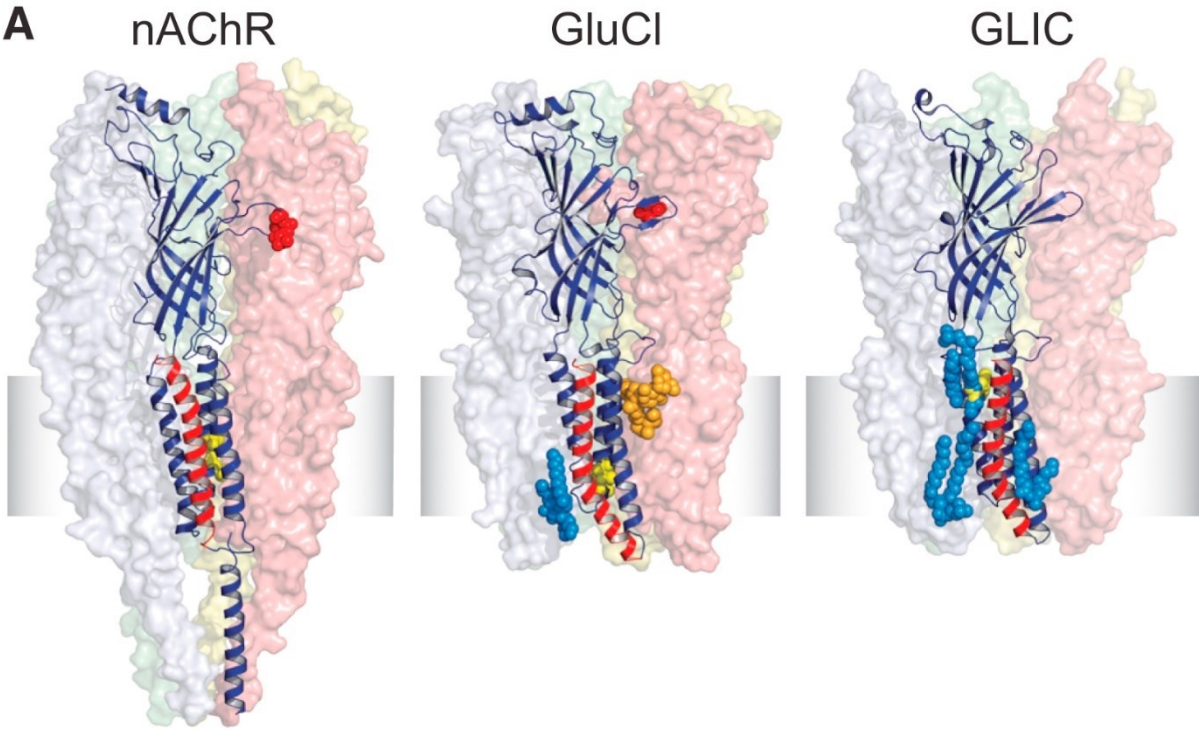
A
nAChR
GluCl
GLIC

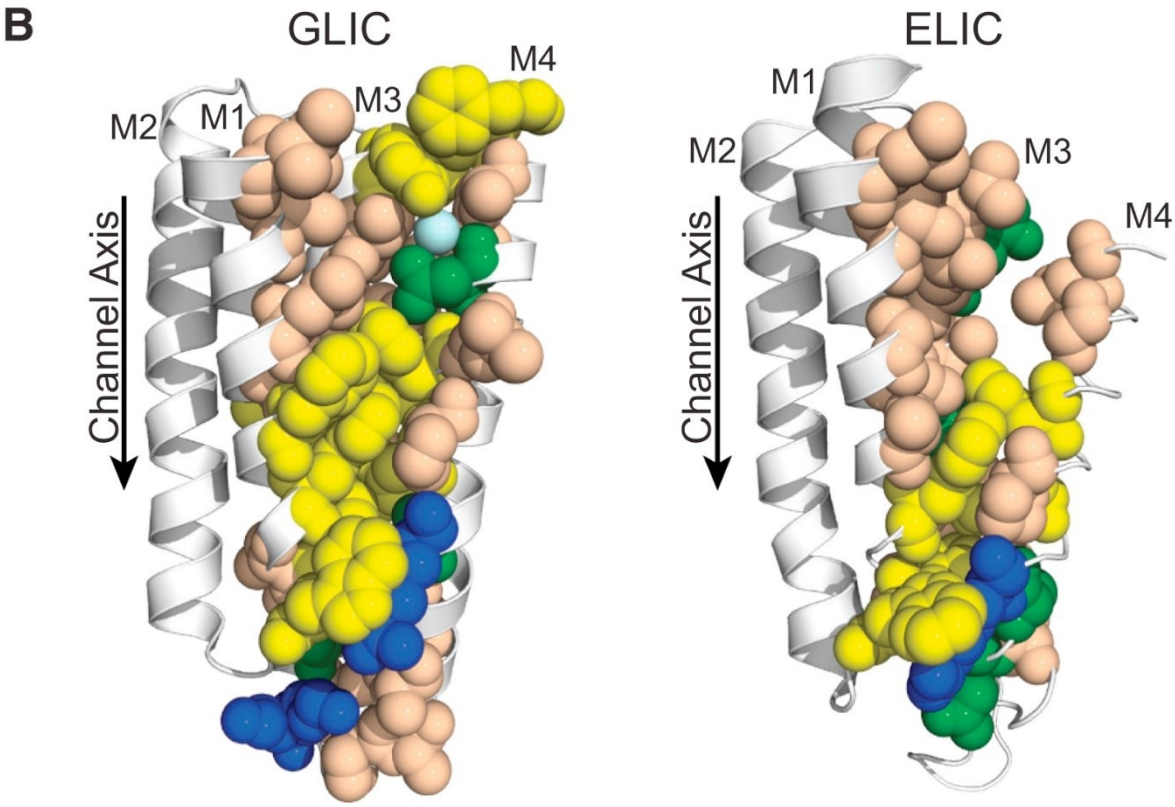
B
GLIC
M4
M3
M2
M1
Channel Axis
ELIC
M1
M2
M3
M4
Channel Axis

interaction energies. If strong M4-M1/M3 interactions promote coupling between the agonist site and channel gate, then variable M4-M1/M3 interaction energies should lead to variable coupling efficiencies. nAChR subunits with weak M4-M1/M3 interactions should also be more sensitive to allosteric modulators that act on M4.

The two structurally well-characterized prokaryotic pLGICs, GLIC and ELIC (Figure 5.1) (Bocquet et al., 2009; Hilf and Dutzler, 2008, 2009; Pan et al., 2012; Sauguet et al., 2013), are excellent models for probing the role of M4 in pLGIC function, as both share a similar tertiary/quaternary fold yet have distinct M4 conformations. In GLIC, M4 interacts tightly with M1/M3 along its entire length. In ELIC, the C-terminal half of M4 tilts away from M1/M3 with the final five residues unresolved in the crystal structure. Aromatic interactions are key determinants that energetically drive the binding of M4 to M1/M3 during folding of the homologous glycine receptor (Haeger et al., 2010). GLIC exhibits an extensive network of interacting aromatic residues at the M4-M1/M3 interface, including a cluster of three aromatic residues that may be essential for linking the C-terminus of M4 to both M1/M3 and the β6-β7 loop (see Figures 5.1B and 5.3). Intriguingly, this C-terminal M4 aromatic cluster is absent in ELIC. Through aromatic substitutions, functional studies, and molecular dynamics simulations, we examine here the effects of aromatic residues at the M4-M1/M3 interface on the conformation of M4, and how the resulting changes in conformation influence channel function. We also examine whether TMD modulators influence pLGIC function by modulating M4-M1/M3 interactions.

5.4 Results

5.4.1 Aromatic Residues Promote M4-M1/M3 Interactions

GLIC exhibits nine aromatic residues at the M4-M1/M3 interface (Figure 5.1B), labeled as aromatics (1) M4 F315, (2) M4 F314, (3) M3 Y254, (4) M4 F303, (5) M3 F265, (6) M3 Y266, (7) M1 W213, (8) M4 F299, and (9) M1 F216 (see Figure 5.3). Although the aromatics at positions 4, 7, 8, and 9 are conserved in ELIC, the entire M4 C-terminal aromatic cluster (aromatics 1–3) and the aromatic side chains at positions 5 and 6 on M3 are absent. We postulated that the distinct profiles of aromatic interactions at the M4-M1/M3 interface in GLIC and ELIC lead to the different conformations of M4 observed in the crystal structures. The different M4 conformations, however, could also result from differential crystal packing and/or detergent-solubilization effects prior to crystallization (daCosta and Baenziger, 2013).

To probe whether aromatic substitutions at the M4-M1/M3 interfaces influence the conformation of M4 in a folded pLGIC structure located within a membrane environment, we turned to molecular dynamics simulations. Simulations were run for both wild-type GLIC (WT-GLIC) and a mutant where the five non-conserved aromatic residues were mutated to Ala (5Ala-GLIC: aromatic-to-Ala substitutions at positions 1, 2, 3, 5, and 6). In both cases, simulations were performed using intact pentamers, as well as with a single-subunit-TMD. Both sets were run in palmitoyl-oleoyl-phosphatidylcholine (POPC) bilayers, a membrane that supports GLIC function (Labriola et al., 2013). The latter simulations revealed intriguing lipid binding poses, which are discussed below. Finally, simulations run for both wild-type ELIC and an ELIC mutant with aliphatic-to-aromatic substitutions at the same positions in the M4-M1/M3 interface were not informative because affected residues in the M4 C-terminus are not defined in the ELIC crystal structure, thus precluding a defined starting conformation.

Consistent with our hypothesis, the simulations show that aromatic residues at the M4-M1/M3 interface influence the interactions of M4 with M1/M3. Specifically, the close contacts between residues along the entire length of M4 and those on M1/M3 in the GLIC crystal structure are maintained throughout the simulations with WT-GLIC. In contrast, the

loss of the C-terminal aromatic cluster leads to a consistent tilting of the C-terminal half of M4 away from M1/M3, with closest C_α-C_α carbon atom contacts on M4-M1 and M4-M3 increasing by roughly 2 Å (Figures 5.2A and online supplemental information): the latter compares directly distances between Y/A254 on M3 and both F/A314 and F/A317 on M4). The differences in M4-M1/M3 interactions are statistically significant based on SEs calculated across the five subunits. The magnitudes of the separations are larger than typical root-mean-squared-deviations among the transmembrane C_α atoms of different pLGICs (Bocquet et al., 2009; Hibbs and Gouaux, 2011; Hilf and Dutzler, 2009; Miller and Aricescu, 2014) or between different conformations of GLIC (Sauguet et al., 2013). The C_α carbon atom separations observed in the M4 C-terminal region contrast with those observed between M4 and M1/M3 near the cytoplasmic side of the bilayer, where the C_α carbon atom separations in 5Ala-GLIC and WT-GLIC converge (C_α atoms separation differences are less than 1 Å) (Figures 5.2A–2C). The latter suggests that the aromatic interactions remaining in the intracellular leaflet of 5Ala-GLIC are sufficient to maintain effective M4-M1/M3 interactions in this region.

The tilt of the C-terminal half of M4 observed in the simulations of the 5Ala-GLIC mutant suggests that aromatic residues are essential for promoting effective M4-M1/M3 interactions. Note that the observed tilt of M4 away from M1/M3 in the simulations of 5Ala-GLIC is similar, but of lesser magnitude than the tilt of M4 observed in the crystal structure of ELIC. In the ELIC crystal structure, the terminal five residues are unresolved, suggesting weak, if any, interaction between the M4 C terminus and M1/M3. The ELIC and GLIC crystal structures support the conclusion that aromatic residues at the M4-M1/M3 interface promote M4 interactions with M1/M3. Detergent solubilization and the removal of lipids may perturb the intrinsically weak interactions between the M4 C-terminus and M1/M3, leading to a greater disruption of M4 conformation than observed in the simulations.

The aromatic-to-Ala substitutions have a substantial effect on the energetics of M4-M1/M3 interactions. In WT-GLIC, M4 C-terminal aromatics 1, 2, and 3 are involved in pairwise interactions within the aromatic cluster, with Ala substitutions of these residues leading to energetic penalties of >1 kcal/mol (Table 5.1). For four of the five subunits, the two-dimensional free energy landscape (Figure 5.2C) calculated from the relative

Figure 5.2 Aromatic Residues Promote M4-M1/M3 Interactions

A) Transmembrane domain of WT-GLIC and 5Ala-GLIC following 300ns of simulation. Helices are shown in surface representation (M1, green; M2, blue; M3, dark gray; M4, orange), with substituted residues shown in stick representation (Y/A254, orange; F/A314, purple; F/A315, green). The M2-M3 loop (yellow) and a portion of the ECD (purple) closest to the interface with the TMD are also shown in surface representation. POPC lipid density, averaged over the final 200 ns of the simulation, is represented by a translucent blue isosurface; the submerged appearance of the 5Ala-GLIC M4 α helices relative to those of WT-GLIC reflects significant lipid penetration of the 5Ala-GLIC subunits. **B)** Representative subunit from WT-GLIC (left) and 5Ala-GLIC (center), showing POPC lipids bound to the M1-M4 interface in stick representation with blue acyl chains and red PC headgroups. A rotated view of 5Ala-GLIC (right) shows a second POPC molecule bound to 5Ala-GLIC, with cyan acyl chains and pink PC headgroups, straddling the 5Ala-GLIC M3-M4 interface. Lines represent the membrane-water interface. **C)** Average distances between Cα atoms on residues at similar register on opposing helices. Substituted residues are highlighted in red. Error bars represent the SE across the five subunits. **D)** Free energy landscape (potential of mean force) for configurations of F314 and F315 relative to Y254 in four of five WT-GLIC subunits, as a function of angle between planar groups and centroid-centroid distance (Equations 1 and 2 in the Additional Materials and Methods). In a fifth subunit, the aromatic cluster disassociates early in the simulation. The blue symbol in each panel indicates the value of the corresponding angle and distance determined from the crystal structure (PDB: 4HFI).

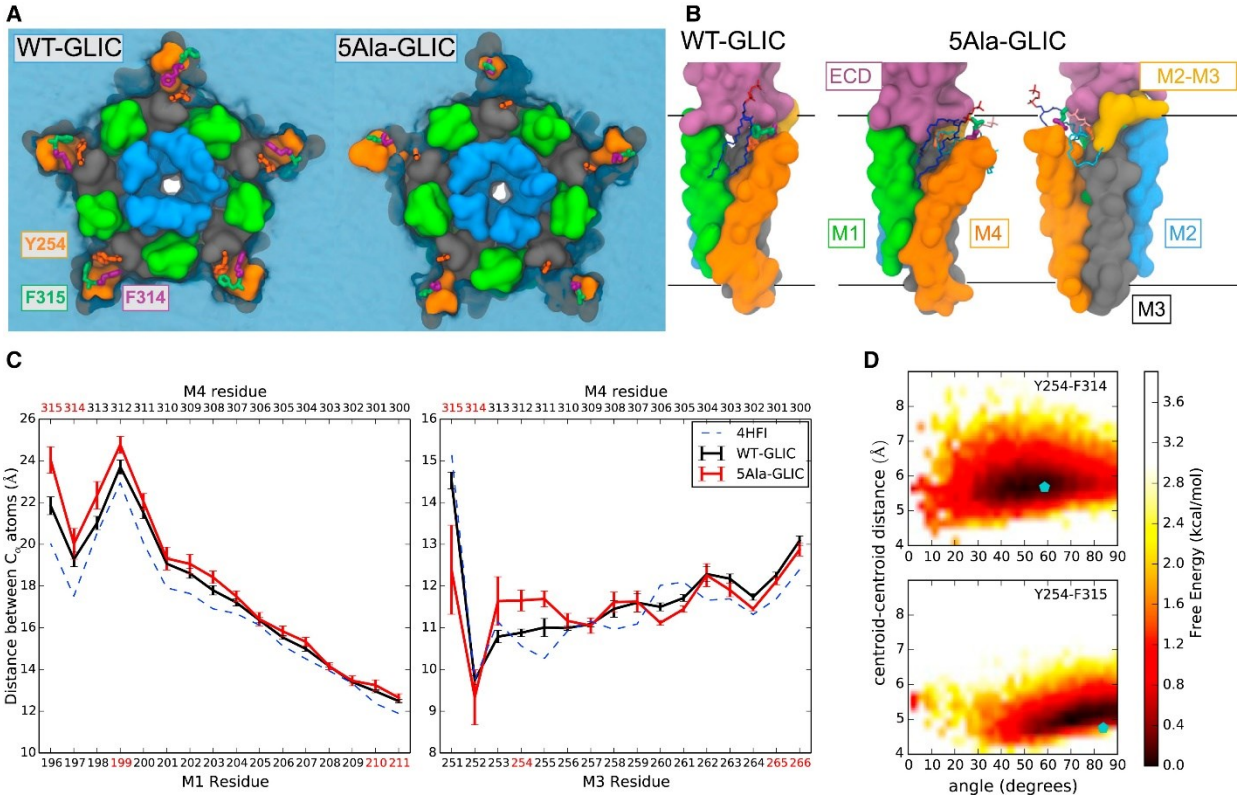
A
WT-GLIC
5Ala-GLIC
Y254
F315
F314
B
WT-GLIC
5Ala-GLIC
ECD
M2-M3
M1
M4
M2
M3
C
M4 residue
315 314 313 312 311 310 309 308 307 306 305 304 303 302 301 300
Distance between Cα atoms (Å)
M1 Residue
196 197 198 199 200 201 202 203 204 205 206 207 208 209 210 211
M4 residue
315 314 313 312 311 310 309 308 307 306 305 304 303 302 301 300
4HFI
WT-GLIC
5Ala-GLIC
M3 Residue
251 252 253 254 255 256 257 258 259 260 261 262 263 264 265 266
D
Y254-F314
Y254-F315
centroid-centroid distance (Å)
angle (degrees)
0 10 20 30 40 50 60 70 80 90
Free Energy (kcal/mol)
0.0 0.4 0.8 1.2 1.6 2.0 2.4 2.8 3.2 3.6

orientations of M3:Y254 (3) and M4:F315 (1) aromatic groups has a strong angular dependence consistent with π-π stacking interactions, with the minima near 90° indicating a T-shaped conformation similar to that found in the crystal structure. In the fifth subunit, F315 dissociates from the cluster and rotates to face the lipids, as also observed in the single-subunit-TMD simulations.

M4 C-terminal aromatics 1, 2, and 3 are also involved in pairwise interactions with other residues that strengthen M4-M3 interactions. An additional strong energy penalty is associated with the loss of a hydrogen bond between the tyrosine hydroxyl of M3:Y254 (aromatic 3) and the carbonyl oxygen of M4:N307. These two residues hydrogen bond via a bridging water in four out of five chains of the highest-resolution crystal structure for GLIC (Sauguet et al., 2013). In the simulations, bridging waters are observed transiently, interspersed with direct hydrogen bonding between the two residues. Also, the mutations weakened several pairwise interactions involving aromatic substituents and non-aromatic polar or hydrophobic residues (Table 5.1).

One intriguing finding of the simulations is that the tilt of the M4 C terminus away from M1/M3 and/or the reduced side-chain volume in 5Ala-GLIC leads to a change in lipid binding. In WT-GLIC, POPC molecules adopt poses at the edge of the M4-M1 and M4-M3 interfaces, as in the GLIC crystal structures. In 5Ala-GLIC, the POPC molecules penetrate deeper into the M1/M3/M4 α-helical bundle, with entire acyl chains becoming embedded at the M1-M4 interface (Figures 5.2A and 5.2B). A second POPC assumes a pose in a cavity formed by the C-terminal end of M4, the M2-M3 loop, and the β6-β7 loop (Figure 5.2B), where one acyl chain fills the increased free volume vacated by M4 F314 and F315 upon mutation of each residue to Ala, while the other acyl chain remains in contact with the bulk membrane. Such interactions are seen across subunits, with one lipid at least partially buried in each of these sites. Buried lipids could potentially mediate some of the effects of the aromatic substitutions, by direct interactions with the M2-M3 and β6-β7 loop and/or indirectly by stabilizing M4 in a conformation with reduced interactions with the ECD. This possibility underscores the potential significance of even slight conformational changes in M4, particularly if they increase the free volume at the M4-M1/M3 interface above the volume required to accommodate a buried lipid. Note also that in single-subunit-TMD

simulations, the absence of steric conflicts with the ECD allows even deeper penetration of the lipid. It appears that even subtle changes in conformation can dramatically alter lipid binding.

5.4.2 Weakened M4-M1/M3 Interactions Inhibit Channel Function

To test experimentally whether M4 conformation influences channel function, non-conserved aromatic residues in GLIC were individually mutated to Ala to weaken M4-M1/M3 interactions, and the effects of the individual substitutions on channel function were assessed using the two-electrode voltage-clamp apparatus. WT-GLIC gates open in response to protons, with a pH value required to elicit half-maximal channel gating of pH_{50} = 5.03 ± 0.08 (n = 38). Each individual aromatic-to-Ala mutation led to a rightward shift in the dose response to protons, with the pH_{50} values decreasing by ~0.4 to ~0.9 pH units: the Y266A mutation at position 6 (Figure 5.3) gave rise to the largest shift down to a pH_{50} = 4.12 ± 0.07 (n = 8). The shifts in pH_{50} correspond to 2- to 8-fold increases in the concentrations of protons required for activation (Figure 5.3; Table 5.2). Simultaneous aromatic-to-Ala substitutions of interacting aromatic pairs were also generated, but none of the double mutants gave observable proton-activated currents. The absence of current could reflect impaired channel function and/or folding and then trafficking to the cell surface (Haeger et al., 2010).

Figure 5.3 Enhanced M4-M1/M3 Interactions Potentiate pLGIC Function

A) The TMD of a single subunit of an ELIC homology model (based on GLIC, PDB: 3EHZ). Aromatic residues conserved in GLIC and ELIC are shown in yellow, while aromatics removed from GLIC or inserted into ELIC are shown in orange, superimposed on wild-type (WT) ELIC residues (red). The M4 sequence alignments highlight key aromatic residues (boxed), and identical (∗), conserved (:), and semi-conserved (.) residues. **B)** Two-electrode data for GLIC (upper) and ELIC (lower), with representative mutants. Ligand concentration jumps (protons or cysteamine for GLIC and ELIC, respectively) are indicated by the horizontal bar. **C)** Dose-response curves obtained for single aromatic-to-Ala substitutions in GLIC (upper) and from either single and multiple aliphatic-to-aromatic substitutions in ELIC (lower). Error bars represent SE. **D)** Changes in EC_{50} relative to the WT for GLIC (pH 5.03) and ELIC (0.92 mM cys). NC, no current. Multiple aromatic substitutions were not generated for GLIC (X). Error bars represent SD. See Table 5.2 for EC_{50} values.

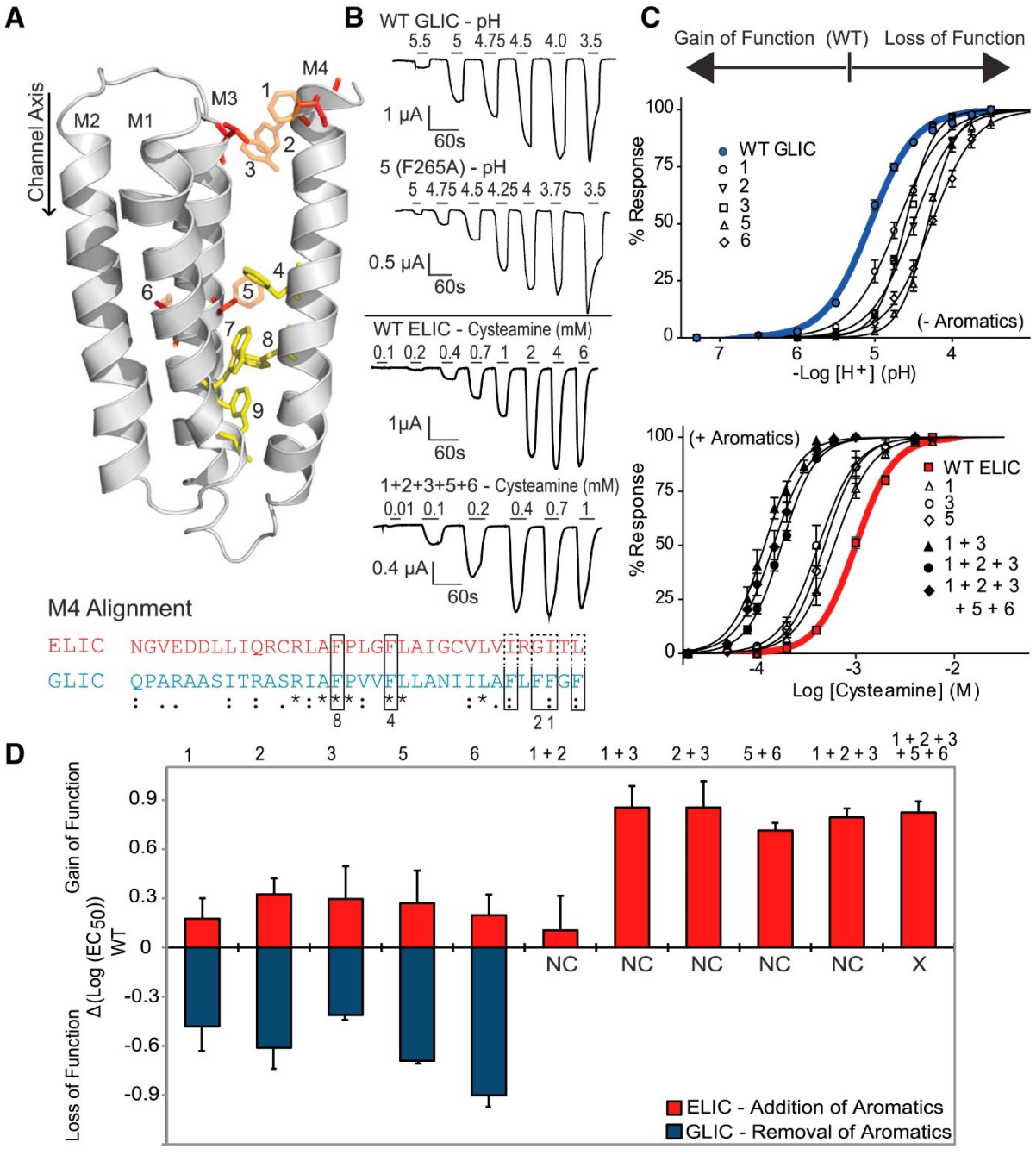
A
Channel Axis
M2
M1
M3
M4
1
2
3
4
5
6
7
8
9
B
WT GLIC - pH
5.5 5 4.75 4.5 4.0 3.5
1 μA
60s
5 (F265A) - pH
5 4.75 4.5 4.25 4 3.75 3.5
0.5 μA
60s
WT ELIC - Cysteamine (mM)
0.1 0.2 0.4 0.7 1 2 4 6
1μA
60s
1+2+3+5+6 - Cysteamine (mM)
0.01 0.1 0.2 0.4 0.7 1
0.4 μA
60s
M4 Alignment
ELIC NGVEDDLLIQRCRLAFPLGFLAIGCVLVIRGIIL
GLIC QPARAASITRASRIAFPVVFLLANIILAFLFFGF
C
Gain of Function (WT) Loss of Function
% Response
WT GLIC
1
2
3
5
6
(- Aromatics)
-Log [H+] (pH)
(+ Aromatics)
WT ELIC
1
3
5
1 + 3
1 + 2 + 3
1 + 2 + 3 + 5 + 6
Log [Cysteamine] (M)
D
1
2
3
5
6
1 + 2
1 + 3
2 + 3
5 + 6
1 + 2 + 3
1 + 2 + 3 + 5 + 6
Gain of Function
Loss of Function
Δ(Log (EC50)) WT
NC
X
ELIC - Addition of Aromatics
GLIC - Removal of Aromatics

Note that the pH_{50} values derived from macroscopic currents depend on both the affinity of the agonist for its binding site and the equilibrium constant governing transitions from closed to open states. In addition, desensitization kinetics can influence the measurement of pH_{50} values. Most of the mutations have little effect on the macroscopic desensitization rates. Given that the proton binding sites for activation are mainly distant from the TMD (Duret et al., 2011), the majority of the changes in pH_{50} likely reflect changes to the equilibrium constant governing channel gating; the decreased pH_{50} values thus likely reflect impaired coupling between agonist binding and channel gating. This interpretation, however, is not unequivocal, as a His235 located on the adjacent M2 α-helix influences proton activation of GLIC (Rienzo et al., 2014; Wang et al., 2012). In particular, the Y266A could directly influence the pH_{50} for gating via this intramembrane protonation site.

5.4.3 Enhanced M4-M1/M3 Interactions Potentiate Channel Function

In contrast to the mutations in GLIC, individual aliphatic-to-aromatic substitutions introduced at the M4-M1/M3 interface to enhance M4-M1/M3 interactions in ELIC each shifted the dose response to cysteamine leftward, whether or not interacting aromatic partners on the adjacent transmembrane α helices were present (Figure 5.3; Table 5.2). Wild-type ELIC required a concentration of cysteamine to elicit half-maximal channel gating of EC_{50} = 0.94 ± 0.16 mM cysteamine (n = 23). Of the individual aliphatic-to-aromatic mutations, G218F (2) led to the largest reduction in EC_{50} = 0.44 ± 0.09 mM cysteamine (n = 13). The changes in EC_{50} values correspond to between 70% and 50% reductions in the concentrations of cysteamine required. Multiple aromatic additions were also introduced, and these led to even further leftward shifts in the EC_{50} values. Engineering either the entire M4 C-terminal aromatic cluster (EC_{50} = 0.18 ± 0.02 mM cysteamine (n = 9)) or the entire aromatic network of GLIC into ELIC (EC_{50} = 0.15 ± 0.04 mM cysteamine (n = 7)) shifted the EC_{50} down to a value approaching 10% of the EC_{50} value of wild-type ELIC. In fact, the largest reductions in EC_{50} were observed with just two interacting aromatic partners engineered into the M4 C-terminal region, one on M3 and the other on M4. Both the I319F/V260Y and G318F/V260Y double mutants gave EC_{50} values of 0.13 mM cysteamine.

The leftward shifts in the dose response observed with aromatic "additions" in ELIC contrast with the rightward shifts observed with aromatic "deletions" in GLIC, with leftward shifts reflecting a gain, as opposed to a loss, of channel function. In contrast to GLIC where the proton-sensitive intramembrane His235 complicates the interpretation of pH_{50} values, the agonist binding site in ELIC is greater than 30 Å distant from even the closest mutations at the M4-M1/M3 interface, suggesting that the mutations do not directly influence the chemistry of the agonist site and, thus, agonist affinity. Furthermore, mutations in M4 of the nAChR have been shown to have no effect on agonist affinity (Bouzat et al., 2000; Mitra et al., 2004; Shen et al., 2006). Although single-channel measurements are required to confirm that the changes in EC_{50} result from direct effects on channel gating, the long distance between M4 and the agonist site suggests that the changes in EC_{50} detected here reflect enhanced channel function, i.e., enhanced coupling between agonist binding and channel gating. The gain-of-function mutations show that residues along the M4-M1/M3 interface in wild-type ELIC are not optimized to promote M4-M1/M3 interactions that support channel function, and that improving the effectiveness of these interactions promotes coupling between the agonist site and channel gate.

We considered the possibility that aromatic additions to the M4-M1/M3 interface promote more effective interactions with bound lipids to enhance function. Interactions between the F315 aromatic residue in GLIC and lipids are observed in both the pentamer and single-subunit-TMD simulations. The lipid-facing F317 and F312 residues were mutated to alanine, leading to gain-of-function and loss-of-function phenotypes, respectively (F317A $pH_{50} = 5.41 \pm 0.05$ (n = 8), F312A $pH_{50} = 4.50 \pm 0.01$ (n = 6)). These results show that it is impossible to predict how interactions between aromatic residues and lipids will influence channel function.

Finally, an important feature of our results is the consistency of the entire dataset. Every aromatic-to-Ala substitution at the M4-M1/M3 interface in GLIC led to reduced channel function while every aliphatic-to-aromatic substitution at the same interface in ELIC led to enhanced channel function. The latter is particularly compelling, given that although optimal aromatic interactions enhance inter-α-helical interactions, the insertion of aromatic side chains at the M4-M1/M3 interface could lead to structural and/or chemical conflicts and,

thus, a loss of channel function. The data highlight the ease with which effective interactions between M4 and M1/M3 in ELIC can be formed to enhance channel function. The consistency of the data suggests that the changes in function are not due to localized changes in structure, which would be expected to have random effects. The molecular dynamics simulations support the hypothesis that aromatic residues at the M4-M1/M3 interface enhance M4-M1/M3 interactions. The gains of function observed with aliphatic-to-aromatic residue substitutions in ELIC thus result, at least in part, from enhanced M4 interactions with M1/M3.

5.4.4 A Lipid-Facing CMS Mutation Potentiates Function by Enhancing M4-M1/M3 Interactions

If M4-M1/M3 interactions in ELIC are intrinsically weaker than in GLIC, leading to relatively poor coupling between the agonist site and channel gate, ELIC may exhibit a greater capacity for potentiation by allosteric modulators that enhance M4-M1/M3 interactions. To test this hypothesis, we focused on a CMS mutation that occurs on the lipid-facing surface of αM4 in the human muscle-type nAChR (C418W). C418W potentiates nAChR channel function roughly 25-fold (EC_{50} = 9.11 ± 1.45μM acetylcholine (n = 31) for wild-type, EC_{50} = 0.34 ± 0.08μM acetylcholine (n = 11) for C418W) by directly altering M4-lipid interactions, although the mutation must ultimately influence interactions between M4 and the remainder of the TMD (Figure 5.4; Table 5.3).

A leucine residue is found in both GLIC and ELIC at the equivalent position. This Leu residue (L304) residue in GLIC was changed to both Cys and Trp, but neither substitution had any effect on channel function (pH_{50} = 5.03 ± 0.02 (n = 6) and pH_{50} = 5.06 ± 0.03 (n = 6)), respectively, possibly because the extensive aromatic network at the M4-M1/M3 interface already promotes effective M4-M1/M3 interactions (Figure 5.4). In contrast, the same L308C and L308W mutations in ELIC both led to gain-of-function phenotypes, with the magnitude of the L308W gain of function (EC_{50} = 0.29 ± 0.05 mM cysteamine (n = 10)) approaching 5-fold relative to the wild-type ELIC. Significantly, the introduction of interacting aromatic residues to enhance intrinsic M4-M1/M3 interactions

Figure 5.4 A CMS Trp Mutation Potentiates Channel Function by Enhancing M4-M1/M3 Interactions

A) Side and top views of the TMD of a single subunit of human α1ChR (homology model based on PDB: 2BG9). Aromatics at the M4-M1/M3 interface are shown in yellow. The lipid-facing residue αC418 is shown as a solid orange sphere, with the potentiating αC418W mutation superimposed as an orange sphere/stick transparent combination. **B)** Proposed mechanism of function for the potentiating effect of αC418W via enhanced M4-M1/M3 interactions. In the absence of M4 C-terminal aromatic contacts, interaction of the bulky αC418W with the lipid bilayer causes M4 to interact more tightly with M1/M3 (red arrow), potentiating activity. In the presence of M4 C-terminal aromatics, M4 already interacts tightly with M1/M3, so αC418W has no effect. **C–E)** Two-electrode data (left) and dose-response curves (right) demonstrating the effect of the αC418 (or equivalent) mutation on **C)** human muscle-type nAChR, **D)** ELIC (L308W), and **E)** GLIC (L304W). Error is represented as SE. **F)** Effect of the L308W mutation on aromatic-substituted ELIC mutants, shown as change in EC_{50} relative to WT ELIC. Error is represented as SD, and mutant numbers correspond to those in Figure 5.2A. See Table 5.3 for complete EC_{50} values.

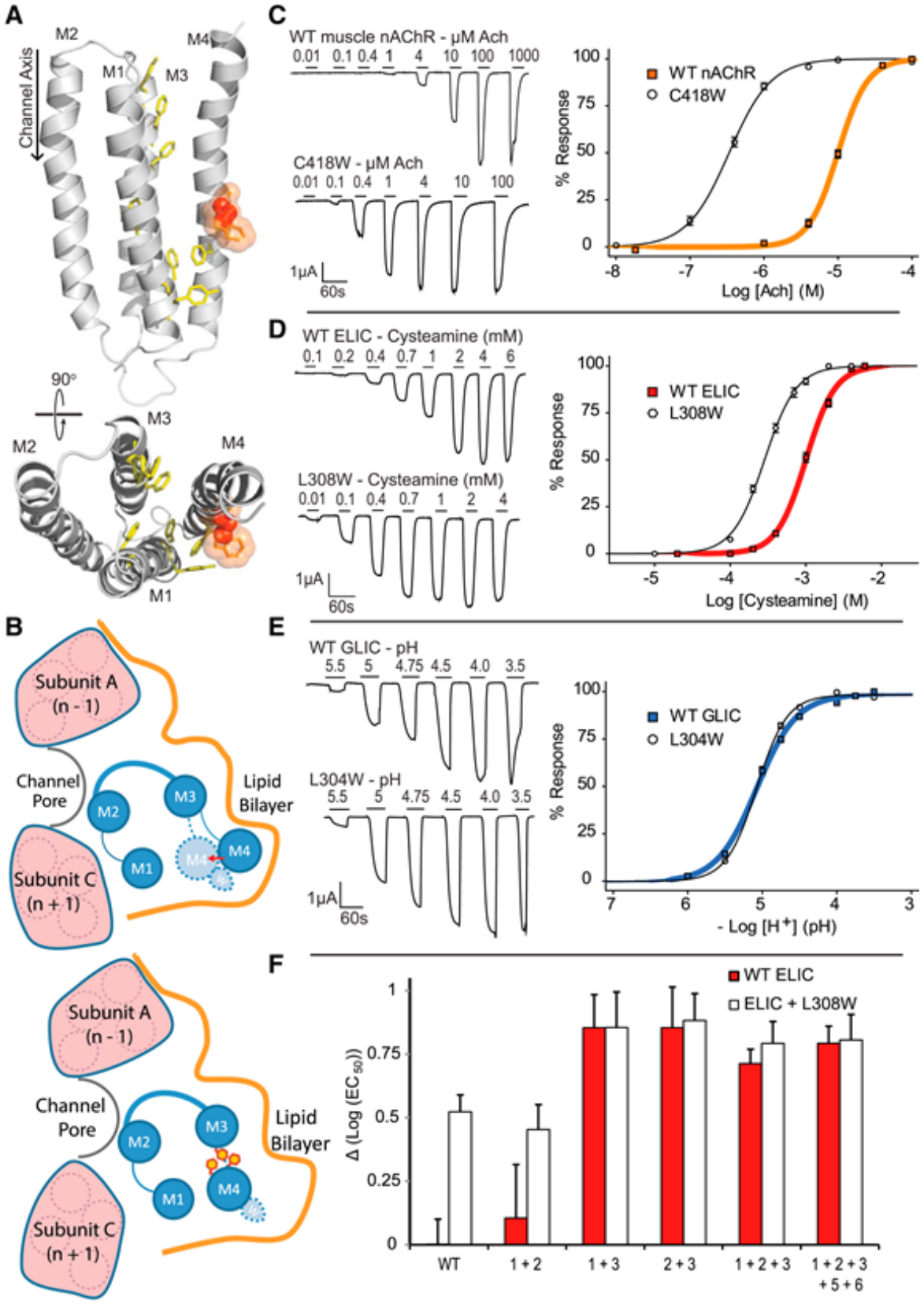
A
M2
M4
M1
M3
Channel Axis
90°
M3
M2
M4
M1
B
Subunit A
(n - 1)
Channel
Pore
M2
M3
Lipid
Bilayer
M1
M4
M4
Subunit C
(n + 1)
Subunit A
(n - 1)
Channel
Pore
M2
M3
Lipid
Bilayer
M1
M4
Subunit C
(n + 1)
C
WT muscle nAChR - µM Ach
0.01 0.1 0.4 1 4 10 100 1000
C418W - µM Ach
0.01 0.1 0.4 1 4 10 100
1µA
60s
WT nAChR
C418W
% Response
Log [Ach] (M)
D
WT ELIC - Cysteamine (mM)
0.1 0.2 0.4 0.7 1 2 4 6
L308W - Cysteamine (mM)
0.01 0.1 0.4 0.7 1 2 4
1µA
60s
WT ELIC
L308W
% Response
Log [Cysteamine] (M)
E
WT GLIC - pH
5.5 5 4.75 4.5 4.0 3.5
L304W - pH
5.5 5 4.75 4.5 4.0 3.5
1µA
60s
WT GLIC
L304W
% Response
- Log [H+] (pH)
F
WT ELIC
ELIC + L308W
Δ (Log (EC50))
WT
1 + 2
1 + 3
2 + 3
1 + 2 + 3
1 + 2 + 3
+ 5 + 6

reduced the potentiating effects of this CMS mutation in ELIC. In fact, L308W had no further effect on the gating of ELIC mutants containing either the three M4 C-terminal cluster aromatics or all five aromatic substitutions. L308W thus potentiates ELIC function in a manner similar to that observed with the introduction of aromatic residues at the M4-M1/M3 interface. These results show that (1) altered lipid-protein interactions promote channel function by enhancing M4-M1/M3 interactions, and (2) the intrinsic strength of M4-M1/M3 interactions influences the functional sensitivity of a pLGIC to altered protein-lipid interactions, including mutations at the lipid-protein interface. The CMS mutation was also superimposed onto various aromatic-to-Ala substituted GLIC mutants, but none of these gave proton-activated currents (data not shown).

5.4.5 Propofol Inhibits Channel Function via an M4-Independent mechanism

M4-M1/M3 interactions might play a role in the allosteric effects of other TMD modulators, such as the inhibitory drug propofol. Propofol binds to GLIC near the extracellular surface of the TMD in a cavity delineated by the four transmembrane α-helices and capped by the β6-β7 loop, with the most extensive interactions occurring between M1 and M3 (Nury et al., 2011a). We tested the possibility that propofol inhibits effective M4-M1/M3 interactions by investigating the effects of propofol on several of the aromatic-substituted mutants of both GLIC and ELIC. None of the aromatic-to-Ala substitutions at the M4-M1/M3 interface of GLIC or the aliphatic-to-aromatic substitutions at the same interface in ELIC, however, had a major effect on propofol inhibition (Figure 5.5). In contrast to our hypothesis, propofol does not inhibit gating by modulating M4-M1/M3 interactions, consistent with both mutational and simulation studies, which suggest that propofol inhibition results from binding closer to the M2 pore lining the α-helix (Nury et al., 2011a), or even from within the channel pore (LeBard et al., 2012).

Figure 5.5 Propofol inhibits GLIC and ELIC function by an M4 independent mechanism

Top) Dose-Response (inhibition) curves showing the minor variations in inhibition of WT and various mutants of ELIC (red) and GLIC (blue) by propofol. **Bottom**) Summary of IC_{50} values from unconstrained fits of the log (inhibitor) vs response (three parameter) analysis (Graphpad Prism). Even in mutants where M4 binding has been affected, inhibition by propofol remains unchanged. Error bars represent standard deviation. For presentation purposes, the curve fits have been constrained to 100% and 0% Response.

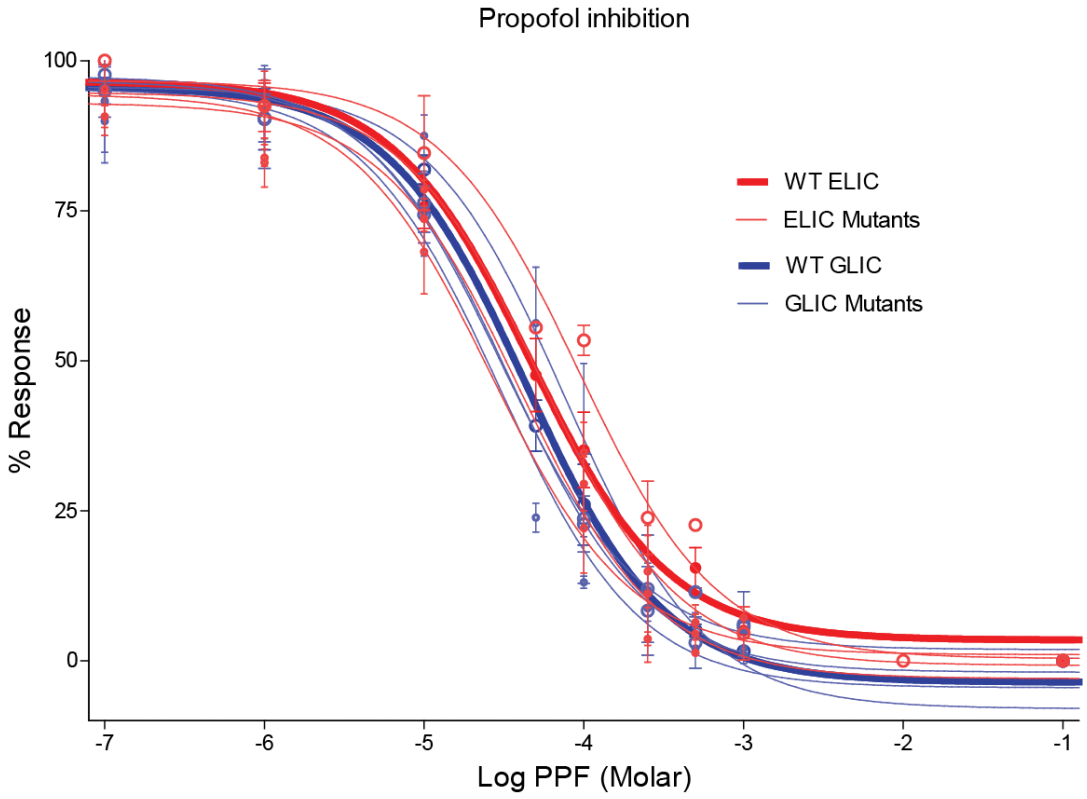

GLIC			ELIC		
Mutant	IC_{50} ± SD	n	Mutant	IC_{50} ± SD	n
WT	43.1 ± 6.6	13	WT	27.9 ± 8.7	3
F313A (1)	64.7 ± 7.9*	10	1 + 2	28.8 ± 9.4	4
F312A (2)	24.8 ± 3.8*	6	1 + 2 + L308W	90.7 ± 13.0	4
Y264A (6)	32.4 ± 9.0	4	1 + 2 + 3	46.1 ± 4.2	3
F263A (5)	35.7 ± 5.3	4	1+2+3+5+6	94.0 ± 36.2	3

*SD Represents the average of individually-calculated SDs for each applied PPF concentration.
IC_{50} values are from unconstrained fits of the log(inhibitor) vs response (three parameter) analysis

5.5 Discussion

Although there are likely other sites of action (Althoff et al., 2014; Brannigan et al., 2008; Jones and McNamee, 1988), a role for M4 in lipid sensing is highlighted by the identification of M4-bound lipids in the crystal structure of GLIC (Bocquet et al., 2009), as well as by mutagenesis data showing that changes in nAChR M4-lipid interactions influence channel function (Bouzat et al., 1998; Lasalde et al., 1996; Lee et al., 1994; Li et al., 1992; Shen et al., 2006; Tamamizu et al., 2000). M4 is also the site of action for neurosteroids (Hosie et al., 2006; Paradiso et al., 2001). In addition, a lipid-facing mutation on M4 in the muscle-type nAChR potentiates channel activity, leading to a CMS (Shen et al., 2006). M4, however, is distant from the channel-lining M2 α-helix, as well as key structures that form the primary allosteric path between the agonist site and the channel gate (i.e., the β1-β2 and β6-β7 loops, the M2-M3 linker), thus raising the question of how changes in M4 structure alter channel function.

Our data show that enhanced M4-M1/M3 interactions potentiate pLGIC function while reduced interactions inhibit pLGIC function. This conclusion is based on four observations. First, molecular dynamics simulations show that aromatic residues at the M4-M1/M3 interface promote strong M4-M1/M3 interactions, with the elimination these aromatic residues leading to increased C_α-C_α carbon atom separations between M4 and M1/M3. Second, aromatic substitutions that promote M4-M1/M3 interactions enhance channel function while aromatic substitutions that weaken M4-M1/M3 interactions reduce channel function. Third, aromatic substitutions that modulate M4-M1/M3 interactions influence the potentiating effects of a lipid-facing M4 CMS mutation. No potentiation was observed when the CMS mutation was introduced into GLIC, which exhibits intrinsically effective M4-M1/M3 interactions, while strong potentiation was observed with ELIC, which lacks M4-M1/M3 stabilizing aromatic interactions. Significantly, engineering aromatic interactions into the M4-M1/M3 interface in ELIC abrogates the potentiating response. Finally, the strength of M4-M1/M3 interactions has no effect on the inhibitory effects of the drug propofol, which acts at a TMD site that does not directly involve M4 (LeBard et al., 2012; Nury et al., 2011a).

Our proposed model of M4 action is supported by biophysical studies, which have shown that the orientation of nAChR M4, and thus presumably the interactions between M4 and M1/M3, is sensitive to its surrounding lipid environment (Antollini et al., 2005; Xu et al., 2005). The nAChR M4 moves halfway along the reaction coordinate between agonist binding and the open state (Mitra et al., 2004). Motion of M4 has also been detected during desensitization of GLIC (Velisetty et al., 2014), consistent with the desensitization effects observed here with some of the M4-M1/M3 interface aromatic residue substitutions.

There appears to be a particularly important role for the M4 C terminus in pLGIC function, in agreement with the proposed role of the M4 C terminus in lipid sensing by the muscle-type nAChR from *Torpedo*. Increasing levels of cholesterol and anionic lipids stabilize increasing proportions of agonist-responsive nAChRs (Baenziger et al., 2000; daCosta et al., 2002, 2009; Hamouda et al., 2006b). In the absence of these activating lipids, the nAChR adopts an uncoupled conformation that exhibits resting-state-like agonist binding, but does not usually undergo agonist-induced conformational transitions (Baenziger et al., 2008; daCosta and Baenziger, 2009; daCosta et al., 2013). The M4 C terminus in both the nAChR and GLIC interacts directly with the β6-β7 loop, an important link between the agonist site and the transmembrane gate (Jha et al., 2007; Lee et al., 2009). The M4 C-terminus also interacts with M3 adjacent to the M2-M3 linker, a structure that controls the orientation of the M2 gating α-helix. Tighter M4 interactions with M1/M3 may facilitate interactions between the M4 C terminus and the β6-β7-loop, to form a β6-β7-loop conformation that participates optimally in channel gating (daCosta and Baenziger, 2009). Interestingly, the M4 C terminus does not interact directly with the β6-β7 loop in the ELIC crystal structure, which is significant because crystallized ELIC does not undergo channel gating (Gonzalez-Gutierrez et al., 2012). Weak M4 C-terminal interactions with M1/M3, as a consequence of detergent solubilization, may lead ELIC to adopt an uncoupled conformation (daCosta and Baenziger, 2013).

Finally, a key finding of our study is the demonstration that variable chemistry at the interface between M4 and M1/M3 in different pLGICs leads to variable M4-M1/M3 interactions, different "efficiencies" of coupling binding to gating, and different susceptibilities to potentiation by allosteric modulators, in this case a CMS mutation that acts

on M4. GLIC has an extensive aromatic network at this interface that leads to effective M4-M1/M3 interactions along the entire length of M4, rendering the TMD less malleable and less sensitive to M4-targeting modulators. GLIC is insensitive to the potentiating effects of the lipid-facing M4 CMS mutation. GLIC also maintains efficient gating in lipid environments that stabilize an uncoupled nAChR (Labriola et al., 2013). ELIC, with no aromatic interactions in the C-terminal half of M4, exhibits weak M4-M1/M3 interactions in this region. ELIC is more sensitive than GLIC to M4-targeting modulators, such as the CMS mutation and lipids, although aromatic substitutions at the M4-M1/M3 abrogate sensitivity to both (Carswell et al., 2015a). The nAChR, with relatively few inter-α-helix aromatic interactions, likely exhibits relatively weak M4-M1/M3 interactions along the entire length of M4, and is even more sensitive than ELIC to both the CMS mutation and lipids. Note that although the *Torpedo* nAChR structure does not exhibit tight interactions between M4 and M1/M3, M4 is not tilted away from M1/M3 as it is in the ELIC structure. The nAChR structure, however, was solved by cryo-electron microscopy using native nAChR membranes (Unwin, 2005; Unwin and Fujiyoshi, 2012), while the ELIC structure was solved by X-ray diffraction using crystals formed from detergent-solubilized ELIC (Hilf and Dutzler, 2008; Pan et al., 2012). In the native *Torpedo* membranes, there are "activating" lipids (cholesterol, anionic lipids, etc.) that stabilize a functional conformation, where M4 may associate effectively with M1/M3.

The chemistry at the M4-M1/M3 interface varies across human nAChR subunits, suggesting that human nAChRs exhibit variable M4-M1/M3 interactions, and thus possibly different sensitivities to allosteric modulators that act on M4. Knowledge of the subunit-specific roles of M4 in nAChR function may prove to be important for understanding the mechanisms by which cholinergic activity is modulated by changes in lipid composition that occur during the course of neurodegenerative disease.

5.6 Supplementary Information

5.6.1 Supplementary Materials and Methods

For Materials and Methods concerning RNA constructs for oocyte expression, electrophysiology, and drug inhibition assays, see Chapter 2. The following methods pertain to experiments performed by our collaborating authors.

5.6.1.1. Molecular Dynamics Simulations

Two systems containing GLIC from PDB: 4HFI (Sauguet et al., 2013) were prepared by protonating residues according to their standard states at pH 4.6, followed by either no mutations (WT-GLIC) or five simultaneous mutations (5Ala-GLIC) corresponding to the sites 1, 2, 3, 5, and 6 investigated in the experiments. Resolved lipids in the PDB structure were not included, although after about 50 ns of simulation, lipids bound to WT-GLIC in poses similar to those in PDB: 4HFI. For each system, the intact pentamer was placed in a 110 3 110 A ° POPC membrane aligned parallel to the xy plane using CHARMM-GUI Membrane Builder (Jo et al., 2009). The system was solvated with a total height in z of 155 A° and neutralized, for a total of about 175,000 atoms per system. Atomistic molecular dynamics simulations were run with NAMD v2.9 (Phillips et al., 2005). The CHARMM36 force field was used for protein (Best et al., 2012; MacKerell et al., 1998) and phospholipid (Klauda et al., 2010) parameters, with parameters for TIP3P waters (Jorgensen et al., 1983) and ions (Beglov and Roux, 1994) corresponding to those traditionally used with CHARMM-based force fields. All simulations used periodic boundary conditions and particle mesh Ewald electrostatics.

Interactions between non-bonded atoms were cut off at 12 Å, and bonds involving hydrogen were constrained using the SHAKE/RATTLE algorithm. A Langevin thermostat and barostat were used to maintain a temperature and pressure of 303.15 K and 1 atm, respectively, and vanishing surface tension was imposed. The simulation timestep was 2 fs. 20000 minimization steps and a 0.725 ns equilibration protocol that gradually released restraints on the protein were performed on each system prior to a 300 ns production run. Analysis of MD simulations was performed using scripts written in VMD (Humphrey et al., 1996). Potential

of mean force plots were generated by calculating the centroid distance r and angle θ between the vectors normal to the planar groups for each frame and calculating a two dimensional histogram $\Delta N(r,\theta)$ with bin widths Δr and Δθ using MATLAB. The normalized distribution function $G(r,\theta)$ in R, θ space is:

$$G(r,\theta) = \Delta N(r,\theta)/(2\pi r 2 \sin\theta\, \Delta r \Delta\theta) \qquad (1)$$

and the potential of mean force is:

$$W(r,\theta) = -RT \ln G(r,\theta) \qquad (2)$$

5.6.2 Supplementary Data

Table 5.1 - Inter-residue interactions significantly affected by aromatic-to-Ala mutation[1]

M3 Residue	M4 Residue	ΔE (kcal/mol)	Comments
Y254(3)	F314(2)	3.6	Interactions display expected behavior for π-π stacking in WT-GLIC
Y254(3)	N307	3.4	Loss of hydrogen bond between residues in 5Ala-GLIC
Y254(3)	F315(1)	1.8	Interactions display expected behavior for π-π stacking in WT-GLIC
T253	F314(2)	1.6	Pair residues widely separated in 5Ala-GLIC compared to WT-GLIC; equivalent loss of both electrostatic and van der Waals interactions
M252	F314(2)	1.1	Hydrophobic interactions reduced significantly in 5Ala-GLIC
M252	F315(1)	1.1	Electrostatic interactions between terminal dipole on F315A and M252 backbone in 5Ala-GLIC are not present in WT-GLIC, in which F315 interacts more strongly with T253

Table 5.1 relates to figure 5.2

[1]Pair interactions significantly affected by mutation. Non-bonded energies (van der Waals and electrostatic) were measured for each pair involving a substitution in both WT-GLIC and 5Ala-GLIC simulated receptors and the resulting energy difference $\Delta E = E_{5Ala} - E_{WT}$ was calculated. Those pairs with $|\Delta E| > 1.0$kcal/mol are listed here, in order of descending effect. Numbers shown in parentheses correspond to the residue numbering scheme in Figure 5.3.

Table 5.2 Effects of Aromatic Substitutions in ELIC and GLIC on channel function[a]

		Dose Response[b]			I_{max} Values[c]		
	Aromatic Mutant	pH_{50}/EC_{50}	Hill Slope	n	I_{max}	ng injected	n
GLIC		pH_{50}					
	WT	5.03 ± 0.08	1.42 ± 0.49	38	4.59 ± 1.85	6.6	25
1	F315A	4.68 ± 0.15	1.46 ± 0.40	8	2.12 ± 2.95	3.3	6
2	F314A	4.47 ± 0.13	1.88 ± 0.53	10	3.11 ± 2.49	3.3	7
3	Y254A	4.58 ± 0.03	2.25 ± 0.41	8	4.50 ± 1.30[d]	20	8
5	F265A	4.31 ± 0.01	2.87 ± 1.95	8	2.40 ± 0.77[e]	20	8
6	Y266A	4.12 ± 0.07	1.28 ± 0.25	8	3.13 ± 0.61[d]	20	8
1+2	F315A+F314A				No Current[f]	20	10
1+3	F315A+Y254A				No Current[f]	20	10
2+3	F314A+Y254A				No Current[f]	20	12
5+6	F265A+Y266A				No Current[f]	20	15
ELIC		EC_{50} (mM Cys)					
	WT	0.94 ± 0.16	2.13 ± 0.36	23	2.77 ± 0.91	0.2	11
1	I319F	0.62 ± 0.18	2.48 ± 0.40	6	4.68 ± 1.45	0.2	6
2	G218F	0.44 ± 0.09	2.69 ± 1.05	13	3.43 ± 2.65	0.2	8
3	V260Y	0.47 ± 0.21	2.37 ± 0.33	4	1.35 ± 0.38	0.2	4
5	S271F	0.50 ± 0.21	3.44 ± 0.91	10	3.19 ± 0.38	0.4	3
6	I272Y	0.59 ± 0.14	2.55 ± 0.33	10	2.80 ± 0.87[g]	0.6	4
1+2	I319F+G318F	0.73 ± 0.37	3.19 ± 0.83	8	2.40 ± 0.12	0.2	2
1+3	I319F+V260Y	0.13 ± 0.05	3.01 ± 1.08	6	2.69 ± 0.76	0.4	6
2+3	G318F+V260Y	0.13 ± 0.05	2.51 ± 0.40	6	4.47 ± 3.28	0.4	6
5+6	S271F+I272Y	0.26 ± 0.09	2.24 ± 0.24	8	2.98 ± 2.77[g]	0.6	4
1+2+3	I319F+G318F+ V260Y	0.18 ± 0.02	2.60 ± 0.16	9	2.97 ± 1.73	0.4	9
1+2+3 +5+6	I319F+G318F+V260Y +S271F+ I272Y	0.15 ± 0.04	2.59 ± 0.35	7	1.41 ± 1.73	5.0	3

[a]Table S2 relates to Figure 3
[b]Measurements performed 1-4 days after cRNA injection (V_{hold} ranging from -10 to -60 mV). Error values represent standard deviation.
[c]Recorded (except where noted) 1 day after cRNA injection with a V_{hold} of -20 mV (GLIC) or -40 mV (ELIC). Error values represent standard deviation.
[d]Measured at a V_{hold} of -20 mV, after 4 days cRNA injection
[e]Measured at a V_{hold} of -40 mV, after 4 days cRNA injection
[f]No significant current observed up to 4 days after cRNA injection
[g]Measured at a V_{hold} of -40 mV, after 2 days cRNA injection

Table 5.3 Effects of the Congenital Myasthenic Syndrome (CMS) Mutation on the function of the nAChR, ELIC, GLIC, and on both ELIC and GLIC mutants[a]

	Aromatic Mutant	CMS Mutant	Dose Response[b]			I_{max} Values[c]		
			EC_{50}	Hill Slope	n	I_{max}	ng injected	n
nAChR[d] (μM ACh)	WT		9.11 ± 1.45	1.94 ± 0.48	31	2.73 ± 2.7	5 (α)	31
		αC418W	0.34 ± 0.08	1.71 ± 0.36	11	4.82 ± 3.7	5 (α)	8
ELIC (mM Cys)	WT	L308C	0.46 ± 0.14	2.07 ± 0.41	10	4.59 ± 2.87	0.1	10
		L308W	0.29 ± 0.05	2.12 ± 0.30	10	3.21 ± 1.87	0.1	10
	1 + 2	L308C	0.36 ± 0.04	2.93 ± 1.35	8	5.40 ± 1.04	0.2	4
		L308W	0.33 ± 0.07	2.92 ± 0.29	8	6.10 ± 2.20	0.2	6
	1 + 3	L308C	0.18 ± 0.03	2.85 ± 0.21	8	6.39 ± 2.00	0.2	6
		L308W	0.12 ± 0.06	1.82 ± 0.42	9	2.45 ± 0.20	0.2	4
	2 + 3	L308C	0.32 ± 0.09	3.02 ± 0.62	7	3.27 ± 1.65	0.2	6
		L308W	0.15 ± 0.03	1.56 ± 0.28	6	1.34 ± 0.39	0.2	6
	1 + 2 + 3	L308C	0.24 ± 0.07	2.85 ± 0.21	8	5.53 ± 2.03	0.4	7
		L308W	0.12 ± 0.06	1.82 ± 0.42	9	1.94 ± 0.82	0.4	5
	1 + 2 + 3 + 5 + 6	L308C	0.18 ± 0.04	1.95 ± 0.47	10	2.59 ± 1.85	5	6
		L308W	0.15 ± 0.04	1.87 ± 0.44	8	2.29 ± 1.78	5	7
GLIC (pH)	WT	L304C	5.03 ± 0.02	1.73 ± 0.43	6	4.42 ± 3.21	3.3	6
		L304W	5.06 ± 0.03	2.01 ± 0.21	6	4.35 ± 1.39	3.3	6
	1	L304C	4.58 ± 0.04	2.06 ± 0.61	8	1.40 ± 0.54	6.6	8
		L304W				No Current[e]	20	10
	2	L304C	4.78 ± 0.03	1.97 ± 0.21	8	4.54 ± 2.15	6.6	8
		L304W				No Current[e]	20	10
	3	L304C	4.46 ± 0.03	1.89 ± 0.25	8	1.86 ± 0.46[f]	20	8
		L304W				No Current[e]	20	10
	5	L304C	4.39 ± 0.07	2.25 ± 0.54	8	2.71 ± 0.96[f]	20	8
		L304W				No Current[e]	20	10
	6	L304C	3.99 ± 0.13	0.83 ± 0.08	6	7.01 ± 3.05[d]	20	6
		L304W				No Current[f]	20	10
	1 + 2	L304C			10	No Current[f]	20	10
		L304W			10	No Current[f]	20	10

[a]Table 5.3 relates to Figure 5.4
[b]Measurements performed 1-4 days after cRNA injection EC_{50} units are μM Acetylcholine (nAChR), mM Cysteamine (ELIC) and pH (GLIC). Error values are SD.
[c]Measured with V_{hold} at -20mV after 1 day for GLIC, V_{hold} at -30 to -40mV after 1 day for ELIC, and V_{hold} at -60mV after 4 days for the nAChR.
[d]RNA amounts for other nAChR muscle-type subunits were injected stoichiometrically based on ng of α injected (2:1:1:1)
[e]No significant current observed up to 4 days after cRNA injection
[f]Measured at a V_{hold} of -20 mV, 4 days after cRNA injection

Chapter 6. Manuscript 4

Hénault, C.M., Govaerts, C., Spurny, R., Brams, M., Estrada-Mondragon, A., Lynch, J., Bertrand, D., Pardon, E., Evans, G.L., Woods, K., et al. (2019). A lipid site shapes the agonist response of a pentameric ligand-gated ion channel. Nat. Chem. Biol. *15*, 1156–1164.

Adapted as a post-print from Nat. Chem Biol, http://dx.doi.org/10.1016/j.str.2015.06.020

6.1 Preface

This manuscript is the fourth of four first-author manuscripts presented in this thesis. Although it represents a collaborative work between multiple labs and authors, and not just my own, it is presented in its entirety to allow the complexity of the story it tells to be understood.

I designed, generated the mutants for, and performed the TEVC experiments that led to this work, as well as the further mutational/electrophysiological analysis of the residues within the lipid binding pocket that was discovered crystallographically and computationally as a result. I also wrote the original draft of the manuscript, which was later expanded on by Dr Baenziger and Dr Ulens, as well as all contributing authors, in their respective sections.

Cedric Govaerts performed structure building and refinement. Radovan Spurny designed and performed protein purification, crystallization, X-ray data collection and structure determination, building and refinement. Marijke Brams designed and performed protein purification, crystallization, cysteine crosslinking, mutagenesis, RNA transcription and analyzed data. Argel Estrada-Mondragon designed, performed and analyzed VCF recordings. Joseph Lynch. supervised voltage clamp recordings, data analysis and acquired funding. Daniel Bertrand. designed, performed and analyzed HiClamp recordings. Els Pardon designed, performed and analyzed all aspects of nanobody production. Genevieve Evans performed structure validation and data analysis. Kristen Woods contributed to all aspects of MD simulations. Benjamin Elberson. contributed to lipid vesicle recordings. Luis Cuello designed, performed and analyzed lipid vesicle recordings and contributed funding. Grace Brannigan designed, performed, analyzed MD simulations and acquired funding. Hughes Nury performed X-ray structure building and refinement. Jan Stayaert contributed to all aspects of nanobody production and acquired funding. John Baenziger supervised the project, performed experimental design, data analysis and acquired funding. Chris Ulens supervised the project, performed experimental design, contributed to all aspects of X-ray crystallography and acquired funding.

6.2 Abstract

Phospholipids are key components of cellular membranes and are emerging as important functional regulators of different membrane proteins, including pentameric ligand-gated ion channels (pLGICs). Here, we take advantage of the prokaryote channel ELIC (Erwinia ligand-gated ion channel) as a model to understand the determinants of phospholipid interactions in this family of receptors. A high-resolution structure of ELIC in a lipid-bound state reveals a phospholipid site at the lower half of pore-forming transmembrane helices M1 and M4 and at a nearby site for neurosteroids, cholesterol or general anesthetics. This site is shaped by an M4-helix kink and a Trp-Arg-Pro triad that is highly conserved in eukaryote $GABA_{A/C}$ and glycine receptors. A combined approach reveals that M4 is intrinsically flexible and that M4 deletions or disruptions of the lipid-binding site accelerate desensitization in ELIC, suggesting that lipid interactions shape the agonist response. Our data offer a structural context for understanding lipid modulation in pLGICs.

6.3 Introduction

Increasing knowledge of membrane protein structures is shedding light on the molecular interplay between lipids and proteins that regulates both membrane protein and lipid bilayer function (Norimatsu et al., 2017; Dawaliby et al., 2016; Martens et al., 2016; She et al., 2018; Laganowsky et al., 2014; Whorton and MacKinnon, 2011). For pLGICs, this interplay has been the subject of intense investigation since the earliest attempts at defining the structural domains responsible for ligand binding and channel gating in the nicotinic acetylcholine receptor (nAChR) (Heidmann et al., 1980). Although these studies suggest that lipids regulate nAChR function by stabilizing different proportions of activatable versus non-activatable conformations, and by controlling the transitions between these states, the molecular interactions that underlie these mechanisms remain poorly defined (Baenziger et al., 2015; Barrantes, 2015; daCosta et al., 2009, 2013).

All members of the pLGIC family share a common topology, composed of an extracellular ligand-binding domain, a pore-forming transmembrane domain and an intracellular regulatory domain, which is absent in prokaryote receptors. The ligand-binding domain of each subunit is largely composed of β-sheets, β1–10, which harbor the residues on 'loops' A–C of the principal (+) subunit and 'loops' D–F of the complementary (−) subunit that together form the neurotransmitter binding site. The transmembrane pore domain (TMD) of each subunit is α-helical, M1–M4, with the M2 α-helix facing the central ion pore and the M4 α-helix facing the lipid membrane.

A wide range of experimental evidence obtained from different pLGICs has highlighted a role for the outermost transmembrane α-helix, M4, of each subunit in both channel function and lipid sensing (Carswell et al., 2015b; Cory-Wright et al., 2018; Haeger et al., 2010; Hénault et al., 2015b, 2015a). M4 is conformationally dynamic during channel gating (Mitra et al., 2004). M4 is implicated in lipid-dependent desensitization (Basak et al., 2017; Velisetty et al., 2014). Mutations along the lipid–protein interface influence channel gating, demonstrating that altered M4–lipid interactions influence channel function (Bouzat et al., 1998; Lasalde et al., 1996). M4 may act as a lipid sensor, influencing channel function

via interactions with the adjacent transmembrane α-helices, M1 and M3 (Carswell et al., 2015a; Domville and Baenziger, 2018; Labriola et al., 2013).

An important role for M4 in mediating lipid–protein interactions is further suggested by recent structures, which have identified lipid recognition sites in pLGICs. One crystal structure of the bacterial homolog, GLIC, reveals three phospholipids bound at the interface between M4 and M1/M3 in each of the five pLGIC subunits (Bocquet et al., 2009), although the bound lipid in the cytoplasmic leaflet extends to interact with M3 from the adjacent subunit. Interestingly, the binding of one of these lipids to the M4 and M1/M3 interface is displaced by the inhibitory anesthetic, propofol (Nury et al., 2011b). A cytoplasmic leaflet site at the interface between M4 and M1/M3 has also been shown to bind neurosteroids in various α1- or α5-based $GABA_A$ receptor chimeras (Chen et al., 2018; Laverty et al., 2017; Miller et al., 2017). The M3/M4 interface also serves as a binding site for cholesterol or PIP_2 in structures of the heteromeric human $GABA_A$ receptor (Laverty et al., 2019; Zhu et al., 2018).

Here, we take advantage of the prokaryotic channel ELIC as a model to understand the structural determinants of lipid action at this family of receptors. Using nanobodies to facilitate structural studies, we determined new ELIC structures, revealing bound lipids as well as distinct conformational states of the M4 helix. A phospholipid site is formed in the lower half of the pore-forming transmembrane domain near a previously identified binding site for neurosteroids, cholesterol and general anesthetics. A major part of this site is shaped by the M4 α-helix, which contains a characteristic kink at a conserved proline residue and is also found in eukaryote anion-selective channels. Using mutagenesis studies, we relate structure to function and demonstrate that perturbations of the lipid-binding site accelerate desensitization in ELIC, a phenomenon that is mimicked by reconstitution of ELIC into membranes with different lipid compositions. Together with mutant ELIC structures, crosslinking studies, molecular dynamics (MD) simulations and voltage clamp fluorometry (VCF), we further demonstrate the intrinsic flexibility of M4, thus providing novel mechanistic detail into the role of M4 in lipid sensing and offering a structural context for understanding desensitization in the family of pLGICs.

6.4 Results

6.4.1 High-resolution ELIC structure in a lipid-bound state.

In this study, we took advantage of nanobodies, which are antibody fragments derived from llamas that facilitate structural studies by promoting crystallogenesis and by stabilizing conformationally transient states (Manglik et al., 2017). This is especially useful for the prokaryote channel ELIC, for which almost 30 structures have been determined, all in the same nonconducting conformation and at relatively moderate resolution (Hilf and Dutzler, 2008). We screened a range of ELIC constructs, in combination with different nanobodies, to identify previously unresolved conformational states and crystals with improved diffraction quality. We focus here on the structure of one of these constructs, ELIC with a cysteine mutation at the 7′ position of the pore-lining M2 helix bound to nanobody 72 (Nb72). This structure was solved at a resolution of 2.5 Å, which is the highest resolution yet for an ELIC structure (Figure 6.1a,b). At this resolution, densities that were absent from previous lower resolution structures are now revealed, enabling a more detailed view with bound ions, lipids and detergent molecules. ELIC 7′C is functionally almost identical to wild-type ELIC (half-maximum effective concentration (EC_{50}) value of GABA = 7.6 ± 0.3 mM, n = 9), but gave better electron density for bound lipids.

The ELIC pentamer is bound by five Nb72 molecules, one to each monomer. Nb72 interacts with the extracellular ligand-binding domain forming extensive contacts on each subunit with the β9 and β10 strands of the C-loop, which forms a flexible part of the orthosteric binding site, as well as with N-terminal residues of the β6–β7 loop. The β6–β7 loop extends down toward the TMD and plays a role in coupling agonist binding to channel gating. The nanobody also extends across the subunit interface to form contacts with the β8–β9 loop of the adjacent subunit. These intersubunit contacts could prevent intersubunit movements to stabilize the receptor in a single conformational state (Figure 6.1c). Indeed, functional data show that Nb72 reduces the agonist-induced response.

The Nb72-stabilized conformation of ELIC is similar to previously published structures, although we observe that the 7′C pore is slightly more closed compared to wild-type ELIC. At the 6′ pore position, the T237 side chain points toward the center of the pore

and interacts with a sodium ion. Significantly, we identify a lipid molecule at a site in the lower half of the transmembrane domain located between the M1 and M4 helices of one subunit and the M3 helix of a neighboring subunit (Figure 6.1 b,d). We identify the lipid as phosphatidylethanolamine (PE) based on electron density features and in line with biochemical conditions. Indeed, PE is the most abundant lipid component of the *Escherichia coli* lipid extract (58% PE, 15% phosphatidyl glycerol (PG), and 10% cardiolipin), which is added as an essential part of the crystallization mix. The lipid site lies close to a previously identified binding site for neurosteroids in α1- or α5-based $GABA_A$ receptor chimeras (Chen et al., 2018; Laverty et al., 2017; Miller et al., 2017) as well as a cholesterol-binding site in the α1β2γ2 $GABA_A$ receptor structure (Zhu et al., 2018) (Fig 6.1d–f). This conservation of a lipid-binding site between prokaryote and eukaryote channels suggests an important functional role. In addition to lipids and ions, we are able to assign a previously unexplained region of density in lower resolution ELIC structures, near W206 at the top of the M1 helix, as the head group of an undecylmaltoside detergent molecule (See online supplemental material). The lipid tail of the undecylmaltoside molecule points down and in between the upper half of the M3 and M4 helices. Together, these results offer a detailed view of the ELIC channel and interacting ions, lipids and detergents.

Figure 6.1 High-resolution ELIC structure in a lipid-bound state.

a,b) Top and side views of the crystal structure of ELIC 7′C pore mutant (blue) in complex with nanobody 72 (Nb72, red) in a lipid-bound state. Protein is shown in cartoon representation, lipid in sphere representation. Yellow corresponds to carbon, blue to nitrogen and red to oxygen. **c**, Detailed view of the interaction between Nb72 and orthosteric binding site in ELIC, including loop C. **d)** Detailed view of the lipid interaction at a transmembrane site. One subunit is shown in blue and its neighboring subunit in white. PE is shown in transparent sphere and sticks. The lipid site is formed at the M1–M4 interface of one subunit and M3 of the neighboring subunit. This site overlaps with a known neurosteroid binding site in the β3/α5 chimeric $GABA_A$-R (**e**) and a cholesterol-binding site in the α1β2γ2 $GABA_A$-R(**f**).

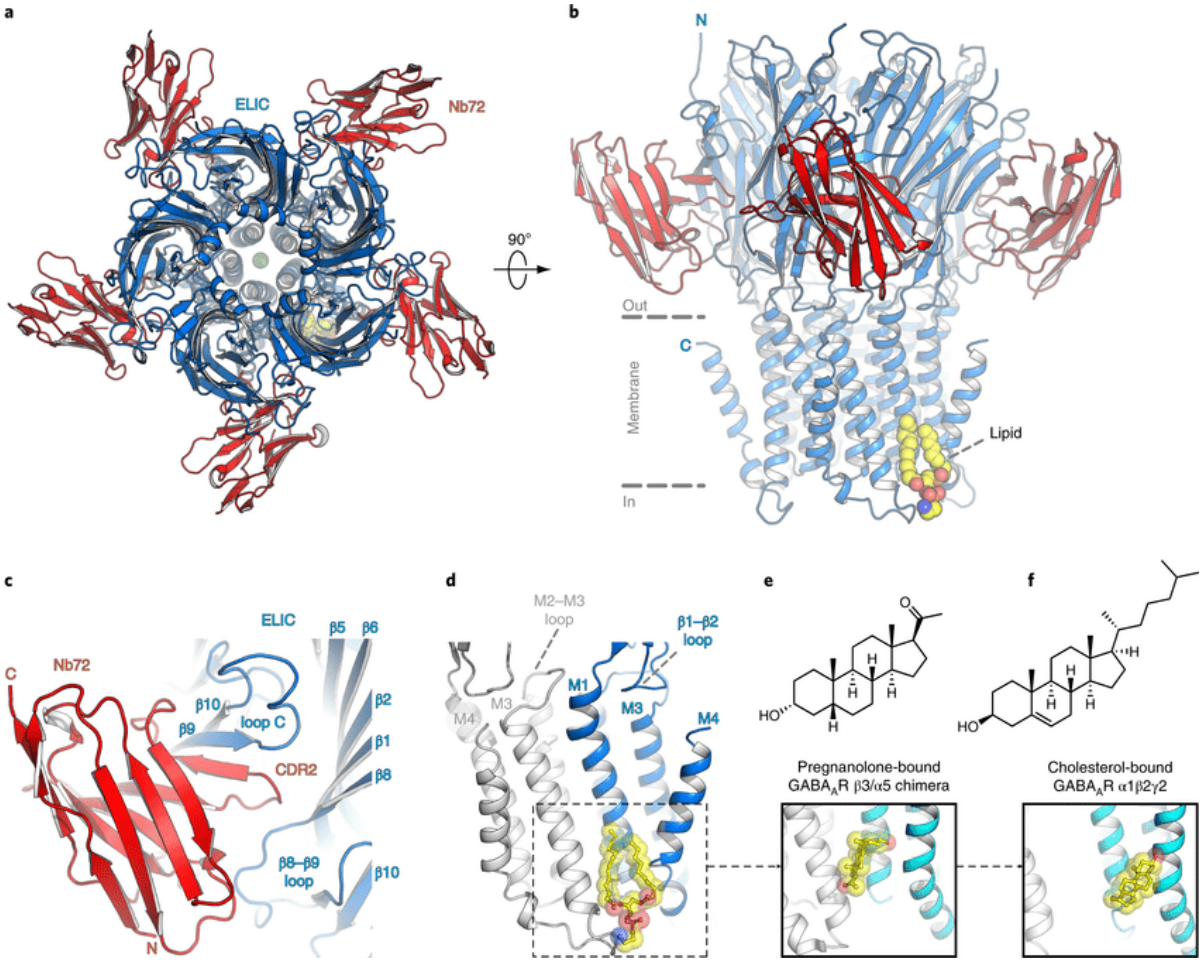
a
ELIC
Nb72
90°
b
N
Out
C
Membrane
Lipid
In
c
ELIC
β5
β6
C
Nb72
β10
β9
loop C
CDR2
β2
β1
β8
β8–β9
loop
β10
N
d
M2–M3
loop
β1–β2
loop
M1
M3
M4
M3
M4
e
HO
H
O
Pregnanolone-bound
GABA$_A$R β3/α5 chimera
f
HO
H
Cholesterol-bound
GABA$_A$R α1β2γ2

Figure 6.2 Sequence alignment of residues forming the lipid binding site in ELIC

The sequence alignment shows highly conserved residues of the lipid binding site in ELIC and compared to anion-selective eukaryote pLGICs. “Gly” indicates glycine receptors, “GAB” indicates GABAA receptors and GluCl indicates the invertebrate glutamate-activated chloride channel. Shades of blue indicate sequence conservation with an identity threshold of 40%. Residues of the W-R-P triad are highlighted in yellow.

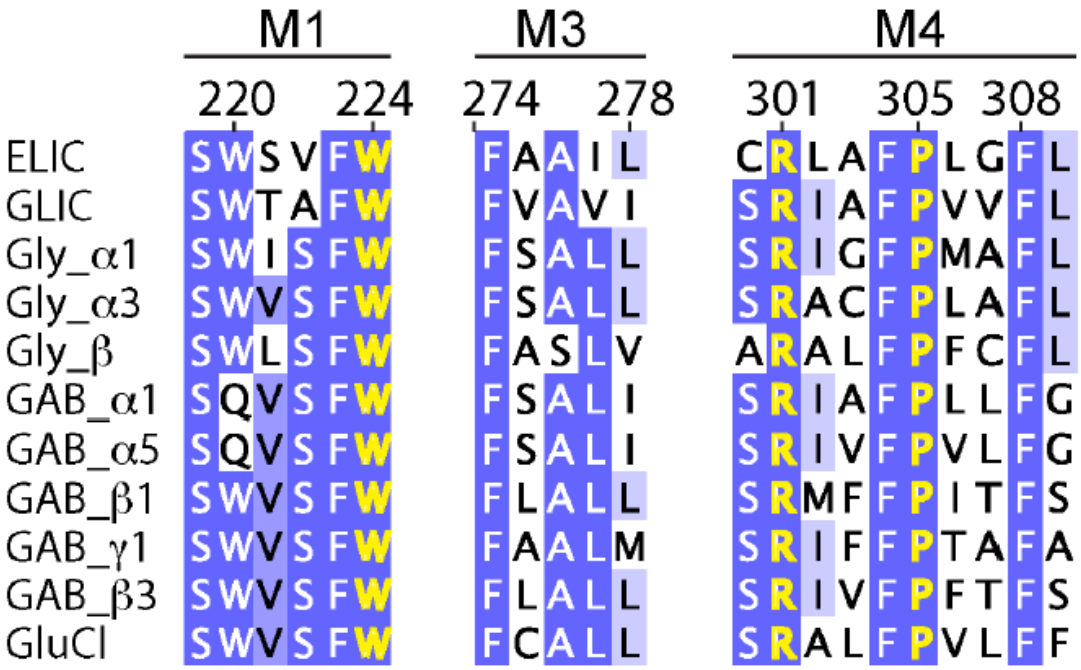
M1
M3
M4
220
224
274
278
301
305
308
ELIC
GLIC
Gly_α1
Gly_α3
Gly_β
GAB_α1
GAB_α5
GAB_β1
GAB_γ1
GAB_β3
GluCl

6.4.2 Lipid site conservation in ELIC and eukaryote channels

A detailed view of amino acids composing the lipid-binding site in ELIC (Figure 6.3a,b) reveals that this site is shaped in part by a characteristic kink, induced by P305, in the M4 helix. This orients R301 one helical turn down along M4 to interact with W224 in the M1 helix via a cation–π interaction (Figure 6.3b). Consequently, W224 is oriented nearly perpendicular to the membrane and creates a wedge between the two lipid tails of the PE lipid molecule (Figure 6.3b). This triad of interactions W–R–P is strictly conserved between ELIC and anion-selective eukaryote pLGICs (Figure 6.2) but not in cation-selective eukaryote pLGICs, and suggests an important structural and functional role. In addition to the triad residues, we find other aromatic residues in M4, F308, and M1, W220, which are also strongly conserved. These residues on the complementary (−) subunit form the majority of the lipid-binding site, with additional residues, F274 (strongly conserved), L278 (semi-conserved) and I281 (Ala in most anionic pLGICs), on the M3 helix of the principal (+) subunit also contributing to lipid binding (Figure 6.3b). Consequently, the sequence alignment reveals characteristic motifs in anion-selective pLGICs, namely SWxxFW (M1), FxALx (M3) and SRxxFPxxFx (M4), with residues of the triad interaction underlined. From a structural perspective (Figure 6.3d), the W–R–P triad creates a characteristic bend in the M4 helix, which is observed in all anion-selective pLGICs determined to date, α1 and α3 GlyR, (Du et al., 2015; Huang et al., 2017) human β3 $GABA_AR$ (Miller and Aricescu, 2014), human α1β(1–3)γ2 $GABA_AR$ (Laverty et al., 2019; Masiulis et al., 2019; Phulera et al., 2018; Zhu et al., 2018), glutamate-gated chloride channel from *Caenorhabditis elegans* GluCl (Althoff et al., 2014; Hibbs and Gouaux, 2011), but not in cation-selective pLGICs, for example human α4β2 nAChR (Morales-Perez et al., 2016; Walsh et al., 2018). In this last example, the triad amino acids structurally align with Y–I–L (Figure 6.3d). As a consequence of M4 helix bending in anion-selective pLGICs the top of M4 moves back toward the M1 and M3 helices and the conserved Cys-loop, forming an interaction interface that plays a crucial role in the coupling of ligand binding to the channel opening. The absence of the M4 helix bend in cation-selective pLGICs suggests that the two branches of the family have evolved different signaling mechanisms via M4.

Figure 6.3 Lipid interactions at a highly conserved Pro kink in the M4 helix

a,b) Surface/sticks and cartoon/sticks representation of the lipid-binding site in ELIC. One subunit is shown in blue, the neighboring subunit in white, and lipid in yellow (carbon). The dashed line indicates a cation–π interaction between R301 and W224. **c)** Electrophysiological recordings of purified ELIC reconstituted in vesicles with known lipid content. All recordings were repeated in 4 to 26 independent experiments. The time constant for desensitization (τ) is mentioned as the mean ± s.e.m. **d)** Architectural conservation of the M4 helix Pro kink and cation–π (R–W) interaction in anion-selective eukaryotic receptors, but not in cation-selective receptors, for example, α4β2 nAChR.

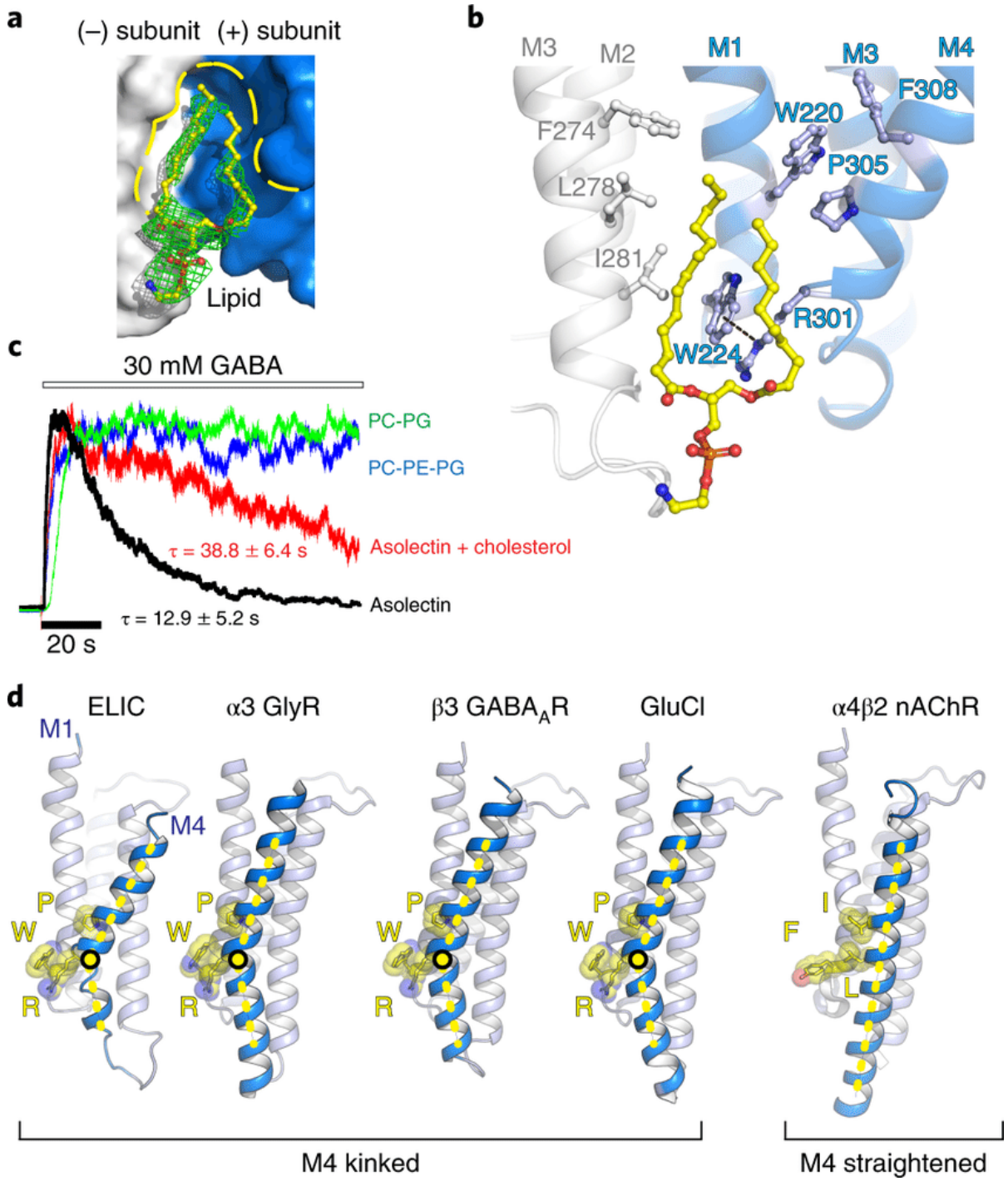
a
(–) subunit
(+) subunit
Lipid
b
M3
M2
M1
M3
M4
F308
W220
F274
P305
L278
I281
R301
W224
c
30 mM GABA
PC-PG
PC-PE-PG
τ = 38.8 ± 6.4 s
Asolectin + cholesterol
Asolectin
τ = 12.9 ± 5.2 s
20 s
d
ELIC
α3 GlyR
β3 GABA$_A$R
GluCl
α4β2 nAChR
M1
M4
P
W
R
I
F
L
M4 kinked
M4 straightened

6.4.3 Lipids influence rate of agonist-induced desensitization

Preliminary studies suggested that in defined membranes composed exclusively of phosphatidylcholine (PC), ELIC is locked in a nonconducting state, while in membranes composed of soybean asolectin, ELIC responds to agonist, albeit with enhanced rates of desensitization (Carswell et al., 2015a). Using electrophysiological recordings from giant unilamellar vesicles, we confirm here that ELIC in membranes composed of soybean asolectin, a complex mixture of phospholipids, responds to agonist, but with relatively rapid desensitization kinetics (Figure 6.3c). Desensitization is slowed in membranes composed of asolectin with 25% cholesterol, an intriguing observation given that the PE binding site in ELIC overlaps with the cholesterol-binding site in the α1β2γ2 $GABA_A$ receptor (Zhu et al., 2018). Strikingly, the rapid decay of the agonist-induced response in asolectin is eliminated when ELIC is reconstituted into either PC/PG or PC/PG/PE membranes (Figure 6.3c). These functional data show that lipids have a profound effect on agonist-induced desensitization and thus have the capacity to shape the agonist-induced response.

Figure 6.4 Electrophysiological characterization of ELIC mutants in the lipid binding site.

Functional characterization of single mutants of amino acid residues composing the PE lipid binding site. Mutants were expressed in *Xenopus* oocytes and responses to increasing concentrations of the agonist cysteamine were measured using two electrode voltage clamp recordings. All identified mutations have relatively minor changes in the EC_{50}-values for cysteamine, except F282A which becomes more 20-fold more sensitive than wild type ELIC. Compared to wild type ELIC, all other mutants display more rapid desensitization kinetics, which is similar but less drastic than the P305A mutant. Representative traces are shown from 3-9 independent experiments for each construct. Slope values for these mutants are reported in Table 6.1 and were obtained by plotting the reciprocal time constant of activation (1/t) as a log function of agonist concentration.

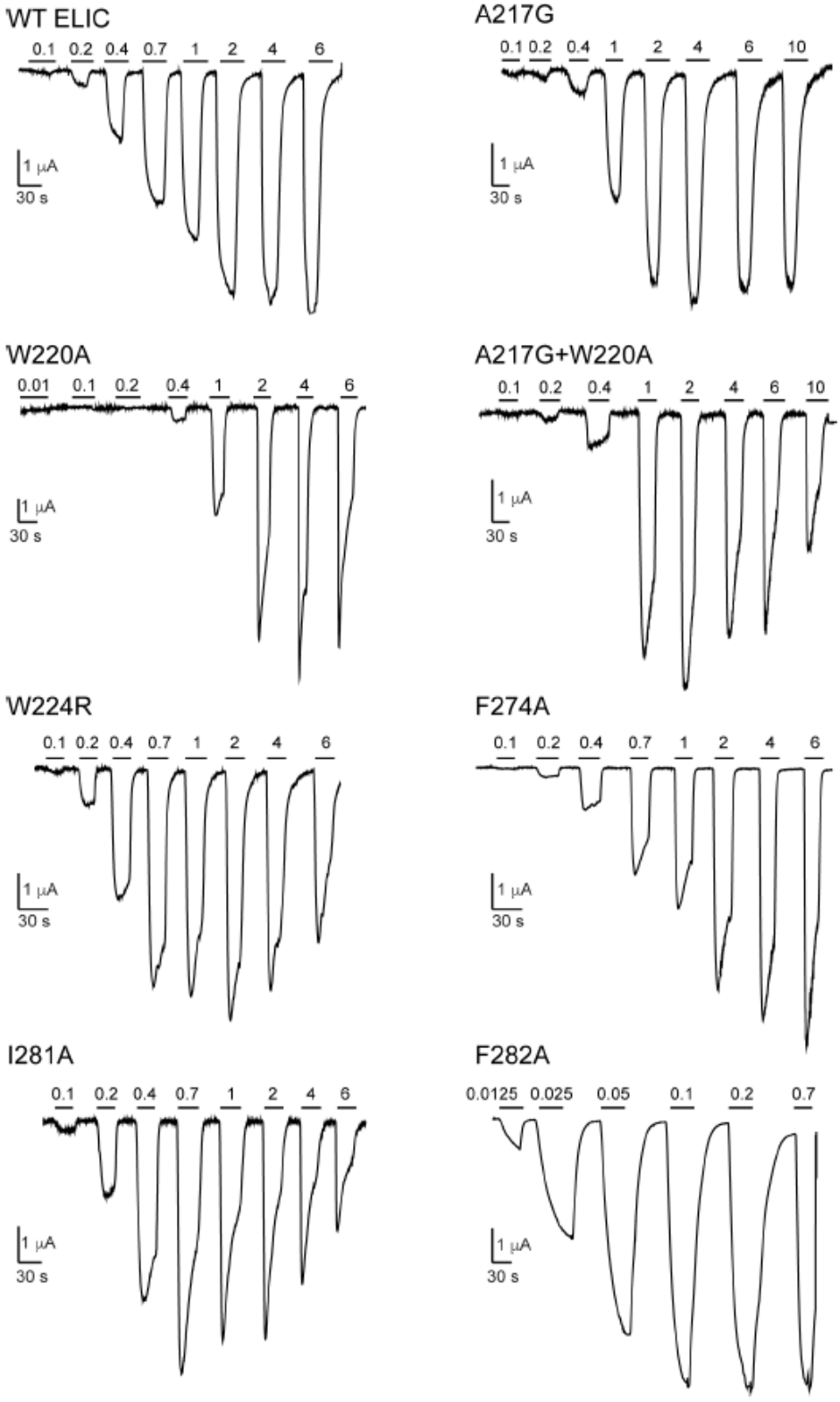
WT ELIC
0.1 0.2 0.4 0.7 1 2 4 6
1 μA
30 s
A217G
0.1 0.2 0.4 1 2 4 6 10
1 μA
30 s
W220A
0.01 0.1 0.2 0.4 1 2 4 6
1 μA
30 s
A217G+W220A
0.1 0.2 0.4 1 2 4 6 10
1 μA
30 s
W224R
0.1 0.2 0.4 0.7 1 2 4 6
1 μA
30 s
F274A
0.1 0.2 0.4 0.7 1 2 4 6
1 μA
30 s
I281A
0.1 0.2 0.4 0.7 1 2 4 6
1 μA
30 s
F282A
0.0125 0.025 0.05 0.1 0.2 0.7
1 μA
30 s

Table 6.1 Data statistics for electrophysiological recordings of ELIC mutants in the lipid binding site

Mutant	Slope ($s^{-1}M^{-1}$)	EC_{50} Cysteamine (mM)
I281A	3.07 ± 0.80 (n=6)	0.26 ± 0.02
A217G+W220A	2.39 ± 1.08 (n=3)	0.69 ± 0.08
W220A	1.28 ± 0.61 (n=9)	0.76 ± 0.18
W224R	0.98 ± 1.45 (n=7)	0.42 ± 0.08
F274A	0.82 ± 0.76 (n=8)	0.96 ± 0.12
A217G	< 0.01 (n=8)	0.91 ± 0.17
F282A	< 0.01 (n=7)	0.045 ± 0.02

Slope values and EC50-values for mutants in the lipid binding site.

Traces are shown in Figure 6.4. The slope values reported in this table are obtained from the reciprocal time constant of activation (1/t) plotted as a log function of agonist concentration (the procedure is shown in Figure 6.6). Data are reported as the mean ± SEM from 3 to 9 independent experiments.

6.4.4 Lipid site mutagenesis accelerates ELIC desensitization

We used single point mutations with channels expressed in *Xenopus* oocytes to test whether the composition of the lipid-binding site plays a role in ELIC function. Single Ala mutations of implicated residues (Figure 6.3b and Figure 6.4) lead to relatively small changes in the EC_{50} for the agonist cysteamine relative to the EC_{50} of wild-type ELIC (Hénault et al., 2015b) (Table 6.1), suggesting that the lipid-binding site does not strongly affect receptor activation. The F274A, I281A, W220A and P305A mutations, however, each lead to a more rapid desensitizing phenotype (Figure 6.4 and Figure 6.5a,b), as did the W224R mutation, which should disrupt the lipid-binding site through electrostatic repulsion with the adjacent R301 on M4. Significantly, P305A, which is expected to disrupt the M4-helix kink that shapes the lipid-binding site, exhibits a particularly rapid rate of desensitization (Figure 6.5b). To reposition the kink in the M4 helix we inserted new Pro residues onto the P305A background, with each Pro insertion occurring either one turn higher (P305A+L309P) or one turn lower (P305A+R301P) or two turns lower (P305A+I297P) on the M4 helix (Figure 6.5c–e). Each of these mutants exhibits more rapid desensitization rates than wild-type ELIC, but less rapid than ELIC with an unkinked M4 (P305A). To quantify the differences in desensitization kinetics for all mutants, we measured the time constant for the rate of decay of the whole-cell agonist-induced response over multiple agonist concentrations. We then plotted the reciprocal of the decay constant versus the agonist concentration (Figure 6.6) and summarize slope values in Table 6.2. Note that desensitization of the wild-type ELIC is too slow to accurately determine a slope value (slope value < 0.01 in Table 6.2).

Figure 6.5 Site-directed mutagenesis of the ELIC M4 helix accelerates desensitization

a–h Whole-cell two-electrode voltage clamp electrophysiological traces recorded from oocytes expressing wild-type ELIC (**a**), P305A mutant (**b**), M4 proline-shifted (**c–e**) and M4 deletion (**f–h**) mutants of ELIC. Ligand (cysteamine) concentration jumps (mM) are indicated by the horizontal bars. Representative traces are shown from four to eight independent experiments for each construct. Cartoon representations of the M4 helix indicate the proline-induced kink and deletion sites.

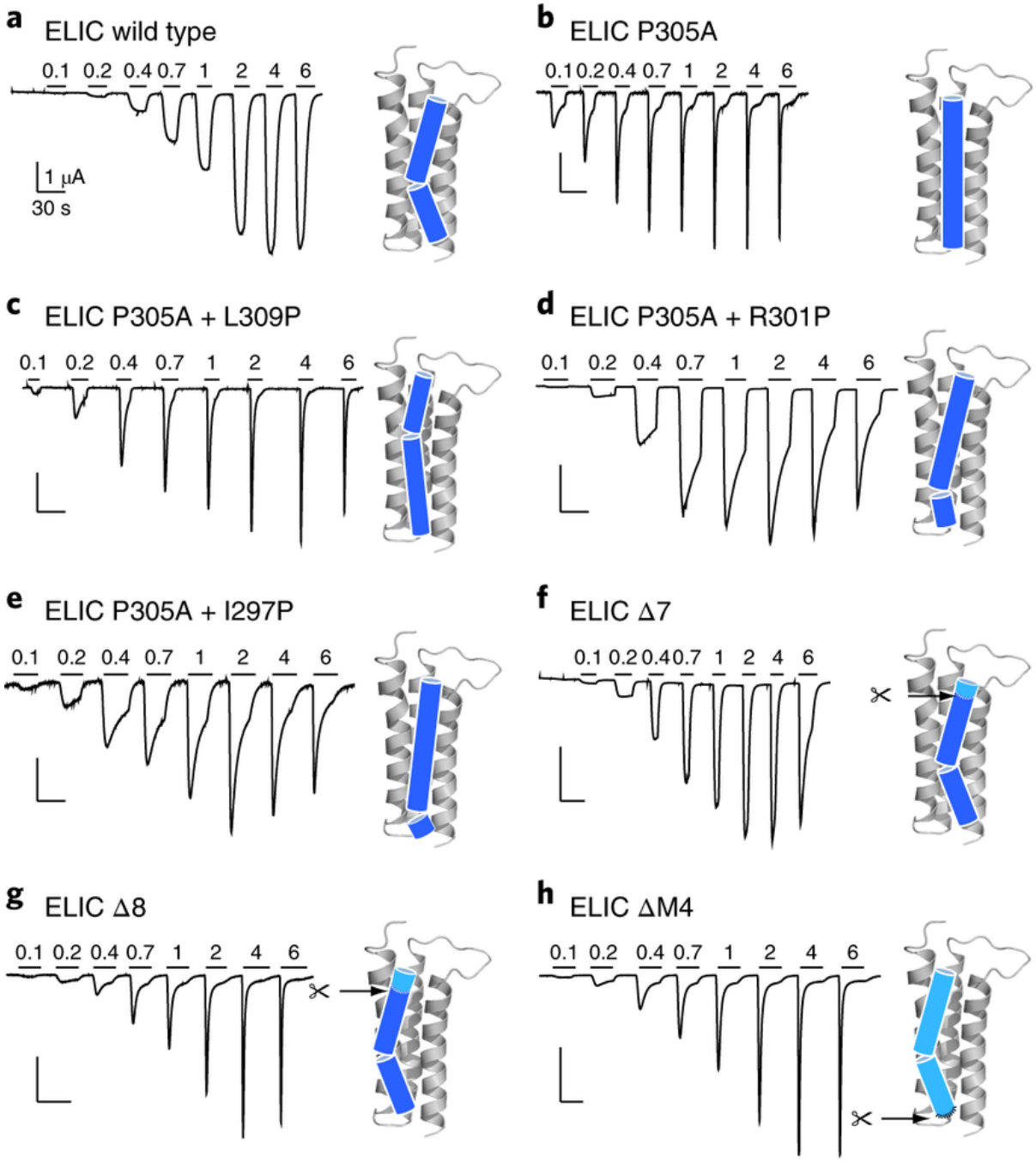
a
ELIC wild type
0.1 0.2 0.4 0.7 1 2 4 6
1 μA
30 s
b
ELIC P305A
0.1 0.2 0.4 0.7 1 2 4 6
c
ELIC P305A + L309P
0.1 0.2 0.4 0.7 1 2 4 6
d
ELIC P305A + R301P
0.1 0.2 0.4 0.7 1 2 4 6
e
ELIC P305A + I297P
0.1 0.2 0.4 0.7 1 2 4 6
f
ELIC Δ7
0.1 0.2 0.4 0.7 1 2 4 6
g
ELIC Δ8
0.1 0.2 0.4 0.7 1 2 4 6
h
ELIC ΔM4
0.1 0.2 0.4 0.7 1 2 4 6

The P305A mutation and additional Pro insertions on the P305A background probably not only distort the lipid-binding pocket or affect lipid binding, but more generally alter how the M4 helix interacts with the remainder of the TMD. To further probe the role of M4–M1/M3 interactions in channel function, we deleted progressive parts of M4. Functional recordings revealed that the deletion of up to seven residues in ELIC has little effect on either expression or function, with all the C-terminal deletion mutants exhibiting EC_{50} values for the agonist cysteamine that are within 0.5 log units of the wild-type EC_{50} value (Figure 6.5f). Notably, these deletions are not tolerated in the related prokaryote channel GLIC, where deletion of the final three or four residues at the M4 C-terminus leads to a strong reduction or a complete loss of expression and/or function, respectively (Carswell et al., 2015b). Additionally, deletions of the entire M4 are also not tolerated in 5-HT3Rs or GlyRs (Haeger et al., 2010). Remarkably, even ELIC mutants with up to eight or more residues deleted from the M4 C-terminus (Δ7 and Δ8, Figure 6.5f,g), including a mutant that lacked the entire M4 α-helix (ΔM4, Figure 6.5h), still gave rise to robust agonist-induced currents. In each case, however, the agonist-induced currents exhibit very rapid desensitization compared to both wild-type ELIC and the ELIC deletion mutants with up to seven residues removed from the C terminus (Δ7, Figure 6.5f). The rapid desensitization of the ELIC deletion mutants is similar to that observed for the therapeutically important α7 nAChR (Figure 6.6 and Table 6.2), which is one of the fastest desensitizing pLGICs in this channel family. We determined that the M4 deletion mutants have rates of agonist-dependent desensitization similar to that of P305A (Figure 6.6 and Table 6.2). These results demonstrate that perturbations of the M4 helix and specifically the residues that compose the lipid-binding site profoundly affect desensitization, consistent with the above observation that the lipid composition of the environment surrounding ELIC influences desensitization.

Figure 6.6 Quantitative analysis of ELIC desensitization kinetics

Analysis of densensitization kinetics for the ELIC current traces shown in Figure 6.5. This data plot is the reciprocal time constant of activation ($1/\tau$) as a log function of agonist concentration. Cysteamine was used as agonist for ELIC, acetylcholine for the α7 nAChR. Values are presented as the mean ± SEM from 4 to 8 independent experiments. These data were fit with a linear function and the slope values are reported in Table 6.2. Example traces on top are shown for the slowest desensitizing channel in this study, ELIC, as well one of the fastest desensitizing mutants (ΔM4), which has comparable fast desensitization kinetics to the human α7 nAChR. Representative traces are shown from 4-8 independent experiments for each construct.

A

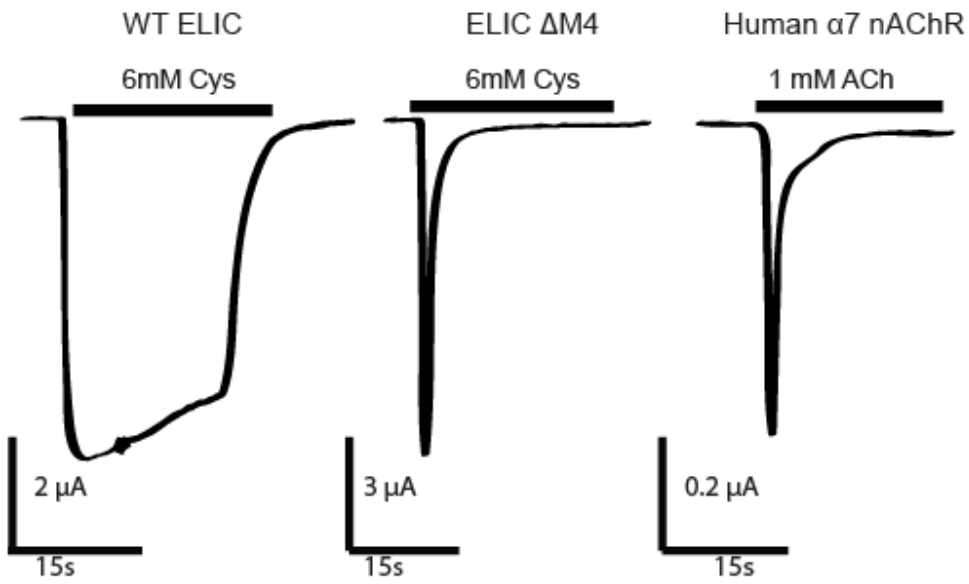
WT ELIC
6mM Cys
ELIC ΔM4
6mM Cys
Human α7 nAChR
1 mM ACh
2 μA
15s
3 μA
15s
0.2 μA
15s

B

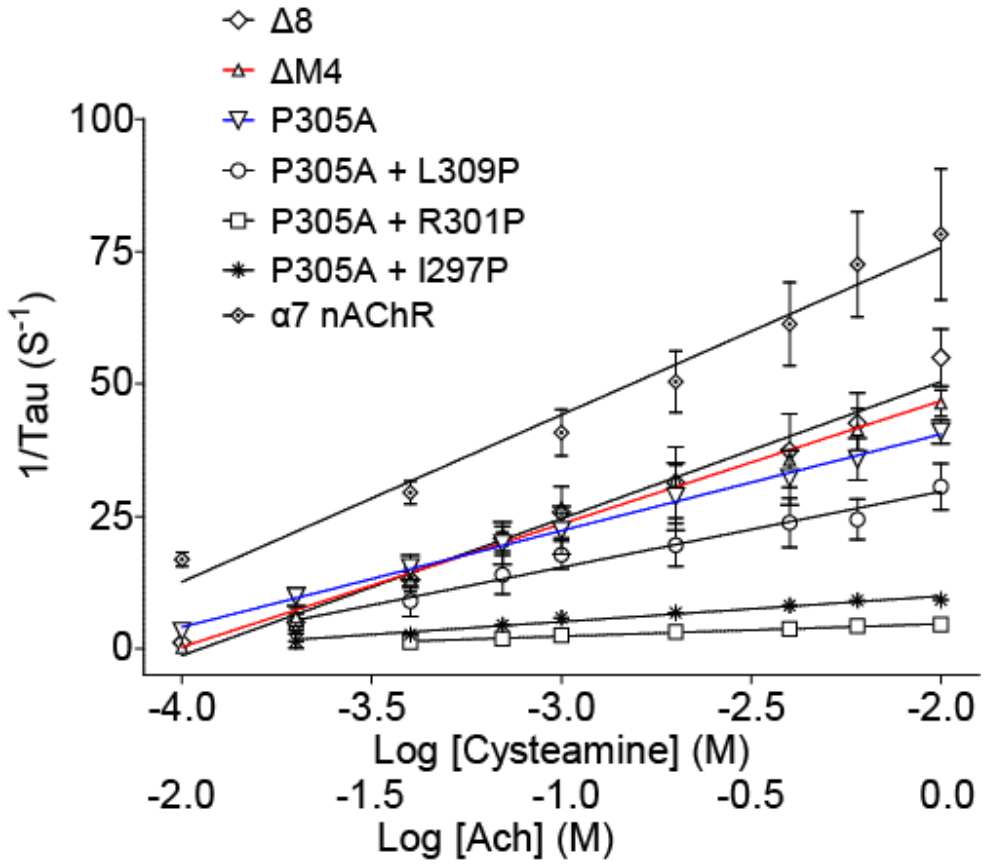
Δ8
ΔM4
P305A
P305A + L309P
P305A + R301P
P305A + I297P
α7 nAChR
1/Tau (S-1)
100
75
50
25
0
-4.0
-3.5
-3.0
-2.5
-2.0
Log [Cysteamine] (M)
-2.0
-1.5
-1.0
-0.5
0.0
Log [Ach] (M)

Table 6.2 Quantitative analysis of ELIC desensitization kinetics

	Slope ($s^{-1}M^{-1}$)
α7 nAChR	32.43 ± 2.97 (n=8)
ELIC Δ8	26.84 ± 1.43 (n=5)
ELIC ΔM4	23.48 ± 1.23 (n=4)
ELIC P305A	18.21 ± 0.37 (n=5)
ELIC P305A+L309P	14.30 ± 0.94 (n=6)
ELIC P305A+I297P	4.83 ± 0.33 (n=4)
ELIC P305A+R301P	2.34 ± 0.12 (n=6)
wild type ELIC	< 0.01

The slope values reported in this table are obtained from the reciprocal time constant of activation (1/τ) plotted as a log function of agonist concentration (Figure 6.6). Values are presented as the mean ± SEM from 4 to 8 independent experiments.

Figure 6.7 M4-helix truncation increases the dynamics of the lower half of the channel pore region

a) Cartoon 'putty' representation of the ELIC 7′C structure and ELIC Δ8 deletion mutant both in complex with Nb72 (not shown). Residues are colored according to the average temperature B-factor, ranging from 25 Å2 (blue) to 250 Å2 (red) and for intermediate values according to the color shading indicated in the spectrum bar. The M4 helix and M3–M4 linker are structurally flexible in the ELIC Δ8 structure and are indicated with a gray dashed line. **b**, Plot of the average B-factor per residue as a function of residue number for ELIC 7'C and ELIC Δ8 structures. **c**, MD simulations of ELIC 7'C (blue) and P305A (red) reveal that the M4 undergoes a conformational change in P305A, which unkinks the helix and causes a conformational tilt toward the complementary subunit. The solid line represents the average of five subunits and the shading represents the s.e.m. The dashed line indicates the distance measured between the Cα of residue V316 in both conformations.

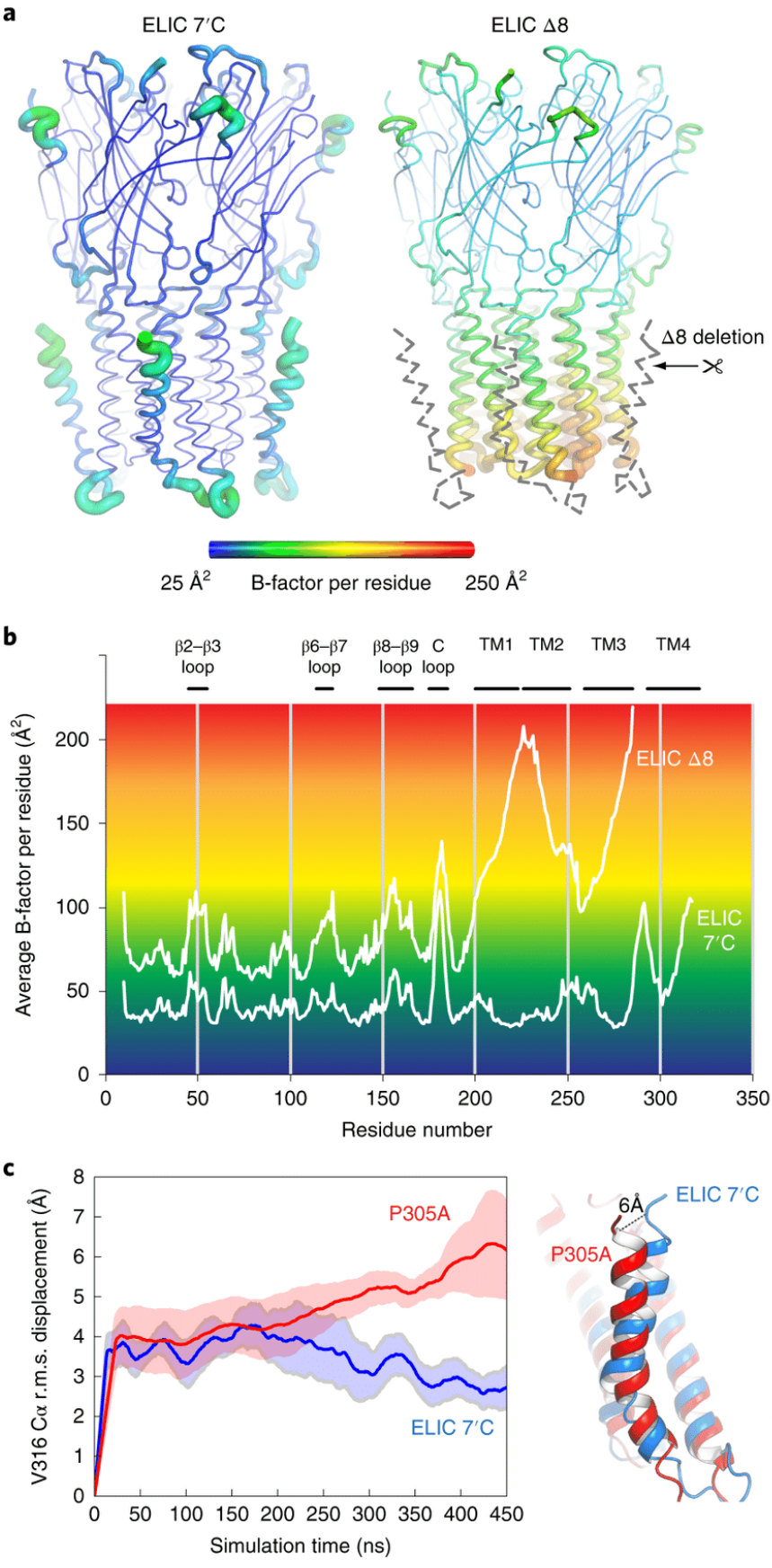
a
ELIC 7′C
ELIC Δ8
Δ8 deletion
25 Å²
B-factor per residue
250 Å²
b
β2–β3 loop
β6–β7 loop
β8–β9 loop
C loop
TM1
TM2
TM3
TM4
ELIC Δ8
ELIC 7′C
Average B-factor per residue (Å²)
Residue number
c
P305A
ELIC 7′C
V316 Cα r.m.s. displacement (Å)
Simulation time (ns)
6Å
P305A
ELIC 7′C

6.4.5 Mutant structure and MD simulation reveal M4 flexibility

To obtain a structural context for understanding M4 dynamics we used X-ray crystal structures and MD simulations of M4 deletion mutants and P305A single mutants. We solved the crystal structure of the Nb72-bound ELIC Δ8 at 2.78 Å resolution (Figure 6.7a), which is the construct displaying the fastest desensitization in *Xenopus* oocytes. Remarkably, proper density is lacking for the whole M4 helix, the M3–M4 linker and the bound lipid. The absence of density, extending far beyond the eight C-terminal residues, indicates that the remainder of M4 and the connecting loop are intrinsically disordered in ELIC Δ8.

Additionally, we also observe that the entire lower half of the M1–M3 transmembrane pore domain becomes less resolved in the electron density map, resulting in a marked increase of the average B-factor per residue, which is used as an indicator of vibrational movement in different parts of the structure. A visual representation of the B-factor distribution is given by the familiar sausage or 'putty' representation in Figure 6.5a with yellow-red residues having the highest B-factors. The plot of average B-factors per residue (Figure 6.7b) indicates that the B-factor distribution in the extracellular domain is overall similar between ELIC and ELIC Δ8, with the most pronounced increase seen for the tip of loop C (residues 175–185). The biggest difference for ELIC Δ8 is seen in the lower half of the transmembrane pore domain, with B-factors sharply rising for the lower half of M1 (residues 214–224), the M1–M2 linker (225–230), the lower half of M2 (231–241) and the lower half of M3 (274–285) (Figure 6.7b). MD simulations also indicate a particularly dynamic Δ8 M4 helix: the r.m.s. displacement of the ELIC M4 backbone is 4.3 ± 0.5 Å (n = 5) in the ELIC Δ8 structure, compared to 3.6 ± 0.2 Å (n = 5) in the reference ELIC structure. The largest displacement observed in a single subunit is 6.3 Å for ELIC Δ8 and 4.1 Å for wild type. This result confirms the enhanced flexibility of the M4 helix in the Δ8 mutant.

Together, the ELIC Δ8 structure and dynamics suggest that the M4 is intrinsically flexible and probably dissociates from the bound lipid. In addition, the Δ8 mutation leads to destabilization of the lower half of the pore domain. Previous deletion and complementation studies have shown that constructs of the human GlyR and mouse 5-HT_{3A}R lacking M4 do not form pentamers and are not functional (Haeger et al., 2010). These truncated constructs

can be rescued by co-expression of M4 (Haeger et al., 2010). In contrast, ELIC still forms functional pentamers when part of, or the entire, M4 is removed. The ELIC Δ8 structure, with its destabilized lower membrane domain, provides a mechanistic hint on how the absence of M4 could lead, in more fragile receptors, to the loss of receptor integrity. In particular, recent studies have suggested that the activation and desensitization gates of pLGICs are distinct, with the desensitization gate located near the lower half (the intracellular side) of the M2 helices (Gielen and Corringer, 2018). The increased dynamics of the lower half of the pore domain with the Δ8 mutation may directly influence the dynamics of the desensitization gate leading to the fast-desensitizing phenotype.

To further substantiate our understanding of M4 dynamics we conducted MD simulations of ELIC P305A, which produces fast desensitizing channels. In the MD simulations, we observe that M4 changes its conformation and undergoes a straightening at the Pro kink, effectively forming a continuous transmembrane helix rather than two helices separated by the Pro kink in the reference structure. In addition, the simulations indicate that the orientation of M4 is highly dependent on lipid exposure to the M1 and M3 helices. The analysis indicates a continuum of conformational shifts between two principal directions. In the first direction, the conformational change of the M4 helix results in a tilt toward the complementary (−) subunit and amounts to a distance of 5.0–7.5 Å when measured between the Cα atoms of the carboxyterminal residue V316 in both conformations, after 450 ns of simulation (Figure 6.7c). By 450 ns, M4 is continuing to tilt, and this distance will likely increase further as the structure reaches equilibrium. In the second principal direction, the simulations suggest that the M4 helix could tilt away from the pore domain and into the membrane, similar to an uncoupled conformation. These MD simulations are consistent with the observations from the crystal structures presented in this and the subsequent section that the M4 helix is intrinsically flexible and possibly adopts different conformations depending on the lipid environment.

Figure 6.8 Alternative conformation of an unkinked M4 helix forming novel intersubunit interactions

a,b) Cartoon representation of the ELIC structure with the M4 helix in an alternative unkinked conformation (red) compared to the original kinked conformation (blue). In the unkinked conformation the M4 helix is pinched between W220 and W224 and sterically hinders lipid interactions. In this conformation residues of the M4 helix, including F308 and I311, come within close range of residues of the M3 helix (white) of its neighboring subunit, including L278 and F274, respectively. In the kinked M4 conformation these residues do not interact (15–20 Å apart). **c**) VCF of post-M4 ELIC mutants G319C, I320C, T321C and L322C labeled with methanethiosulfonate-rhodamine. Black traces represent cysteamine-induced current responses, red traces represent corresponding changes in fluorescence. Representative traces are shown from five to seven independent experiments for each construct. Panels on the right show normalized current and fluorescence responses as the mean ± s.e.m.

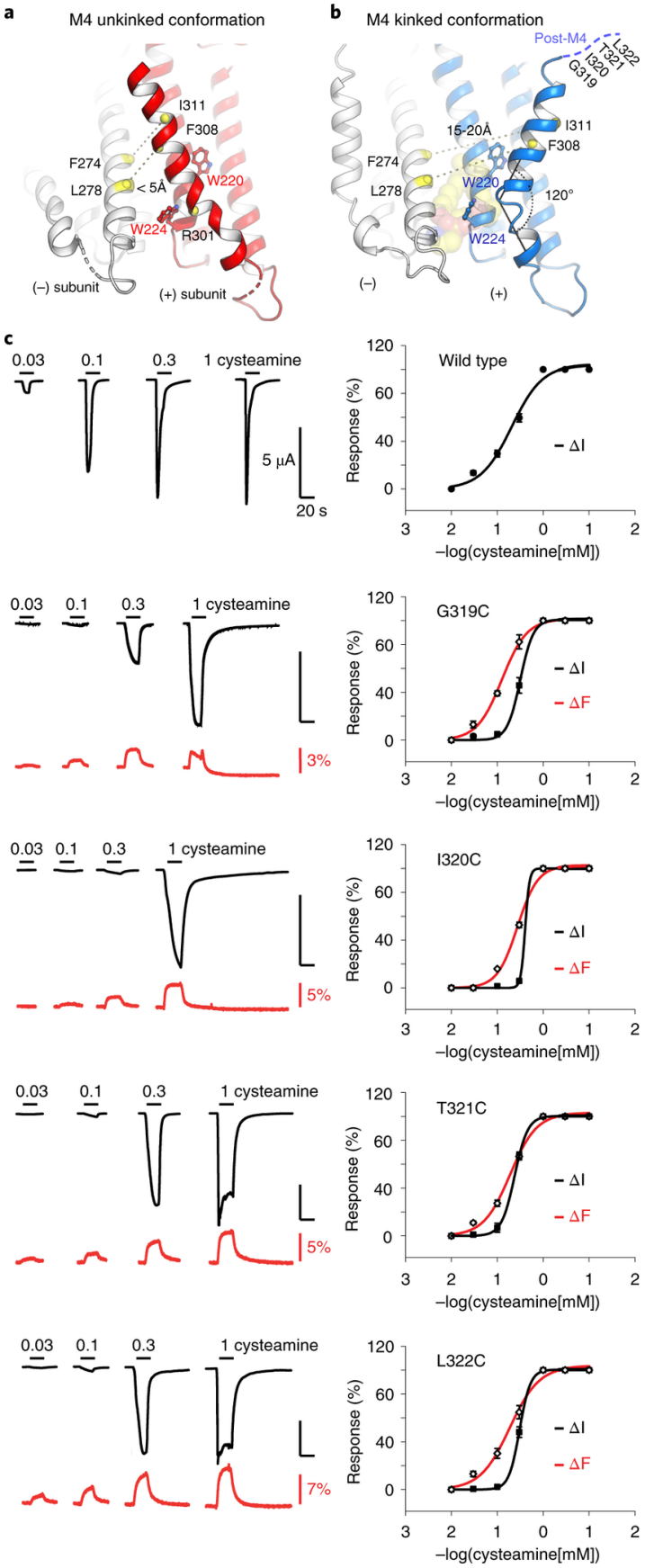
a
M4 unkinked conformation
I311
F308
F274
L278
< 5Å
W220
W224
R301
(–) subunit
(+) subunit
b
M4 kinked conformation
Post-M4
L322
T321
I320
G319
15-20Å
I311
F308
F274
L278
W220
120°
W224
(–)
(+)
c
0.03
0.1
0.3
1 cysteamine
5 µA
20 s
Wild type
Response (%)
– ΔI
–log(cysteamine[mM])
G319C
– ΔF
3%
I320C
5%
T321C
L322C
7%

6.4.6 ELIC structure with an alternate conformation of M4

In over more than a decade of structural studies on ELIC, we have obtained three different datasets in a resolution range of 3.45–3.92 Å that each have several subunits with M4 in an alternate conformation compared to previously published structures of pLGICs. These structures were obtained serendipitously and might be the result of subtle variations in the solubilization and/or relipidation of ELIC before crystallization. Additionally, a detailed survey of the Protein Data Bank (PDB) revealed several ELIC structures solved by other groups and that contain densities indicating occupancy of M4 in this same alternate conformation. Examples are ELIC F16′A (PDB code 2yks) (Zimmermann and Dutzler, 2011) and ELIC F16′L (PDB code 3uq4) (Gonzalez-Gutierrez et al., 2012), suggesting that a 16′ pore mutation might stabilize the alternate M4 conformation in ELIC.

Figure 6.8a shows the 3.45 Å resolution structure of ELIC with pore mutation F16′S, which illustrates this alternate M4 conformation. In this structure, the M4 helix is not kinked post R301 but instead continues along the helical trajectory of the pre-301 residues. Consequently, the M4 helix of one subunit extends over to form inter-subunit interactions with the M3 helix of its neighboring subunit. This amounts to a movement of 19.4 Å when measured between the Cα atoms of I317 in the two conformations. In its new conformation, M4 is pinched between W220 and W224 in M1, which we identified as key components of the lipid-binding site. Consequently, access to the lipid-binding site is sterically hindered. This alternate conformation could represent a mechanism for modulating lipid binding to the ELIC channel, or vice versa. Among the newly formed interactions are residues F304, F308 and I311 on M4 and residues F274, L278, I281 on M3 of the neighboring subunit. In the kinked conformation, these residues are 15–20 Å apart, for example, F308 and L278 or I311 and F274, whereas in the alternate conformation these residues come within less than 4 Å from each other. MD simulations further confirm that the alternate conformation is stable over a time span of 300 ns, with an r.m.s. deviation of 2.8 Å.

To investigate whether this conformational state is sampled in the M4 dynamic landscape, we designed two pairs of cysteine mutations, which are within crosslinking distance in the alternate conformation, but not in the kinked conformation. These double

mutants are L278C/F308C or F274C/I311C engineered in the background of a cysteine-free ELIC. Using mutant protein expressed in *E. coli* and purified in detergent solution we investigated band shifts with SDS–PAGE analysis. Under reducing conditions, we observe that the ELIC band migrates exclusively as monomers with an apparent molecular size around 30 kDa. However, under oxidizing conditions, we identified a characteristic redistribution of bands, which we identified as 2-mer, 3-mer, 4-mer and 5-mer, consistent with the formation of inter-subunit crosslinks as predicted by the ELIC crystal structure with the alternate M4 conformation. Similar observations were made for the F274C/I311C double mutant. This crosslinking does not occur with the cysteine-free ELIC, indicating specific disulfide bond formation between introduced cysteines in L278C/F308C and F274C/I311C. These experiments suggest that, at least under detergent-solubilized conditions, the ELIC M4 helix may transiently adopt a conformation that is similar to the alternate conformation observed in the crystal structure.

Finally, we used VCF to investigate the M4 dynamics in the context of ELIC expressed in a lipid bilayer environment. VCF simultaneously monitors current changes and fluorescence changes, obtained from an environmentally sensitive and thiol-reactive fluorophore attached to single cysteine mutants in the M4 domain. We focused on the post-M4 residues, which are unresolved in the crystal structure, namely G319C, I320C, T321C and L322C, labeled with MTS-rhodamine (Figure 6.8c). In each of these mutants, we observe an upward deflection of the fluorescence signal, which correlates with channel opening induced by increasing concentrations of the agonist cysteamine. These results suggest that the local environment around these residues changes during channel opening and is indicative of a conformational change in the post-M4 domain. Second, we probed residues of M4 buried further in the lipid bilayer with the unnatural fluorescent amino acid ANAP (Chatterjee et al., 2013). We focused on residues around P305, namely F304, P305, L306 and G307. At each of these positions we observe that incorporation of ANAP results in a robust agonist-induced response, but none of these positions reported a fluorescence change. We do observe an acceleration of the desensitization kinetics, in agreement with the mutagenesis data in Figure 6.7b. This does not exclude a possible conformational change of

M4 in a lipid bilayer, but it indicates that the net hydrophobicity of the fluorophore environment is unchanged as the channel pore opens and closes.

Together, these results confirm the conformational dynamics of the M4 domain in ELIC and its sensitivity to lipid binding in this region. We have now obtained an alternate conformational snapshot of M4 as an example of a possible transient state of M4, which most likely regulates lipid interaction and may modulate channel desensitization.

Figure 6.9 Model for lipid modulation of channel desensitization

A conserved architectural feature in ELIC and anion-selective pLGICs is a kinked M4 helix, which interacts with lipids. This M4 helix is conformationally dynamic and based on functional recordings from mutant channels, such as ELIC ΔM4, we establish that perturbations of the M4 Pro kink drastically accelerate receptor desensitization.

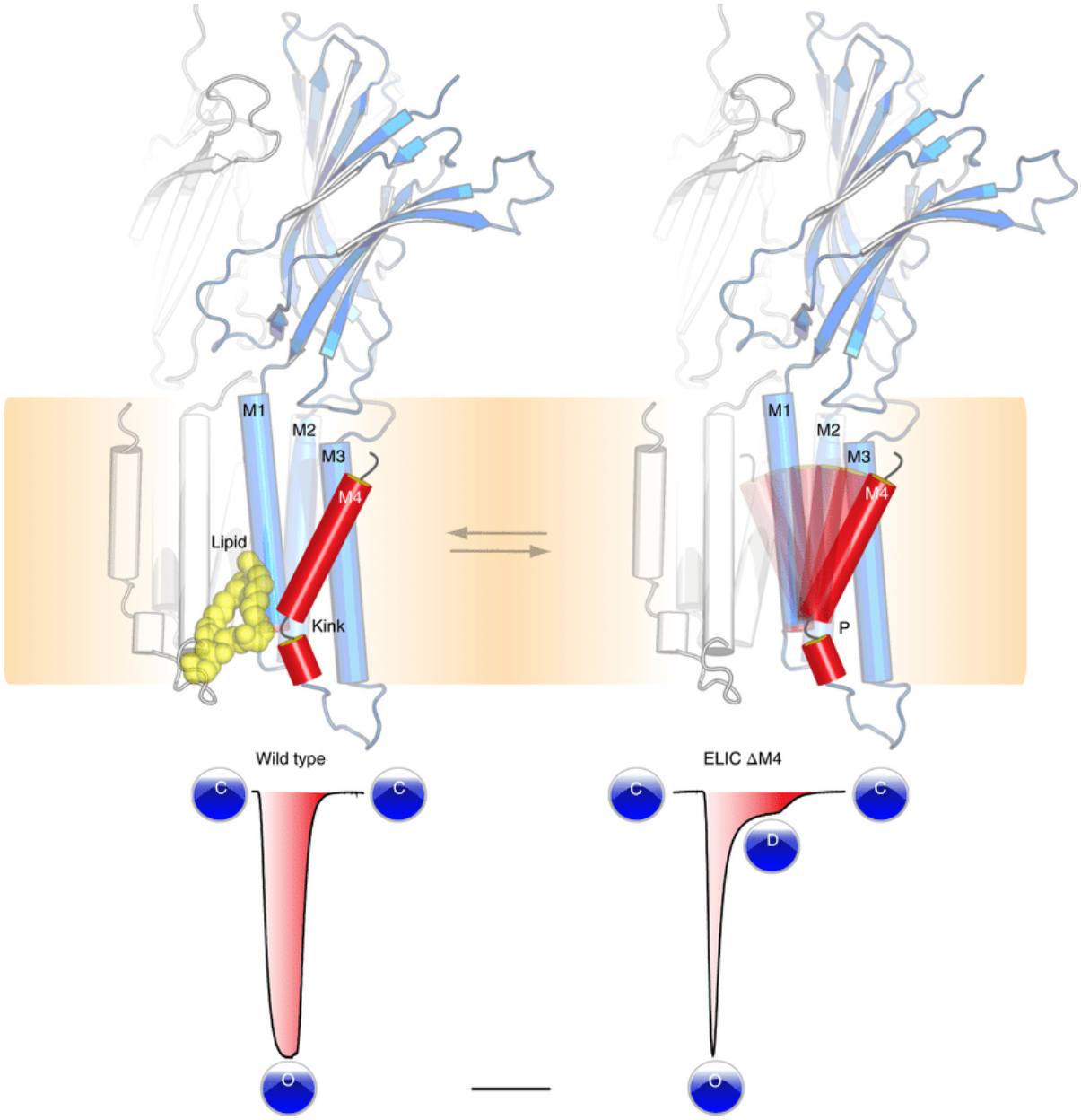
M1
M2
M3
M4
Lipid
Kink
M1
M2
M3
M4
P
Wild type
C
C
O
ELIC ΔM4
C
C
D
O

6.5 Discussion

With this study, we have provided new insights into the conformational dynamics and lipid interactions of the M4 transmembrane domain of a pLGIC (Figure 6.9). Alternate conformations of M4 have so far proved elusive from structural studies. By using ELIC as a model ion channel and applying a set of comprehensive techniques we have revealed an alternate conformational state of the M4 helix. In this alternate state, M4 adopts an unkinked conformation and undergoes a tilting motion to interact with the M3 helix of its neighboring subunit. The entry of the M4 helix into this state precludes interaction with a phospholipid molecule, which we identified near a highly conserved Pro kink in the ELIC M4, also found in eukaryote anion-selective pLGICs. Using mutagenesis studies, we found that perturbations of the conserved Pro residue drastically accelerate receptor desensitization, suggesting that the lipid-binding site allosterically couples to channel gating. The phenomenon of accelerated desensitization in ELIC can be mimicked by altering the lipid environment, adding further evidence to a regulatory role of lipids. Together, these results provide a structural context for understanding how lipids influence channel function. Given the strong conservation of the kinked architectural fold of M4 in anion-selective channels, we suggest that the mechanistic insights derived from this study extend across the anion-selective subfamily of pLGICs. The phospholipid-binding site closely overlaps with known sites for neurosteroids, cholesterol and general anesthetics, thus offering strategies for the design of new therapeutics that can modulate channel function in human disease.

6.6 Supplementary Information

Full supplemental material is available online, only the most relevant information has been included in this document.

6.6.1 Supplementary Materials and Methods

The following methods pertain to experiments performed by our collaborating authors and are included to facilitate understanding of the overall conclusions of the paper. For mutagenesis, electrophysiology and desensitization kinetics analysis methods see Chapter 2.

6.6.1.1. ELIC expression and purification

ELIC expression and purification. ELIC mutants were expressed and purified as previously described for wild-type ELIC (Spurny et al., 2012) (UniProt P0C7B7), but with minor modifications. ELIC cDNA was cloned as a synthetic gene with optimized codon usage (Genscript) into the pET-11a plasmid (Novagen) and expressed as an N-terminal fusion to maltose-binding protein (MBP) and a 3C protease cleavage site for removal of the fusion tag. Site-directed mutants were engineered using a QuikChange strategy and verified by sequencing. The MBP-ELIC fusion protein was expressed in the C43 *E. coli* strain, which was grown to an absorbance A600 ~ 1.8 and induced with 200 μM isopropyl β-D-1-thiogalactopyranoside (IPTG) at 20 °C overnight. The membrane fraction was collected by ultracentrifugation at 125,000g and solubilized with 2% (w/v) anagrade n-undecyl-β-D-maltoside (Anatrace) at 4 °C overnight. The cleared supernatant was batch purified by affinity chromatography on amylose resin (New England Biolabs). Column-bound ELIC was cleaved off by 3CV protease in the presence of 1 mM EDTA + 1 mM DTT at 4 °C overnight and further purified on a Superdex 200 10/300 GL (GE Healthcare) column equilibrated wdith buffer containing 10 mM Na-phosphate (pH 8.0), 150 mM NaCl, and 0.15% n-undecyl-β--maltoside (UDM). Concentrated protein (10 mg ml−1) was supplemented with 0.5 mg ml−1 *E. coli* lipids (Avanti Polar Lipids). Cysteine pore mutants of ELIC were engineered in the background of a previously described cysteine-free channel (Nys et al., 2016), which was obtained by substituting two non-conserved cysteines in the M4 domain

(C300S/C313S) and functionally behaves as wild-type ELIC. For nanobody production and selection a series of ELIC pore mutants were produced, including 6′C (T237C), 7′C (L238C) and 8′C (M239C) as candidates to identify previously unidentified conformational states of ELIC. For the structural characterization of M4 domain mutants, we produced ELIC Δ8 (deletion L_{315}VIRGITL_{322}), ELIC ΔM4 (deletion entire M4 helix starting D294 until end) and P305A, which were identified as ELIC variants with fast desensitization kinetics using TEVC recordings (see below). For the crosslinking experiments, we engineered two constructs in the background of cysteine-free ELIC, namely L278C/F308C and F274C/I311C.

6.6.1.2. Nanobody selection, expression and purification

A llama was immunized with 2 mg, in total, of purified wild-type ELIC over a period of 6 weeks using a previously established protocol (Pardon et al., 2014). Briefly, from the anticoagulated blood of the immunized llama, lymphocytes were used to prepare cDNA. This cDNA served as a template to amplify the open reading frames coding for the variable domains of the heavy-chain only antibodies, also called nanobodies. The PCR fragments were ligated into the pMESy4 phage display vector and transformed in *E. coli* TG1 cells. A nanobody library of 1.1×10^8 transformants was obtained. For the discovery of ELIC specific nanobodies, we selected four different targets, all fused to the MBP: wild-type ELIC-MBP, ELIC 6′C-MBP, ELIC 7′C-MBP and ELIC 8′C-MBP.

Phage particles displaying the nanobody repertoire of the library were added to each of the ELIC-MBP fusion proteins trapped on amylose resin (New England Biolabs). Selections were done in 10 mM Na-phosphate (pH 8.0), 150 mM NaCl, 0.15% UDM, 0.05% BSA in the presence of 10 mM GABA and 10 mM DTT. Either after 15 min or 2 h of incubation aspecific phages were washed off. Specific phages were eluted by incubating the differently coated amylose resin with 100 µl of trypsin (250 µg ml−1) for 30 min. Although a high background was seen on the MBP-only-coated amylose resin, 184 clones in total were sent for sequence analysis. Sequence alignment revealed eight nanobody families that were enriched. All clones were produced and purified as previously described (Pardon et al., 2014).

A series of 16 nanobodies were individually expressed in the periplasm of *E. coli* strain WK6, which was grown in TB media supplemented with 1 mM carbenicillin, 0.1% glucose and 2 mM $MgCl_2$ to an absorbance A600 ~ 0.7 at 37 °C. The culture was induced with 1 mM IPTG and incubated overnight at 28 °C. Cells were harvested by centrifugation, resuspended in ice-cold TES buffer (200 mM TRIS, pH 8.0; 0.5 mM EDTA and 500 mM sucrose) and washed four times in diluted TES buffer. Next, this fraction was centrifuged at 10,000g to remove cell debris. The supernatant was applied on nickel sepharose resin (GE Healthcare) and incubated for 1 h at room temperature. The column was then consecutively washed with phosphate buffer 1 (50 mM Na-phosphate, pH 7.0 and 1 M NaCl) and phosphate buffer 2 (50 mM Na-phosphate, pH 6.0 and 1 M NaCl). Nanobody was eluted from the column with 50 mM Na-acetate (pH 4.5), 1 M NaCl and neutralized by 1 M TRIS (pH 7.5). The protein was concentrated to less than 1 ml on a 3 kDa cutoff Vivaspin concentrating column (Sartorius) and further purified on a Superdex 75 10/300 GL column (GE Healthcare) equilibrated with 10 mM Na-phosphate (pH 8.0) and 150 mM NaCl. Peak fractions corresponding to nanobody were pooled and spin-concentrated to ~50 mg ml−1. The formation of stable ELIC + nanobody complexes in solution was evaluated by size exclusion chromatography on a Superdex 200 10/300 GL (GE Healthcare) column based on a shift of the peak fraction containing pentameric ELIC and evaluation of co-eluting protein bands on a Coomassie-stained SDS–PA gel.

6.6.1.3. Protein Crystallization

A large combinatorial crystallization screen was set up using ELIC 6′C, 7′C or 8′C in combination with the selection of 16 nanobodies. ELIC mutant and nanobody were mixed in a molar ratio 1:1.2 calculated as monomers and incubated at room temperature 2 h before setting up crystallization trials at 20 °C by vapor diffusion of sitting drops. Automated dispensing was carried out using a nanoliter Mosquito crystallization robot and MRC plates (Molecular Dimensions). Crystals for ELIC 7′C + Nb72 grew under conditions containing 100 mM MES (pH 6.5) and 30% PEG400. Crystals for ELIC Δ8 + Nb72 grew under conditions containing 300 mM ammonium formate, 50 mM TRIS pH 9.0 and 33% PEG monomethylether 550. Cryo-protection was achieved by adding 10% glycerol to the mother liquor. Crystals for ELIC F16′S with the alternate M4 straight conformation grew under

conditions containing 200 mM ammonium sulfate, 50 mM ADA (N-(2-acetamido)iminodiacetic acid) (pH 6.5), and 9–12% (v/v) PEG4000. Cryo-protection was achieved by adding 30% (v/v) glycerol to the mother liquor. Crystals were cryo-cooled by immersion in liquid nitrogen and transported to synchrotron radiation sources in a dry shipper.

6.6.1.4. X-ray crystallography

The structure of ELIC 7′C in complex with the Nb72 was solved with X-ray diffraction data at a resolution of 2.50 Å, which were collected at the X06A beamline of the Swiss Light Source using 0.91958 Å wavelength light. Diffraction data were integrated with XDS (Kabsch, 2010) and scaled in Aimless as part of the CCP4 suite (Winn et al., 2011). For this and subsequent datasets, the high-resolution limit was set using a CC1/2 -value of 30% as a cutoff criterium. Initial phases were obtained using molecular replacement with Phaser (Winn et al., 2011) using the ELIC pentamer coordinates of PDB deposition 2yoe as one ensemble and the nanobody coordinates of PDB deposition 2p0g as the second ensemble. All nonprotein atoms were removed from the coordinates before running the search procedure. As previously published (Spurny et al., 2012), all our ELIC structures contain a Gly residue at position 164, which was missing in the initially published ELIC structure with PDB deposition code 2vl0, and this changes the residue numbering +1 from position 164 onward. Additionally, we previously also indicated a change in the sequence register of the β8 strand compared to 2vl0 and these observations are now confirmed in the higher resolution structure. The ELIC + Nb72 structure was rebuilt and refined through iterative cycles of manual building in Coot (Emsley et al., 2010) and automated refinement in Phenix (Adams et al., 2010). The final refinement steps were done in Buster (Smart et al., 2012) using basic TLS (Translation/Libration/Screw) and automated NCS (non-crystallographic symmetry) restraints. The electron density of the lipid-bound to ELIC subunit A was improved after extending the protein mask by 6 Å. Mask extension was removed for the final refinement steps. The density was interpreted as phosphatidylethanolamine since this is the major lipid component in the *E. coli* lipid extract added before crystallization. The density was sufficiently clear to build a 12-carbon and 9-carbon lipid tail, respectively. The head group in this subunit benefits from a crystal interaction between the phosphate group and K49 in a

neighboring pentamer. The lipid densities in other subunits are present but less clear than subunit A. Structure validation was done in MolProbity (Chen et al., 2010b). The MolProbity score of this structure is 1.09 and is in the 100th percentile for this resolution range. Ramachandran statistics indicate 96.04% of residues are in the favored region and 0.05% are outliers. All composite omit maps reported in this study were calculated in Phenix (Adams et al., 2010) using Cartesian simulated annealing at start and final temperatures of 5,000 and 300 K, respectively.

The structure of ELIC Δ8 + Nb72 was solved with X-ray diffraction data at a resolution of 2.78 Å, which were collected at the ID30B beamline of the European Synchrotron Radiation Facility using 0.9754 Å wavelength light. Diffraction data were integrated with XDS (Kabsch, 2010) and scaled in Aimless (Winn et al., 2011). Initial phases were determined using molecular replacement in Molrep (Winn et al., 2011) and the coordinates of ELIC + Nb72 from which the non-protein atoms, as well as the last eight carboxyterminal residues in ELIC, were removed. The resulting electron density map revealed missing density not only for the last eight amino acids but the entire M4 helix and M3–M4 linker, suggesting this domain is flexible in the Δ8 structure. Consequently, the ELIC Δ8 structure was truncated at the end of M3 (H285) and further improved with iterative cycles of manual rebuilding in Coot (Emsley et al., 2010) and refinement in Refmac (Winn et al., 2011). The final refinement steps were done in Buster (Smart et al., 2012) using basic TLS and automated NCS restraints. The MolProbity score of this structure is 1.38 and is in the 100th percentile for this resolution range. Ramachandran statistics indicate 97.03% of residues are in the favored region and 0.4% are outliers.

Over years of structural studies with ELIC, thousands of crystals were screened, and we obtained three datasets in which M4 adopts the alternate straight conformation, which we assume has occurred as a result of unexpected variations in the solubilization, lipidation or crystallization conditions for these crystals. The highest resolution set was for an ELIC F16′S mutant at 3.45 Å, which was collected at the X06DA beamline of the Swiss Light Source using 1.000 Å wavelength light. The same alternate M4 conformation could be observed in two other datasets for wild-type ELIC at 3.92 Å and 3.87 Å, so we conclude that the alternate M4 can occur independently of the F16′S mutation. Diffraction data were integrated with

XDS (Kabsch, 2010) and scaled in Scala (Winn et al., 2011). The initial phases were obtained using molecular replacement with Phaser using the coordinates of PDB deposition 4twd from which the nonprotein atoms were removed. The structure was improved with iterative cycles of manual rebuilding in Coot (Emsley et al., 2010) and refinement in Refmac (Winn et al., 2011). The MolProbity score of this structure is 1.82 and is in the 100th percentile for this resolution range. Ramachandran statistics indicate 95.56% of residues are in the favored region and 0.03% are outliers. All figures were prepared using PyMOL (Schrödinger).

6.6.1.5. Lipid vesicle recordings

The ELIC channel was reconstituted at a 1:200 protein to lipid ratio (weight to weight) in liposomes of different lipid compositions, such as soy polar extract (as a control condition) or soy polar extract supplemented with 25% Cholesterol, 50% POPC (1-palmitoyl-2-oleoyl-glycero-3-phosphocholine):25% POPG (1-palmitoyl-2-oleoyl-sn-glycero-3-phospho-(1′-rac-glycerol)):25% POPE (1-palmitoyl-2-oleoyl-sn-glycero-3-phosphoethanolamine) or 75 % POPC:25% POPG, following a published protocol (Cuello et al., 2017). The desired phospholipid composition dissolved in chloroform (25 mg ml−1) was dried for 4 h in a roto-evaporator. The dried phospholipid film was resuspended in resuspension buffer (5 mM MOPS pH 7.0, 200 mM KCl) and sonicated in a bath-sonicator until the liposome suspension was translucent. The ELIC channel freshly eluted from a size exclusion chromatography column, Enrich SEC 650 (Bio-Rad), equilibrated in (buffer 50 mM Tris-Cl, pH 8.0, 150 mM KCl, 1 mM n-dodecyl-β-D-maltoside) was mixed with the liposome suspension for 30 min at room temperature. The ELIC containing liposomes suspension was incubated for 1 h with 30 mg of Bio-Beads SM-2 (Bio-Rad) at room temperature. Followed by two additional cycles of 30 mg of Bio-Beads additions + 1-h incubation. Finally, the ELIC containing proteoliposomes suspension was incubated at 4 °C overnight with an extra 100 mg of Bio-Beads. Next day, the ELIC containing proteoliposomes were harvested by pelleting them at 150,000g for 2 h. The resultant pellet was resuspended by pipetting in precisely 40 µl of resuspension buffer until the solution was homogeneous. Normally, three drops (10 µl each) were laid over a glass microscope slide and dehydrated, in the dark at 4 °C overnight. The next day, the ELIC containing

proteoliposomes were rehydrated by adding 20 µl of resuspension buffer and incubated in the dark at 4 °C for 24 h, which normally produced giant liposomes, before performing patch clamp experiments. ELIC electrophysiological recordings in different phospholipid composition were performed in symmetrical 5 mM MOPS at pH 7.0 in the presence of 200 mM KCl. ELIC macroscopic currents were elicited by the application of 30 mM GABA with a BioLogic fast perfusion system RSC-200 and recorded from several independent experiments (n = 4 to 26 repeats) with a patch clamp amplifier Axopatch 200 B. ELIC currents were sampled at 40 kHz with an analog filter set to 10 kHz. Borosilicate patch pipettes, after fire-polishing, displayed a resistance of 2.0 MΩ. Patch pipettes were filled with 200 mM KCl, 5 mM MOPS buffer at pH 7.0 and 5 mM MgSO4. The time constant for desensitization (τ) of the ELIC channel reconstituted in different lipid compositions after an application of 30 mM GABA was calculated by fitting a single exponential curve to the experimental data. The reported values are the mean ± s.e.m. of 4 to 26 independent experiments.

6.6.1.6. Cysteine crosslinking

For cysteine crosslinking of ELIC, we designed two cysteine pair mutants, L278C/F308C and F274C/I311C. These cysteine mutants were engineered in the background of cysteine-free ELIC and cloned into the pET-11a plasmid with a native ELIC signal sequence, an aminoterminal hexahistidine tag and a 3CV protease cleavage site followed by the mature ELIC sequence. The protein was expressed and purified as described above, but here membranes were solubilized in buffer containing 2% (w/v) anagrade n-dodecyl-β-D-maltoside (Anatrace) at 4 °C overnight. The cleared supernatant was loaded on a 1 ml HisTrap Fast Flow column (GE Healthcare) with buffer containing 50 mM Na-phosphate (pH 8.0), 150 mM NaCl and 0.05% n-dodecyl-β-D-maltoside plus 40 mM imidazole. The column was washed until the UV absorbance at 280 nm reached a baseline value and then a second wash step with buffer plus 80 mM imidazole was used. The protein was eluted using buffer plus 250 mM imidazole. The peak fraction was spin-concentrated to a volume <1 ml and loaded on a Superdex 200 10/300 GL (GE Healthcare) column equilibrated with buffer containing 10 mM Na-phosphate (pH 8.0), 150 mM NaCl, and 0.05% n-dodecyl-β-D-maltoside. The peak fractions corresponding to pentameric ELIC were pooled and spin-

concentrated to a concentration of 1–2 mg ml−1. Each cysteine mutant was reduced in the presence of β-mercaptoethanol or DTT and crosslinking was initiated by addition of a 1:2 molar ratio of Cu2+ and 1,10-phenanthroline at a final concentration of 100 μM. Reactions were quenched at given time points with 100 mM N-ethyl maleimide and sample buffer without reducing agent was added. Samples were then loaded onto Mini-PROTEAN TGX precast gradient (4–15%) gels for SDS–polyacrylamide gel electrophoresis analysis.

6.6.1.7. VCF using MTS-rhodamine or ANAP

Adult female *Xenopus laevis* frogs (Xenopus Express) were anesthetized (1.3 mg ml−1 MS-222), and oocytes were surgically removed via a small incision to the abdomen. Oocytes were then defolliculated with 1.5 mg ml−1 collagenase (Sigma) for 2 h. VCF with rhodamine-labeled ELIC was used to characterize post-M4 residues in ELIC G319C, I320C, T321C and L322C engineered in the background of a cysteine-free channel. cDNA encoding ELIC was inserted into the pGEM-HE expression vector and mRNA was transcribed in-vitro using the mMESSAGE mMACHINE T7 transcription kit (Ambion) as previously described. Mutants were constructed using a QuikChange strategy (Stratagene) and confirmed by sequencing. Mature stage V or VI oocytes were isolated and rinsed with calcium-free OR-2 solution containing 82.5 mM NaCl, 2 mM KCl, 1 mM $MgCl_2$, 5 mM HEPES (pH 7.4). Oocytes were injected with 10 ng ELIC cRNA using a Nanoliter 2000 microinjector (WPI Inc.) and incubated at 16 °C in ND-96 storage solution, containing 96 mM NaCl, 2 mM KCl, 1 mM $MgCl_2$, 1.8 mM $CaCl_2$, 5 mM HEPES, 50 μg ml^{-1} gentamicin, 2.5 mM sodium pyruvate, and 0.5 mM theophylline (pH 7.4). Fluorescent labeling of oocytes was conducted 3–5 days after injection by a 1 min incubation in a solution containing 10 mM methanethiosulfonate-rhodamine (MTSR, Toronto Research Chemicals) in ND-96 solution (96 mM NaCl, 2 mM KCl, 1.8 mM $CaCl_2$, 1 mM $MgCl_2$ and 5 mM HEPES, pH 7.5). The oocytes were then washed three times in ND-96 and stored at 18°C in the dark until the start of recordings. A Lambda LS 175 W xenon arc lamp was used as a light source for an inverted Nikon Eclipse TE300 microscope (Nikon Instruments), equipped with a high-Q TRITC filter set (Chroma Technology). A Lambda 10-2 unit (Sutter

Instruments) was used for selection of excitation and emission wavelengths. Light was focused onto the dark pole of the oocyte using a Plan Fluor ×40 objective lens (Nikon Instruments), and fluorescence detection was achieved with an H7360–03 photomultiplier (Hamamatsu Photonics) coupled to a PMT400R photomultiplier subsystem (Ionoptix).

ANAP-labeled ELIC was produced with the pANAP plasmid from Addgene (plasmid No. 48696). ANAP was a kind gift from Dr.S. Pless (University of Copenhagen). Amber stop-codon (TAG) mutants, ELIC $F304_{TAG}$, $P305_{TAG}$, $L306_{TAG}$ and $G307_{TAG}$, were constructed using QuikChange mutagenesis. One day after oocyte isolation, 2 mM ANAP and 10–20 ng of ELIC mRNA were injected separately into the pANAP-expressed oocytes. Recordings were obtained 2–3d after injection. ANAP fluorescence was detected using an inverted microscope (Ti-S, Nikon Instruments) equipped with a DAPI filter set (49000, Chroma Technology) and a CFI Fluor 40X water immersion objective (N.A. 0.80, MRF07420, Nikon Instruments). A Lambda LS 175 W xenon arc lamp served as a light source and was coupled to the microscope via a liquid light guide (Sutter Instruments). Fluorescence was detected using an H7360-03 photomultiplier (Hamamatsu Photonics) coupled to a PMT400R photomultiplier subsystem (Ionoptix). In both MTS-rhodamine and ANAP experiments, oocytes were placed securely in the bath and were continually perfused with ND-96 solution. Agonists were dissolved in the same solution and were applied to the oocytes via a gravity-fed perfusion system. Currents were recorded via two-electrode voltage clamp using 0.2–2 MΩ resistance glass pipettes filled with 3M KCl. Oocytes were voltage-clamped at −40 mV, and currents were recorded using a Gene Clamp 500B amplifier (Molecular Devices). ΔI (change in current) and ΔF (change in fluorescence) signals were digitized at 2 kHz via a Digidata 1322A interface and pCLAMP 9.2 software (Molecular Devices).

6.6.1.8. MD Simulations

Simulation systems were prepared by embedding the ELIC 7′C pore mutant with bound lipid (mapped to 1,2-dilauroyl-sn-glycero-3-phosphoethanolamine, DLPE) in a lipid bilayer composed of 1-palmitoyl-2-oleoyl-sn-glycero-3-phosphocholine (POPC).

Nanobodies and detergent were removed from the simulated system, and the ELIC-DLPE complex was embedded in the membrane, solvated and ionized with 0.15 M of neutralizing ions using CHARMM-GUI Membrane builder (Jo et al., 2009). In addition to the ELIC 7′C pore mutant, a second system was run with an additional P305A substitution in all five M4 helices, while a third terminated all M4 helices at residue 314 to form the Δ8 mutant. Both in silico modifications were also made using CHARMM-GUI Membrane builder. All simulated systems contained about 250 phospholipid molecules and about 160,000 total atoms.

All simulations used the NAMD2.12 MD package (Phillips et al., 2005) and the CHARMM36 Forcefield (Brooks et al., 2009; Klauda et al., 2010) for proteins, phospholipids, ions and water. A Langevin thermostat and barostat maintained a constant temperature of 310 K and a constant pressure of 1 atm, respectively. A cutoff of 1.2 nm was used for nonbonded interactions, with a switching function starting at 1.0 nm. The smooth particle mesh Ewald method with a grid spacing of 1 Å handled long-range electrostatics. Periodic boundary conditions were employed in a rectilinear box. All bonds to the hydrogen atoms were constrained using the SHAKE/RATTLE algorithm, which permitted a high-frequency time step of 2 fs within a multiple time-step rRESPA method. After 10,000 steps of energy minimization, the simulations followed the default equilibration protocol established in the files output by CHARMM-GUI, followed by 450 ns of production simulation. An r.m.s. displacement analysis was conducted by aligning the structure in each frame to minimize the r.m.s. displacement for all M1, M2 and M3 helices, and then calculating Cα r.m.s. displacement for each M4 helix separately.

Chapter 7. Conclusion

7.1 Thesis highlights

The research presented in this thesis focused primarily on elucidating the complex relationship between protein-protein and lipid-protein interactions within a functional membrane-embedded domain. Specifically, I examined the role of the transmembrane α-helix, M4, as a lipid-sensor in two prokaryotic pLGIC, ELIC and GLIC, and explored how changes to the M4-M1/M3 interface impact both pLGIC function and lipid sensing. Understanding how the structure and chemical composition of a transmembrane protein can influence overall protein activity may provide a path to the development of targeted allosteric modulators specifically designed for the treatment of pLGIC-linked disorders and diseases. Notably, the capacity of the M4 helix to influence a broad range of pLGIC functions suggests that it could be targeted by therapeutics to treat dysfunction resulting from alterations in desensitization rates, the coupling of agonist binding to channel gating, channel stability, lipid-dependent uncoupling, etc. Over the course of the work presented here I developed and refined a potential model for how lipid binding modulates ELIC channel function.

In Chapter 3, I investigated the role of individual domains in both agonist-induced channel gating and thermal stability by creating ECD/TMD swapped chimeras of GLIC and ELIC. A notable feature in GLIC is the complex network of aromatic interactions at the M4 region - M1/M3 interface, which in another pLGIC has been shown to be important in subunit assembly and function (Haeger et al., 2010). In analyzing the functional properties of the two chimeras, I confirmed that unlike ELIC, the GLIC TMD plays a role in agonist (proton) sensing (Rienzo et al., 2014; Wang et al., 2012). My findings suggested a divergence in evolution between the two channels, with GLIC possessing a way to modulate gating activity from *within* the gating domain. I further showed that aromatic residues in the TMD are the driving factor determining the different thermal stabilities and lipid sensitivities of the two pLGICs (Carswell et al., 2015a; Labriola et al., 2013). This work also constituted one of the early strides at validating the two prokaryotic pLGICs as possible models for understanding vertebrate nAChRs. It provided preliminary evidence supporting shared roles

for the functional domains (ECD and TMD) across the pLGIC family, but also suggested that there is less structural complementarity between the ECD of GLIC and the TMD of ELIC, than between the same two domains in other pLGICs.

In chapter 4, I built on the chimera results, particularly the observations that the TMD of each pLGIC drives its thermal stability, to probe in more detail the role of M4 in GLIC and ELIC in channel function. Because of the membrane-embedded nature of the TMD, it follows that lipid-protein interactions likely play a role in stability as well. As the M4 helix forms most of the lipid-exposed surface of the TMD, I sought to test how changes to the M4 helix affect interactions between M4 and M1/M3 to alter channel function. I did this through both Ala-scanning mutagenesis and C-terminal deletions, and found that M4 in GLIC and ELIC play different roles in channel maturation and function. Specifically, the M4 C-terminus plays an essential role in both maturation and function in GLIC, whereas the role of the M4 C-terminus in ELIC is less defined. The findings further highlighted the important and unique roles of aromatic residues in the TMDs of each channel.

In Chapter 5, I directly tested the hypothesis that aromatic residues are key drivers of M4-M1/M3 interactions. To do this, I performed aromatic-to-Ala or aliphatic-to-aromatic insertions in GLIC and ELIC, respectively. In essence, I made the ELIC M4-M1/M3 interface more GLIC-like, and the GLIC M4-M1/M3 interface more ELIC-like. My findings confirmed that in both ELIC and GLIC, enhanced M4-M1/M3 interactions promote channel function. Furthermore, to test how aromatic residues at the M4-M1/M3 interface impact lipid sensing, I explored how the same Ala substitution and aromatic insertions impact the ability of a lipid-facing tryptophan substitution, which in the nAChR causes a gain of function, to potentiate ELIC and GLIC channel function. While the precise location of this tryptophan substitution has since been revised, my findings again supported the hypotheses that enhanced M4-M1/M3 interactions promote channel function and reduce lipid sensitivity, while weaker interactions reduced channel function and increase lipid-sensitivity.

Finally, the work presented in Chapter 6 backtracks to an early observation from the Chapter 4 Ala-scan where I had identified an interesting result with the mutation of the P305 residue. This highly conserved proline is found across the majority of anion-selective

pLGICs and naturally creates a kink in the M4 helix. When mutated to alanine in ELIC, it leads to a rapidly desensitizing phenotype. In a combined approach, we found that the proline kink likely gives access to a lipid binding pocket, and that through dynamic M4 straightening movements, the pocket can be occluded to prevent lipid access, which significantly affects desensitization. Likewise, M4 deletions or other disruptions of the lipid-binding site accelerate desensitization in ELIC, suggesting that lipid interactions allosterically shape the agonist response.

7.2 Significance and future directions

It was something of a surprise, considering ELIC's often "free-spirited" responses to mutations, that we were able to glean so much insight into the mechanisms of lipid sensing using ELIC. It was also surprising to find that despite unique functional elements, ELIC can serve as a model for the more complex eukaryotic pLGICs. In fact, the very nature of ELIC's ability to adapt to severe mutations without losing function is what makes it such a strong and unique model. For instance, the alanine substitution of the M4 kink-inducing proline in GLIC results in a non-functional channel and, we believe, an experimental dead-end. In contrast, we were stunned to find that the equivalent M4 proline to alanine substitution in ELIC led to a fast-desensitizing phenotype similar to the rapid desensitizing phenotype of the wild type neuronal (α7) nAChR. Likewise, the fact that we were able to remove the entire ELIC M4 and retain channel function was not only unexpected but also served to highlight the fact that ELIC is a flexible tool that can be stressed far beyond what other more "stable" channels can tolerate, allowing us access to unprecedented mechanistic insight.

As a further testament to ELIC's flexibility of function, I was able to enhance ELIC function through the addition of aromatic residues at the M4-M1/M3 interface. Interestingly. the importance of aromatic residues continues to be emphasized beyond our own findings. Recently, an X-ray structure of the human α7 nAChR has been published (Noviello et al., 2021). Although we originally believed that the α7 receptor lacked interacting M4-M1/M3 aromatics, this new structure provides us with an up-to-date view of the channel in which there are not only multiple interacting aromatic pairs, but also a distinct C-terminus that is proposed to determine the functional state of the channel via an aromatic-driven latching

mechanism with the ECD, an interaction reminiscent of the one proposed in my papers above. This is an interesting example of functional knowledge, namely that aromatics drive M4 interactions with M1/M3, preceding structures, but allowing greater insight. In this case, once the structure is obtained, with the functional knowledge in hand, the novel mechanism is easily seen and understood. Indeed, in light of this updated and corrected structure, avenues which we had considered closed could potentially be re-opened and re-attempted. For instance, when I noted the α7-like activity of the ELIC P305A mutant, I attempted to insert prolines into the α7 M4 in an attempt to generate a slow-desensitizing α7 mutant, however none of these channels were functional (unpublished data). Now however, equipped with the correctly-aligned α7 structure, I know that these insertion sites were not located at equivalent positions in the α7 M4 helix as in the ELIC M4. Although we assumed that the proline was simply too disruptive to a highly sensitive neuronal channel, it is possible that it will be possible to generate a slow-desensitizing α7-proline mutant.

The findings described in this thesis have shed important new light on both the role of the TMD in pLGIC function and the mechanisms underlying pLGIC lipid sensing. The model of ELIC lipid-sensing presented in Chapter 6 represents the most plausible, detailed model yet of how lipids, in this case a bound lipid, influence the function of a pLGIC. Despite the extensive evidence, however, this model still requires rigorous testing. Specifically, a direct correlation between lipid binding to the intracellular leaflet site and reduced M4 dynamics leading to slower rates of desensitization remains to be firmly established. Interestingly, and perhaps reinforcing the strength of our conclusions, a recent paper looking at a cryo-EM structure of ELIC likewise shows a lipid bound in the pocket formed by the M4 proline (Kumar et al., 2021). In this case the bound lipid was identified as phosphatidylglycerol, rather than the PE molecule seen in our crystal structure. This may support the theory that the occupancy of the lipid site is not a question of binding specificity, but rather that lipids may enter and exit the site according to a dynamic equilibrium, and indeed, that different lipids/polar head groups binding to the site with differing on/off rates may contribute towards the lipid-dependent desensitization presented in Chapter 6. However, it is also worth noting that the bound PG molecule may simply reflect the bilayer composition used in the experiment. Also of interest was the observed impact of cardiolipin on ELIC function.

Essentially, the authors found that cardiolipin also bound in an M4-adjacent location, though in the extracellular leaflet. They found that when cardiolipin is added to inactivating POPC membranes, it could rescue ELIC function, which is largely lost in POPC. It is worth noting however that this rescue effect is only seen in bilayers that lack PE, PG and other anionic lipids. One interpretation is that cardiolipin exerts its effect by binding to the proline pocket, rather than suggesting a unique role for cardiolipin in ELIC function. There may be a low affinity occupancy of the proline pocket by cardiolipin in the absence of the more favoured anionic lipids.

Further insight could be obtained by generating ELIC mutants that block lipid binding, such as P305A or other mutations, and then testing the ability of different membrane lipid compositions to influence the rates of desensitization. For example, it would be interesting to characterize the P305A mutant in reconstituted azolectin membranes both with or without PE/PG. If the addition of PE/PG to the membranes still slows the rates of desensitization of the P305A mutant, this would argue against our lipid binding hypothesis. One could also combine P305A with the three aromatic insertions on M3 and the M4 C terminus to test whether the enhanced interactions between M3 and M4 reduce M4 dynamics and thus the impact of P305A. Again, it would be interesting to characterize the rates of desensitization of these mutations in azolectin membranes either with or without PE/PG. Finally, although we could not obtain crystal structure of ELIC P305A, advancements in cryo-EM now allow structures of ELIC to be solved in lipid nanodiscs. It would be interesting to solve structures of ELIC P305A in nanodiscs composed of both azolectin and asolectin plus PE/PG.

Another intriguing avenue to investigate is that of the TMD phospholipid-binding site guarded by a kinked M4. With the M4 kink conserved across nearly all anion-selective pLGIC families, this suggests a conserved modulatory site, though it may serve different roles in different pLGICs due to differing chemical interactions at the M4-M1/M3 interface. This site closely overlaps with known binding sites for neurosteroids, cholesterol and general anesthetics, thus offering strategies for the design of new therapeutics that modulate channel function in human disease. It would be interesting to examine in more detail the roles of the Pro-induced kink in mammalian pLGIC function, as well as its role in lipid binding to anion-selective pLGICs.

While my studies with ELIC and GLIC have provided the first glimpses into the mechanisms by which lipids influence pLGIC function, with new pLGIC structures arriving rapidly and providing more and more insight into the modes of lipid binding, there is clearly much more work to be done to fully understand the mechanisms by which lipids influence pLGIC function, particularly in a biological context.

Chapter 8. Appendix

8.1 Review Article 1

Hénault, C.M., Sun, J., Therien, J.P.D., DaCosta, C.J.B., Carswell, C.L., Labriola, J.M., Juranka, P.F., and Baenziger, J.E. (2015). The role of the M4 lipid-sensor in the folding, trafficking, and allosteric modulation of nicotinic acetylcholine receptors. Neuropharmacology *96*, 157–168.

http://dx.doi.org/10.1016/j.neuropharm.2014.11.011

8.1.1 Preface

This manuscript is the first of two review articles presented in this thesis. It was published in the journal Neuropharmacology in 2015 as part of the Special Issue entitled 'The Nicotinic Acetylcholine Receptor: From Molecular Biology to Cognition'.

I collaborated with my supervisor and Dr Corrie DaCosta, with particular contributions to the introduction and sections 8.1.6.4, 8.1.6.6, 8.1.6.7, and 8.1.7. I also edited the full document and made figure 4, with contributions to figs 1, 2 and 5.

8.1.2 Graphical Abstract

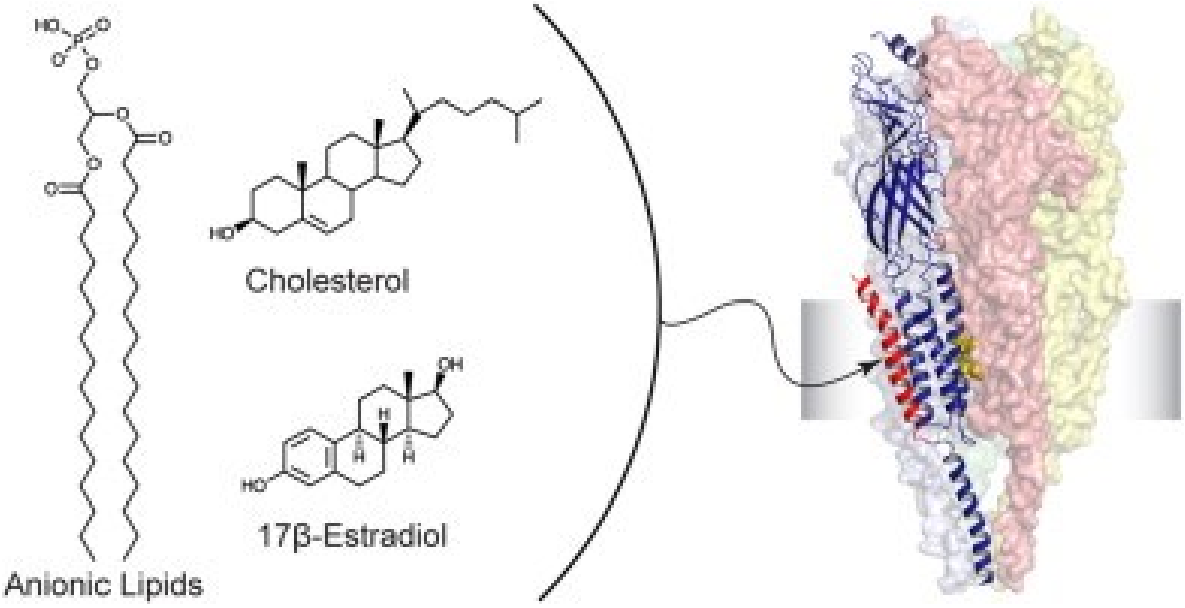

8.1.3 Abstract

With the availability of high-resolution structural data, increasing attention has focused on the mechanisms by which drugs and endogenous compounds allosterically modulate nicotinic acetylcholine receptor (nAChR) function. Lipids are potent modulators of the nAChR from *Torpedo*. Membrane lipids influence nAChR function by both conformational selection and kinetic mechanisms, stabilizing varying proportions of pre-existing resting, open, desensitized, and uncoupled conformations, as well as influencing the transitions between these conformational states. Structural and functional data highlight a role for the lipid-exposed M4 transmembrane α-helix of each subunit in lipid sensing, and suggest that lipids influence gating by altering the binding of M4 to the adjacent transmembrane α-helices, M1 and M3. M4 has also been implicated in both the folding and trafficking of nAChRs to the cell surface, as well as in the potentiation of nAChR gating by neurosteroids. Here, we discuss the roles of M4 in the folding, trafficking, and allosteric modulation of nAChRs. We also consider the hypothesis that variable chemistry at the M4-M1/M3 transmembrane α-helical interface in different nAChR subunits governs the capacity for potentiation by activating lipids.

8.1.4 Introduction

Nicotinic acetylcholine receptors (nAChRs) are pentameric ligand-gated ion channels that are found in pre-, post-, and non-synaptic membranes of the central and peripheral nervous system where they perform important roles in both synaptic communication and information processing (Dani and Bertrand, 2007; Kalamida et al., 2007; Mineur and Picciotto, 2008; Mufson et al., 2008; Taly et al., 2009). nAChRs have been implicated in a variety of physiological processes including voluntary motion, sleep, wakefulness, reward, and pain. They play roles in development and synaptic plasticity, and participate in learning, memory, and attention. Altered cholinergic function contributes to Alzheimer's disease, Parkinson's disease, autism, epilepsy, schizophrenia, dementia with Lewy bodies, and addictive behavior. nAChRs are even found in non-neuronal cells where they likely respond to paracrine acetylcholine.

Subtle modifications of nAChR activity by either endogenous or exogenous compounds have profound effects on human biology. In this context, the exquisite functional sensitivity of the prototypic nAChR, the muscle-type nAChR from the electric fish *Torpedo*, to its lipid environment raises the possibility that lipid-nAChR interactions play an important role in human biology. In support of this assertion, a genetic mutation that alters the lipid-protein interface of the muscle-type nAChR potentiates nAChR gating leading to a congenital myasthenic syndrome (Shen et al., 2006). Changes in the nAChR lipid micro-environment during both normal and abnormal brain function could modulate nAChR function *in vivo*.

In the past decade, a 4 Å resolution cryo-electron microscopy model of the *Torpedo* nAChR (Unwin, 2005), along with X-ray crystal structures of homologous pentameric ligand-gated ion channels (Figure 8.1) (pLGICs) (Althoff et al., 2014; Bocquet et al., 2009; Hassaine et al., 2014; Hibbs and Gouaux, 2011; Hilf and Dutzler, 2008, 2009; Miller and Aricescu, 2014; Nury et al., 2011b) and water-soluble homologs of the nAChR extramembranous agonist-binding domain (Brejc et al., 2001; Dellisanti et al., 2007) have provided an increasingly detailed picture of both nAChR structure and the nature of ligand-induced conformational change. With these structures in hand, we are now poised to translate

functional data on nAChR-lipid interactions into a structural/mechanistic context. In this review, we briefly describe the structural properties of the nAChR, and then discuss current understanding of the molecular mechanisms of nAChR-lipid interactions, focusing on the proposed role of the outermost transmembrane α-helix, M4, in lipid sensing. We highlight new insight that has been derived from studies of prokaryotic homologs of the nAChR. We also discuss increasing evidence suggesting that M4 not only plays an important role in both the gating and allosteric modulation of nAChRs, but also in the folding and trafficking of nAChRs to the cell surface.

Figure 8.1 The nAChR and its prokaryotic homologs

The nAChR and its prokaryotic homologs. Structures of **A**) the Torpedo nAChR (PDB code 2BG9) and its prokaryotic homologs **B**) ELIC (PDB code 2VL0) and **C**) GLIC (PDB code 3P50). In each side view (top), one subunit is shown in a blue cartoon diagram, with the lipid-exposed M4 α-helix in red. For the nAChR, the agonist binding site (αTrp149) is represented as red spheres, and the proposed channel gate (αLeu251, αVal255) and homologous residues in the β, γ, and δ subunits) as yellow spheres. Pore constricting residues are also highlighted as yellow spheres in ELIC (Leu239, Phe246) and GLIC (Ile233, Ile240, Ile241). For ELIC, the agonist GABA from a different structure (PDB code 2YOE) is shown as red spheres. For GLIC, the general anesthetic propofol is shown as orange spheres, with the lipids modeled into the electron density of a different structure (PDB code 3EAM) superimposed as tan spheres. The bottom panel shows a top view of the TMD of each pLGIC with conserved coloring.

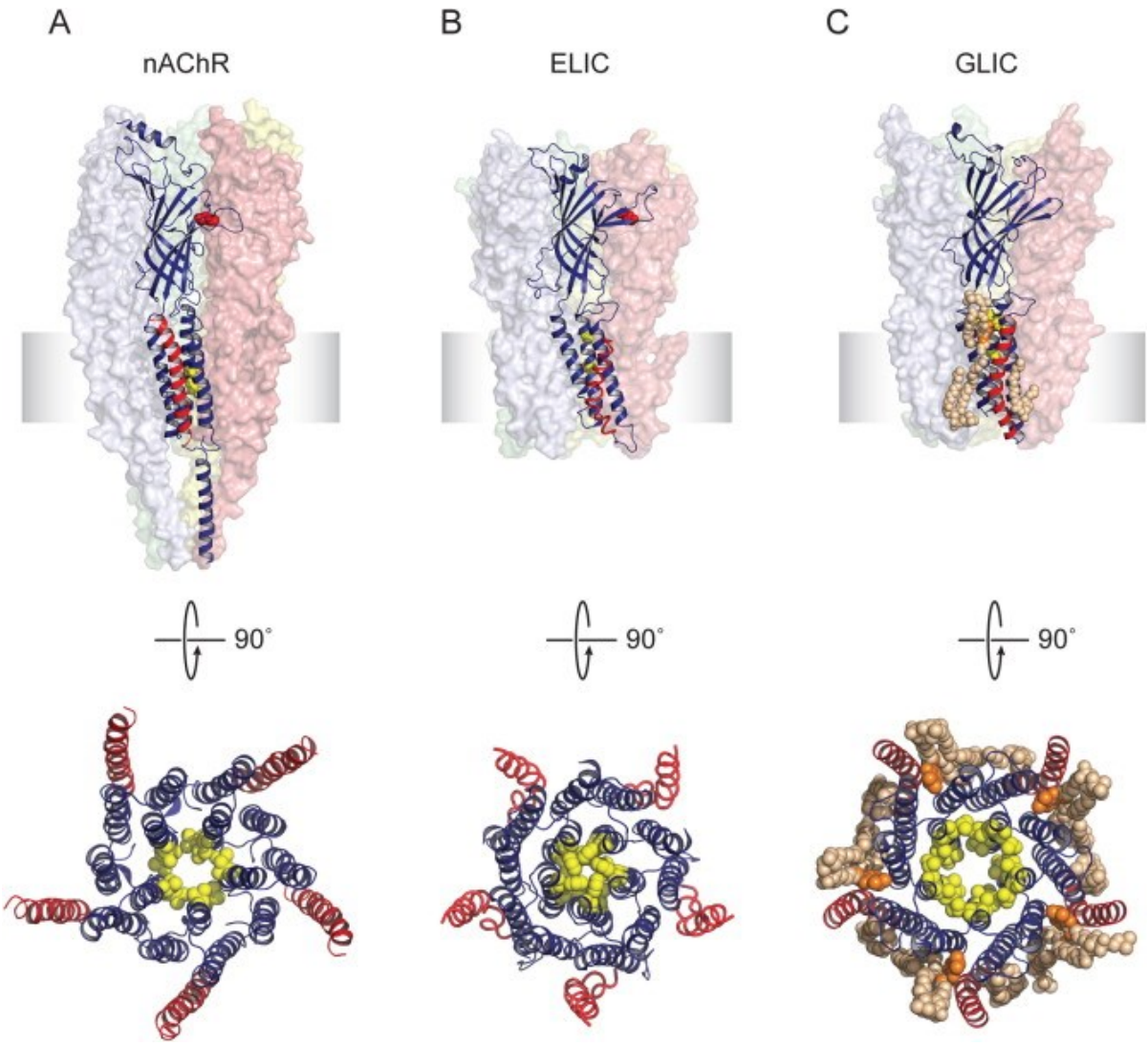
A
nAChR
B
ELIC
C
GLIC
90°
90°
90°

8.1.5 nAChR Structure

Seventeen genes that code for seventeen homologous nAChR subunits have been identified in mammals (α1-α10, β1-β4, γ, ε, and δ)., with additional variations found in invertebrates, such as the nematode, *Caenorhabditis elegans*, and the honey bee, *Apis mellifera* (Jones and Sattelle, 2010). The various gene products combine to form either homomeric or heteromeric channels, with the five identical or non-identical subunits arranged pseudo-symmetrically around a central axis that functions as an ion channel (Figure 8.1). The muscle-type nAChR, highly homologous to the nAChR found in *Torpedo* electroplaque membranes, is formed from four distinct subunits organized in an $(\alpha1)_2\beta1\gamma\delta$ stoichiometry, with the γ-subunit replaced by ε in adult muscle. Although heteromeric α4β2 nAChRs are most abundant in the human brain, homomeric α7 and other nAChR subtypes play important roles in a variety of neuronal processes (Dani and Bertrand, 2007; Taly et al., 2009).

The two primary functions of these ligand-gated ion channels, ligand binding and ion channel conductance, occur in distinct structural domains: a roughly 200-residue long N-terminal extracellular domain (ECD) and a roughly 150-residue long C-terminal transmembrane domain (TMD), respectively (Unwin, 2005). These two adjacent domains are demarked by an abrupt change in secondary structure and meet at an interface located close to the extracellular bilayer surface (Figure 8.2). In addition, a cytoplasmic domain is present between transmembrane a-helices M3 and M4 (see below) in eukaryotic pLGICs and is characterized by high variability in both sequence and length, with only one α-helix per subunit seen, in electron microscopic images, extending away from the membrane surface. A short peripheral α-helix oriented parallel to the membrane surface is also seen in structures of the 5-HT3 receptor (Hassaine et al., 2014).

Each ECD consists primarily of 10 β-strands (β1-β10) forming two β-sheets that fold into a classic β-sandwich. The β-sandwich structures of each subunit interact with those of two adjacent subunits to ultimately form the pentamer, with between two and five neurotransmitter binding sites located at the interfaces between the subunits. The principal face of each agonist site is located on an α-subunit near the two vicinal cross-linked cysteine

Figure 8.2 M4 and the interface between the ECD and TMD

Structures of M4 and the ECD/TMD interface of **A**) the nAChR (PDB code 2BG9), **B**) ELIC (PDB code 2Vl0), and **C**) GLIC (PDB code 3EAM). In each case, post-M4, the β1–β2 loop, the β6–β7 loop (Cys-loop), and the M2–M3 linker are highlighted in orange, light blue, green, and red, respectively. For the nAChR, direct interactions between post-M4 (Gln435) and the Cys-loop (Phe137) are circled. For GLIC, a lipid molecule (beige space filling model) bridges interactions between post-M4 (Phe315) and the β6–β7 loop (Phe121).

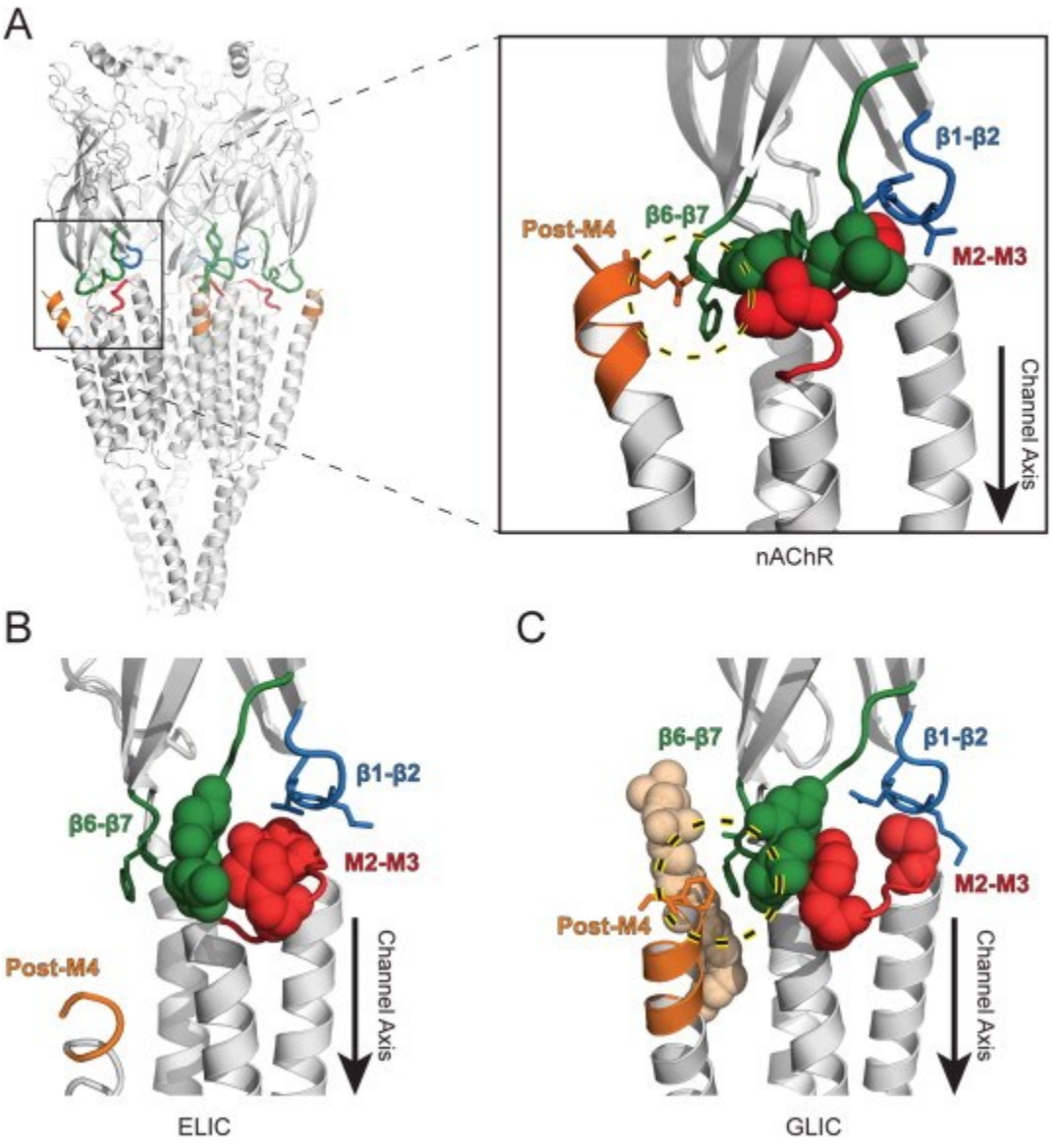
A
β1-β2
β6-β7
Post-M4
M2-M3
Channel Axis
nAChR
B
β1-β2
β6-β7
M2-M3
Post-M4
Channel Axis
ELIC
C
β6-β7
β1-β2
M2-M3
Post-M4
Channel Axis
GLIC

residues that define α versus non-α subunits (Kao and Karlin, 1986). Four aromatic residues (in *Torpedo*, Tyr93, Trp149, Tyr190, and Tyr198) from three separate loops (loops A, B, and C) play a key role in agonist binding (Dennis et al., 1988; Galzi et al., 1990; Middleton and Cohen, 1991). In muscle-type nAChRs, the complementary face of the binding site is formed from three loops (D, E, and F) located on the adjacent γ/ε- and δ-subunits (Corringer et al., 1995; Czajkowski et al., 1993). The agonist binding sites in heteromeric nAChRs are often distinct, each having a unique pharmacological profile.

The transmembrane domain forms a single ion channel along the pseudo-symmetry axis of the protein (Corringer et al., 2000; Miyazawa et al., 2003; Unwin, 2005). Each subunit contributes four transmembrane α-helices (M1-M4) organized in a classic four helix bundle. The M2 α-helices from each subunit contribute to the channel pore, while M1 and M3 form a ring of α-helices that shield M2 from the membrane. The M4 α-helices are located on the periphery of each subunit and are highly exposed to the lipid bilayer. Extensive mutational analysis shows that residues at the cytoplasmic border of M2 contribute substantially to the selectivity filter of the channel, which discriminates ions mainly according to their charge (Corringer et al., 1999; Galzi et al., 1992; Keramidas et al., 2004).

Communication between the ECD and TMD in each subunit is mediated primarily by the covalent link between the C-terminus of β10 in the ECD and the N-terminus of M1 in the TMD, as well as by non-covalent connections between the β1/β2 and β6/β7 loops (the latter is referred to as the Cys-loop in eukaryotic pLGICs) of the ECD and the M2-M3 loop of the TMD (Jha et al., 2007; Lee and Sine, 2005) (Figure 8.2). Although the detailed structural changes that occur when agonist binding couples to channel gating remain to be defined, it is thought that concerted movements of the two β-sheets in the ECD lead to changes in structure of both the β1-β2 and β6- β7 loops, which then translate into movement of the pore-lining M2 α-helices via direct interactions with the M2-M3 linker (Bocquet et al., 2009; Hibbs and Gouaux, 2011; Hilf and Dutzler, 2009; Lee and Sine, 2005; Lummis et al., 2005; Sauguet et al., 2014; Unwin and Fujiyoshi, 2012). In the closed state, the ion channel is occluded by hydrophobic residues located near the center of the bilayer that provide a barrier to the flow of a solvated ion (Figure 8.1) (Beckstein and Sansom, 2006). Upon gating, a twisting and tilting of the pore-lining M2 α-helices lead to a widening of the channel pore by

~3 Å, allowing the flow of solvated ions down their electrochemical gradient into (Na^+ and Ca^{2+}) or out of (K^+) the cell. Prolonged exposure to agonist also leads to the formation of one or more poorly-defined desensitized conformations, which are characterized by both a relatively high affinity for acetylcholine and channel inactivity (Changeux and Edelstein, 2005) (Figure 8.3A).

Figure 8.3 The lipid-dependent uncoupled nAChR

A) nAChR function is usually interpreted in terms of a conformational scheme involving resting (R), open (O), and desensitized (D) conformations (Scheme 2). The membrane reconstituted *Torpedo* nAChR can also adopt a non-responsive uncoupled (U) conformation (Scheme 1). **B**) Uncoupling may involve altered interactions between post-M4 and the Cys-loop, leading to both a functional and structural weakening of the contacts between ECD and TMD. **C**) The uncoupled (PC membrane) nAChR undergoes both more rapid and more extensive peptide N–1H/N–2H exchange when exposed to 2H2O buffer than the coupled (resting or desensitized) nAChR in PC/PA/cholesterol membranes. **D**) The uncoupled nAChR binds acetylcholine with a resting-state-like affinity and does not transition to the high-affinity acetylcholine-binding desensitized conformation, as does the resting nAChR in PC/PA/cholesterol membranes.

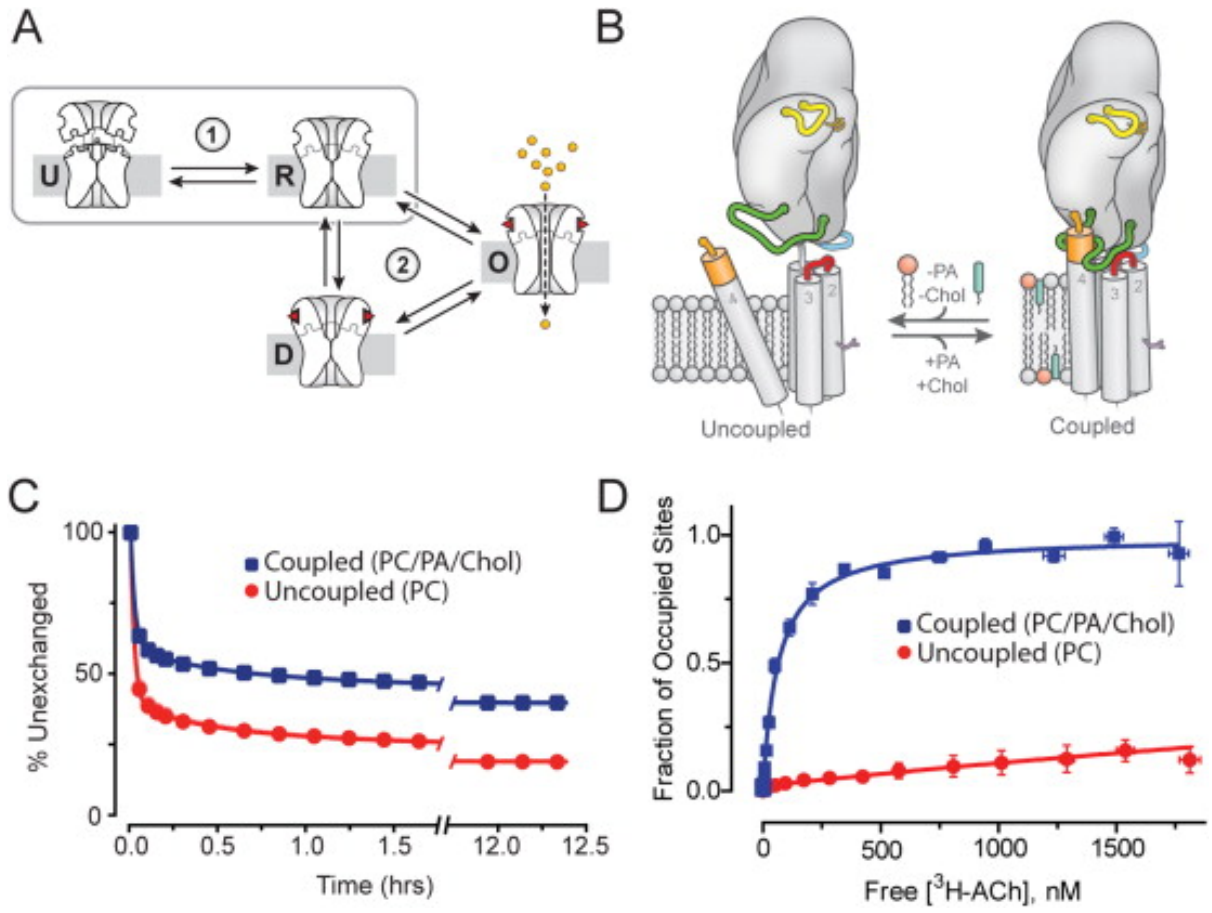
A
U
R
D
O
1
2
B
-PA
-Chol
+PA
+Chol
Uncoupled
Coupled
C
% Unexchanged
100
50
0
Coupled (PC/PA/Chol)
Uncoupled (PC)
0.0
0.5
1.0
1.5
12.0
12.5
Time (hrs)
D
Fraction of Occupied Sites
1.0
0.5
0.0
Coupled (PC/PA/Chol)
Uncoupled (PC)
0
500
1000
1500
Free [3H-ACh], nM

8.1.6 Lipids as modulators of nAChR function

Early attempts to isolate and reconstitute neurotransmitter-induced channel gating in model membranes led to the discovery that the activity of the *Torpedo* nAChR is sensitive to lipids. To retain agonist-induced channel flux, the receptor must be solubilized and purified in the presence of lipid, and then placed in a membrane with an appropriate lipid composition (Criado et al., 1982; Epstein and Racker, 1978; Fong and McNamee, 1986; Heidmann et al., 1980). Both anionic lipids, such as phosphatidic acid (PA) or phosphatidylserine (PS), and neutral lipids, such as cholesterol, are important for nAChR activity (Criado et al., 1982; daCosta et al., 2002; Fong and McNamee, 1986; Hamouda et al., 2006a; Rankin et al., 1997; Ryan et al., 1996).

It was initially suggested that lipid composition influences nAChR function by a conformational selection mechanism, whereby lipids modulate the natural equilibrium between activatable resting and non-activatable desensitized states (Figure 8.3) (Baenziger et al., 2000; Hamouda et al., 2006b; McCarthy and Moore, 1992). In addition to the canonical resting and desensitized conformations, the nAChR in reconstituted membranes adopts an "uncoupled" conformation that exhibits resting state-like agonist binding, but does not undergo agonist-induced conformational transitions (see below). The proposed conformational selection mechanism was thus expanded to include uncoupled nAChRs (daCosta et al., 2009).

Membranes composed of phosphatidylcholine (PC) and PA are quite effective at stabilizing an activatable resting nAChR, while mixtures of PC and PS are not (daCosta et al., 2004; Sturgeon and Baenziger, 2010). The distinct effects of PA and PS on nAChR function suggest that bulk membrane physical properties influence nAChR conformational equilibria. A role for membrane physical properties in modulating nAChR function is further suggested by the observation that although the nAChR in PC membranes lacking activating lipids is stabilized in an uncoupled conformation, "thick" PC membranes with di22:1 acyl chains support slow, ligand-induced conformational transitions from uncoupled to ultimately

the desensitized state (daCosta et al., 2013). Bulk membrane physical properties influence the energy barriers, and thus the transition kinetics between different conformations.

8.1.6.1. The lipid-dependent uncoupled state

Recent studies have shown that the inactive nAChR in PC membranes adopts primarily an uncoupled, as opposed to a desensitized conformation (Baenziger et al., 2008; daCosta et al., 2009). The uncoupled nAChR retains the ability to bind agonist, but does not undergo allosteric transitions (i.e. binding and gating are uncoupled) (Figure 8.3). The uncoupled nAChR is distinguished from the desensitized nAChR by its relatively low affinity for ligands, such as acetylcholine and ethidium, which bind with characteristically high affinity to the desensitized state. On the other hand, the labeling pattern of the uncoupled nAChR with the hydrophobic photoactivatable probe, 3-trifluoromethyl-3-(m-[^{125}I]-iodophenyl)diazirine ([^{125}I]-TID), is incompatible with a resting state (daCosta et al., 2002; Hamouda et al., 2006a; McCarthy and Moore, 1992).

Anecdotal evidence suggests that neuronal nAChRs may adopt an uncoupled conformation. For example, one study showed that although the open probability for activated α4β2 nAChRs expressed on the surface of human embryonic kidney (HEK) cells is greater than 80%, less than 10% of the surface receptors contribute to the whole cell currents. The remaining surface-expressed nAChRs bind agonist, but do not undergo agonist-induced channel gating, consistent with the existence of a large pool of uncoupled nAChRs (Fenster et al., 1999; Li and Steinbach, 2010). In addition, some nAChR subtypes, including those with α6 subunits, exist in oligomeric structures on cell surfaces but do not flux cations in response to ACh-binding (Broadbent et al., 2006; Drenan et al., 2008). In fact, the β3 subunit is essential for the biogenesis of α6α4β2β3 nAChRs, yet β3 suppresses acetylcholine-evoked currents. It is possible that the β3 subunit favors formation of an uncoupled state. The normalized current (current per ACh binding site on the surface of the cell) also increases with time after injection of muscle-type cRNA into oocytes, suggesting a time-dependent maturation in “folding” to activatable conformations (Li et al., 1990). As discussed above, thicker membranes, such as those found in lipid rafts, promote slow conformational transitions from uncoupled to coupled conformations (daCosta et al., 2013). Neuronal

nAChRs require lipid rafts for trafficking to the cell surface (Bruses et al., 2001; Marchand et al., 2002). A lipid raft dependent transition from uncoupled to coupled conformations may represent a final step in the folding and trafficking of nAChRs to the cell surface (See section 8.1.8).

While these hypotheses are all provocative, it must be emphasized that definitive evidence for the existence of uncoupled nAChRs in biological membranes is lacking. The main conclusion to be drawn from the above work is that while uncoupling is central to lipid-nAChR interactions and thus a focus of this review, specific chemical probes are still required to both test for the existence of uncoupled nAChRs in biological membranes and to probe the hypothesized role of uncoupling in cholinergic function.

8.1.6.2. Sites of lipid-nAChR interactions

There are likely annular and non-annular sites of lipid action at the nAChR. Non-annular cholesterol binding sites located between transmembrane α-helices were originally proposed based on fluorescence quenching studies with brominated lipids (Jones and McNamee, 1988) and are supported by both molecular dynamics simulations and bioinformatics studies (Baier et al., 2011; Brannigan et al., 2008). Cholesterol binding to non-annular cavities located between the nAChR transmembrane α-helices stabilizes the transmembrane domain structure, facilitating interactions with the ECD (Brannigan et al., 2008). A modulatory lipid binding site has also been identified at the interface between subunits in the homologous glutamate-activated chloride channel (Althoff et al., 2014).

As discussed in more detail below, the M4 transmembrane αhelix is the most lipid-exposed of the transmembrane a-helices and is thus likely a site for mediating both specific and non-specific nAChR-lipid interactions. Both cholesterol and anionic lipids also show a strong affinity for the annulus of lipids that surrounds the lipid-exposed surface of the nAChR (Ellena et al., 1983; Fernandez Nievas et al., 2008; Marsh and Barrantes, 1978). At any given moment in time, both cholesterol and anionic lipids in this annulus are “bound” to

the surface of the nAChR and thus likely interacting with M4. In support of this assertion, a photoactivatable cholesterol analog labels sites on the lipid-exposed surface of the nAChR, including predominantly residues on M4 (Hamouda et al., 2006a). Another cholesterol analog covalently linked to PC, which presumably resides within the bulk membrane environment, is as effective as cholesterol in supporting nAChR function, consistent with the existence of a membrane-exposed-surface-site for cholesterol action (Addona et al., 1998). In fact, the entire lipid-exposed surface of the nAChR may serve as an "allosteric site" that is sensitive to bulk membrane physical properties.

8.1.6.3. Role of M4 as a lipid sensor

Chemical labeling studies in the early 1990's with the hydrophobic photo-reactive probe, [^{125}I]-TID, showed that the M4 transmembrane α-helix forms the predominant interface between the TMD and the lipid environment (Blanton and Cohen, 1992, 1994), a finding that has been confirmed in all pLGIC structures. The location of M4 at the periphery of the TMD led to the suggestion that M4 plays a central role in lipid-sensing (Antollini et al., 2005; Xu et al., 2005). To test this hypothesis, numerous mutations of lipid-facing residues on both *Torpedo* and muscle-type nAChRs have been constructed, and many were found to alter channel function (Bouzat et al., 1998; Lasalde et al., 1996; Lee et al., 1994; Li et al., 1992; Shen et al., 2006; Tamamizu et al., 2000). These studies confirm that even though M4 is distant from both the agonist site and channel gate, its structure influences gating. The amino acid changes studied to date have typically altered channel opening and closing rates. Interestingly, homologous mutations on different subunits often have opposing effects on channel gating, with some mutations leading to gain, and others to loss of function phenotypes (Bouzat et al., 1998, 2000, 2002).

When shifting between resting and open conformational states, M4 is by no means a static structural element. In fact, the different motions of the M4 α-helices in the different subunits upon gating may account for the divergent functional effects observed with homologous lipid-facing M4 mutations on different subunits. When gating, the two αM4 α-helices in the $(\alpha1)_2\beta1\varepsilon\delta$ pentamer move synchronously, each moving as a unit roughly

halfway along the reaction coordinate between agonist binding and the open transition state (Mitra et al., 2004). The motions of the εM4 and βM4 follow that of αM4, while δM4 has no apparent motion during gating. The temporal differences in various M4 positions can conceivably permit the pentamer to present a unique binding surface to the lipid bilayer in each distinct conformation and/or while transitioning between them. Such structural changes in M4 could then expose or mask lipid binding sites, allowing for stronger or weaker interactions with the lipid bilayer that preferentially stabilize different conformations or promote/inhibit transitions between these states. In addition, biophysical measurements and molecular dynamics simulations suggest that the orientation of M4 relative to the membrane normal depends on the presence of cholesterol and bilayer thickness (Antollini et al., 2005; Xu et al., 2005). Lipids may preferentially stabilize different orientations of M4 relative to the remainder of the TMD, altering gating kinetics as M4 moves along the reaction coordinate leading from agonist binding to the open state.

Note that M4-swapped chimeric constructs of the homologous glycine receptor α1 and α3 subunits demonstrate that subunit-specific agonist efficacy is driven in large part by M4, with agonist sensitivity mediated by differences in M4-lipid interactions (Chen et al., 2009). These studies further highlight the importance of M4 as a functional modulator, and suggest that M4 may play a role in lipid-sensing in all members of the broader pLGIC family (see also below).

8.1.6.4. The M4 lipid sensor model of uncoupling

With publication of the nAChR structure (Unwin, 2005), existing functional/biophysical data on lipid-nAChR interactions were consolidated into a structural model of uncoupling. As noted, considerable evidence had implicated the transmembrane α-helix, M4, in lipid-sensing. The atomic model and subsequent mutagenesis studies further highlighted the importance of noncovalent interactions between loops at the ECD/TMD interface in coupling agonist binding to channel gating (Jha et al., 2007; Lee et al., 2009). It was known that although the quaternary/secondary structures and thermal denaturation temperature of the uncoupled nAChR are both similar to that of resting and desensitized nAChRs (Bhushan and McNamee, 1990; daCosta et al., 2005; Methot et al., 1995), the

uncoupled nAChR undergoes more rapid peptide N-^{1}H/N-^{2}H exchange (Figure 8.3C). Significantly, the changes in peptide hydrogen exchange kinetics suggest that uncoupling is accompanied by the solvent exposure of previously buried peptide hydrogens (Baenziger and Methot, 1995; daCosta and Baenziger, 2009; Methot et al., 1995). Although the regions of the nAChR that become solvent-exposed were not defined in this experiment, the critical importance of the ECD/TMD interface in channel function led to the hypothesis that uncoupling results from structural changes at the ECD/TMD interface. Weakened interactions leading to an increased physical separation between the ECD and TMD could account for both the loss of function and the increased solvent accessibility observed in the uncoupled state.

It is also evident from the nAChR structure that the C-terminus of M4 (post-M4, specifically Gln435) extends beyond the lipid bilayer to interact with a conserved residue (Phe137) in the Cys-loop (Figure 8.2). Given that the Cys-loop plays a central role at the interface between the ECD and TMD, it was postulated that interactions between post-M4 and the Cys-loop are important for coupling agonist-binding to channel gating, and that lipids influence nAChR function by modulating post-M4 interactions with the Cys-loop. Ineffective post-M4/Cys-loop interactions could lead to partial dissociation of the ECD from the TMD to form the uncoupled state, thus accounting for the increased solvent exposure of the peptide backbone (daCosta et al., 2009).

The M4 lipid-sensor model is clearly speculative, and many facets of this model require rigorous testing using structural, functional, and biophysical approaches. The importance of the model is that it provides a starting point for understanding the molecular mechanisms that underlie lipid-sensing. It should be noted, however, that the model is supported by considerable data. A central feature is the postulate that the ECD adopts an independent structure that can at least partially dissociate from the TMD to form the uncoupled conformation. The proposed structural independence of the ECD is supported by the existence of stable pentameric water- soluble AChBPs, which are homologous to the ECD of the nicotinic ACh receptor (Brejc et al., 2001). Folded, stable, water soluble ECDs of both the nicotinic ACh receptor a-subunit and GLIC can also be expressed independently

of their respective TMDs (Dellisanti et al., 2007; Nury et al., 2010b). Both pentameric and hexameric structures of the GLIC ECD have been solved by X-ray crystallography.

The assertion that direct interactions between post-M4 and the Cys-loop are important for nAChR activity is also supported by functional studies. Shortening M4 in the *Torpedo* nAChR alters both channel function and trafficking to the cell surface (Tobimatsu et al., 1987). M4 C-terminal deletions have deleterious effects on an α7-5HT_{3A} chimera, leading to the suggestion that interactions between the penultimate tyrosine in M4 and the Cys-loop lock the chimera in a mature agonist binding conformation that traffics to the cell surface (Pons et al., 2004). The C-terminus of M4 is also essential for neurosteroid-induced potentiation of α4β2 nAChRs, as discussed in Section 8.1.7.

Finally, crystal structures of the prokaryotic pLGIC, ELIC, provide direct structural evidence for the proposed model of uncoupling. As discussed below, the ELIC structure exhibits many of the proposed features of the uncoupled state. Furthermore, crystallized ELIC adopts a conformation that does not gate open in response to agonist binding (see Section 8.1.6.5).

8.1.6.5. Insight from crystal structures of prokaryotic pLGICs

The identification of homopentameric prokaryotic pLGICs, GLIC and ELIC, that are homologous to the nAChR represents a major advance in the structural characterization of pLGICs (Bocquet et al., 2007; Tasneem et al., 2005). Both GLIC and ELIC have been expressed in *Escherichia coli* at levels sufficient for both biochemical and structural studies, and each has yielded several high-resolution crystal structures (Figure 8.1) (Bocquet et al., 2009; Hilf and Dutzler, 2008; Sauguet et al., 2013; Zimmermann and Dutzler, 2011). These structures reveal two key features that impact on our understanding of lipid-nAChR interactions.

First, crystal structures of GLIC exhibit electron density located at the periphery of the TMD, suggesting the presence of partially ordered lipid molecules (Figure 8.1 and 8.2) (Bocquet et al., 2009). Two of the three lipid binding sites on each subunit are found at the interfaces between M4 and the adjacent TMD a-helices M1 and M3. One of these bridges

interactions between post-M4 (F315) and the β6-β7 loop (F121), the loop analogous to the Cys-loop in eukaryotic pLGICs. Intriguingly, the lipid bridging post-M4 to the β6-β7 loop in the GLIC structure is displaced slightly by the inhibitory anesthetic, propofol, suggesting that the lipid occupies an allosteric site (Nury et al., 2011b). The finding that lipids bind to the interface between M4 and, M1 and M3, in the GLIC structure supports the hypothesis that lipids influence M4-M1/M3 interactions.

Second, the crystal structures of ELIC (Figure 8.1 and 8.2) (Gonzalez-Gutierrez et al., 2012; Zimmermann and Dutzler, 2011) provide insight into the lipid-dependent uncoupled conformation. Structures solved in the presence of agonist exhibit electron density in the agonist site likely corresponding to bound agonist, but show no structural rearrangements in the TMD pore relative to crystal structures solved in the absence of agonist. In fact, no movement of the pore-lining M2 α-helices was detected with mutants that prolong channel opening and exhibit no propensity to desensitize. The lack of change in the structure of the pore-lining a-helices in *apo* and *holo* forms of both desensitizing wild type and non-desensitizing mutant ELIC structures, as well as other functional data, were interpreted to suggest that the structures reflect a non-desensitized conformation that is refractory to agonist-induced conformational transitions (Gonzalez-Gutierrez and Grosman, 2010) - i.e. a conformation that is functionally equivalent to the lipid-dependent uncoupled state (daCosta and Baenziger, 2013; Gonzalez-Gutierrez et al., 2012).

Significantly, the ELIC structures exhibit many of the proposed structural features of the uncoupled nAChR. The M4 α-helix in this potentially uncoupled structure is partially unwound and tilted away from the remaining TMD, with several C-terminal M4 residues not observed. In contrast to the nAChR structure, the ELIC structure shows no direct contact between post-M4 and the β6-β7 loop. The tilting of M4 away from the remainder of the TMD is also accompanied by reduced contact between both the β1-β2 and β6-β7 loops of the ECD and the M2-M3 linker of the TMD. In the nAChR structure, the extended side chains of the β1-β2 and β6-β7 loops engage the M2-M3 linker in a fashion reminiscent of vice grips attached to a metal pipe (Figure 8.2). In ELIC, the β1-β2 and β6-β7 loops no longer surround the M2-M3 linker, which itself tilts towards the membrane surface so that it approaches the β8-β9 loop on the complementary face of the adjacent subunit. In effect, reduced interactions

between M4 and M1/M3 are accompanied by weakened interactions between the ECD and TMD - as predicted by the M4 lipid-sensor model.

Note also that the tilted orientation of the M4 α-helix away from the main body of the TMD in crystal structures of ELIC contrasts the conformation of the M4 α-helix in the GLIC structures (Figure 8.2C), where M4 binds tightly to the adjacent TMD α-helices, M1 and M3. These structural differences between ELIC and GLIC are intriguing given the important role of aromatic residues in the binding of M4 to M1/M3 during folding of the homologous glycine receptor (Haeger et al., 2010). GLIC has nine aromatic residues at the interfaces between M1, M3, and M4 that are involved in extensive π- π interactions. Four of these are conserved in ELIC, with the remaining five aromatics replaced in ELIC by aliphatic residues. In particular, ELIC lacks a cluster of three aromatic residues located near post-M4 that may be essential for effective binding of post-M4 to the remainder of the TMD and/or the β6-β7 loop (see Section 8.1.6.7 for a more detailed discussion of the chemistry at the M1/M3/M4 interface). The lower number of aromatic interactions at the M4-M1/M3 interface may render M4 binding to M1/M3 weaker in ELIC and thus make ELIC more susceptible to the perturbing effects of detergent solubilization during crystallization than GLIC (daCosta and Baenziger, 2013).

8.1.6.6. The role of M4 in prokaryotic pLGIC function

Functional studies with prokaryotic pLGICs provide further support for the proposed role of M4 in lipid sensing. The role of M4 in both ELIC and GLIC channel function has been tested by Ala-scanning mutagenesis (Hénault et al., 2015b). Many of the Ala substitutions of residues on both the protein-facing and lipid-facing surfaces of M4 in GLIC and ELIC showed altered EC_{50} values for channel activation, consistent with the proposed modulatory role of M4 in nAChR function (Figure 8.4). Interestingly, Ala substitutions along M4 in GLIC typically led to loss of function phenotypes, with the largest changes in activity observed near the C-terminus of the M4 α-helix (extracellular end). In contrast, the Ala substitutions in ELIC typically led to gain of function phenotypes, with the largest effects occurring near the N-terminus (cytoplasmic end) of M4. The changes in function show that the structure of M4 influences gating, even in primitive prokaryotic pLGICs. In addition, the

consistent gain of function observed with the Ala substitutions along M4 in ELIC suggests that, unlike GLIC, the structure of M4 and/or the interactions between M4 and M1/M3 in ELIC are not intrinsically optimized for channel gating.

The effect of altered M4-M1/M3 interactions on channel activity was explored further through Ala substitutions of aromatic residues at the M4-M1/M3 interface in GLIC, and through aliphatic to aromatic residue substitutions at the same interface in ELIC (Carswell et al., 2015b). In all cases, the elimination of aromatics at the M4-M1/M3 interface in GLIC to weaken M4 binding (Haeger et al., 2010) reduced channel function. In contrast, the introduction of new aromatic residues into the M4-M1/M3 interface of ELIC, which should promote M4 binding, enhanced channel function. In fact, the introduction of a pair of interacting aromatic residues on the C-terminus of M4 and the N-terminus of M3 decreased the EC_{50} for channel gating almost 10-fold, implying close to a 10-fold potentiation of channel function. The data are consistent with the hypothesis that enhanced interactions between M4 and M1/M3 promote coupling between the agonist binding site and channel gate.

Figure 8.4 ELIC and GLIC M4 Ala-scan heat map

Changes in the EC_{50} for channel gating that result from sequential mutation of each M4 residue to Ala are heat-mapped onto M4 for both **A**) a homology model of ELIC (based on the GLIC structure) and **B**) GLIC (4HFI). The magnitude of the shift in EC_{50} is depicted via color intensity, with no change in EC_{50} in white, a gain of function in red, and a loss of function in blue. Non-functional mutations are shown in black. An altered function mutation for which accurate EC_{50} data could not be obtained is colored in gray.

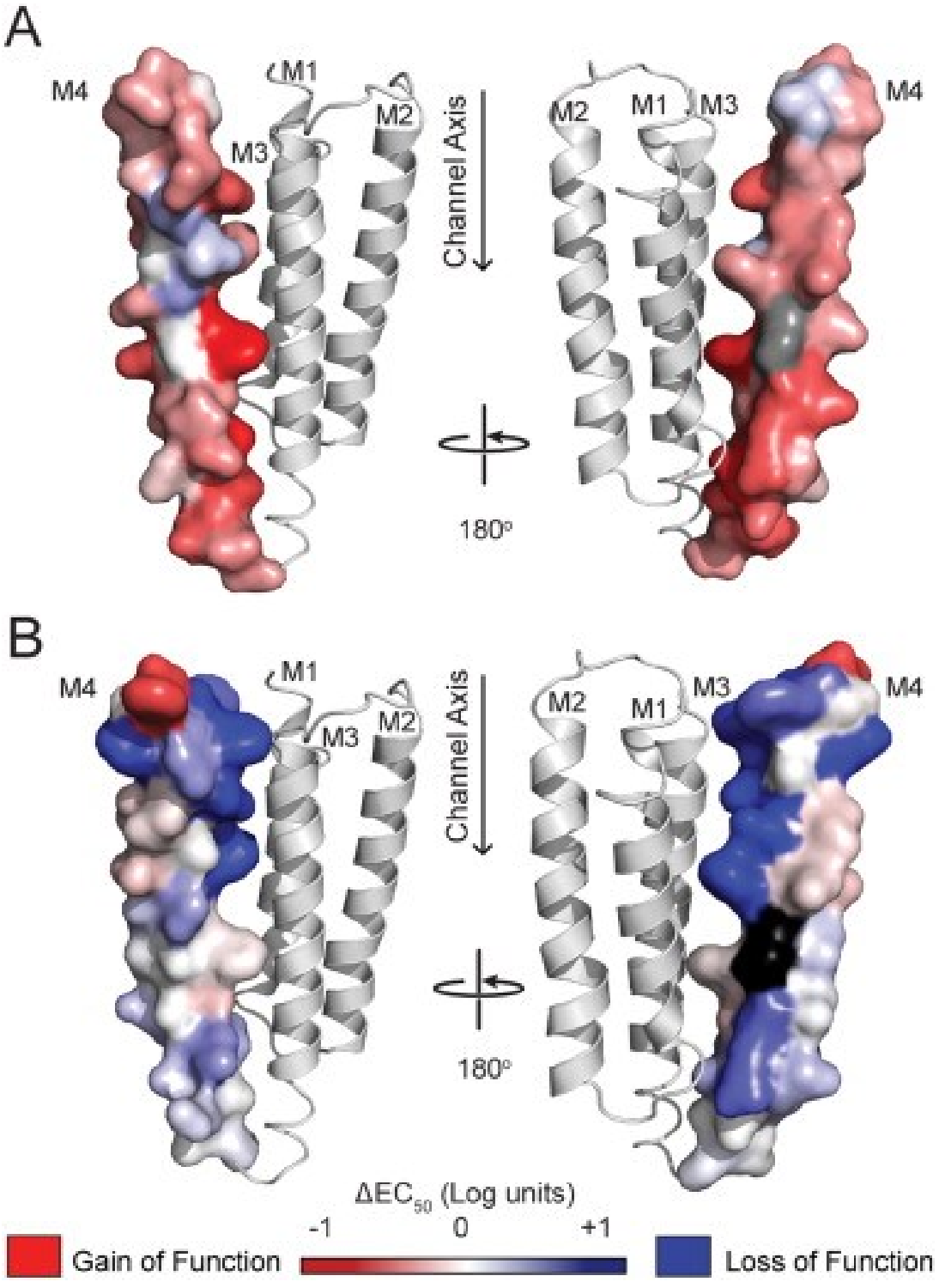
A
M4
M1
M2
M3
Channel Axis
M2
M1
M3
M4
180°
B
M4
M1
M3
M2
Channel Axis
M2
M1
M3
M4
180°
ΔEC50 (Log units)
-1
0
+1
Gain of Function
Loss of Function

8.1.6.7. Interhelical chemistry and the sensitivity of pLGICs to potentiation

Of the four transmembrane a-helices in each subunit, M4 exhibits the greatest sequence variability (Figure 8.5). This should lead to subunit-specific interactions at the interface between M4 and M1/M3, and thus variable affinities for M4 binding to M1/M3. Although a detailed analysis of the chemical interactions at the interface between M4 and M1/M3 in different human nAChR subunits is of interest, it is complicated by the lack of high-resolution structural data. Chemical variability at this interface, however, is evident in the crystal structures of the two prokaryotic homopentameric pLGICs (Figure 8.5), GLIC and ELIC (Bocquet et al., 2009; Hilf and Dutzler, 2008). GLIC has an abundance of both aromatic and polar interactions, whereas many of the corresponding residues are replaced in ELIC by aliphatic residues. There are many close van der Waals contacts along the entire length of the interface between M4 and M1/M3 in GLIC, whereas in ELIC the C-terminal half of M4 tilts away from the remainder of the TMD leading to weak, if any, van der Waals contacts. Both the greater abundance of aromatic/polar interactions and the close van der Waals contacts at the M4-M1/M3 interface suggest that M4 binds with higher apparent affinity to M1/M3 in GLIC than in ELIC.

Recent studies suggest that the variable chemistries at the M4-M1/M3 interfaces in GLIC and ELIC influence the sensitivities of these two prokaryotic homologs to altered lipid-protein interactions. GLIC retains robust proton-induced gating in the minimal PC membranes that stabilize the nAChR in an uncoupled state (Labriola et al., 2013). In the same PC membranes, ELIC does not gate open in response to agonist binding. An ELIC mutant with engineering aromatic interactions at the M4-M1/M3 interface to tighten M4 binding, however, retains channel activity in these minimal PC membranes (Carswell et al., 2015a). Aromatic interactions at this interface, which strengthen the apparent binding of M4 to M1/M3, thus appear to play a role in the sensitivity of these prokaryotic pLGICs to their surrounding membrane.

Figure 8.5 Variable chemistries at the M1/M3/M4 interface

A) Residues located at the M1/M3/M4 are shown as spheres for the nAChR (PDB code 2BG9), ELIC (PDB code 2VL0) and GLIC (PDB code 4HFI), with aliphatic residues colored tan, aromatic residues yellow, negative residues red, positive residues blue, and polar/H-bonding residues green. **B**) Sequence alignment of Torpedo muscle-type nAChR subunits with human α4, α7, β2 nAChRs, as well as ELIC and GLIC. The colors highlight residues at the M1/M3/M4 interface using the same format as in (A).

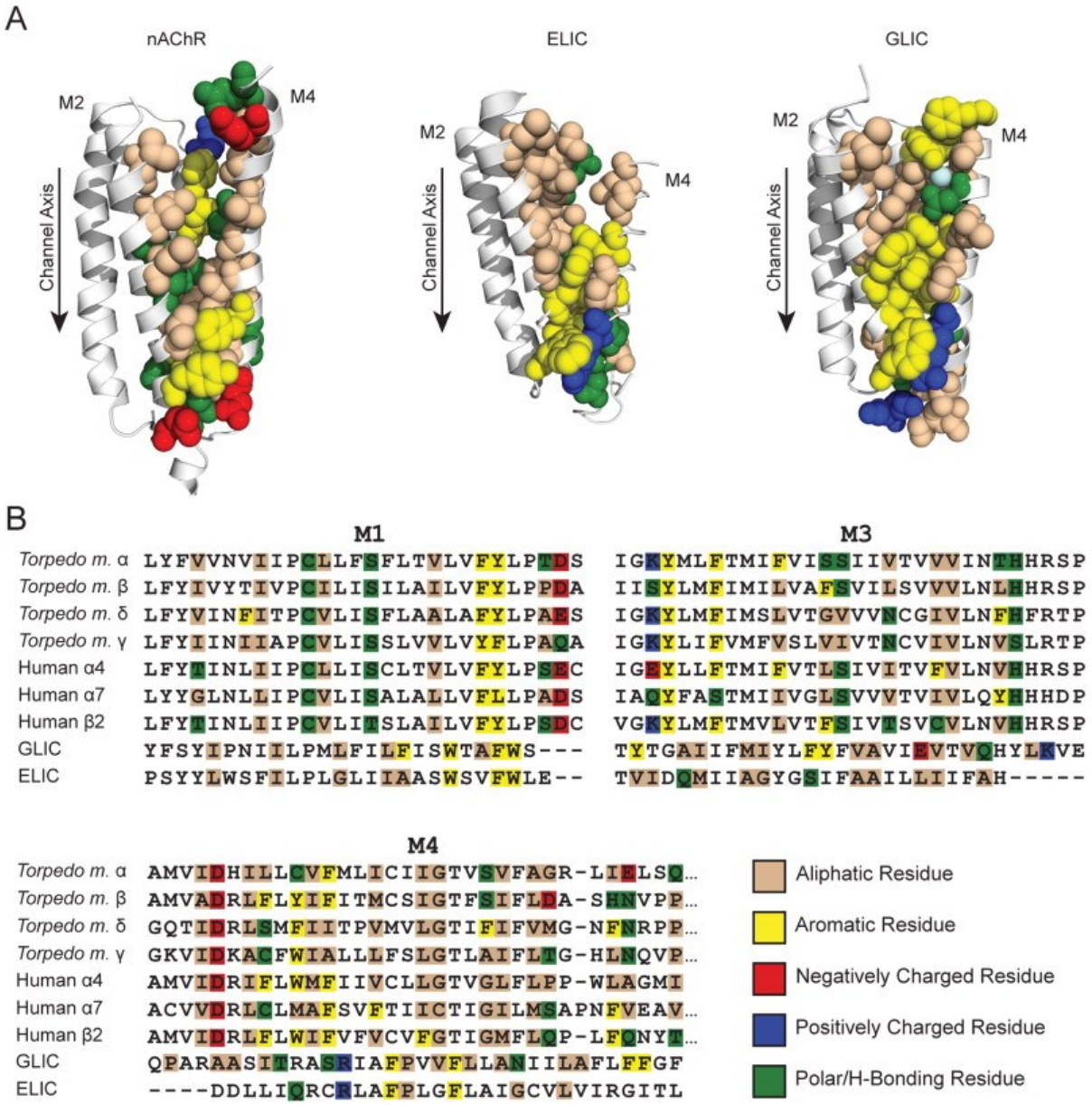
A
nAChR
ELIC
GLIC
M2
M4
Channel Axis
B
M1
M3
M4
Torpedo m. α LYFVVNVIIPCLLFSFLTVLVFYLPTDS IGKYMLFTMIFVISSIIVTVVVINTHHRSP
Torpedo m. β LFYIVYTIVPCILISILAILVFYLPPDA IISYLMFIMILVAFSVILSVVVLNLHHRSP
Torpedo m. δ LFYVINFITPCVLISFLAALAFYLPAES IGKYLMFIMSLVTGVVVNCGIVLNFHFRTP
Torpedo m. γ LFYIINIIAPCVLISSLVVLVYFLPAQA IGKYLIFVMFVSLVIVTNCVIVLNVSLRTP
Human α4 LFYTINLIIPCLLISCLTVLVFYLPSEC IGEYLLFTMIFVTLSIVITVFVLNVHHRSP
Human α7 LYYGLNLLIPCVLISALALLVFLLPADS IAQYFASTMIIVGLSVVVTVIVLQYHHHDP
Human β2 LFYTINLIIPCVLITSLAILVFYLPSDC VGKYLMFTMVLVTFSIVTSVCVLNVHHRSP
GLIC YFSYIPNIILPMLFILFISWTAFWS--- TYTGAIIFMIYLFYFVAVIEVTVQHYLKVE
ELIC PSYYLWSFILPLGLIIAASWSVFWLE-- TVIDQMIIAGYGSIFAAILLIIFAH-----
Torpedo m. α AMVIDHILLCVFMLICIIGTVSVFAGR-LIELSQ...
Torpedo m. β AMVADRLFLYIFITMCSIGTFSIFLDA-SHNVPP...
Torpedo m. δ GQTIDRLSMFIITPVMVLGTIFIFVMG-NFNRPP...
Torpedo m. γ GKVIDKACFWIALLLFSLGTLAIFLTG-HLNQVP...
Human α4 AMVIDRIFLWMFIIVCLLGTVGLFLPP-WLAGMI
Human α7 ACVVDRLCLMAFSVFTIICTIGILMSAPNFVEAV...
Human β2 AMVIDRLFLWIFVFVCVFGTIGMFLQP-LFQNYT...
GLIC QPARAASITRASRIAFPVVFLLANIILAFLFFGF
ELIC ----DDLLIQRCRLAFPLGFLAIGCVLVIRGITL
Aliphatic Residue
Aromatic Residue
Negatively Charged Residue
Positively Charged Residue
Polar/H-Bonding Residue

8.1.7 M4 and neurosteroid-induced potentiation

Although endogenous neurosteroids are potent modulators of the nAChR and other pLGICs, particularly $GABA_A$ receptors, the functional effects of these modulators are complex. Some neurosteroids, such as progesterone, inhibit, while others, such as 17β-estradiol, potentiate nAChR activity. Similar complex allosteric effects ranging from inhibition to potentiation and/or direct activation are also observed with $GABA_A$ receptors. The complex effects of neurosteroids on both nAChR and $GABA_A$ receptor function suggest the existence of multiple neurosteroid binding sites on each pLGIC (Hosie et al., 2006; Paradiso et al., 2001).

Considerable evidence implicates the transmembrane α-helix, M4, in the allosteric modulation of nAChR activity by both neurosteroids and other sterols, such as cholesterol. Distinct binding sites and/or cholesterol recognition motifs have been identified along the length of M4 (Baier et al., 2011; Blanton et al., 1999; Garbus et al., 2002). Of particular relevance, however, are the effects of the neurosteroid, 17β-estradiol, on neuronal α4β2 nAChRs. 17β-estradiol potentiates human α4β2 nAChRs, but has no effect on rat α4β2 nAChRs. Through formation of chimeras between human and rat nAChRs, the final four amino acid residues in post-M4 were shown to form part of the binding site for 17β-estradiol (Paradiso et al., 2001). Steroid binding to these and the other residues in the TMD could promote interactions between post-M4 and the Cys-loop to promote channel gating. Significantly, the steroid binding site can be moved to the β2 subunit, without loss of the potentiating effects (Jin and Steinbach, 2011). The structure of M4 is thus important to gating whether or not M4 is located on an a- or a non α-subunit.

A similar approach using chimeras formed between murine and *Drosophila* subunits has also been used to map the sites of neurosteroid-induced potentiation of $GABA_A$ receptors. Further mutagenesis and docking studies localized the neurosteroid potentiation site to a pocket extending from M1 towards post-M4, with hydrogen bonds formed between the steroid and polar residues on both of these transmembrane α-helices (Hosie et al., 2006; Ueno et al., 2004). It is striking that the insertion of a bulky steroid ring in between M4 and

M1/M3 in α4β2 nAChRs and $GABA_A$ receptors, and that the insertion of bulky interacting aromatic residues at the same interface of ELIC both potentiate activity.

8.1.8 M4 and the folding and trafficking of nAChRs

Many factors are known to influence folding, assembly, and trafficking of nAChRs to the cell surface, including structural features in both the ECD and ICD, as well as the palmitoylation of the cytoplasmic loops, etc. (Amici et al., 2012; Beeson et al., 2003; Tsetlin et al., 2011). Considerable evidence also suggests an important role for M4. In particular, while the hydrophobic transmembrane portion of M4 can be replaced with transmembrane α-helices from other proteins with minimal functional consequences, post-M4 appears to be critical for surface expression (Tobimatsu et al., 1987).

The role of M4 in the folding and trafficking of nAChRs has been studied extensively using a variety of mutants. These studies identified an endoplasmic reticulum retention signal, PL(Y/F)(F/Y)xxN, in the pre-M1 region at the interface between the ECD and TMD in muscle-type nAChRs (Wang et al., 2002). For nAChRs to traffic from intracellular vesicles to the cell surface, the retention signal must be masked, which occurs upon both binding of M4 to M1/M3 and upon the co-assembly of multiple subunits. This retention signal is found in neuronal α2-α6 and β2-β4 subunits, but not in the homomeric α7, α8, and α9 subunits. In homomeric receptors, a conserved "RRR" motif directly preceding the site of the heteromeric ER retention signal has been implicated in assembly, folding and trafficking (Alves et al., 2011; Vicente-Agullo et al., 2001). Positive charges of this motif may interact with the electronegative residues on post-M4 to mediate this process. A pair of positively charged residues (His408 and Arg429) flanking the αM4 transmembrane α-helix in the muscle-type nAChR at the level of the polar heads of the phospholipid bilayer is also critical for cell-surface expression (Roccamo and Barrantes, 2007).

A critical role for M4 binding to M1/M3 has also been demonstrated in the folding and trafficking of other pLGICs. When expressed in oocytes, the glycine receptor is cleaved within the intracellular loop, but still undergoes agonist-induced channel gating. To monitor

the role of M4 binding in folding, a truncated glycine receptor containing both the ectodomain and the first three TMD α-helices was expressed in oocytes, but the resulting protein product aggregated in intracellular membranes (Haeger et al., 2010). Co-expression with a second construct coding for the M4 α-helix, however, rescued both folding and cell surface expression. The cell-surface expressed channels were indistinguishable from wild type channels in terms of their gating behavior. Also revealed was the need for complementarity between M4 and the M1/M3 interface, as cross-combinations of separately expressed glycine and 5HT3 N-terminal truncations and M4 helices failed to co-assemble into functional channels. Significantly, aromatic interactions at the interface between M1, M3, and M4 were found to be critical for M4 binding to M1/M3, and thus in the folding and trafficking of these pLGICs.

Additional studies highlight the role of post-M4. Deletion of C-terminal residues from M4 in the homologous GABAρ1 (Reyes-Ruiz et al., 2010) and 5-HT_{3A} (Butler et al., 2009) receptors leads to non-functional channels. In the latter case, elimination of 2 or more residues prevents trafficking to the cell surface, suggesting that the masking of an ER retention motif in cell surface trafficking is a feature of many pLGICs. Notably, the role of M4 in trafficking and folding of pLGICs is not limited to masking ER retention signals. M4 binding to M1/M3 in a homomeric α7/$5HT_{3A}$ chimera locks the chimera in a functional conformation via direct post-M4/Cys-loop interactions (Pons et al., 2004).

In this context, it is intriguing to note that several naturally occurring congenital myasthenic syndrome mutations occur in the M4 transmembrane α-helix of muscle type nAChRs. Although the αM4 C418W mutation discussed above has only modest effects on nAChR expression in HEK cells, the surface levels of various Cys418 mutants expressed in Xenopus oocytes were heavily dependent on the nature of the amino acid replacement, ranging from a slight reduction (C418S/H) to a total abolishment (C418G) (Tamamizu et al., 1999). Substantial changes in expression of nAChRs at the motor endplate have also been observed with other congenital myasthenic syndrome mutations, particularly in the case of mutations in the ε-subunit. A cysteine residue in post-M4 (Cys470) appears to be essential for the maturation and surface expression of adult nAChRs (Ealing et al., 2002).

Finally, the observation that thick membranes support slow agonist-induced conformational transitions from uncoupled to coupled conformations may be relevant. Neuronal nAChRs traffic to the cell surface via lipid rafts, and disruption of these rafts leads to both altered cell surface exposure and altered nAChR function (Baenziger and daCosta, 2013; Baier et al., 2010; Borroni and Barrantes, 2011). Integral membrane proteins with shorter transmembrane α-helices tend to remain in intracellular membrane compartments, possibly because they hydrophobically match the thinner intracellular membranes more favorably (Bretscher and Munro, 1993; Lundbaek et al., 2003). Partitioning of the nAChR into thicker lipid rafts could favor transitions from uncoupled to coupled conformations, as we observe in the thicker di22:1 PC model membranes. If the transition from an uncoupled to a coupled conformation leads to a preferential alignment of M4 perpendicular to the membrane surface, the increased hydrophobic length of M4 should promote trafficking to the cell surface. Such a mechanism could explain why nicotine acts as a chaperone to promote cell-surface expression of the high affinity $(\alpha4)_2(\beta2)_3$ nAChR versus the lower affinity $(\alpha4)_3(\beta2)_2$ nAChR (Xiao et al., 2009). Preferential nicotine binding could lead to maturation of the high affinity $(\alpha4)_2(\beta2)_3$ nAChRs toward coupled (resting or desensitized) conformations where M4 is aligned closer to the bilayer normal to promote cell-surface expression. In this scenario, limited binding would thus have minimal effect on the cell-surface trafficking of low affinity $(\alpha4)_3(\beta2)_2$ nAChRs.

8.1.9 Conclusions

There are complex and diverse roles for the outermost transmembrane α-helix, M4, in nAChR function. M4 is often referred to as the "lipid-sensor", emphasizing its putative role in the functional sensitivity of the *Torpedo* nAChR to its membrane environment. M4 also plays an important role in both the assembly and trafficking of nAChRs to the cell surface, as well as in the potentiation of nAChRs by neurosteroids. Although not discussed in detail here, M4 often contributes to the binding sites for a variety of TMD modulators.

Current structural data highlight the interfaces between M4 and the adjacent transmembrane α-helices, M1 and M3, as sites for lipid binding. Both lipid binding and bulk membrane properties may influence interactions between M4 and M1/M3. These inter-α-

helical sites of action are reminiscent of the binding sites for allosteric agonists, which are located at interfaces between subunits in the ECD. Although individual transmembrane α-helices are not typically regarded as “domains”, these secondary structural elements function as distinct structural units during gating (Mitra et al., 2004). The potential intra-subunit movement of M4 relative to M1 and M3 to position post-M4/Cys-loop interactions could underlie both lipid- and neurosteroid-induced potentiation.

A lipid-dependent uncoupled conformation has been identified that may form as a result of an M4-dependent loss of physical contact between the ECD and the TMD. While this conformation has only been conclusively demonstrated for *Torpedo* nAChRs in reconstituted membranes, it may also exist for other pLGICs. Functionally equivalent conformations have been detected with neuronal nAChRs, and with the detergent-solubilized prokaryotic pLGIC, ELIC. An important goal will be to test for existence of uncoupled nAChRs in biological membranes, and whether lipids or other allosteric modulators enhance the transition from uncoupled to coupled conformations to enhance synaptic communication. The uncoupled state may play a role in the potentiation of pLGICs that is observed with a variety of natural and exogenous effectors.

There is considerable interest in the role of nAChRs in neurodegenerative diseases, such as Alzheimer's disease, Parkinson's disease, as well as in other neurological disorders, such as epilepsy and schizophrenia. The role of lipid-nAChR interactions in disease progression remains to be studied. It is known, however, that neurodegenerative diseases and aging are accompanied by changes in lipid composition (Ledesma et al., 2012; Martin et al., 2010; Sebastiao et al., 2013). Altered lipid profiles leading to altered lipid-nAChR interactions could lead to altered cholinergic activity, with small functional changes resulting in severe physiological effects. An important recent finding is that the chemistry at the M4-M1/M3 interface governs the strength of M4 binding to M1/M3 in a manner that dictates the sensitivities of prokaryotic pLGICs to membrane lipids. The chemistry at this interface varies from one human nAChR subunit to another, suggesting that human nAChRs may exhibit variable M4 binding affinities and thus variable sensitivities to their membrane environments. Fundamental knowledge of the subunit-specific roles of M4 in nAChR

function may prove to be important for understanding the mechanisms of altered cholinergic activity during the course of human disease.

8.2 Review Article 2

Baenziger, J.E., Hénault, C.M., Therien, J.P.D., and Sun, J. (2015). Nicotinic acetylcholine receptor-lipid interactions: Mechanistic insight and biological function. Biochim. Biophys. Acta - Biomembr. *1848*, 1806–1817.

http://dx.doi.org/10.1016/j.bbamem.2015.03.010

8.2.1 Preface

This manuscript is the second of two review articles presented in this thesis. It was published in the journal BBA Biomembranes in 2015 as part of a Special Issue entitled: Lipid–protein interactions. My supervisor and I wrote it, in collaboration with lab members. I contributed particularly to sections 8.2.6.4, 8.2.7.1 and 8.2.7.2 as well as revising the entire document and making figure 8.10.

8.2.2 Graphical Abstract

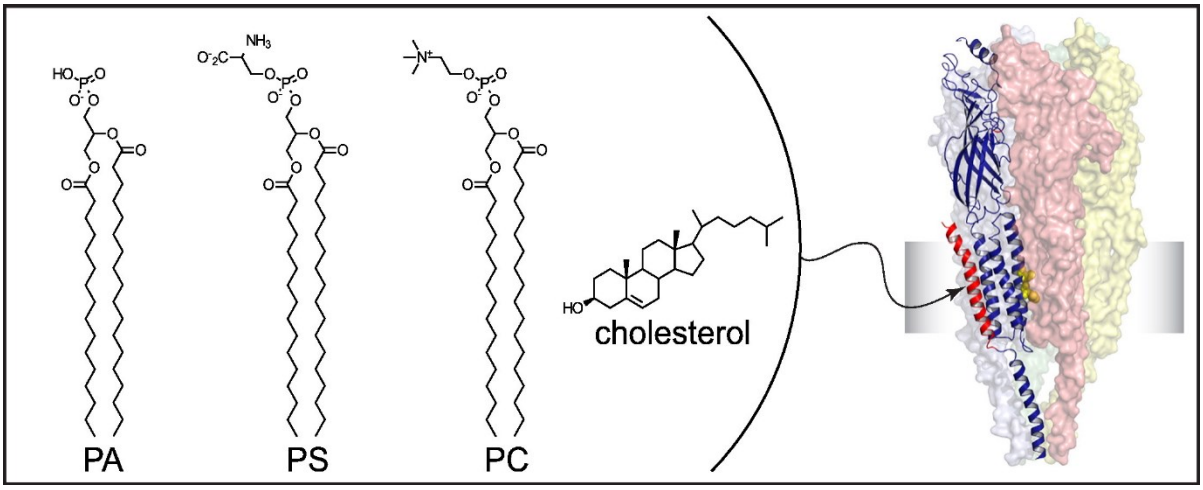

8.2.3 Abstract

Membrane lipids are potent modulators of the nicotinic acetylcholine receptor (nAChR) from *Torpedo*. Lipids influence nAChR function by both conformational selection and kinetic mechanisms, stabilizing varying proportions of activatable versus non-activatable conformations, as well as influencing the transitions between these conformational states. Of note, some membranes stabilize an electrically silent uncoupled conformation that binds agonist but does not undergo agonist-induced conformational transitions. The uncoupled nAChR, however, does transition to activatable conformations in relatively thick lipid bilayers, such as those found in lipid rafts. In this review, we discuss current understanding of lipid–nAChR interactions in the context of increasingly available high resolution structural and functional data. These data highlight different sites of lipid action, including the lipid-exposed M4 transmembrane α-helix. Current evidence suggests that lipids alter nAChR function by modulating interactions between M4 and the adjacent transmembrane α-helices, M1 and M3. These interactions have also been implicated in both the folding and trafficking of nAChRs to the cell surface. We review current mechanistic understanding of lipid–nAChR interactions, and highlight potential biological roles for lipid–nAChR interactions in modulating the synaptic response.

8.2.4 Introduction

The nicotinic acetylcholine receptor (nAChR) from *Torpedo* is the prototypic member of a broad family of pentameric ligand-gated ion channels (pLGICs) that are found in pre-, post-, and non-synaptic membranes of the central and peripheral nervous systems. These neurotransmitter receptors perform important roles in both synaptic communication and information processing, have been implicated in a variety of neurological processes and diseases, and are targets of numerous pharmaceuticals (Dani and Bertrand, 2007; Kalamida et al., 2007; Mineur and Picciotto, 2008; Mufson et al., 2008; Taly et al., 2009).

Early attempts to isolate and reconstitute the *Torpedo* nAChR in model membranes first highlighted the functional sensitivity of the nAChR to lipids. To retain agonist-induced channel flux, the nAChR must be solubilized and purified in the presence of lipid, and then placed in a membrane with an appropriate lipid composition (Criado et al., 1982; Epstein and Racker, 1978; Fong and McNamee, 1986; Heidmann et al., 1980). The exquisite lipid sensitivity of the *Torpedo* nAChR is of interest because even subtle changes in human nAChR activity have profound effects on human biology (Schaaf, 2014; Shen et al., 2006). In addition, the lipid environment of the human nAChR changes as the nAChR traffics from intracellular membranes to its pre-, post-, or non-synaptic locations in the plasma membrane, as well as during both aging and neurodegenerative disease (Ledesma et al., 2012; Martin et al., 2010; Sebastiao et al., 2013). These changes in the nAChR lipid micro-environment during both normal and abnormal brain functions likely influence cholinergic biology to alter synaptic communication.

The relative abundance of the nAChR in the electric fish *Torpedo* has made it the ideal model for studies of ligand-gated ion channel structure/function relationships. Biophysical and biochemical studies over the past three decades have led to an extensive literature on lipid–nAChR interactions, which has been summarized in several comprehensive reviews (Baenziger and Corringer, 2011; Barrantes, 2002, 2004, 2007; Fantini and Barrantes, 2009). In the past decade, a 4 Å resolution cryo-electron microscopy model of the *Torpedo* nAChR (Figure 8.6) (Unwin, 2005), as well as X-ray crystal structures of homologous pLGICs (Althoff et al., 2014; Bocquet et al., 2009; Hassaine et al., 2014;

Hibbs and Gouaux, 2011; Hilf and Dutzler, 2008, 2009; Miller and Aricescu, 2014; Nury et al., 2011a; Sauguet et al., 2013) and water-soluble homologs of the nAChR extramembranous agonist-binding domain (Brejc et al., 2001; Dellisanti et al., 2007), and NMR structures of nAChR transmembrane domains (Bondarenko et al., 2010, 2014) have provided an increasingly detailed picture of both nAChR structure and the nature of ligand-induced conformational change. With this structural data in hand, we are now in an unprecedented position to probe the mechanisms underlying lipid–nAChR interactions at a structural/mechanistic level.

This review focuses on our current understanding of lipid–nAChR interactions in the context of these recently solved pLGIC structures. We review the structural properties of the *Torpedo* nAChR, the *Torpedo* nAChR's lipid requirements, and current models of lipid–nAChR interactions. We also highlight potential roles for lipids in the folding, cell-surface trafficking, and domain localization of the nAChRs in mammalian tissues.

Figure 8.6 Structure of the A) nAChR, B) GLIC, and C) ELIC

A) A side view of the *Torpedo* nAChR structure (PDB ID: 2BG9) is shown on the left with the agonist-binding domain (ABD) in red, the transmembrane domain (TMD) in blue, and the cytoplasmic domain (CD) in green. Residues contributing to the proposed channel gate (αLeu251, αVal255 and homologous residues in the β, γ, and δ subunits) are shown as yellow spheres. The agonist binding site αTrp149 is shown as cyan spheres. Top down views of the ECD and TMD are shown on the right. B) Side view of the GLIC structure (PDB ID: 3EAM) with coloring as in A). Residues contributing to the proposed channel gate (I233, I240, L241) are shown as yellow spheres. C) Side view of the ELIC structure (PDB ID: 2VL0) with coloring as in A). Residues contributing to the proposed channel gate (L239 and F246) are shown as yellow spheres. The agonist binding site F187 is shown as cyan spheres.

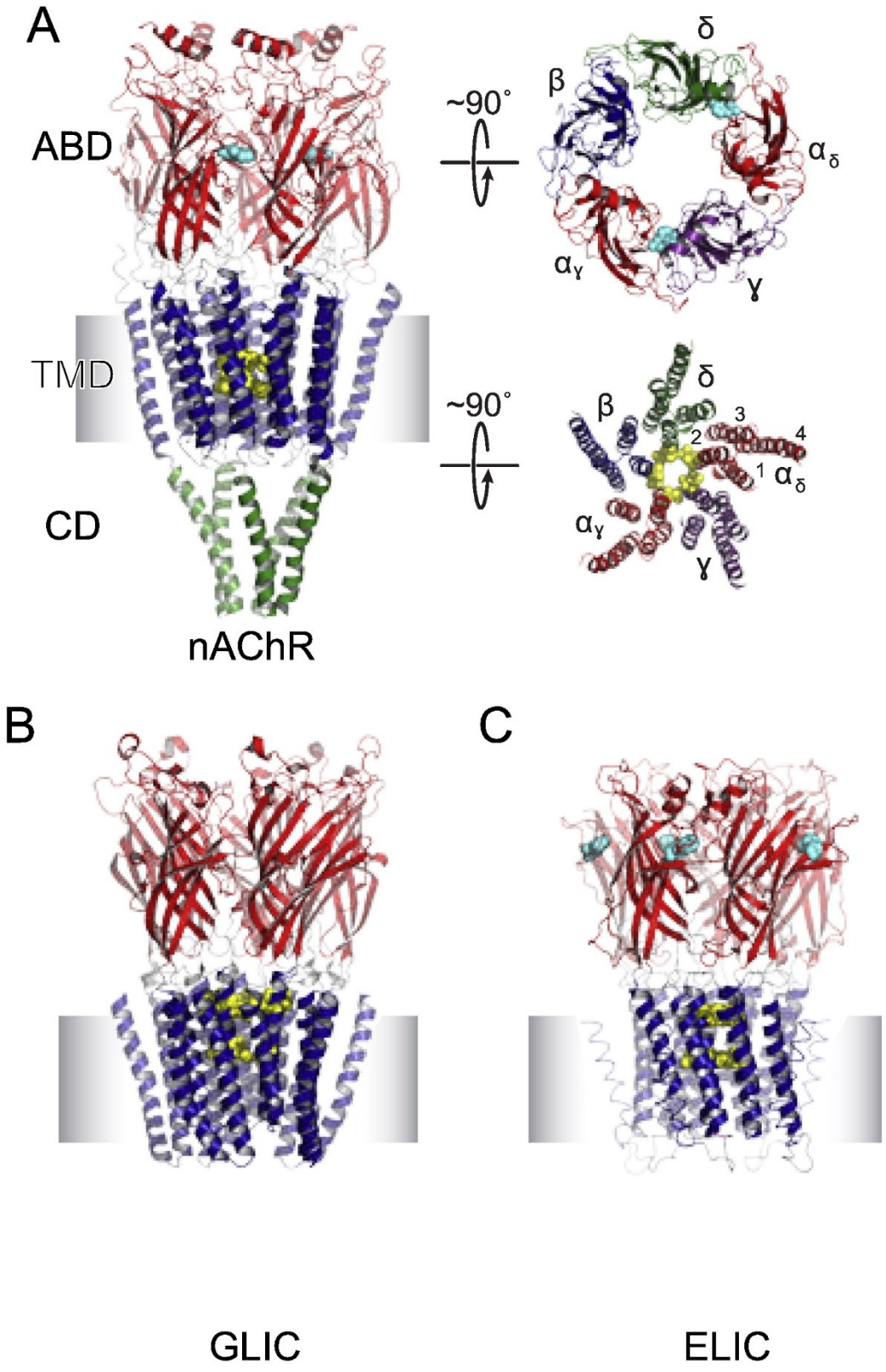
A
ABD
TMD
CD
nAChR
~90°
~90°
δ
β
α_δ
α_γ
γ
δ
β
3
2
4
1
α_δ
α_γ
γ
B
C
GLIC
ELIC

8.2.5 nAChR structure

There are seventeen homologous nAChR subunits in mammals (α1–α10, β1–β4, γ, ε, and δ) that combine to form a variety of either homo-pentameric or hetero-pentameric structures(Jones and Sattelle, 2010). The *Torpedo* nAChR is most similar to the muscle-type nAChR found at the neuromuscular junction, being formed from four distinct subunit types organized in an $(\alpha1)_2\beta1\gamma\delta$ pentamer. In the adult muscle, the fetal γ-subunit of the $(\alpha1)_2\beta1\gamma\delta$ pentamer is replaced by the ε-subunit. nAChRs are also an important part of the central nervous system, with both heteromeric α4β2 and homomeric α7 nAChRs abundant throughout the human brain, and less abundant combinations, such as α3β4, α3β2, and α6β2β3 nAChRs, targeted to specific brain regions (Dani and Bertrand, 2007; Taly et al., 2009).

The five subunits of the *Torpedo* nAChR pentamer are arranged pseudo-symmetrically around a central axis that functions as an ion channel (Figure 8.6A) (Unwin, 2005). Each subunit contributes three distinct domains, a roughly 200-residue long N-terminal extracellular domain (ECD) responsible for agonist binding, a roughly 150-residue long transmembrane domain (TMD) responsible for ion channel conductance, and a cytoplasmic domain of variable length that links to the cytoskeleton. The ECD of each subunit consists of 10 β-strands (β1–β10) forming two β-sheets that fold into a classic β-sandwich. The α-subunit contributes the principal face of each agonist site (Kao and Karlin, 1986), with the complementary face formed by the adjacent γ- and δ-subunits (Corringer et al., 1995; Czajkowski et al., 1993). The TMD of each subunit contributes four transmembrane α-helices (M1–M4) organized in a four-helix bundle.

The five M2 α-helices line the channel pore, while M1 andM3 from each subunit form a ring of α-helices that shield M2 from the membrane (Corringer et al., 2000; Miyazawa et al., 2003; Unwin, 2005). The M4 α-helices are located on the periphery of each subunit where they are exposed to the lipid bilayer. The cytoplasmic domain of each subunit contributes an α-helix that extends away from the membrane surface. The cytoplasmic domain is located in a long loop positioned between transmembrane α-helices M3 and M4.

Communication between the ECD and TMD in each subunit is mediated primarily by the covalent link between the C-terminus of β10 in the ECD and the N-terminus of M1 in the TMD, as well as by noncovalent connections between the β1/β2 and β6/β7 loops (the latter is referred to as the Cys-loop in eukaryotic pLGICs) of the ECD and the M2–M3 linker of the TMD (Figure 8.7) (Jha et al., 2007; Lee and Sine, 2005). Although the detailed structural changes that occur when agonist binding couples to channel gating remain controversial, it is thought that concerted movements of the two β-sheets in the ECD lead to changes in structure of both the β1–β2 and β6–β7 loops, which are then proposed to translate into movement of the pore-lining M2 α-helices via direct interactions with the M2–M3 linker (Bocquet et al., 2009; Hibbs and Gouaux, 2011; Hilf and Dutzler, 2009; Lee and Sine, 2005; Lummis et al., 2005; Sauguet et al., 2014; Unwin and Fujiyoshi, 2012). In the closed resting conformation, the ion channel is occluded by hydrophobic residues located near the center of the bilayer that provide a barrier to the flow of a solvated ion (Figure 8.6) (Beckstein and Sansom, 2006). Upon gating to the open state, a proposed twisting and tilting of the M2 α-helices widen the pore by ~3 Å, allowing the flow of solvated ions down their electrochemical gradient. Prolonged exposure to agonist leads to the formation of one or more poorly defined channel inactive desensitized conformations, which are characterized by a relatively high affinity for agonist (Changeux and Edelstein, 2005).

Figure 8.7 Conformations of M4 at the ECD/TMD interface of the nAChR, GLIC and ELIC

Structures are for the A) nAChR (PDB ID: 2BG9), B) GLIC (PDB ID: 3EAM), and C) ELIC (PDB ID: 2VL0). In each case, post-M4, the β1–β2 loop, the β6–β7 loop (Cys-loop), and the M2–M3 linker are highlighted in orange, light blue, green, and red, respectively. For the nAChR, direct interactions between post-M4 (Gln435) and the Cys-loop (Phe137) are circled. For GLIC, a lipid molecule (beige space filling model) bridges interactions between post-M4 (Phe315) and the β6–β7 loop (Phe121).

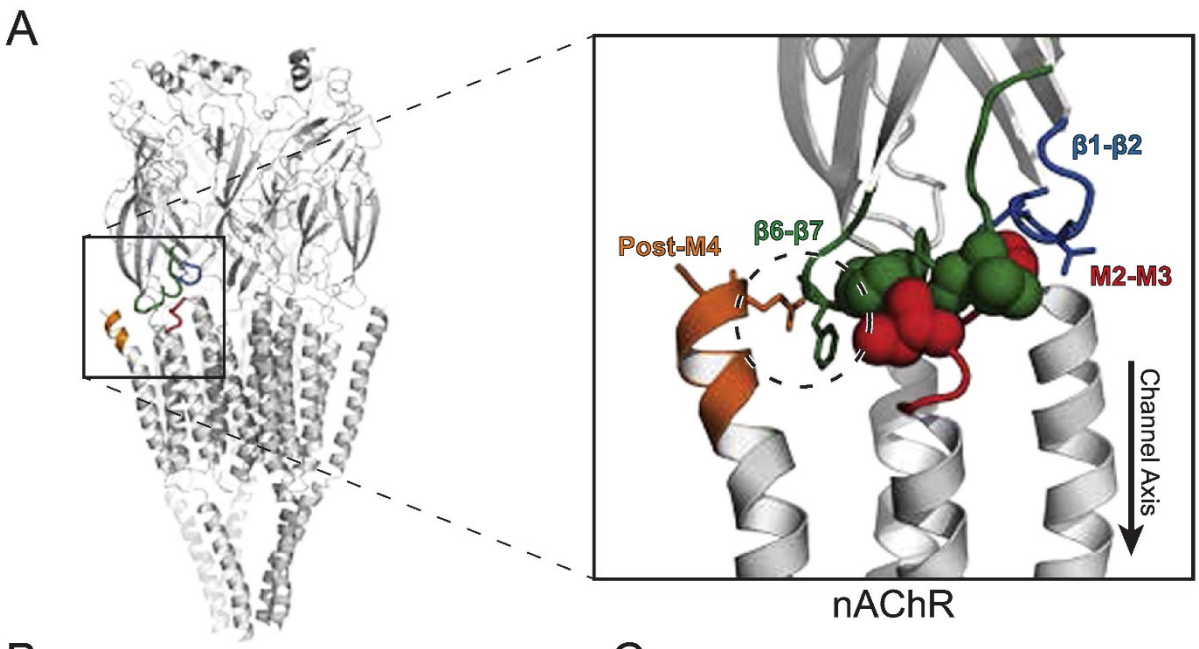
A
β1-β2
Post-M4
β6-β7
M2-M3
Channel Axis
nAChR

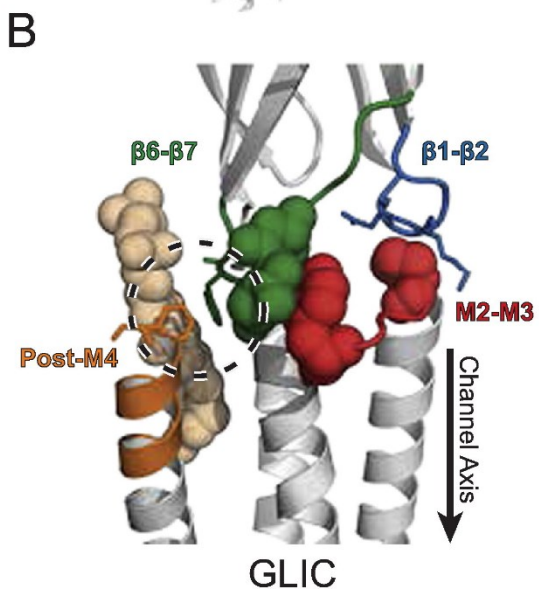
B
β6-β7
β1-β2
M2-M3
Post-M4
Channel Axis
GLIC

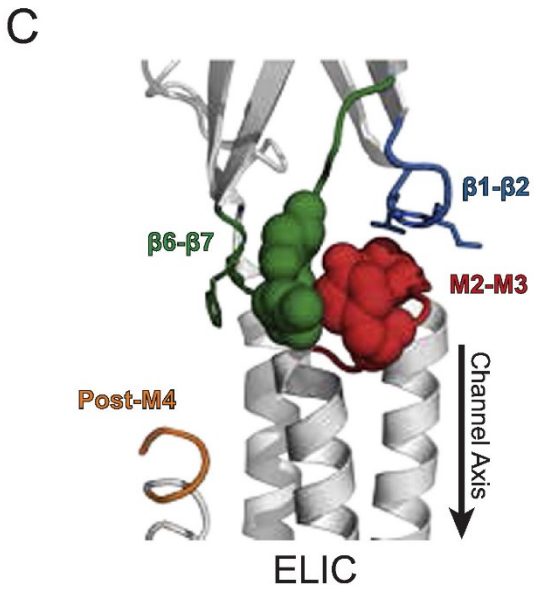
C
β1-β2
β6-β7
M2-M3
Post-M4
Channel Axis
ELIC

8.2.6 Lipid-dependent modulation of nAChR function

8.2.6.1. The nAChR's lipid requirements

Studies in the 1980s established that the ability of the *Torpedo* nAChR to both undergo agonist-induced state transitions and flux cations across the membrane depends on the nAChR's surrounding lipid environment (Criado et al., 1982, 1984; Fong and McNamee, 1986; Ochoa et al., 1983; Rankin et al., 1997). Although a variety of lipids and membrane properties were found to influence the nAChR, both cholesterol and anionic lipids quickly emerged as being critical for channel function. The role of cholesterol in promoting nAChR function is not surprising given that cholesterol is a major component of native *Torpedo* membranes (~35 mol%). Anionic lipids are also common (~15 mol%), with phosphatidylserine (PS) being the dominant anionic lipid (~10 mol%) and phosphatidylinositol (PI), phosphatidic acid (PA), and cardiolipin found in lesser amounts (Mantipragada et al., 2003). The lipid requirements of the nAChR in reconstituted membranes thus reflect the natural lipid composition of *Torpedo* membranes.

Many of the original assays designed to survey lipid requirements, however, simply probed whether the inclusion of a particular lipid in a PC membrane stabilized a measurable pool of functional nAChRs. As these assays could not accurately quantify the relative proportions of activatable versus non-activatable conformations, membranes were typically characterized as either supporting channel function or stabilizing a non-functional nAChR. For example, PC membranes containing cholesterol and an anionic lipid at a 3:1:1molar ratio were found to stabilize a large pool of agonist-responsive nAChRs, while 3:1 molar ratios of PC/cholesterol, PC/PS, PC/PA, or PC alone did not (Fong and McNamee, 1986). Subsequent studies revealed that lipids influence nAChR function primarily via a conformational selection mechanism, modulating the equilibria between functional and non-functional conformations (see section 8.2.6.3) (Baenziger et al., 2000; Ryan et al., 1996). Increasing levels of either cholesterol or PA alone in a PC membrane were found to stabilize an increasing proportion of agonist activatable resting state nAChRs, with even low dosages of either lipid having measurable effects (Baenziger et al., 2000). Even though the levels of cholesterol or PA in a PC membrane that are required to *optimally* support nAChR channel

function are beyond those found in native membranes, these findings suggest that neither cholesterol nor anionic lipids are absolutely essential for the nAChR to undergo agonist-induced state transitions.

The lack of a specific requirement for cholesterol is supported further by the observation that several cholesterol analogs and other neutral lipids, such as diacylglycerol, effectively replace cholesterol in PC/anionic lipid bilayers to support channel function (Labriola et al., 2010; Sunshine and McNamee, 1992). On the other hand, while anionic lipids are broadly effective at promoting agonist-induced flux in the presence of PC and cholesterol (Sunshine and McNamee, 1992), distinct efficacies emerge in the absence of cholesterol. Binary mixtures of PC and PA stabilize a large pool of agonist-responsive nAChRs, while mixtures of PC and PS stabilize predominantly non-activatable conformations (daCosta et al., 2002, 2004). There is clearly more to the effects of anionic lipids on nAChR function than the net anionic lipid charge.

The observed complexities in lipid–nAChR interactions may stem from the fact that lipids exert their effects on channel function via both specific and non-specific mechanisms. Cholesterol may bind to sites within the nAChR TMD (see Section 8.2.6.2). It may also influence nAChR function by increasing the order of PC bilayers, thus influencing other bulk membrane properties, such as bilayer thickness(Barrantes, 2004; Lundbaek et al., 2003). Bulk membrane effects would explain the ability of cholesterol analogs and other neutral lipids to substitute for cholesterol in promoting channel function, as well as why a cholesterol analog covalently linked to PC, which presumably resides within the bulk membrane environment, is as effective as free cholesterol in supporting nAChR function (Addona et al., 1998).

The distinct efficacies of PA and PS in supporting nAChR function in the absence of cholesterol can also be rationalized in terms of both specific and non-specific lipid–nAChR interactions. The anionic lipid charge may be required to promote effective electrostatic interactions within the nAChR (see, for example (Xiu et al., 2005)), but such interactions may only be effective when the nAChR is immersed in an appropriate bulk membrane physical environment—such as that created in the presence of cholesterol. High levels of the

anionic lipid PA in a PC membrane may be uniquely effective at stabilizing a functional nAChR because PA has both an anionic charge and a small head group. Given the small head group, incorporation of PA into a PC bilayer leads to an ordering of the membrane and an increase in its gel-to-liquid phase transitions (daCosta et al., 2002), which may mimic the ordering effects of cholesterol. In contrast, high levels of PS, which has a larger head group, in a PC membrane, have little effect on reconstituted membrane physical properties (daCosta et al., 2004).

The role of bulk membrane physical properties in modulating nAChR function has been debated in numerous publications, with some studies concluding that bulk membrane effects are the key modulators of channel function, and others concluding that lipid chemistry, and thus presumably the binding of lipids to specific sites on the nAChR, is more important (daCosta et al., 2004; Fong and McNamee, 1986; Sunshine and McNamee, 1994). Part of the controversy likely stems from the fact that membrane physical properties have typically been assessed using bilayer gel-to-liquid crystal phase transition temperatures and/or either fluorescent or spin-labeled probes, the latter providing a numerical measure of membrane order. These bulk membrane parameters may not be sufficiently robust to capture the complex physical environment of a reconstituted nAChR membrane. It is also difficult to probe the influence of bulk membrane properties, such as membrane hydrophobic thickness, curvature stress and bilayer ordering, without changing the bilayer lipid chemistry, complicating the interpretation of the experimental findings. A recent study, however, showed that while the nAChR in PC membranes containing di18:1 or shorter acyl chains is locked in a non-activatable "uncoupled" conformation, the nAChR in relatively thick PC membranes with di22:1 acyl chains undergoes agonist-induced conformational transitions, even in the absence of cholesterol or anionic lipids (daCosta et al., 2013). The latter provides definitive evidence that membrane properties influence agonist-induced state transitions, and highlights the need for further studies to better understand the link between the nAChR and its membrane physical environment.

Finally, it should be noted that the lipid requirements of the nAChR in simple reconstituted membranes may not accurately reflect the lipid requirements of the nAChR in natural membrane environments. Biological membranes are asymmetric with an uneven

distribution of lipids in the two leaflets of the lipid bilayer (Barrantes, 2004). The possibility that lipids have different effects on nAChR function when included in different leaflets has not yet been rigorously tested. As well, natural membranes exhibit lateral separations of lipids into micro-domains/lipid rafts, with the lipid composition in the microenvironment surrounding the nAChR not matching the bulk membrane lipid composition. Finally, an intriguing study showed that the inclusion of only 1.6 mol% PA in a complex synthetic membrane composed of PC, PS, PI, and cholesterol has a measurable effect on the proportion of agonist-responsive nAChRs, while the inclusion of 1.6% PA in a minimal PC membrane does not (Hamouda et al., 2006b). It appears that PA has synergistic effects with other anionic lipids on nAChR function. These studies collectively show that the levels of a particular lipid required to measurably influence nAChR function in a simple homogeneous reconstituted membrane do not necessarily match the levels of the same lipid that are required in a biological membrane to influence function, where lipid distributions are heterogeneous and where synergistic effects on function likely occur. Even trace lipids may have an important role in nAChR function in biological membranes. The possibility that lipids involved in signaling influence nAChR function is obviously of considerable importance, particularly if signaling lipids are enriched in the nAChR's lipid microenvironment.

In summary, although many lipids and membrane properties influence nAChR function, mixtures of both cholesterol and anionic lipids are particularly effective at stabilizing the nAChR in a functional conformation. Bulk membrane physical properties have an important, yet poorly understood role. Additional research is still required to elucidate how a variety of biologically relevant lipids influence nAChR function, especially in the context of the complex lipid compositions and heterogeneous distributions of lipids that are found in biological membranes. An important remaining goal is to extrapolate the findings from studies of lipid–nAChR interactions in reconstituted nAChR membranes to biological membranes. Such studies are essential to understanding the role of lipid–nAChR interactions at the biological synapse.

Figure 8.8 Phospholipids bound to the surface of A) GluCl and B) GLIC

Top panel: GluCl (PDB ID: 4TNW) and GLIC (PDB ID: 3EAM) are shown in a membrane-embedded surface representation, with one subunit as a blue cartoon diagram and the lipid-exposed M4 α-helix in red. Residues contributing to the channel gate are highlighted as yellow spheres. Lipids modeled into the electron density are presented as tan spheres. Three lipids are bound to each subunit in GLIC. In GluCl, the lipid binding site is at the inter-subunit interface. *Bottom panel*: top view of the TMD looking from the extracellular membranous surface.

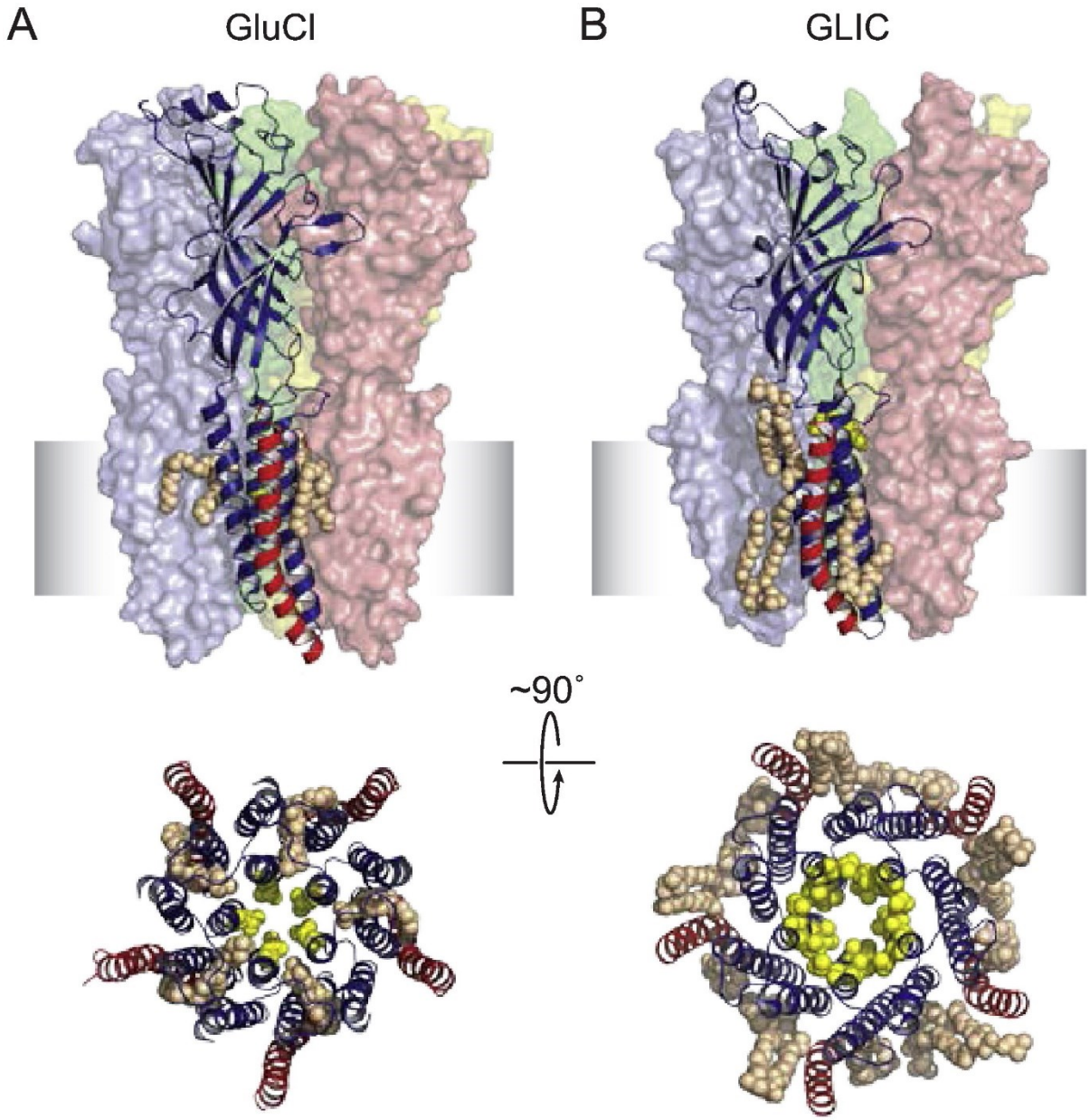
A
GluCl
B
GLIC
~90˚

8.2.6.2. Sites of lipid-nAChR interactions

There are likely both annular and non-annular sites of lipid action at the nAChR (Antollini and Barrantes, 1998; Jones and McNamee, 1988). Non-annular cholesterol binding sites between transmembrane α-helices were originally proposed based on fluorescence quenching studies with brominated lipids (Jones and McNamee, 1988), and are supported by both molecular dynamics simulations and bioinformatics studies (Baier et al., 2011; Brannigan et al., 2008) (see also (Hénin et al., 2014)). Cholesterol binding to non-annular cavities located between α-helices within the TMD α-helical bundles stabilizes the transmembrane domain structure, facilitating interactions with the ECD (Brannigan et al., 2008). A putative modulatory PC binding site located at the interface between subunits in the homologous glutamate-activated chloride channel, GluCl, has also been identified (Figure 8.8A) (Althoff et al., 2014).

Cholesterol and anionic lipids show a strong preference for the annulus of lipids that surrounds the outer surface of the nAChR (Ellena et al., 1983; Fernandez Nievas et al., 2008; Leibel et al., 1987; Marsh and Barrantes, 1978). At any given moment in time, both cholesterol and anionic lipids in this annulus are "bound" to the nAChR surface, although each bound lipid exchanges rapidly with others in the bulk membrane environment. Annular lipid binding sites have been observed in crystal structures of the prokaryotic nAChR homolog, GLIC (Figure 8.8B) (Bocquet et al., 2009). In fact, the entire lipid-exposed surface of the nAChR may serve as an "allosteric site" that is sensitive to bulk membrane physical properties, such as membrane hydrophobic thickness.

Chemical labeling studies in the early 1990s showed that the M4 transmembrane α-helix forms the predominant interface between the TMD of each subunit and the lipid environment (Blanton and Cohen, 1992, 1994). The location of M4 at the periphery of the TMD led to the suggestion that M4, in particular, plays a central role in lipid-sensing (Antollini et al., 2005; Barrantes, 2003; Xu et al., 2005). In support of this assertion, a photoactivatable cholesterol analog labels sites on the lipid-exposed surface of the nAChR, including predominant residues on M4 (Corbin et al., 1998; Hamouda et al., 2006a). Two of the three lipid binding sites observed in the crystal structure of GLIC are found at the

interfaces between M4 and the adjacent TMD α-helices M1 and M3 (see Section 8.2.7.1). Numerous mutations of M4 lipid-facing residues on both *Torpedo* and muscle-type nAChRs, which alter M4–lipid interactions, also alter channel function (Bouzat et al., 1998; Lasalde et al., 1996; Lee et al., 1994; Li et al., 1992; Shen et al., 2006; Tamamizu et al., 2000), with the amino acid changes studied to date typically affecting channel opening and closing rates (Bouzat et al., 1998, 2000, 2002). Finally, M4-swapped chimeric constructs of the homologous glycine receptor α1 and α3 subunits demonstrate that subunit-specific agonist efficacy is driven in large part by M4, with agonist sensitivity mediated by differences in M4–lipid interactions (Chen et al., 2009). M4 thus likely plays a lipid-sensing role in all members of the broader pLGIC family.

8.2.6.3. Conformational selection and kinetic mechanisms

To understand the mechanisms underlying lipid–nAChR interactions, research initially focused on elucidating the structural changes induced in the *Torpedo* nAChR in the presence of activating lipids. Although preliminary studies using infrared spectroscopy reported substantial changes in secondary structure in the presence of cholesterol and anionic lipids (Butler and McNamee, 1993; Fernandez-Ballester et al., 1994; Fong and McNamee, 1987), it was subsequently shown that the observed spectral changes were due instead to distinct levels of peptide N-^{1}H/N–^{2}H exchange (note that for technical reasons, infrared spectra are recorded in $^{2}H_2O$) (Baenziger et al., 1999; Methot et al., 1995). In fact, the non-functional nAChR in PC membranes (PC-nAChR) retains a native-like secondary and quaternary structure (Bhushan and McNamee, 1990; Methot et al., 1995). PC-nAChR also undergoes thermal denaturation at a temperature comparable to that of resting and desensitized nAChRs (daCosta and Baenziger, 2009; daCosta et al., 2005). The folded PC-nAChR binds agonist, but lacks the capacity to undergo agonist-induced conformational change.

Early chemical labeling and infrared difference measurements suggested that PC-nAChR does not flux cations because it adopts a desensitized conformation, whereas increasing levels of both cholesterol and anionic lipids in PC membranes stabilizes an increasing proportion of activatable resting state nAChRs (Baenziger et al., 2000; Hamouda

et al., 2006b; McCarthy and Moore, 1992; Ryan et al., 1996). These observations led to the hypothesis that membranes influence nAChR function by modulating the natural equilibrium between resting and desensitized conformations, which in native *Torpedo* membranes strongly favors the resting state (Boyd and Cohen, 1980; Heidmann and Changeux, 1979). Subsequent studies, however, showed that the non-functional PC-nAChR does not exhibit the high agonist-binding affinity characteristic of the desensitized conformation (Baenziger et al., 2008; daCosta and Baenziger, 2009). The conformational selection mechanism was thus expanded to include a non-activatable conformation, referred to as the uncoupled state (Figure 8.9) (see section 8.2.6.4). Some membrane environments favor activatable resting (PC/PA/cholesterol), while others favor uncoupled (PC alone) and/or desensitized (PC/PS) nAChRs (daCosta et al., 2009). Lipids also influence the transitions between conformations.

Increasing membrane hydrophobic thickness lowers the activation energy barrier between uncoupled and coupled (resting, open, and desensitized) conformations (daCosta et al., 2013). Mutations to the lipid facing surface of M4 influence both channel opening and closing kinetics. In effect, lipids/membranes influence nAChR function by both conformational selection and kinetic mechanisms. They modify the magnitude of the agonist-induced response by altering the relative proportions of resting, desensitized, open, and uncoupled conformations, as well as the agonist-induced transitions between each of these states.

Note that to fully understand the mechanisms underlying lipid–nAChR interactions, one must have intimate knowledge of the structures of each conformation/transition state, and then elucidate how each lipid/membrane environment interacts preferentially with these states to influence their relative populations, as well as the transitions between them. While this alone is a complex undertaking, a detailed mechanistic understanding is further confounded by the aforementioned possibility that lipids influence function via both direct and indirect mechanisms. The latter raises the possibility that a particular lipid could have one effect on channel function, by preferential binding to one conformation (for example, the resting state), while at the same time have an opposite effect on channel function by changing bulk membrane physical properties to favor another conformation (for example, a

non-activatable desensitized or uncoupled conformation). Deciphering the mechanisms underlying nAChR–lipid interactions remains a daunting task.

Figure 8.9 Conformational selection and kinetic mechanisms of lipid–nAChR interaction

A) nAChR function is usually interpreted in terms of a conformational scheme involving resting (R), open (O), and desensitized (D) conformations (scheme 2). The membrane-reconstituted *Torpedo* nAChR can also adopt a non-responsive uncoupled (U) conformation (scheme 1). B) Left panel: Reaction coordinate diagrams illustrating qualitatively the effects of both lipid composition and membrane bulk properties affect the structure and function of the nAChR. Anionic lipids and cholesterol influence the relative proportion of uncoupled versus coupled conformations by interacting preferentially with "coupled" conformations (i.e., conformations where agonist binding and gating are allosterically coupled), thus lowering their energy relative to uncoupled conformations (a conformational selection mechanism). Membrane thickness influences the transitions between uncoupled and coupled states by lowering the activation energy between these conformations (a kinetic mechanism). Note that the reaction coordinate diagrams are qualitative representations. Individual lipids or lipid mixtures may influence function by a combination of both conformational selection and kinetic mechanisms. Right panel: Proposed models of uncoupling in the context of conformational selection versus kinetic mechanisms of lipid–nAChR interactions.

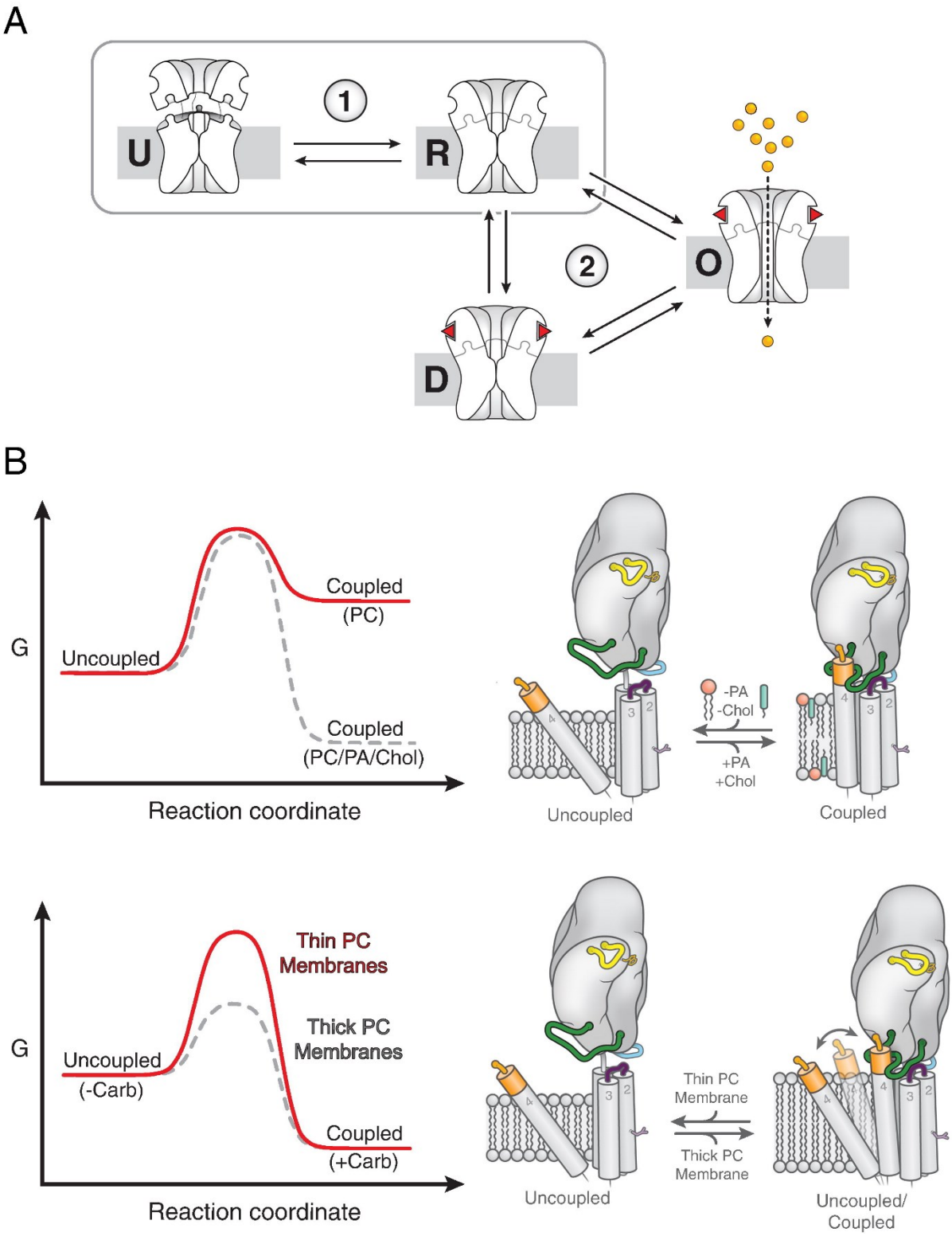
A
U
1
R
2
O
D
B
G
Uncoupled
Coupled
(PC)
Coupled
(PC/PA/Chol)
Reaction coordinate
-PA
-Chol
+PA
+Chol
Uncoupled
Coupled
G
Thin PC
Membranes
Thick PC
Membranes
Uncoupled
(-Carb)
Coupled
(+Carb)
Reaction coordinate
Thin PC
Membrane
Thick PC
Membrane
Uncoupled
Uncoupled/
Coupled

8.2.6.4. The uncoupled nAChR

The proposed conformational selection and kinetic mechanisms that underlie lipid–nAChR interactions likely apply to all membrane proteins, with subtle changes in lipid composition/bilayer physical properties having subtle effects on channel function. As described above, a unique feature of lipid–nAChR interactions is that a functionally silent, uncoupled conformation is stabilized when the *Torpedo* nAChR is reconstituted in PC membranes lacking cholesterol and anionic lipids. The uncoupled conformation exhibits resting-state-like agonist binding, but does not flux cations or undergo agonist-induced transitions to the high affinity agonist-binding desensitized state (daCosta et al., 2009). The fact that the uncoupled nAChR still binds agonist, but does not desensitize indicates that the activation energy barrier between uncoupled and coupled conformations is insurmountably high over the minute time scale of most biophysical measurements. This implies that the structural differences between uncoupled and coupled conformations are energetically more substantial than those between resting, open, and desensitized nAChRs (daCosta et al., 2013).

The identification of a lipid-dependent uncoupled conformation of the *Torpedo* nAChR may be relevant to human cholinergic biology, as anecdotal evidence suggests that neuronal nAChRs also adopt a functionally equivalent conformation. A large proportion of α4β2 nAChRs expressed on the surface of human embryonic kidney cells bind agonist, but do not undergo agonist-induced channel gating, consistent with the existence of a large pool of uncoupled receptors (Fenster et al., 1999; Li and Steinbach, 2010). Some nAChR subtypes, including those with the α6 subunits, exist in oligomeric structures on cell surfaces but do not flux cations in response to acetylcholine binding (Broadbent et al., 2006; Drenan et al., 2008). In fact, the β3 subunit is essential for the biogenesis of α6α4β2β3 nAChRs, yet β3 suppresses acetylcholine-evoked currents. It is possible that the β3 subunit favors formation of an uncoupled state. The normalized current (current per acetylcholine binding site on the surface of the cell) also increases with time after injection of muscle-type cRNA into oocytes, suggesting a time dependent maturation in “folding” to activatable conformations (Li et al., 1990). Chronic nicotine exposure upregulates nAChR trafficking to the cell surface, but there appears to be a role for inactive nAChRs in this process (Nashmi et

al., 2007), with chronic nicotine exposure potentially leading to the activation of previously assembled but inactive nAChRs (Vallejo et al., 2005).

As noted, thicker membranes, such as those found in lipid rafts (Lundbaek et al., 2003; Vuong et al., 2010), promote slow conformational transitions from uncoupled to coupled conformations (daCosta et al., 2013). Neuronal nAChRs require lipid rafts for trafficking to the cell surface (Bruses et al., 2001; Marchand et al., 2002). The above observations raise the intriguing speculation that a lipid raft-dependent transition from uncoupled to coupled conformations represents a final step in the folding and trafficking of nAChRs to the cell surface, as discussed in more detail in 8.2.8.

8.2.6.5. Structural insight into lipid–nAChR interactions

Both crystallographic and functional studies have increasingly provided insight into the nature of nAChR structure and conformational change, opening the door for a more detailed understanding of lipid–nAChR interactions. Kinetic studies show that the structure of the lipid-exposed α-helix, M4, is dynamic when the nAChR shifts between resting and open conformations. When gating, the two αM4 α-helices in the (α1)2β1εδ pentamer move synchronously, each moving as a unit roughly halfway along the reaction coordinate between agonist binding and the open transition state (Mitra et al., 2004). The motions of the εM4 and βM4 follow that of αM4, while δM4 has no apparent motion during gating. The temporal differences in various M4 positions should permit the pentamer to present a unique binding surface to the lipid bilayer in each distinct conformation and/or while transitioning between them. Movement of M4 has also been suggested in the desensitized state (Velisetty et al., 2014). Such structural changes in M4 could expose or mask lipid binding sites, allowing for stronger or weaker interactions with the lipid bilayer that preferentially stabilize different conformations or promote/inhibit transitions between these states. In addition, biophysical measurements and molecular dynamics simulations suggest that the orientation of M4 relative to the membrane normal depends on the presence of cholesterol and bilayer thickness (Antollini et al., 2005; Xu et al., 2005). Lipids may preferentially stabilize different orientations of M4 relative to the remainder of the TMD, altering gating kinetics as M4 moves along the reaction coordinate leading from agonist binding to the open state.

A role has also been proposed for M4 in formation of the lipid dependent uncoupled conformation. The uncoupled nAChR undergoes more extensive peptide N-^{1}H/N-^{2}H exchange than either resting or desensitized nAChRs. Curve-fitting the peptide hydrogen/deuterium exchange curves shows that uncoupling is accompanied by the solvent exposure of previously buried peptide hydrogens (daCosta and Baenziger, 2009). Although the regions of the nAChR that become solvent-exposed have not been defined, the critical importance of the ECD/TMD interface in channel function (Jha et al., 2007; Lee et al., 2009) led to the hypothesis that uncoupling results from structural changes at this interface. One model proposes that weakened interactions leading to an increased physical separation between the ECD and TMD accounts for both the loss of function and the increased solvent accessibility in the uncoupled state (daCosta and Baenziger, 2009). The proposed structural independence of the ECD is supported by a number of crystallographic studies (Brejc et al., 2001; Dellisanti et al., 2007; Nury et al., 2010a).

The nAChR structure also shows that the C-terminus of M4 (post-M4, specifically Gln435) extends beyond the lipid bilayer to interact with a conserved residue (Phe137) in the Cys-loop (Figure 8.7). Given that the Cys-loop plays a central role at the interface between the ECD and TMD, it was postulated that interactions between post-M4 and the Cys-loop are important for coupling agonist-binding to channel gating (daCosta and Baenziger, 2009). Considerable functional data support a role for post-M4 in channel function (Paradiso et al., 2001; Pons et al., 2004; Tobimatsu et al., 1987). The M4 lipid-sensor model proposes that lipids influenceM4 binding toM1/M3 to modulate post-M4/Cys-loop interactions and thus channel function. Ineffective post-M4/Cys-loop interactions could lead to partial dissociation of the ECD from the TMD to form the uncoupled state (daCosta and Baenziger, 2009). Modulatable binding has been discussed in terms of both the conformational selection and kinetic effects of lipids on nAChR function (Figure 8.9) (daCosta et al., 2013).

8.2.7 Prokaryotic pLGICs as models of lipid–nAChR interactions

8.2.7.1. Insight from crystal structures of prokaryotic pLGICs

The homologous homopentameric prokaryotic pLGICs, GLIC and ELIC, are expressed in *Escherichia coli* at levels sufficient for both biochemical and structural studies, and each has yielded several high-resolution crystal structures (Figure 8.6) (Bocquet et al., 2007, 2009; Hilf and Dutzler, 2008, 2009; Sauguet et al., 2013; Tasneem et al., 2005; Zimmermann and Dutzler, 2011). These structures reveal two key features that impact on our understanding of lipid–nAChR interactions.

First, the crystal structures of GLIC exhibit electron density located at the periphery of the TMD, suggesting the presence of partially-ordered lipid molecules (Figure 8.8) (Bocquet et al., 2009). Two of the three lipid binding sites on each subunit are found at the interfaces between M4 and the adjacent TMD α-helices M1 and M3. One of these bridges interactions between post-M4 (F315) and the β6–β7 loop (F121), the loop analogous to the Cys-loop in eukaryotic pLGICs. Intriguingly, the lipid bridging post-M4 to the β6–β7 loop in the GLIC structure is displaced slightly by the inhibitory anesthetic propofol, suggesting that the lipid occupies an allosteric site (Nury et al., 2011a). The finding that lipids bind to theM4–M1/M3 interface in the GLIC structure supports the hypothesis that lipids influence M4–M1/M3 interactions.

Second, crystal structures of ELIC solved in the presence of agonist exhibit electron density in the agonist site, but show no structural rearrangements in the TMD pore relative to crystal structures solved in the absence of agonist (Gonzalez-Gutierrez and Grosman, 2010; Gonzalez-Gutierrez et al., 2012; Zimmermann and Dutzler, 2011). In fact, no movement of the pore-lining M2 α-helices was detected with mutants that prolong channel opening and exhibit no propensity to desensitize. It has been suggested that the ELIC structures reflect a conformation that is refractory to agonist binding (Gonzalez-Gutierrez and Grosman, 2010) — i.e., a conformation that is functionally equivalent to the lipid-dependent uncoupled state of the *Torpedo* nAChR (daCosta and Baenziger, 2013). Significantly, the ELIC structures

exhibit multiple proposed features of the uncoupled nAChR (Figures 8.6 and 8.7): 1) The M4 α-helix is partially unwound and tilted away from the remaining TMD, with several C-terminal M4 residues unresolved. 2) In contrast to the nAChR structure, ELIC shows no direct contact between post-M4 and the β6–β7 loop, and 3) the tilting of M4 away from the remainder of the TMD is accompanied by reduced contact between both the β1–β2 and β6–β7 loops of the ECD and the M2–M3 linker of the TMD. In the nAChR structure, the extended side chains of the β1–β2 and β6–β7 loops engage the M2–M3 linker in a fashion reminiscent of vice grips attached to a metal pipe. In ELIC, the β1–β2 and β6–β7 loops no longer surround the M2–M3 linker, which itself tilts toward the membrane surface so that it approaches the β8–β9 loop on the complementary face of the adjacent subunit. In effect, reduced interactions between M4 and M1/M3 are accompanied by weakened interactions between the ECD and TMD — as predicted by the M4 lipid-sensor model.

8.2.7.2. Testing the role of M4 in pLGIC lipid-sensing

The noted difference in the position of M4 in the crystal structures of ELIC and GLIC is intriguing given the demonstrated importance of aromatic residues in the binding of M4 to M1/M3 during folding of the homologous glycine receptor (Haeger et al., 2010). GLIC has nine aromatic residues at the interfaces between M4 and M1/M3 that are involved in extensive π–π interactions (Figure 8.10A). These strong interactions likely contribute to the apparent tight interactions between M4 and M1/M3 in the GLIC crystal structure. Four of these aromatic residues at the M4–M1/M3 interface are conserved in ELIC. The remaining five aromatics are replaced in ELIC by aliphatic residues (Figure 8.10B). In particular, ELIC lacks a cluster of three aromatic residues located near post-M4 that may be essential in GLIC for effective binding of post-M4 to the remainder of the TMD and/or the β6–β7 loop. The absence of this post-M4 cluster in ELIC may lead to the aforementioned tilting of the C-terminus of M4 away from the main body of the TMD in the crystal structure of ELIC. The lower number of aromatic interactions at the M4–M1/M3 interface may render M4 binding to M1/M3 weaker in ELIC and thus make ELIC more susceptible to the perturbing effects of detergent solubilization during crystallization than GLIC (daCosta and Baenziger, 2013).

Figure 8.10 Aromatic residues at the M4–M1/M3 interface of A) GLIC and B) ELIC

Top panel: Side view of a single TMD from both GLIC and ELIC highlighting aromatic residues at the M4–M1/M3 interface as yellow sticks. *Bottom panel*: Top view from the extracellular surface of a single TMD.

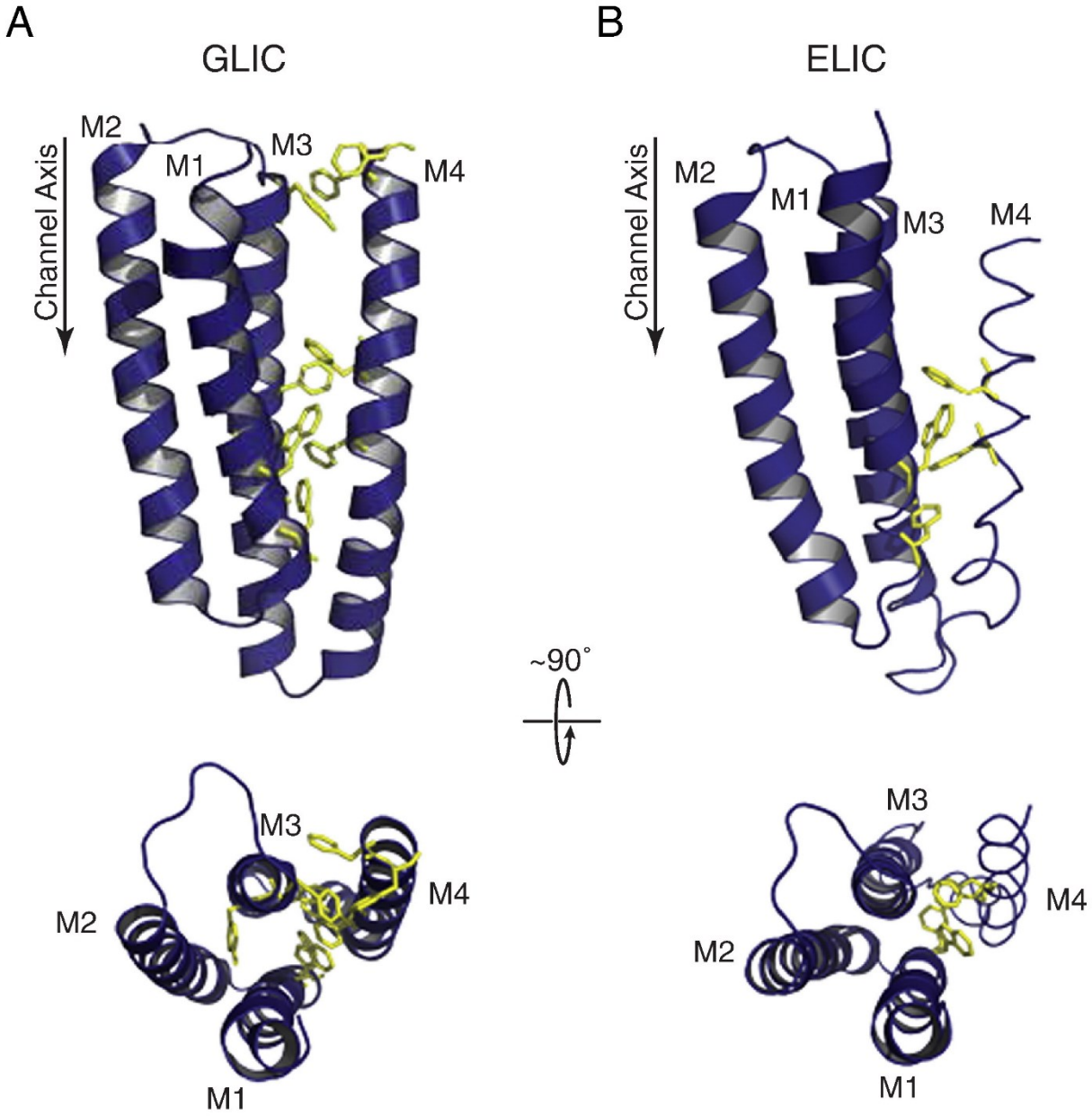
A
GLIC
Channel Axis
M2
M1
M3
M4
M3
M4
M2
M1
~90˚
B
ELIC
Channel Axis
M2
M1
M3
M4
M3
M4
M2
M1

In light of the above structural differences, aromatic substitutions were used to test the effects of altered M4–M1/M3 interactions on pLGIC activity (Carswell et al., 2015a). Ala substitutions of aromatic residues were introduced into the M4–M1/M3 interface of GLIC to weaken M4 binding (Haeger et al., 2010), with every aromatic substitution leading to reduced channel function. Conversely, aliphatic to aromatic substitutions were introduced at the same interface in ELIC to promote M4 binding, with every aromatic addition leading to enhanced channel function. In fact, the introduction of a single pair of interacting aromatic residues on the C-terminus of M4 and the N-terminus of M3 decreased the EC_{50} for ELIC channel gating almost 10-fold, implying close to a 10-fold potentiation of channel function. The data support a key tenet of the M4 lipid-sensor model, that enhanced interactions between M4 and M1/M3 promote coupling between the agonist binding site and channel gate.

Additional studies suggest that modulatable M4 binding to M1/M3 plays a role in pLGIC lipid sensing. Protocols for reconstituting GLIC and ELIC into lipid bilayers have been developed (Carswell et al., 2015a; Dellisanti et al., 2013; Labriola et al., 2013; Velisetty and Chakrapani, 2012; Velisetty et al., 2012). As noted, the extensive aromatic network at the M4–M1/M3 interface in GLIC contributes to relatively strong M4–M1/M3 interactions along the entire length of M4. In contrast to the nAChR, which exhibits few aromatic interactions at the M4–M1/M3 interface, GLIC retains robust agonist-induced gating in the minimal PC membranes that stabilize the uncoupled nAChR (Labriola et al., 2013). In fact, electrophysiological measurements suggest that GLIC function is relatively insensitive to its lipid environment (Dellisanti et al., 2013; Velisetty and Chakrapani, 2012). The intrinsic strength of M4–M1/M3 interactions in GLIC may be sufficient to maintain effective M4–M1/M3 interactions and retain channel function, even in PC membranes lacking cholesterol and anionic lipids. In contrast, although the conserved aromatic residues at the cytoplasmic end of the M4–M1/M3 interface in ELIC appear to be sufficient to stabilize M4–M1/M3 interactions in this region, ELIC does not gate open in response to agonist in these minimal PC membranes. This lack of function may be due to the absence of effective post-M4 aromatic interactions. Significantly, engineering the post-M4 aromatic cluster into ELIC

restores the ability of ELIC to gate open in PC bilayers (Carswell et al., 2015a). Modulatable post-M4–M1/M3 interactions thus play a role in ELIC lipid-sensing.

8.2.8 Lipids and the folding and trafficking of nAChRs

The proposed role of M4 binding toM1/M3 in lipid sensing may also be relevant to the folding, assembly, and trafficking of nAChRs to the cell surface. Although many factors are known to influence mammalian nAChR trafficking (Amici et al., 2012; Beeson et al., 2003; Tsetlin et al., 2011) (see also (Hénault et al., 2015a)), a role for M4 binding to M1/M3 has been clearly demonstrated in the homologous glycine receptor. When expressed in oocytes, the glycine receptor is cleaved within the intracellular loop, but still undergoes agonist-induced channel gating. A truncated glycine receptor containing both the ectodomain and the first three TMD α-helices fails to traffic to the cell surface (Haeger et al., 2010). Co-expression with the M4 α-helix, however, rescued both folding and cell surface expression, with the cell-surface expressed channels indistinguishable from wild type channels in terms of their gating behavior. Aromatic interactions at the interface between M4 and M1/M3 were found to be critical for M4 binding and thus in the folding and trafficking of these pLGICs.

Post-M4 appears to be critical for the surface expression of *Torpedo* nAChRs in frog oocytes (Tobimatsu et al., 1987). Deletion of C-terminal residues from M4 in the homologous GABAρ1 (Reyes-Ruiz et al., 2010) and 5-HT_{3A} (Butler et al., 2009) receptors also leads to non-functional channels. In the latter case, elimination of 2 or more residues prevents trafficking to the cell surface, suggesting that post-M4 plays an important role in cell surface trafficking of many pLGICs. M4 binding to M1/M3 in a homomeric α7/5HT3A chimera locks the chimera in a functional conformation via direct post-M4/ Cys-loop interactions (Pons et al., 2004).

As noted above, thick membranes support slow agonist-induced conformational transitions from uncoupled to coupled conformations. Lipid rafts/microdomains are typically enriched in cholesterol, which orders and increases the hydrophobic thickness of the bilayer (Lundbaek et al., 2003; Simons and Sampaio, 2011). Both muscle-type and neuronal nAChRs require lipid rafts for trafficking to the plasma membrane, with the raft-forming lipids cholesterol, sphingolipids, and ceramides being important (Baier and Barrantes, 2007;

Baier et al., 2010; Bruses et al., 2001; Gallegos et al., 2007; Marchand et al., 2002). Disruption of these rafts leads to both altered cell surface exposure and altered nAChR function (Baier et al., 2010; Borroni and Barrantes, 2011). Integral membrane proteins with shorter transmembrane α-helices tend to remain in intracellular membrane compartments, possibly because they hydrophobically match the thinner intracellular membranes more favorably (Bretscher and Munro, 1993; Lundbaek et al., 2003). Partitioning of the nAChR into thicker lipid rafts could favor transitions from uncoupled to coupled conformations, as we observe in the thicker di22:1PC model membranes. If this transition leads to a preferential alignment of M4 perpendicular to the membrane surface, the increased hydrophobic length of M4 should promote trafficking to the cell surface. Such a mechanism could explain why nicotine acts as a chaperone to promote cell-surface expression of the high affinity $(\alpha4)_2(\beta2)_3$ nAChR versus the lower affinity $(\alpha4)_3(\beta2)_2$ nAChR (Xiao et al., 2009). Preferential nicotine binding could lead to maturation of the high affinity $(\alpha4)_2(\beta2)_3$ nAChRs toward coupled (resting or desensitized) conformations where M4 is aligned closer to the bilayer normal to promote cell-surface expression. In this scenario, limited binding would thus have minimal effect on the trafficking of the low affinity $(\alpha4)_3(\beta2)_2$ nAChR.

8.2.9 Role of lipids in the clustering of nAChRs in the plasma membrane

Both the clustering of nAChRs on the plasma membrane and the internalization of cytoplasmic membrane-located nAChRs are lipid raft-dependent(Zhu et al., 2006). Lowering cholesterol levels to disrupt lipid rafts leads to altered nAChR clustering and mobility on cell surfaces, rapid internalization, and ultimately enhances function of the surface-retained nAChRs (Almarza et al., 2014; Borroni and Barrantes, 2011; Borroni et al., 2007).

Although the molecular mechanisms underlying nAChR lipid-raft associations remain obscure, it has been shown that incorporation of the nAChR into model membranes containing anionic lipids, particularly PA, leads to a change in the packing properties of the surrounding bilayer (daCosta et al., 2002; Wenz and Barrantes, 2005). The nAChR concentrates cations, including protons, at the bilayer surface, facilitating the ordering of nearby anionic lipids (daCosta et al., 2004; Sturgeon and Baenziger, 2010). There appear to

be favorable interactions between the nAChR and ordered lipids, such as those found in lipid rafts.

Another intriguing observation is that affinity-purified and detergent solubilized *Torpedo* nAChR exhibits a PA-specific phospholipase C activity (Labriola et al., 2010). The hydrolysis product of PA, diacylglycerol, is a potent nAChR activator (Labriola et al., 2010). A nAChR-associated phospholipase activity could allow the nAChR itself to alter its own lipid micro-environment, which could have two effects. In the context of a lipid raft-associated receptor, nAChR-induced changes in the lipid micro-environment could lead to relatively long-term changes in nAChR activity and thus synaptic strength. Secondly, PA hydrolysis would reduce the number of negatively charged PA head groups in the nAChR micro-environment. Given the nAChR's ability to concentrate cations and interact preferentially with negative lipids, particularly PA, a loss of PA could create less favorable interactions between the nAChR and its surrounding lipids, which may ultimately lead to nAChR trafficking from a less favorable to more favorable lipid microenvironments. While the existence of this phospholipase activity in native membranes and its relation to nAChR activity *in vivo* both remain to be defined, these speculative hypotheses highlight the fact that we are just beginning to understand the complexities underlying nAChR–lipid interactions and the potential importance of these interactions *in vivo*.

8.2.10 Conclusions

Three decades of research have revealed both an exquisite sensitivity of the *Torpedo* nAChR to its surrounding lipid environment and a tremendous complexity to lipid–nAChR interactions. While many lipids likely influence function, cholesterol and anionic lipids play a vital role in stabilizing the nAChR in a functional conformation. Membrane physical properties also play a poorly understood role. Recent research has shown that even trace lipids found in complex membrane environments can impact on nAChR function. Considerable research is still required to fully understand how different lipids influence nAChR function in a biological context.

Lipids/membranes influence the nAChR by both conformational selection and kinetic mechanisms. Different lipids/membranes stabilize varying proportions of pre-existing

resting, open, desensitized, and uncoupled conformations, as well as influence the transitions between these conformational states. Although the mechanisms by which lipids/membranes interact preferentially with these different conformations/transition states to influence function remain obscure, increasing evidence points to a role for the outermost transmembrane α-helix in lipid sensing. Both lipid binding and bulk membrane effects likely influence M4 interactions with M1/M3 to alter function. One hypothesis is that lipid-sensitive interactions between M4 with M1/M3 ultimately influence interactions between post-M4 and the Cys-loop to regulate nAChR activity, although this still hypothesis requires rigorous testing.

A lipid-dependent uncoupled conformation has been identified that may form as a result of an M4-dependent loss of physical contact between the ECD and the TMD. While this conformation has only been conclusively demonstrated for *Torpedo* nAChRs in reconstituted membranes, it may also exist for other pLGICs. Functionally equivalent conformations have been detected with neuronal nAChRs, and with the detergent-solubilized prokaryotic pLGIC, ELIC. An important goal will be to test for existence of uncoupled nAChRs in biological membranes, and whether lipids or other allosteric modulators enhance the transition from uncoupled to coupled conformations to enhance synaptic communication.

There is considerable interest in the role of nAChRs in neurodegenerative diseases, such as Alzheimer's disease, Parkinson's disease, as well as in other neurological disorders, such as epilepsy and schizophrenia. The role of lipid–nAChR interactions in disease progression remains to be studied. Altered lipid profiles leading to altered lipid–nAChR interactions could lead to altered cholinergic activity, with small functional changes resulting in severe physiological effects. Fundamental knowledge of how different neuronal nAChRs respond to changes in their lipid environments may prove important for understanding the mechanisms of altered cholinergic activity during the course of human disease.

Chapter 9. References

Adams, P.D., Afonine, P.V., Bunkóczi, G., Chen, V.B., Davis, I.W., Echols, N., Headd, J.J., Hung, L.-W., Kapral, G.J., Grosse-Kunstleve, R.W., et al. (2010). PHENIX: a comprehensive Python-based system for macromolecular structure solution. Acta Crystallogr. D Biol. Crystallogr. *66*, 213–221.

Addona, G.H., Sandermann, H., Kloczewiak, M.A., Husain, S.S., and Miller, K.W. (1998). Where does cholesterol act during activation of the nicotinic acetylcholine receptor? Biochim Biophys Acta *1370*, 299–309.

Addona, G.H., Sandermann, H., Kloczewiak, M.A., and Miller, K.W. (2003). Low chemical specificity of the nicotinic acetylcholine receptor sterol activation site. Biochim Biophys Acta *1609*, 177–182.

Almarza, G., Sánchez, F., and Barrantes, F.J. (2014). Transient cholesterol effects on nicotinic acetylcholine receptor cell-surface mobility. PloS One *9*, e100346.

Althoff, T., Hibbs, R.E., Banerjee, S., and Gouaux, E. (2014). X-ray structures of GluCl in apo states reveal a gating mechanism of Cys-loop receptors. Nature *512*, 333–337.

Alves, D.S., Castello-Banyuls, J., Faura, C.C., and Ballesta, J.J. (2011). An extracellular RRR motif flanking the M1 transmembrane domain governs the biogenesis of homomeric neuronal nicotinic acetylcholine receptors. FEBS Lett *585*, 1169–1174.

Amici, S.A., McKay, S.B., Wells, G.B., Robson, J.I., Nasir, M., Ponath, G., and Anand, R. (2012). A highly conserved cytoplasmic cysteine residue in the alpha4 nicotinic acetylcholine receptor is palmitoylated and regulates protein expression. J Biol Chem *287*, 23119–23127.

Antollini, S.S., and Barrantes, F.J. (1998). Disclosure of discrete sites for phospholipid and sterols at the protein-lipid interface in native acetylcholine receptor-rich membrane. Biochemistry *37*, 16653–16662.

Antollini, S.S., Xu, Y., Jiang, H., and Barrantes, F.J. (2005). Fluorescence and molecular dynamics studies of the acetylcholine receptor gM4 transmembrane peptide in reconstituted systems. Mol Membr Biol *22*, 471–483.

Baenziger, J.E., and Corringer, P.-J. (2011). 3D structure and allosteric modulation of the transmembrane domain of pentameric ligand-gated ion channels. Neuropharmacology *60*, 116–125.

Baenziger, J.E., and daCosta, C.J.B. (2013). Molecular mechanisms of acetylcholine receptor-lipid interactions: from model membranes to human biology. Biophys Rev *5*, 1–9.

Baenziger, J.E., and Methot, N. (1995). Fourier transform infrared and hydrogen/deuterium exchange reveal an exchange-resistant core of alpha-helical peptide hydrogens in the nicotinic acetylcholine receptor. J Biol Chem *270*, 29129–29137.

Baenziger, J.E., Darsaut, T.E., and Morris, M.L. (1999). Internal dynamics of the nicotinic acetylcholine receptor in reconstituted membranes. Biochemistry *38*, 4905-11.

Baenziger, J.E., Morris, M.L., Darsaut, T.E., and Ryan, S.E. (2000). Effect of membrane lipid composition on the conformational equilibria of the nicotinic acetylcholine receptor. J Biol Chem *275*, 777–784.

Baenziger, J.E., Ryan, S.E., Goodreid, M.M., Vuong, N.Q., Sturgeon, R.M., and daCosta, C.J.B. (2008). Lipid composition alters drug action at the nicotinic acetylcholine receptor. Mol Pharmacol *73*, 880–890.

Baenziger, J.E., Hénault, C.M., Therien, J.P.D., and Sun, J. (2015). Nicotinic acetylcholine receptor-lipid interactions: Mechanistic insight and biological function. Biochim. Biophys. Acta - Biomembr. *1848*, 1806–1817.

Baenziger, J.E., Domville, J.A., and Therien, J.P.D. (2017). The Role of Cholesterol in the Activation of Nicotinic Acetylcholine Receptors. Curr. Top. Membr. *80*, 95–137.

Baier, C.J., and Barrantes, F.J. (2007). Sphingolipids are necessary for nicotinic acetylcholine receptor export in the early secretory pathway. J Neurochem *101*, 1072–1084.

Baier, C.J., Gallegos, C.E., Levi, V., and Barrantes, F.J. (2010). Cholesterol modulation of nicotinic acetylcholine receptor surface mobility. Eur Biophys J *39*, 213–227.

Baier, C.J., Fantini, J., and Barrantes, F.J. (2011). Disclosure of cholesterol recognition motifs in transmembrane domains of the human nicotinic acetylcholine receptor. Sci Rep *1*, 69.

Barrantes, F.J. (2002). Lipid matters: nicotinic acetylcholine receptor-lipid interactions. Mol Membr Biol *19*, 277–284.

Barrantes, F.J. (2003). Modulation of nicotinic acetylcholine receptor function through the outer and middle rings of transmembrane domains. Curr Opin Drug Discov Devel *6*, 620–632.

Barrantes, F.J. (2004). Structural basis for lipid modulation of nicotinic acetylcholine receptor function. Brain Res Brain Res Rev *47*, 71–95.

Barrantes, F.J. (2007). Cholesterol effects on nicotinic acetylcholine receptor. J Neurochem *103 Suppl 1*, 72–80.

Barrantes, F.J. (2015). Phylogenetic conservation of protein-lipid motifs in pentameric ligand-gated ion channels. Biochim Biophys Acta *1848*, 1796–1805.

Basak, S., Chatterjee, S., and Chakrapani, S. (2016). Site Directed Spin Labeling and EPR Spectroscopic Studies of Pentameric Ligand-Gated Ion Channels. J. Vis. Exp. JoVE.

Basak, S., Schmandt, N., Gicheru, Y., and Chakrapani, S. (2017). Crystal structure and dynamics of a lipid-induced potential desensitized-state of a pentameric ligand-gated channel. ELife *6*.

Beckstein, O., and Sansom, M.S. (2006). A hydrophobic gate in an ion channel: the closed state of the nicotinic acetylcholine receptor. Phys Biol *3*, 147–159.

Beeson, D., Webster, R., Ealing, J., Croxen, R., Brownlow, S., Brydson, M., Newsom-Davis, J., Slater, C., Hatton, C., Shelley, C., et al. (2003). Structural abnormalities of the AChR caused by mutations underlying congenital myasthenic syndromes. Ann N Acad Sci *998*, 114–124.

Beglov, D., and Roux, B. (1994). Finite representation of an infinite bulk system: Solvent boundary potential for computer simulations. J. Chem. Phys. *100*, 9050–9063.

Best, R.B., Zhu, X., Shim, J., Lopes, P.E.M., Mittal, J., Feig, M., and Mackerell, A.D. (2012). Optimization of the additive CHARMM all-atom protein force field targeting improved sampling of the backbone φ, ψ and side-chain χ(1) and χ(2) dihedral angles. J. Chem. Theory Comput. *8*, 3257–3273.

Bhushan, A., and McNamee, M.G. (1990). Differential scanning calorimetry and Fourier transform infrared analysis of lipid-protein interactions involving the nicotinic acetylcholine receptor. Biochim Biophys Acta *1027*, 93–101.

Blanton, M.P., and Cohen, J.B. (1992). Mapping the lipid-exposed regions in the *Torpedo californica* nicotinic acetylcholine receptor [published erratum appears in Biochemistry 1992 Jun 30;31(25):5951]. Biochemistry *31*, 3738–3750.

Blanton, M.P., and Cohen, J.B. (1994). Identifying the lipid-protein interface of the Torpedo nicotinic acetylcholine receptor: secondary structure implications. Biochemistry *33*, 2859–2872.

Blanton, M.P., Xie, Y., Dangott, L.J., and Cohen, J.B. (1999). The steroid promegestone is a noncompetitive antagonist of the Torpedo nicotinic acetylcholine receptor that interacts with the lipid-protein interface. Mol Pharmacol *55*, 269–278.

Bocquet, N., Prado de Carvalho, L., Cartaud, J., Neyton, J., Le Poupon, C., Taly, A., Grutter, T., Changeux, J.P., and Corringer, P.J. (2007). A prokaryotic proton-gated ion channel from the nicotinic acetylcholine receptor family. Nature *445*, 116–119.

Bocquet, N., Nury, H., Baaden, M., Le Poupon, C., Changeux, J.P., Delarue, M., and Corringer, P.J. (2009). X-ray structure of a pentameric ligand-gated ion channel in an apparently open conformation. Nature *457*, 111–114.

Bondarenko, V., Tillman, T., Xu, Y., and Tang, P. (2010). NMR structure of the transmembrane domain of the n-acetylcholine receptor beta2 subunit. Biochim Biophys Acta *1798*, 1608–1614.

Bondarenko, V., Mowrey, D.D., Tillman, T.S., Seyoum, E., Xu, Y., and Tang, P. (2014). NMR structures of the human alpha7 nAChR transmembrane domain and associated anesthetic binding sites. Biochim Biophys Acta *1838*, 1389–1395.

Borroni, V., and Barrantes, F.J. (2011). Cholesterol modulates the rate and mechanism of acetylcholine receptor internalization. J Biol Chem *286*, 17122–17132.

Borroni, V., Baier, C.J., Lang, T., Bonini, I., White, M.M., Garbus, I., and Barrantes, F.J. (2007). Cholesterol depletion activates rapid internalization of submicron-sized acetylcholine receptor domains at the cell membrane. Mol Membr Biol *24*, 1–15.

Bouzat, C., Bren, N., and Sine, S.M. (1994). Structural basis of the different gating kinetics of fetal and adult acetylcholine receptors. Neuron *13*, 1395–1402.

Bouzat, C., Roccamo, A.M., Garbus, I., and Barrantes, F.J. (1998). Mutations at lipid-exposed residues of the acetylcholine receptor affect its gating kinetics. Mol Pharmacol *54*, 146–153.

Bouzat, C., Barrantes, F., and Sine, S. (2000). Nicotinic receptor fourth transmembrane domain: hydrogen bonding by conserved threonine contributes to channel gating kinetics. J Gen Physiol *115*, 663–672.

Bouzat, C., Gumilar, F., del Carmen Esandi, M., and Sine, S.M. (2002). Subunit-selective contribution to channel gating of the M4 domain of the nicotinic receptor. Biophys J *82*, 1920–1929.

Bouzat, C., Gumilar, F., Spitzmaul, G., Wang, H.L., Rayes, D., Hansen, S.B., Taylor, P., and Sine, S.M. (2004). Coupling of agonist binding to channel gating in an ACh-binding protein linked to an ion channel. Nature *430*, 896–900.

Boyd, N.D., and Cohen, J.B. (1980). Kinetics of binding of [3H]acetylcholine to Torpedo postsynaptic membranes: association and dissociation rate constants by rapid mixing and ultrafiltration. Biochemistry *19*, 5353–5358.

Brannigan, G., Henin, J., Law, R., Eckenhoff, R., and Klein, M.L. (2008). Embedded cholesterol in the nicotinic acetylcholine receptor. Proc Natl Acad Sci U A *105*, 14418–14423.

Brejc, K., van Dijk, W.J., Klaassen, R.V., Schuurmans, M., van Der Oost, J., Smit, A.B., and Sixma, T.K. (2001). Crystal structure of an ACh-binding protein reveals the ligand-binding domain of nicotinic receptors. Nature *411*, 269–276.

Bretscher, M.S., and Munro, S. (1993). Cholesterol and the Golgi apparatus. Science *261*, 1280–1281.

Broadbent, S., Groot-Kormelink, P.J., Krashia, P.A., Harkness, P.C., Millar, N.S., Beato, M., and Sivilotti, L.G. (2006). Incorporation of the beta3 subunit has a dominant-negative effect on the function of recombinant central-type neuronal nicotinic receptors. Mol Pharmacol *70*, 1350–1357.

Brooks, B.R., Brooks, C.L., MacKerell, A.D., Nilsson, L., Petrella, R.J., Roux, B., Won, Y., Archontis, G., Bartels, C., Boresch, S., et al. (2009). CHARMM: The Biomolecular Simulation Program. J. Comput. Chem. *30*, 1545–1614.

Bruses, J.L., Chauvet, N., and Rutishauser, U. (2001). Membrane lipid rafts are necessary for the maintenance of the (alpha)7 nicotinic acetylcholine receptor in somatic spines of ciliary neurons. J Neurosci *21*, 504-12.

Budelier, M.M., Cheng, W.W.L., Chen, Z.-W., Bracamontes, J.R., Sugasawa, Y., Krishnan, K., Mydock-McGrane, L., Covey, D.F., and Evers, A.S. (2019). Common binding sites for cholesterol and neurosteroids on a pentameric ligand-gated ion channel. Biochim. Biophys. Acta Mol. Cell Biol. Lipids *1864*, 128–136.

Butler, D.H., and McNamee, M.G. (1993). FTIR analysis of nicotinic acetylcholine receptor secondary structure in reconstituted membranes. Biochim Biophys Acta *1150*, 17–24.

Butler, A.S., Lindesay, S.A., Dover, T.J., Kennedy, M.D., Patchell, V.B., Levine, B.A., Hope, A.G., and Barnes, N.M. (2009). Importance of the C-terminus of the human 5-HT3A receptor subunit. Neuropharmacology *56*, 292–302.

Caballero-Rivera, D., Cruz-Nieves, O.A., Oyola-Cintron, J., Torres-Nunez, D.A., Otero-Cruz, J.D., and Lasalde-Dominicci, J.A. (2012). Tryptophan scanning mutagenesis reveals distortions in the helical structure of the deltaM4 transmembrane domain of the Torpedo californica nicotinic acetylcholine receptor. Channels Austin *6*, 111–123.

Carswell, C.L., Rigden, M.D., and Baenziger, J.E. (2008). Expression, purification, and structural characterization of CfrA, a putative iron transporter from *Campylobacter jejuni*. J Bacteriol *190*, 5650–5662.

Carswell, C.L., Sun, J., and Baenziger, J.E. (2015a). Intramembrane Aromatic Interactions Influence the Lipid Sensitivities of Pentameric Ligand-gated Ion Channels. J Biol Chem *290*, 2496–2507.

Carswell, C.L., Hénault, C.M., Murlidaran, S., Therien, J.P.D., Juranka, P.F., Surujballi, J.A., Brannigan, G., and Baenziger, J.E. (2015b). Role of the Fourth Transmembrane α Helix in the Allosteric Modulation of Pentameric Ligand-Gated Ion Channels. Structure *23*, 1655–1664.

Chakrapani, S. (2015). EPR Studies of Gating Mechanisms in Ion Channels. Methods Enzym. *557*, 279–306.

Changeux, J.P., and Edelstein, S.J. (2005). Allosteric mechanisms of signal transduction. Science *308*, 1424–1428.

Changeux, J.P., Kasai, M., and Lee, C.Y. (1970). Use of a snake venom toxin to characterize the cholinergic receptor protein. Proc Natl Acad Sci U A *67*, 1241-7.

Chatterjee, A., Guo, J., Lee, H.S., and Schultz, P.G. (2013). A genetically encoded fluorescent probe in mammalian cells. J. Am. Chem. Soc. *135*, 12540–12543.

Chen, Q., Cheng, M.H., Xu, Y., and Tang, P. (2010a). Anesthetic binding in a pentameric ligand-gated ion channel: GLIC. Biophys J *99*, 1801–1809.

Chen, Q., Wells, M.M., Arjunan, P., Tillman, T.S., Cohen, A.E., Xu, Y., and Tang, P. (2018). Structural basis of neurosteroid anesthetic action on GABAA receptors. Nat. Commun. *9*, 3972.

Chen, V.B., Arendall, W.B., Headd, J.J., Keedy, D.A., Immormino, R.M., Kapral, G.J., Murray, L.W., Richardson, J.S., and Richardson, D.C. (2010b). MolProbity: all-atom structure validation for macromolecular crystallography. Acta Crystallogr. D Biol. Crystallogr. *66*, 12–21.

Chen, X., Webb, T.I., and Lynch, J.W. (2009). The M4 transmembrane segment contributes to agonist efficacy differences between alpha1 and alpha3 glycine receptors. Mol Membr Biol *26*, 321–332.

Chen, Z., Dillon, G.H., and Huang, R. (2004). Molecular determinants of proton modulation of glycine receptors. J Biol Chem *279*, 876–883.

Cheng, W.W.L., Chen, Z.-W., Bracamontes, J.R., Budelier, M.M., Krishnan, K., Shin, D.J., Wang, C., Jiang, X., Covey, D.F., Akk, G., et al. (2018). Mapping two neurosteroid-modulatory sites in the prototypic pentameric ligand-gated ion channel GLIC. J. Biol. Chem. *293*, 3013–3027.

Chiara, D.C., Jayakar, S.S., Zhou, X., Zhang, X., Savechenkov, P.Y., Bruzik, K.S., Miller, K.W., and Cohen, J.B. (2013). Specificity of intersubunit general anesthetic-binding sites in the transmembrane domain of the human α1β3γ2 γ-aminobutyric acid type A (GABAA) receptor. J. Biol. Chem. *288*, 19343–19357.

Corbin, J., Wang, H.H., and Blanton, M.P. (1998). Identifying the cholesterol binding domain in the nicotinic acetylcholine receptor with [125I]azido-cholesterol. Biochim Biophys Acta *1414*, 65–74.

Corringer, P.J., Galzi, J.L., Eisele, J.L., Bertrand, S., Changeux, J.P., and Bertrand, D. (1995). Identification of a new component of the agonist binding site of the nicotinic alpha 7 homooligomeric receptor. J Biol Chem *270*, 11749–11752.

Corringer, P.J., Bertrand, S., Galzi, J.L., Devillers-Thiery, A., Changeux, J.P., and Bertrand, D. (1999). Molecular basis of the charge selectivity of nicotinic acetylcholine receptor and related ligand-gated ion channels. Novartis Found Symp *225*, 215–224; discussion 224-30.

Corringer, P.J., Le Novere, N., and Changeux, J.P. (2000). Nicotinic receptors at the amino acid level. Annu Rev Pharmacol Toxicol *40*, 431–458.

Cory-Wright, J., Alqazzaz, M., Wroe, F., Jeffreys, J., Zhou, L., and Lummis, S.C.R. (2018). Aromatic Residues in the Fourth Transmembrane-Spanning Helix M4 Are Important for GABAρ Receptor Function. ACS Chem. Neurosci. *9*, 284–290.

Criado, M., Eibl, H., and Barrantes, F.J. (1982). Effects of lipids on acetylcholine receptor. Essential need of cholesterol for maintenance of agonist-induced state transitions in lipid vesicles. Biochemistry *21*, 3622–3629.

Criado, M., Eibl, H., and Barrantes, F.J. (1984). Functional properties of the acetylcholine receptor incorporated in model lipid membranes. Differential effects of chain length and head group of phospholipids on receptor affinity states and receptor-mediated ion translocation. J Biol Chem *259*, 9188–9198.

Cuello, L.G., Cortes, D.M., and Perozo, E. (2017). The gating cycle of a K+ channel at atomic resolution. ELife *6*.

Czajkowski, C., Kaufmann, C., and Karlin, A. (1993). Negatively charged amino acid residues in the nicotinic receptor delta subunit that contribute to the binding of acetylcholine. Proc Natl Acad Sci U A *90*, 6285–6289.

daCosta, C.J.B., and Baenziger, J.E. (2009). A lipid-dependent uncoupled conformation of the acetylcholine receptor. J Biol Chem *284*, 17819–17825.

daCosta, C.J.B., and Baenziger, J.E. (2013). Gating of pentameric ligand-gated ion channels: structural insights and ambiguities. Structure *21*, 1271–1283.

daCosta, C.J.B., and Sine, S.M. (2013). Stoichiometry for drug potentiation of a pentameric ion channel. Proc. Natl. Acad. Sci. *110*, 6595–6600.

daCosta, C.J.B., Ogrel, A.A., McCardy, E.A., Blanton, M.P., and Baenziger, J.E. (2002). Lipid-protein interactions at the nicotinic acetylcholine receptor. A functional coupling between nicotinic receptors and phosphatidic acid-containing lipid bilayers. J Biol Chem *277*, 201–208.

daCosta, C.J.B., Wagg, I.D., McKay, M.E., and Baenziger, J.E. (2004). Phosphatidic acid and phosphatidylserine have distinct structural and functional interactions with the nicotinic acetylcholine receptor. J Biol Chem *279*, 14967–14974.

daCosta, C.J.B., Kaiser, D.E., and Baenziger, J.E. (2005). Role of glycosylation and membrane environment in nicotinic acetylcholine receptor stability. Biophys J *88*, 1755–1764.

daCosta, C.J.B., Medaglia, S.A., Lavigne, N., Wang, S., Carswell, C.L., and Baenziger, J.E. (2009). Anionic lipids allosterically modulate multiple nicotinic acetylcholine receptor conformational equilibria. J Biol Chem *284*, 33841–33849.

daCosta, C.J.B., Michel Sturgeon, R., Hamouda, A.K., Blanton, M.P., and Baenziger, J.E. (2011). Structural characterization and agonist binding to human a4b2 nicotinic receptors. Biochem Biophys Res Commun *407*, 456–460.

daCosta, C.J.B., Dey, L., Therien, J.P., and Baenziger, J.E. (2013). A distinct mechanism for activating uncoupled nicotinic acetylcholine receptors. Nat Chem Biol *9*, 701–707.

Dani, J.A., and Bertrand, D. (2007). Nicotinic acetylcholine receptors and nicotinic cholinergic mechanisms of the central nervous system. Annu Rev Pharmacol Toxicol *47*, 699–729.

Dawaliby, R., Trubbia, C., Delporte, C., Masureel, M., Van Antwerpen, P., Kobilka, B.K., and Govaerts, C. (2016). Allosteric regulation of G protein-coupled receptor activity by phospholipids. Nat. Chem. Biol. *12*, 35–39.

Dellisanti, C.D., Yao, Y., Stroud, J.C., Wang, Z.Z., and Chen, L. (2007). Crystal structure of the extracellular domain of nAChR alpha1 bound to alpha-bungarotoxin at 1.94 A resolution. Nat Neurosci *10*, 953–962.

Dellisanti, C.D., Ghosh, B., Hanson, S.M., Raspanti, J.M., Grant, V.A., Diarra, G.M., Schuh, A.M., Satyshur, K., Klug, C.S., and Czajkowski, C. (2013). Site-directed spin labeling reveals pentameric ligand-gated ion channel gating motions. PLoS Biol *11*, e1001714.

Dennis, M., Giraudat, J., Kotzyba-Hibert, F., Goeldner, M., Hirth, C., Chang, J.Y., Lazure, C., Chretien, M., and Changeux, J.P. (1988). Amino acids of the Torpedo marmorata acetylcholine receptor alpha subunit labeled by a photoaffinity ligand for the acetylcholine binding site. Biochemistry *27*, 2346–2357.

Diaz-De Leon, R., Otero-Cruz, J.D., Torres-Nunez, D.A., Casiano, A., and Lasalde-Dominicci, J.A. (2008). Tryptophan scanning of the acetylcholine receptor's betaM4 transmembrane domain: decoding allosteric linkage at the lipid-protein interface with ion-channel gating. Channels Austin *2*, 439–448.

Domville, J.A., and Baenziger, J.E. (2018). An allosteric link connecting the lipid-protein interface to the gating of the nicotinic acetylcholine receptor. Sci. Rep. *8*, 3898.

Drenan, R.M., Nashmi, R., Imoukhuede, P., Just, H., McKinney, S., and Lester, H.A. (2008). Subcellular trafficking, pentameric assembly, and subunit stoichiometry of neuronal nicotinic acetylcholine receptors containing fluorescently labeled alpha6 and beta3 subunits. Mol Pharmacol *73*, 27–41.

Du, J., Lu, W., Wu, S., Cheng, Y., and Gouaux, E. (2015). Glycine receptor mechanism elucidated by electron cryo-microscopy. Nature *526*, 224–229.

Duret, G., Van Renterghem, C., Weng, Y., Prevost, M., Moraga-Cid, G., Huon, C., Sonner, J.M., and Corringer, P.J. (2011). Functional prokaryotic-eukaryotic chimera from the pentameric ligand-gated ion channel family. Proc Natl Acad Sci U A *108*, 12143–12148.

Ealing, J., Webster, R., Brownlow, S., Abdelgany, A., Oosterhuis, H., Muntoni, F., Vaux, D.J., Vincent, A., and Beeson, D. (2002). Mutations in congenital myasthenic syndromes reveal an epsilon subunit C-terminal cysteine, C470, crucial for maturation and surface expression of adult AChR. Hum Mol Genet *11*, 3087–3096.

Eisele, J.L., Bertrand, S., Galzi, J.L., Devillers-Thiery, A., Changeux, J.P., and Bertrand, D. (1993). Chimaeric nicotinic-serotonergic receptor combines distinct ligand binding and channel specificities. Nature *366*, 479–483.

Eldefrawi, M.E., Eldefrawi, A.T., Seifert, S., and O'Brien, R.D. (1972). Properties of lubrol-solubilized acetylcholine receptor from Torpedo electroplax. Arch Biochem Biophys *150*, 210–218.

Ellena, J.F., Blazing, M.A., and McNamee, M.G. (1983). Lipid-protein interactions in reconstituted membranes containing acetylcholine receptor. Biochemistry *22*, 5523–5535.

Emsley, P., Lohkamp, B., Scott, W.G., and Cowtan, K. (2010). Features and development of Coot. Acta Crystallogr. D Biol. Crystallogr. *66*, 486–501.

Epstein, M., and Racker, E. (1978). Reconstitution of carbamylcholine-dependent sodium ion flux and desensitization of the acetylcholine receptor from *Torpedo californica*. J Biol Chem *253*, 6660–6662.

Fantini, J., and Barrantes, F.J. (2009). Sphingolipid/cholesterol regulation of neurotransmitter receptor conformation and function. Biochim Biophys Acta *1788*, 2345–2361.

Fenster, C.P., Whitworth, T.L., Sheffield, E.B., Quick, M.W., and Lester, R.A.J. (1999). Upregulation of Surface α4β2 Nicotinic Receptors Is Initiated by Receptor Desensitization after Chronic Exposure to Nicotine. J. Neurosci. *19*, 4804–4814.

Fernandez Nievas, G.A., Barrantes, F.J., and Antollini, S.S. (2008). Modulation of nicotinic acetylcholine receptor conformational state by free fatty acids and steroids. J Biol Chem *283*, 21478–21486.

Fernandez-Ballester, G., Castresana, J., Fernandez, A.M., Arrondo, J.L., Ferragut, J.A., and Gonzalez-Ros, J.M. (1994). A role for cholesterol as a structural effector of the nicotinic acetylcholine receptor. Biochemistry *33*, 4065–4071.

Fong, T.M., and McNamee, M.G. (1986). Correlation between acetylcholine receptor function and structural properties of membranes. Biochemistry *25*, 830-40.

Fong, T.M., and McNamee, M.G. (1987). Stabilization of acetylcholine receptor secondary structure by cholesterol and negatively charged phospholipids in membranes. Biochemistry *26*, 3871–3880.

Forman, S.A., and Miller, K.W. (2016). Mapping General Anesthetic Sites in Heteromeric γ-Aminobutyric Acid Type A Receptors Reveals a Potential For Targeting Receptor Subtypes. Anesth. Analg. *123*, 1263–1273.

Forman, S.A., Chiara, D.C., and Miller, K.W. (2015). Anesthetics target interfacial transmembrane sites in nicotinic acetylcholine receptors. Neuropharmacology *96*, 169–177.

Gallegos, C.E., Pediconi, M.F., and Barrantes, F.J. (2007). Ceramides modulate cell-surface acetylcholine receptor levels. Biochim Biophys Acta.

Galzi, J.L., Revah, F., Black, D., Goeldner, M., Hirth, C., and Changeux, J.P. (1990). Identification of a novel amino acid alpha-tyrosine 93 within the cholinergic ligands-binding sites of the acetylcholine receptor by photoaffinity labeling. Additional evidence for a three-loop model of the cholinergic ligands-binding sites. J Biol Chem *265*, 10430–10437.

Galzi, J.L., Devillers-Thiery, A., Hussy, N., Bertrand, S., Changeux, J.P., and Bertrand, D. (1992). Mutations in the channel domain of a neuronal nicotinic receptor convert ion selectivity from cationic to anionic. Nature *359*, 500–505.

Garbus, I., Roccamo, A.M., and Barrantes, F.J. (2002). Identification of threonine 422 in transmembrane domain alpha M4 of the nicotinic acetylcholine receptor as a possible site of interaction with hydrocortisone. Neuropharmacology *43*, 65–73.

Gharpure, A., Teng, J., Zhuang, Y., Noviello, C.M., Walsh, R.M., Cabuco, R., Howard, R.J., Zaveri, N.T., Lindahl, E., and Hibbs, R.E. (2019). Agonist Selectivity and Ion Permeation in the α3β4 Ganglionic Nicotinic Receptor. Neuron *104*, 501-511.e6.

Ghosh, B., Satyshur, K.A., and Czajkowski, C. (2013). Propofol binding to the resting state of the gloeobacter violaceus ligand-gated ion channel (GLIC) induces structural changes in the inter- and intrasubunit transmembrane domain (TMD) cavities. J Biol Chem *288*, 17420–17431.

Gielen, M., and Corringer, P.-J. (2018). The dual-gate model for pentameric ligand-gated ion channels activation and desensitization. J. Physiol. *596*, 1873–1902.

Gonzalez-Gutierrez, G., and Grosman, C. (2010). Bridging the gap between structural models of nicotinic receptor superfamily ion channels and their corresponding functional states. J Mol Biol *403*, 693–705.

Gonzalez-Gutierrez, G., and Grosman, C. (2015). The atypical cation-conduction and gating properties of ELIC underscore the marked functional versatility of the pentameric ligand-gated ion-channel fold. J Gen Physiol *146*, 15–36.

Gonzalez-Gutierrez, G., Lukk, T., Agarwal, V., Papke, D., Nair, S.K., and Grosman, C. (2012). Mutations that stabilize the open state of the *Erwinia chrisanthemi* ligand-gated ion channel fail to change the conformation of the pore domain in crystals. Proc Natl Acad Sci U A *109*, 6331–6336.

Grutter, T., de Carvalho, L.P., Dufresne, V., Taly, A., Edelstein, S.J., and Changeux, J.P. (2005). Molecular tuning of fast gating in pentameric ligand-gated ion channels. Proc Natl Acad Sci U A *102*, 18207–18212.

Haeger, S., Kuzmin, D., Detro-Dassen, S., Lang, N., Kilb, M., Tsetlin, V., Betz, H., Laube, B., and Schmalzing, G. (2010). An intramembrane aromatic network determines pentameric assembly of Cys-loop receptors. Nat Struct Mol Biol *17*, 90–98.

Hamouda, A.K., Chiara, D.C., Sauls, D., Cohen, J.B., and Blanton, M.P. (2006a). Cholesterol Interacts with Transmembrane alpha-Helices M1, M3, and M4 of the Torpedo Nicotinic Acetylcholine Receptor: Photolabeling Studies Using [(3)H]Azicholesterol. Biochemistry *45*, 976–986.

Hamouda, A.K., Sanghvi, M., Sauls, D., Machu, T.K., and Blanton, M.P. (2006b). Assessing the lipid requirements of the *Torpedo californica* nicotinic acetylcholine receptor. Biochemistry *45*, 4327–4337.

Hassaine, G., Deluz, C., Grasso, L., Wyss, R., Tol, M.B., Hovius, R., Graff, A., Stahlberg, H., Tomizaki, T., Desmyter, A., et al. (2014). X-ray structure of the mouse serotonin 5-HT receptor. Nature.

Heidmann, T., and Changeux, J.P. (1979). Fast kinetic studies on the interaction of a fluorescent agonist with the membrane-bound acetylcholine receptor from Torpedo marmorata. Eur J Biochem *94*, 255–279.

Heidmann, T., Sobel, A., Popot, J.L., and Changeux, J.P. (1980). Reconstitution of a functional acetylcholine receptor. Conservation of the conformational and allosteric transitions and recovery of the permeability response; role of lipids. Eur J Biochem *110*, 35–55.

Hénault, C.M., Sun, J., Therien, J.P.D., DaCosta, C.J.B., Carswell, C.L., Labriola, J.M., Juranka, P.F., and Baenziger, J.E. (2015a). The role of the M4 lipid-sensor in the folding, trafficking, and allosteric modulation of nicotinic acetylcholine receptors. Neuropharmacology *96*, 157–168.

Hénault, C.M., Juranka, P.F., and Baenziger, J.E. (2015b). The M4 transmembrane α-helix contributes differently to both the maturation and function of two prokaryotic pentameric ligand-gated ion channels. J. Biol. Chem. *290*, 25118–25128.

Hénin, J., Salari, R., Murlidaran, S., and Brannigan, G. (2014). A predicted binding site for cholesterol on the GABAA receptor. Biophys. J. *106*, 1938–1949.

Hibbs, R.E., and Gouaux, E. (2011). Principles of activation and permeation in an anion-selective Cys-loop receptor. Nature *474*, 54–60.

Hilf, R.J., and Dutzler, R. (2008). X-ray structure of a prokaryotic pentameric ligand-gated ion channel. Nature *452*, 375–379.

Hilf, R.J., and Dutzler, R. (2009). Structure of a potentially open state of a proton-activated pentameric ligand-gated ion channel. Nature *457*, 115–118.

Hilf, R.J., Bertozzi, C., Zimmermann, I., Reiter, A., Trauner, D., and Dutzler, R. (2010). Structural basis of open channel block in a prokaryotic pentameric ligand-gated ion channel. Nat Struct Mol Biol *17*, 1330–1336.

Hille, B. (2001). Ion Channels of Excitable Membranes (Sunderland, Massachusetts U.S.A.: Sinauer Associates, Inc.).

Hosie, A.M., Wilkins, M.E., da Silva, H.M., and Smart, T.G. (2006). Endogenous neurosteroids regulate $GABA_A$ receptors through two discrete transmembrane sites. Nature *444*, 486–489.

Huang, R.Q., and Dillon, G.H. (1999). Effect of extracellular pH on GABA-activated current in rat recombinant receptors and thin hypothalamic slices. J Neurophysiol *82*, 1233–1243.

Huang, X., Shaffer, P.L., Ayube, S., Bregman, H., Chen, H., Lehto, S.G., Luther, J.A., Matson, D.J., McDonough, S.I., Michelsen, K., et al. (2017). Crystal structures of human glycine receptor α3 bound to a novel class of analgesic potentiators. Nat. Struct. Mol. Biol. *24*, 108–113.

Humphrey, W., Dalke, A., and Schulten, K. (1996). VMD: Visual molecular dynamics. J. Mol. Graph. *14*, 33–38.

Jansen, M., Bali, M., and Akabas, M.H. (2008). Modular design of Cys-loop ligand-gated ion channels: functional 5-HT3 and GABA rho1 receptors lacking the large cytoplasmic M3M4 loop. J. Gen. Physiol. *131*, 137–146.

Jha, A., Cadugan, D.J., Purohit, P., and Auerbach, A. (2007). Acetylcholine receptor gating at extracellular transmembrane domain interface: the cys-loop and M2-M3 linker. J Gen Physiol *130*, 547–558.

Jin, X., and Steinbach, J.H. (2011). A portable site: a binding element for 17beta-estradiol can be placed on any subunit of a nicotinic alpha4beta2 receptor. J Neurosci *31*, 5045–5054.

Jo, S., Lim, J.B., Klauda, J.B., and Im, W. (2009). CHARMM-GUI Membrane Builder for mixed bilayers and its application to yeast membranes. Biophys J *97*, 50–58.

Jones, A.K., and Sattelle, D.B. (2010). Diversity of insect nicotinic acetylcholine receptor subunits. Adv Exp Med Biol *683*, 25–43.

Jones, O.T., and McNamee, M.G. (1988). Annular and nonannular binding sites for cholesterol associated with the nicotinic acetylcholine receptor. Biochemistry *27*, 2364–2374.

Jorgensen, W., Chandrasekhar, J., Madura, J., Impey, R., and Klein, M. (1983). Comparison of Simple Potential Functions for Simulating Liquid Water. J Chem Phys *79*, 926–935.

Kabsch, W. (2010). XDS. Acta Crystallogr. D Biol. Crystallogr. *66*, 125–132.

Kalamida, D., Poulas, K., Avramopoulou, V., Fostieri, E., Lagoumintzis, G., Lazaridis, K., Sideri, A., Zouridakis, M., and Tzartos, S.J. (2007). Muscle and neuronal nicotinic acetylcholine receptors. Structure, function and pathogenicity. FEBS J *274*, 3799–3845.

Kao, P.N., and Karlin, A. (1986). Acetylcholine receptor binding site contains a disulfide cross-link between adjacent half-cystinyl residues. J Biol Chem *261*, 8085–8088.

Karlsson, E., Heilbronn, E., and Widlund, L. (1972). Isolation of the nicotinic acetylcholine receptor by biospecific chromatography on insolubilized Naja naja neurotoxin. FEBS Lett *28*, 107–111.

Keramidas, A., Moorhouse, A.J., Schofield, P.R., and Barry, P.H. (2004). Ligand-gated ion channels: mechanisms underlying ion selectivity. Prog Biophys Mol Biol *86*, 161–204.

Kinde, M.N., Chen, Q., Lawless, M.J., Mowrey, D.D., Xu, J., Saxena, S., Xu, Y., and Tang, P. (2015). Conformational Changes Underlying Desensitization of the Pentameric Ligand-Gated Ion Channel ELIC. Structure *23*, 995–1004.

Klauda, J.B., Venable, R.M., Freites, J.A., O'Connor, J.W., Tobias, D.J., Mondragon-Ramirez, C., Vorobyov, I., MacKerell, A.D., and Pastor, R.W. (2010). Update of the CHARMM all-atom additive force field for lipids: validation on six lipid types. J. Phys. Chem. B *114*, 7830–7843.

Kozuska, J.L., and Paulsen, I.M. (2012). The Cys-loop pentameric ligand-gated ion channel receptors: 50 years on. Can. J. Physiol. Pharmacol. *90*, 771–782.

Kumar, P., Cymes, G.D., and Grosman, C. (2021). Structure and function at the lipid–protein interface of a pentameric ligand-gated ion channel. Proc. Natl. Acad. Sci. *118*.

Labriola, J.M., daCosta, C.J.B., Wang, S., Figeys, D., Smith, J.C., Sturgeon, R.M., and Baenziger, J.E. (2010). Phospholipase C activity affinity purifies with the *Torpedo* nicotinic acetylcholine receptor. J Biol Chem *285*, 10337–10343.

Labriola, J.M., Pandhare, A., Jansen, M., Blanton, M.P., Corringer, P.J., and Baenziger, J.E. (2013). Structural sensitivity of a prokaryotic pentameric ligand-gated ion channel to its membrane environment. J Biol Chem *288*, 11294–11303.

Laganowsky, A., Reading, E., Allison, T.M., Ulmschneider, M.B., Degiacomi, M.T., Baldwin, A.J., and Robinson, C.V. (2014). Membrane proteins bind lipids selectively to modulate their structure and function. Nature *510*, 172–175.

Laitko, U., Juranka, P.F., and Morris, C.E. (2006). Membrane stretch slows the concerted step prior to opening in a Kv channel. J Gen Physiol *127*, 687–701.

Lasalde, J.A., Tamamizu, S., Butler, D.H., Vibat, C.R., Hung, B., and McNamee, M.G. (1996). Tryptophan substitutions at the lipid-exposed transmembrane segment M4 of

Torpedo californica acetylcholine receptor govern channel gating. Biochemistry *35*, 14139–14148.

Laverty, D., Thomas, P., Field, M., Andersen, O.J., Gold, M.G., Biggin, P.C., Gielen, M., and Smart, T.G. (2017). Crystal structures of a GABAA-receptor chimera reveal new endogenous neurosteroid-binding sites. Nat. Struct. Mol. Biol. *24*, 977–985.

Laverty, D., Desai, R., Uchański, T., Masiulis, S., Stec, W.J., Malinauskas, T., Zivanov, J., Pardon, E., Steyaert, J., Miller, K.W., et al. (2019). Cryo-EM structure of the human α1β3γ2 GABAA receptor in a lipid bilayer. Nature *565*, 516–520.

LeBard, D.N., Henin, J., Eckenhoff, R.G., Klein, M.L., and Brannigan, G. (2012). General anesthetics predicted to block the GLIC pore with micromolar affinity. PLoS Comput Biol *8*, e1002532.

Ledesma, M.D., Martin, M.G., and Dotti, C.G. (2012). Lipid changes in the aged brain: effect on synaptic function and neuronal survival. Prog Lipid Res *51*, 23–35.

Lee, W.Y., and Sine, S.M. (2005). Principal pathway coupling agonist binding to channel gating in nicotinic receptors. Nature *438*, 243–247.

Lee, W.Y., Free, C.R., and Sine, S.M. (2009). Binding to gating transduction in nicotinic receptors: Cys-loop energetically couples to pre-M1 and M2-M3 regions. J Neurosci *29*, 3189–3199.

Lee, Y.H., Li, L., Lasalde, J., Rojas, L., McNamee, M., Ortiz-Miranda, S.I., and Pappone, P. (1994). Mutations in the M4 domain of Torpedo californica acetylcholine receptor dramatically alter ion channel function. Biophys J *66*, 646–653.

Leibel, W.S., Firestone, L.L., Legler, D.C., Braswell, L.M., and Miller, K.W. (1987). Two pools of cholesterol in acetylcholine receptor-rich membranes from Torpedo. Biochim Biophys Acta *897*, 249–260.

Li, L., and McNamee, M.G. (1992). Modulation of nicotinic acetylcholine receptor channel by pH: a difference in pH sensitivity of Torpedo and mouse receptors expressed in Xenopus oocytes. Cell Mol Neurobiol *12*, 83–93.

Li, P., and Steinbach, J.H. (2010). The neuronal nicotinic alpha4beta2 receptor has a high maximal probability of being open. Br J Pharmacol *160*, 1906–1915.

Li, L., Schuchard, M., Palma, A., Pradier, L., and McNamee, M.G. (1990). Functional role of the cysteine 451 thiol group in the M4 helix of the gamma subunit of Torpedo californica acetylcholine receptor. Biochemistry *29*, 5428–5436.

Li, L., Lee, Y.H., Pappone, P., Palma, A., and McNamee, M.G. (1992). Site-specific mutations of nicotinic acetylcholine receptor at the lipid-protein interface dramatically alter ion channel gating. Biophys J *62*, 61–63.

Lovell, S.C., Davis, I.W., Arendall, W.B., de Bakker, P.I., Word, J.M., Prisant, M.G., Richardson, J.S., and Richardson, D.C. (2003). Structure validation by Calpha geometry: phi,psi and Cbeta deviation.

Lummis, S.C., Beene, D.L., Lee, L.W., Lester, H.A., Broadhurst, R.W., and Dougherty, D.A. (2005). Cis-trans isomerization at a proline opens the pore of a neurotransmitter-gated ion channel. Nature *438*, 248–252.

Lundbaek, J.A., Andersen, O.S., Werge, T., and Nielsen, C. (2003). Cholesterol-induced protein sorting: an analysis of energetic feasibility. Biophys J *84*, 2080–2089.

MacKerell, A.D., Bashford, D., Bellott, M., Dunbrack, R.L., Evanseck, J.D., Field, M.J., Fischer, S., Gao, J., Guo, H., Ha, S., et al. (1998). All-atom empirical potential for molecular modeling and dynamics studies of proteins. J. Phys. Chem. B *102*, 3586–3616.

Manglik, A., Kobilka, B.K., and Steyaert, J. (2017). Nanobodies to Study G Protein-Coupled Receptor Structure and Function. Annu. Rev. Pharmacol. Toxicol. *57*, 19–37.

Mantipragada, S.B., Horvath, L.I., Arias, H.R., Schwarzmann, G., Sandhoff, K., Barrantes, F.J., and Marsh, D. (2003). Lipid-protein interactions and effect of local anesthetics in acetylcholine receptor-rich membranes from Torpedo marmorata electric organ. Biochemistry *42*, 9167–9175.

Marchand, S., Devillers-Thiery, A., Pons, S., Changeux, J.P., and Cartaud, J. (2002). Rapsyn escorts the nicotinic acetylcholine receptor along the exocytic pathway via association with lipid rafts. J Neurosci *22*, 8891–8901.

Marsh, D., and Barrantes, F.J. (1978). Immobilized lipid in acetylcholine receptor-rich membranes from Torpedo marmorata. Proc Natl Acad Sci U A *75*, 4329–4333.

Martens, C., Stein, R.A., Masureel, M., Roth, A., Mishra, S., Dawaliby, R., Konijnenberg, A., Sobott, F., Govaerts, C., and Mchaourab, H.S. (2016). Lipids modulate the conformational dynamics of a secondary multidrug transporter. Nat. Struct. Mol. Biol. *23*, 744–751.

Martin, M., Dotti, C.G., and Ledesma, M.D. (2010). Brain cholesterol in normal and pathological aging. Biochim Biophys Acta *1801*, 934–944.

Masiulis, S., Desai, R., Uchański, T., Serna Martin, I., Laverty, D., Karia, D., Malinauskas, T., Zivanov, J., Pardon, E., Kotecha, A., et al. (2019). GABAA receptor signalling mechanisms revealed by structural pharmacology. Nature *565*, 454–459.

McCarthy, M.P., and Moore, M.A. (1992). Effects of lipids and detergents on the conformation of the nicotinic acetylcholine receptor from Torpedo californica. J Biol Chem *267*, 7655–7663.

McNamee, M.G., and Fong, T.M. (1988). Effects of Membrane Lipids and Fluidity on Acetylcholine Receptor Function. In Lipid Domains and the Relationship to Membrane

Function, R.C. Aloia, C.C. Curtain, and L.M. Gordon, eds. (New York: Alan R. Liss, Inc.), pp. 43–62.

Methot, N., Demers, C.N., and Baenziger, J.E. (1995). Structure of both the ligand- and lipid-dependent channel-inactive states of the nicotinic acetylcholine receptor probed by FTIR spectroscopy and hydrogen exchange. Biochemistry *34*, 15142–15149.

Middleton, R.E., and Cohen, J.B. (1991). Mapping of the acetylcholine binding site of the nicotinic acetylcholine receptor: [3H]nicotine as an agonist photoaffinity label. Biochemistry *30*, 6987–6997.

Miledi, R., Molinoff, P., and Potter, L.T. (1971). Isolation of the cholinergic receptor protein of Torpedo electric tissue. Nature *229*, 554–557.

Miller, P.S., and Aricescu, A.R. (2014). Crystal structure of a human GABAA receptor. Nature *512*, 270–275.

Miller, P.S., Scott, S., Masiulis, S., De Colibus, L., Pardon, E., Steyaert, J., and Aricescu, A.R. (2017). Structural basis for GABAA receptor potentiation by neurosteroids. Nat. Struct. Mol. Biol. *24*, 986–992.

Mineur, Y.S., and Picciotto, M.R. (2008). Genetics of nicotinic acetylcholine receptors: Relevance to nicotine addiction. Biochem Pharmacol *75*, 323–333.

Mitra, A., Bailey, T.D., and Auerbach, A.L. (2004). Structural dynamics of the M4 transmembrane segment during acetylcholine receptor gating. Structure *12*, 1909–1918.

Miyazawa, A., Fujiyoshi, Y., and Unwin, N. (2003). Structure and gating mechanism of the acetylcholine receptor pore. Nature *424*, 949–955.

Moraga-Cid, G., Sauguet, L., Huon, C., Malherbe, L., Girard-Blanc, C., Petres, S., Murail, S., Taly, A., Baaden, M., Delarue, M., et al. (2015). Allosteric and hyperekplexic mutant phenotypes investigated on an alpha1 glycine receptor transmembrane structure. Proc Natl Acad Sci U A *112*, 2865–2870.

Morales-Perez, C.L., Noviello, C.M., and Hibbs, R.E. (2016). X-ray structure of the human a4b2 nicotinic receptor. Nature.

Mufson, E.J., Counts, S.E., Perez, S.E., and Ginsberg, S.D. (2008). Cholinergic system during the progression of Alzheimer's disease: therapeutic implications. Expert Rev Neurother *8*, 1703–1718.

Nashmi, R., Xiao, C., Deshpande, P., McKinney, S., Grady, S.R., Whiteaker, P., Huang, Q., McClure-Begley, T., Lindstrom, J.M., Labarca, C., et al. (2007). Chronic nicotine cell specifically upregulates functional alpha 4* nicotinic receptors: basis for both tolerance in midbrain and enhanced long-term potentiation in perforant path. J Neurosci *27*, 8202–8218.

Norimatsu, Y., Hasegawa, K., Shimizu, N., and Toyoshima, C. (2017). Protein-phospholipid interplay revealed with crystals of a calcium pump. Nature *545*, 193–198.

Noviello, C.M., Gharpure, A., Mukhtasimova, N., Cabuco, R., Baxter, L., Borek, D., Sine, S.M., and Hibbs, R.E. (2021). Structure and gating mechanism of the α7 nicotinic acetylcholine receptor. Cell *184*, 2121-2134.e13.

Nury, H., Bocquet, N., Le Poupon, C., Raynal, B., Haouz, A., Corringer, P.J., and Delarue, M. (2010a). Crystal structure of the extracellular domain of a bacterial ligand-gated ion channel. J Mol Biol *395*, 1114–1127.

Nury, H., Blesneac, I., Ravaud, S., and Pebay-Peyroula, E. (2010b). Structural approaches of the mitochondrial carrier family. Methods Mol Biol *654*, 105–117.

Nury, H., Delarue, M., and Corringer, P.J. (2011a). [X-ray structures of general anesthetics bound to their molecular targets]. Med Sci Paris *27*, 1056–1057.

Nury, H., Van Renterghem, C., Weng, Y., Tran, A., Baaden, M., Dufresne, V., Changeux, J.P., Sonner, J.M., Delarue, M., and Corringer, P.J. (2011b). X-ray structures of general anaesthetics bound to a pentameric ligand-gated ion channel. Nature *469*, 428–431.

Nys, M., Wijckmans, E., Farinha, A., Yoluk, Ö., Andersson, M., Brams, M., Spurny, R., Peigneur, S., Tytgat, J., Lindahl, E., et al. (2016). Allosteric binding site in a Cys-loop receptor ligand-binding domain unveiled in the crystal structure of ELIC in complex with chlorpromazine. Proc. Natl. Acad. Sci. *113*, E6696–E6703.

Ochoa, E.L., Dalziel, A.W., and McNamee, M.G. (1983). Reconstitution of acetylcholine receptor function in lipid vesicles of defined composition. Biochim Biophys Acta *727*, 151–162.

Olsen, R.W., Meunier, J.-C., and Changeux, J.-P. (1972). Progress in the purification of the cholinergic receptor protein from Electrophorus electricus by affinity chromatography. FEBS Lett. *28*, 96–100.

Ortiz-Acevedo, A., Melendez, M., Asseo, A.M., Biaggi, N., Rojas, L.V., and Lasalde-Dominicci, J.A. (2004). Tryptophan scanning mutagenesis of the gammaM4 transmembrane domain of the acetylcholine receptor from Torpedo californica. J Biol Chem *279*, 42250–42257.

Ortiz-Miranda, S.I., Lasalde, J.A., Pappone, P.A., and McNamee, M.G. (1997). Mutations in the M4 domain of the Torpedo californica nicotinic acetylcholine receptor alter channel opening and closing. J Membr Biol *158*, 17–30.

Pan, J., Chen, Q., Willenbring, D., Yoshida, K., Tillman, T., Kashlan, O.B., Cohen, A., Kong, X.P., Xu, Y., and Tang, P. (2012). Structure of the pentameric ligand-gated ion channel ELIC cocrystallized with its competitive antagonist acetylcholine. Nat Commun *3*, 714.

Paradiso, K., Zhang, J., and Steinbach, J.H. (2001). The C terminus of the human nicotinic alpha4beta2 receptor forms a binding site required for potentiation by an estrogenic steroid. J Neurosci *21*, 6561–6568.

Pardon, E., Laeremans, T., Triest, S., Rasmussen, S.G.F., Wohlkönig, A., Ruf, A., Muyldermans, S., Hol, W.G.J., Kobilka, B.K., and Steyaert, J. (2014). A general protocol for the generation of Nanobodies for structural biology. Nat. Protoc. *9*, 674–693.

Phillips, J.C., Braun, R., Wang, W., Gumbart, J., Tajkhorshid, E., Villa, E., Chipot, C., Skeel, R.D., Kalé, L., and Schulten, K. (2005). Scalable molecular dynamics with NAMD. J. Comput. Chem. *26*, 1781–1802.

Phulera, S., Zhu, H., Yu, J., Claxton, D.P., Yoder, N., Yoshioka, C., and Gouaux, E. (2018). Cryo-EM structure of the benzodiazepine-sensitive α1β1γ2S tri-heteromeric GABAA receptor in complex with GABA. ELife *7*.

Pons, S., Sallette, J., Bourgeois, J.P., Taly, A., Changeux, J.P., and Devillers-Thiery, A. (2004). Critical role of the C-terminal segment in the maturation and export to the cell surface of the homopentameric alpha 7-5HT3A receptor. Eur J Neurosci *20*, 2022–2030.

Prevost, M.S., Sauguet, L., Nury, H., Van Renterghem, C., Huon, C., Poitevin, F., Baaden, M., Delarue, M., and Corringer, P.J. (2012). A locally closed conformation of a bacterial pentameric proton-gated ion channel. Nat Struct Mol Biol *19*, 642–649.

Rahman, M.M., Teng, J., Worrell, B.T., Noviello, C.M., Lee, M., Karlin, A., Stowell, M.H.B., and Hibbs, R.E. (2020). Structure of the Native Muscle-type Nicotinic Receptor and Inhibition by Snake Venom Toxins. Neuron *106*, 952-962.e5.

Rankin, S.E., Addona, G.H., Kloczewiak, M.A., Bugge, B., and Miller, K.W. (1997). The cholesterol dependence of activation and fast desensitization of the nicotinic acetylcholine receptor. Biophys J *73*, 2446–2455.

Reyes-Ruiz, J.M., Ochoa-de la Paz, L.D., Martinez-Torres, A., and Miledi, R. (2010). Functional impact of serial deletions at the C-terminus of the human GABArho1 receptor. Biochim Biophys Acta *1798*, 1002–1007.

Rienzo, M., Lummis, S.C., and Dougherty, D.A. (2014). Structural requirements in the transmembrane domain of GLIC revealed by incorporation of noncanonical histidine analogs. Chem Biol *21*, 1700–1706.

Roccamo, A.M., and Barrantes, F.J. (2007). Charged amino acid motifs flanking each extreme of the alphaM4 transmembrane domain are involved in assembly and cell-surface targeting of the muscle nicotinic acetylcholine receptor. J Neurosci Res *85*, 285–293.

Ryan, S.E., Demers, C.N., Chew, J.P., and Baenziger, J.E. (1996). Structural effects of neutral and anionic lipids on the nicotinic acetylcholine receptor. An infrared difference spectroscopy study. J Biol Chem *271*, 24590–24597.

Sauguet, L., Poitevin, F., Murail, S., Van Renterghem, C., Moraga-Cid, G., Malherbe, L., Thompson, A.W., Koehl, P., Corringer, P.J., Baaden, M., et al. (2013). Structural basis for ion permeation mechanism in pentameric ligand-gated ion channels. EMBO J *32*, 728–741.

Sauguet, L., Shahsavar, A., Poitevin, F., Huon, C., Menny, A., Nemecz, A., Haouz, A., Changeux, J.P., Corringer, P.J., and Delarue, M. (2014). Crystal structures of a pentameric ligand-gated ion channel provide a mechanism for activation. Proc Natl Acad Sci U A *111*, 966–971.

Sayeed, W.M., and Baenziger, J.E. (2009). Structural characterization of the osmosensor ProP. Biochim Biophys Acta *1788*, 1108–1115.

Schaaf, C.P. (2014). Nicotinic acetylcholine receptors in human genetic disease. Genet. Med. *16*, 649–656.

Schmandt, N., Velisetty, P., Chalamalasetti, S.V., Stein, R.A., Bonner, R., Talley, L., Parker, M.D., McHaourab, H.S., Yee, V.C., Lodowski, D.T., et al. (2015). A chimeric prokaryotic pentameric ligand-gated channel reveals distinct pathways of activation. J Gen Physiol *146*, 323–340.

Schwede, T., Kopp, J., Guex, N., and Peitsch, M.C. (2003). SWISS-MODEL: An automated protein homology-modeling server. Nucleic Acids Res *31*, 3381–3385.

Sebastiao, A.M., Colino-Oliveira, M., Assaife-Lopes, N., Dias, R.B., and Ribeiro, J.A. (2013). Lipid rafts, synaptic transmission and plasticity: impact in age-related neurodegenerative diseases. Neuropharmacology *64*, 97–107.

She, J., Guo, J., Chen, Q., Zeng, W., Jiang, Y., and Bai, X.-C. (2018). Structural insights into the voltage and phospholipid activation of the mammalian TPC1 channel. Nature *556*, 130–134.

Shen, X.M., Deymeer, F., Sine, S.M., and Engel, A.G. (2006). Slow-channel mutation in acetylcholine receptor alphaM4 domain and its efficient knockdown. Ann Neurol *60*, 128–136.

Simons, K., and Sampaio, J.L. (2011). Membrane organization and lipid rafts. Cold Spring Harb. Perspect. Biol. *3*, a004697.

Smart, O.S., Womack, T.O., Flensburg, C., Keller, P., Paciorek, W., Sharff, A., Vonrhein, C., and Bricogne, G. (2012). Exploiting structure similarity in refinement: automated NCS and target-structure restraints in BUSTER. Acta Crystallogr. D Biol. Crystallogr. *68*, 368–380.

Spurny, R., Ramerstorfer, J., Price, K., Brams, M., Ernst, M., Nury, H., Verheij, M., Legrand, P., Bertrand, D., Bertrand, S., et al. (2012). Pentameric ligand-gated ion channel ELIC is activated by GABA and modulated by benzodiazepines. Proc Natl Acad Sci U A *109*, E3028-34.

Sturgeon, R.M., and Baenziger, J.E. (2010). Cations mediate interactions between the nicotinic acetylcholine receptor and anionic lipids. Biophys J *98*, 989–998.

Sunshine, C., and McNamee, M.G. (1992). Lipid modulation of nicotinic acetylcholine receptor function: the role of neutral and negatively charged lipids. Biochim Biophys Acta *1108*, 240–246.

Sunshine, C., and McNamee, M.G. (1994). Lipid modulation of nicotinic acetylcholine receptor function: the role of membrane lipid composition and fluidity. Biochim Biophys Acta *1191*, 59–64.

Taly, A., Corringer, P.J., Guedin, D., Lestage, P., and Changeux, J.P. (2009). Nicotinic receptors: allosteric transitions and therapeutic targets in the nervous system. Nat Rev Drug Discov *8*, 733–750.

Tamamizu, S., Lee, Y., Hung, B., McNamee, M.G., and Lasalde-Dominicci, J.A. (1999). Alteration in ion channel function of mouse nicotinic acetylcholine receptor by mutations in the M4 transmembrane domain. J Membr Biol *170*, 157–164.

Tamamizu, S., Guzman, G.R., Santiago, J., Rojas, L.V., McNamee, M.G., and Lasalde-Dominicci, J.A. (2000). Functional effects of periodic tryptophan substitutions in the alpha M4 transmembrane domain of the Torpedo californica nicotinic acetylcholine receptor. Biochemistry *39*, 4666–4673.

Tasneem, A., Iyer, L.M., Jakobsson, E., and Aravind, L. (2005). Identification of the prokaryotic ligand-gated ion channels and their implications for the mechanisms and origins of animal Cys-loop ion channels. Genome Biol *6*, R4.

Thompson, M.J., and Baenziger, J.E. (2020). Structural basis for the modulation of pentameric ligand-gated ion channel function by lipids. Biochim. Biophys. Acta Biomembr. *1862*, 183304.

Tillman, T.S., Seyoum, E., Mowrey, D.D., Xu, Y., and Tang, P. (2014). ELIC-alpha7 Nicotinic acetylcholine receptor (alpha7nAChR) chimeras reveal a prominent role of the extracellular-transmembrane domain interface in allosteric modulation. J Biol Chem *289*, 13851–13857.

Tobimatsu, T., Fujita, Y., Fukuda, K., Tanaka, K., Mori, Y., Konno, T., Mishina, M., and Numa, S. (1987). Effects of substitution of putative transmembrane segments on nicotinic acetylcholine receptor function. FEBS Lett *222*, 56–62.

Tol, M.B., Deluz, C., Hassaine, G., Graff, A., Stahlberg, H., and Vogel, H. (2013). Thermal unfolding of a mammalian pentameric ligand-gated ion channel proceeds at consecutive, distinct steps. J Biol Chem *288*, 5756–5769.

Tsetlin, V., Kuzmin, D., and Kasheverov, I. (2011). Assembly of nicotinic and other Cys-loop receptors. J Neurochem *116*, 734–741.

Ueno, S., Tsutsui, M., Toyohira, Y., Minami, K., and Yanagihara, N. (2004). Sites of positive allosteric modulation by neurosteroids on ionotropic gamma-aminobutyric acid receptor subunits. FEBS Lett *566*, 213–217.

Unwin, N. (2005). Refined structure of the nicotinic acetylcholine receptor at 4Å resolution. J Mol Biol *346*, 967–989.

Unwin, N., and Fujiyoshi, Y. (2012). Gating movement of acetylcholine receptor caught by plunge-freezing. J Mol Biol *422*, 617–634.

Vallejo, Y.F., Buisson, B., Bertrand, D., and Green, W.N. (2005). Chronic nicotine exposure upregulates nicotinic receptors by a novel mechanism. J Neurosci *25*, 5563–5572.

Velisetty, P., and Chakrapani, S. (2012). Desensitization Mechanism in Prokaryotic Ligand-gated Ion Channel. J Biol Chem *287*, 18467–18477.

Velisetty, P., Chalamalasetti, S.V., and Chakrapani, S. (2012). Conformational transitions underlying pore opening and desensitization in membrane-embedded *Gloeobacter violaceus* ligand-gated ion channel (GLIC). J Biol Chem *287*, 36864–36872.

Velisetty, P., Chalamalasetti, S.V., and Chakrapani, S. (2014). Structural basis for allosteric coupling at the membrane-protein interface in *Gloeobacter violaceus* ligand-gated ion channel (GLIC). J Biol Chem *289*, 3013–3025.

Vicente-Agullo, F., Rovira, J.C., Sala, S., Sala, F., Rodriguez-Ferrer, C., Campos-Caro, A., Criado, M., and Ballesta, J.J. (2001). Multiple roles of the conserved key residue arginine 209 in neuronal nicotinic receptors. Biochemistry *40*, 8300–8306.

Vuong, N., Baenziger, J.E., and Johnston, L.J. (2010). Preparation of reconstituted acetylcholine receptor membranes suitable for AFM imaging of lipid-protein interactions. Chem Phys Lipids *163*, 117–126.

Walsh, R.M., Roh, S.-H., Gharpure, A., Morales-Perez, C.L., Teng, J., and Hibbs, R.E. (2018). Structural principles of distinct assemblies of the human α4β2 nicotinic receptor. Nature *557*, 261–265.

Wang, H.L., Cheng, X., and Sine, S.M. (2012). Intramembrane proton binding site linked to activation of bacterial pentameric ion channel. J Biol Chem *287*, 6482–6489.

Wang, J.M., Zhang, L., Yao, Y., Viroonchatapan, N., Rothe, E., and Wang, Z.Z. (2002). A transmembrane motif governs the surface trafficking of nicotinic acetylcholine receptors. Nat Neurosci *5*, 963–970.

Wenz, J.J., and Barrantes, F.J. (2005). Nicotinic acetylcholine receptor induces lateral segregation of phosphatidic acid and phosphatidylcholine in reconstituted membranes. Biochemistry *44*, 398–410.

Whorton, M.R., and MacKinnon, R. (2011). Crystal structure of the mammalian GIRK2 K+ channel and gating regulation by G proteins, PIP2, and sodium. Cell *147*, 199–208.

Willenbring, D., Liu, L.T., Mowrey, D., Xu, Y., and Tang, P. (2011). Isoflurane alters the structure and dynamics of GLIC. Biophys J *101*, 1905–1912.

Williamson, P.T., Zandomeneghi, G., Barrantes, F.J., Watts, A., and Meier, B.H. (2005). Structural and dynamic studies of the g-M4 trans-membrane domain of the nicotinic acetylcholine receptor. Mol Membr Biol *22*, 485–496.

Winn, M.D., Ballard, C.C., Cowtan, K.D., Dodson, E.J., Emsley, P., Evans, P.R., Keegan, R.M., Krissinel, E.B., Leslie, A.G.W., McCoy, A., et al. (2011). Overview of the CCP4 suite and current developments. Acta Crystallogr. D Biol. Crystallogr. *67*, 235–242.

Xiao, C., Nashmi, R., McKinney, S., Cai, H., McIntosh, J.M., and Lester, H.A. (2009). Chronic nicotine selectively enhances alpha4beta2* nicotinic acetylcholine receptors in the nigrostriatal dopamine pathway. J Neurosci *29*, 12428–12439.

Xiu, X., Hanek, A.P., Wang, J., Lester, H.A., and Dougherty, D.A. (2005). A unified view of the role of electrostatic interactions in modulating the gating of Cys loop receptors. J Biol Chem *280*, 41655–41666.

Xu, Y., Barrantes, F.J., Luo, X., Chen, K., Shen, J., and Jiang, H. (2005). Conformational dynamics of the nicotinic acetylcholine receptor channel: a 35-ns molecular dynamics simulation study. J Am Chem Soc *127*, 1291–1299.

Zhu, D., Xiong, W.C., and Mei, L. (2006). Lipid rafts serve as a signaling platform for nicotinic acetylcholine receptor clustering. J Neurosci *26*, 4841–4851.

Zhu, S., Noviello, C.M., Teng, J., Walsh, R.M., Kim, J.J., and Hibbs, R.E. (2018). Structure of a human synaptic GABAA receptor. Nature *559*, 67–72.

Zimmermann, I., and Dutzler, R. (2011). Ligand activation of the prokaryotic pentameric ligand-gated ion channel ELIC. PLoS Biol *9*, e1001101.

Zimmermann, I., Marabelli, A., Bertozzi, C., Sivilotti, L.G., and Dutzler, R. (2012). Inhibition of the prokaryotic pentameric ligand-gated ion channel ELIC by divalent cations. PLoS Biol *10*, e1001429.

Curriculum Vitae – Camille Hénault

Profile

Graduate student in Biochemistry at uOttawa. Fast-tracked from MSc into PhD program in January 2015. Fully-funded graduate studies – recipient of NSERC and OGS scholarships at the MSc level, and NSERC at the PhD level, uOttawa Admissions and Excellence scholarships. Due to health concerns, a leave of absence was taken for 2 terms, slightly delaying completion.

Education

Graduate Studies

- University of Ottawa, Ottawa ON, K1N 6N5 (2013-Present)

PhD Biochemistry (transferred from MSc in 2015)

Undergraduate –Magna Cum Laude, May 2013

- University of Ottawa, Ottawa ON, *K1N 6N5* (2009-2013)

Program: Honours Specialization in Biochemistry, Biology minor

Work & Research Experience

Fall 2014 – Teaching Assistant (TA) BCH3170 Molecular Biology (130 hours)

Winter 2014, 2015 – TA BCH3125 Protein Structure and Function (130 hours)

Fall 2013-Present MSc/PhD student, Biochemistry Baenziger Lab

- Congenital myasthenic syndrome mutation in nicotinic acetylcholine receptor
- Membrane protein structural and functional lipid-dependence
- Responsible for training new lab members, and for laboratory inventory
- Graduate level courses:
  - BCH8101 – Physical and Chemical methods in Biochemistry (A+)
  - NSC8105 – Molecular Biology of the neuron (A+)
  - NSC8106 – Mechanisms of neurological disease (A+)
  - BCH8166 – Special Topics in Biochemistry II (A+)

2012 & 2013 (May – April) Summer Student /Honours Project, Baenziger Lab

- Pentameric ligand-gated ion channel characterization of structure and function.
- Protein expression, purification and reconstitution
- Protein thermal stability assays by FTIR
- Electrophysiology (TEVC)
- Molecular biology/Cloning/Mutagenesis

Awards received

- NSERC Canada Graduate Scholarship, PhD – CGS-D 2015-2019; $105,000
- University of Ottawa Dean's Scholarship; $1500
- Award of Excellence in Graduate Studies; $500
- Ontario Graduate Scholarship (OGS), Master's, 2014-2015; $15,000
- 2nd place poster winner, Protein Engineering Conference (Communication)
- NSERC Canada Graduate Scholarship, Master's – CGS-M 2013-2014; $17,500
- 1st place (MSc Biochemistry) in BMI poster day 2014; $100
- Excellence Scholarship/Admission Scholarship uOttawa; 2013-2015; $15,000
- 2x CTPNL Undergraduate Summer Research Award, 2012 & 2013; $2250
- 1st place Honours project poster day, Protein structure-function 2013; $100
- Merit Scholarship, 2012-2013; $1200, Merit Scholarship, 2011-2012; $750
- Dean's Honour list 2010-2013; Annual GPAs of 8.8, 9.3 and 9.8

Publications & Abstracts

Published Research Articles

Hénault, C.M., and Baenziger, J.E. (2017). Functional characterization of two prokaryotic pentameric ligand-gated ion channel chimeras – role of the GLIC transmembrane domain in proton sensing. Biochim. Biophys. Acta - Biomembr. *1859*, 218–227.

Hénault, C.M., Juranka, P.F., and Baenziger, J.E. (2015). The M4 transmembrane α-helix contributes differently to both the maturation and function of two prokaryotic pentameric ligand-gated ion channels. J. Biol. Chem. *290*, 25118–25128.

*Carswell, C.L., ***Hénault, C.M**., Murlidaran, S., Therien, J.P.D., Juranka, P.F., Surujballi, J.A., Brannigan, G., and Baenziger, J.E. (2015). Role of the Fourth Transmembrane α Helix in the Allosteric Modulation of Pentameric Ligand-Gated Ion Channels. Structure *23*, 1655–1664. *Co-First Author

Hénault, C.M., Govaerts, C., Spurny, R., Brams, M., Estrada-Mondragon, A., Lynch, J., Bertrand, D., Pardon, E., Evans, G.L., Woods, K., et al. (2019). A lipid site shapes the agonist response of a pentameric ligand-gated ion channel. Nat. Chem. Biol. *15*, 1156–1164.

Published Review Articles

Hénault, C.M., Sun, J., Therien, J.P.D., DaCosta, C.J.B., Carswell, C.L., Labriola, J.M., Juranka, P.F., and Baenziger, J.E. (2015a). The role of the M4 lipid-sensor in the folding, trafficking, and allosteric modulation of nicotinic acetylcholine receptors. Neuropharmacology *96*, 157–168.

Baenziger, J.E., **Hénault, C.M**., Therien, J.P.D., and Sun, J. (2015). Nicotinic acetylcholine receptor-lipid interactions: Mechanistic insight and biological function. Biochim. Biophys. Acta - Biomembr. *1848*, 1806–1817.

Non-refereed Contributions

Hénault et al, 2015. The role of the transmembrane α-helix, M4, in the potentiation of pentameric ligand-gated ion channels **(Contributed talk)**
1st Annual meeting of the Biophysical Society of Canada (June 2015)

Camille M Hénault*, Casey Carswell*, Sruthi Murlidan, JP Daniel Therien, Peter F Juranka, Julian A Surujballi, Grace Brannigan and John E Baenziger (2015). Role of the transmembrane α-helix, M4, in the potentiation of pentameric ligand-gated ion channels. (Co-first author*) Poster, presented at 59th Biophysical Society Meeting (international)

Camille M Hénault, Peter F Juranaka, Julian A Surujballi and John E Baenziger (2015). Divergent roles for M4 in the gating of two prokaryotic pentameric ligand-gated ion channels. Poster, presented by 2nd author at 59th Biophysical Society Meeting (international)

Camille M Hénault, Peter F Juranka, Julian A Surujballi and John E Baenziger. (2014). Sequence variability leads to distinct roles for M4 as an allosteric regulator of pentameric ligand-gated ion channels. Poster, presented at Canadian Neuroscience Meeting, (international) and at Protein Engineering Canada Conference (international).

Design and Characterization of a prokaryotic pLGIC Chimera. 4Th year honours thesis and poster, presented at uOttawa BMI Poster day. (1st prize)